CZECH TECHNICAL UNIVERSITY IN PRAGUE

Faculty of Civil Engineering
Department of Mechanics

Wang tiling for modelling of heterogeneous materials

DOCTORAL THESIS

Ing. Martin Doškář

Doctoral study programme: Physical and Materials Engineering

Branch of study: Civil Engineering

Doctoral thesis tutor: Ing. Jan Novák, Ph.D.
prof. Ing. Jan Zeman, Ph.D.

Prague, 2019

CZECH TECHNICAL UNIVERSITY IN PRAGUE
Faculty of Civil Engineering
Thákurova 7, 166 29 Praha 6

DECLARATION

Ph.D. student's name: Martin Doškář

Title of the doctoral thesis: Wang tiling for modelling of heterogeneous materials

I hereby declare that this doctoral thesis is my own work and effort written under the guidance of the tutor Ing. Jan Novák, Ph.D., and the co-supervisor prof. Ing. Jan Zeman, Ph.D.
All sources and other materials used have been quoted in the list of references.

The doctoral thesis was written in connection with the following research projects: GAČR 13-24027S and MPO FV10202.

In Prague on 6. 10. 2019

signature

Abstract

The concept of Wang tiles, investigated in this thesis, generalizes the standard microstructural representation based on a Periodic Unit Cell. Replacing a single cell with a set of domains—Wang tiles—with predefined mutual compatibility enables an efficient generation of stochastic, arbitrarily large realizations of the compressed microstructure. The Wang tile concept thus represents a reduced geometrical model for materials with random heterogeneous microstructures, appealing to applications where multiple stochastic realizations are needed.

In the first part of the thesis, two methods for designing the morphology of Wang tiles are presented. The first method modifies an existing design approach reported in Computer Graphics and supplements it with quantification via spatial statistics. The method constructs individual tiles by merging partially overlapping segments of a provided microstructural specimen. Albeit very efficient, this design method struggles with complex geometries such as foams. For these microstructures, an existing framework developed originally for Periodic Unit Cell's design is extended with the generalized periodicity constraints arising in the concept of Wang tiles. This method relies on an implicit description of the microstructural geometry via level-set fields to accelerate a standard packing algorithm and generate foam-like microstructures with simple morphing operations.

The next part of the thesis is focused on concept's applications in numerical homogenization. First, the particular case of a simplified two-dimensional beam model and its suitability for predicting the effective response of Alporas® foam is studied. In particular, the influence of neglecting the real geometry of foam ligaments on the overall response is investigated, comparing the values predicted for the simplified Voronoï and the real geometry. Second, a methodology for identifying the numerical Representative Volume Element size for a user-defined accuracy is developed, utilizing statistical sampling and the Partition theorem, which allows for bounding the apparent properties of a large material sample with calculations performed on a set of sub-samples.

In the final part of the thesis, a numerical scheme suited for macroscale analyses with a fully resolved microstructural geometry generated with the Wang tile concept is proposed. This scheme combines pre-calculated fluctuation fields, obtained without any prior knowledge about the shape of a macroscopic domain or its loading, and the Generalized Finite Element ansatz to construct microstructure-informed reduced modes for a given macroscopic problem.

Abstrakt

Koncept Wangova dláždění, jehož aplikace v úlohách spojených s modelováním materiálů se stochastickou mikrostrukturou jsou řešeny v rámci předkládané disertační práce, představuje zobecnění v současné době hojně využívaného popisu materiálové mikrostruktury pomocí periodické jednotkové buňky (PUC). Nahrazení této buňky sadou více modulů s předem definovanou návaznosti, tzv. Wangových dlaždic, umožňuje velmi efektivně vytvářet virtuální vzorky materiálové mikrostruktury o libovolné velikosti. Tento koncept je především zajímavý pro všechny aplikace, které řeší vliv náhodnosti v mikrostruktuře na odezvu zkoumaného materiálu.

První část disertační práce se věnuje metodám návrhu samotných dlaždic. První metoda kombinuje již existující přístupy počítačové grafiky a statistický popis materiálové mikrostruktury. Jednotlivé dlaždice vznikají spojením částečně se překrývajících poskytnutých materiálových vzorků. Ačkoli je tento přístup výpočetně velmi efektivní, není schopen dobře postihnout materiály, jejichž mikrostruktura obsahuje tenké filamenty. Pro tyto případy je vhodná druhá metoda, která upravuje existující způsob tvorby komplexních pěnových mikrostruktur vyvinutý pro periodickou jednotkovou buňku a rozšiřuje jej tak, aby zahrnoval zobecněnou periodicitu vyskytující se v konceptu Wangova dláždění. Tato metoda využívá implicitního popisu materiálové mikrostruktury založeného na úrovňových množinách k urychlení standardních částicových modelů a následné tvorbě pěnové mikrostruktury pomocí jednoduchých operací.

Druhá část disertační práce řeší aplikace konceptu Wangova dláždění v úlohách výpočetní homogenizace. Prvně je tento koncept využit pro studii vhodnosti dvourozměrného prutového modelu k predikci makroskopických mechanických vlastností hliníkové pěny Alporas®. Především je zde řešená otázku vlivu zjednodušení geometrie porovnáním výsledků pro modely založené na Voroného diagramu a modely, jejichž geometrie odpovídá získanému vzorku materiálu. Dále je v této části vyvinut postup pro určení velikosti representativního objemového vzorku (RVE) na základě uživatelem požadované přesnosti. Tento postup je založen na statistickém výběru a Partition teorému, který umožňuje odhadnout meze efektivní vlastnosti materiálového vzorku ze znalosti mezí určených pro jeho části.

V poslední části práce je představena numerická metoda vyvinutá pro makroskopické úlohy zahrnující materiálovou mikrosturu, která byla vytvořena pomocí konceptu Wangova dláždění. Tato metoda využívá předpočítané charakteristické odezvy Wangových dlaždic na parametrické zatížení. Tyto charakteristické odezvy jsou dále kombinovány se standardní diskretizací makroskopické úlohy v rámci zobecněné metody konečných prvků, čímž vzniká vhodná aproximační báze pro danou makroskopickou úlohu.

Acknowledgement

First and foremost, I would like to express my deepest gratitude to my supervisors, Jan Novák and Jan Zeman, for their friendly and encouraging supervision and support, without which this work could not have been done. Your passion for science and your deep knowledge has always been inspiring.

Words of thanks also belong to my colleagues and friends at Czech Technical University in Prague and the National Library of Technology. Jan, we have been like brothers in arms since our first steps and toy projects at the department. Alenka, Karel, Marek, and Ondřej, I could not wish for better office mates. Martin and Filip, I have really enjoyed our study sessions. Stephanie, thank you for all the time you spent correcting my Czenglish mistakes and the energy and enthusiasm you always share.

During my studies, I was also fortunate to spend some time abroad. Hereby I would like to thank Professor Ronald E. Miller from Carleton University in Ottawa; Professor Petr Krysl from the University of California San Diego (UCSD); Professor Samuel Forest and Professor David Ryckelynck from the Centre des Matériaux, MINES, ParisTech; Professor Felix Fritzen from the University of Stuttgart; and Professor Marc Geers from Eindhoven University of Technology (TU/e) for their hospitality. I am grateful to the Fulbright Commission Czech Republic, French Government Grants, and Ministry of Education, Youth and Sports that funded my research stays at UCSD, Centre des Matériaux, and TU/e, respectively. Frederic, Jean-François, Roxane, Phi, Alireza, Poorya, Rahgu, Juan-Manuel, Varun, Abdullah, Robin, thank you for making my stays such a great experience.

Most importantly, I want to thank my family for always being there for me.

The work was supported by the Czech Science Foundation, project No. 13–24027S, and Ministry of Industry and Trade of the Czech Republic, project No. FV10202. Continued support by the Grant Agency of the Czech Technical University in Prague through student projects Nos. SGS13/034/OHK1/1T/11, SGS14/028/OHK1/1T/11, SGS15/030/OHK1/1T/11, SGS16/037/OHK1/1T/11, SGS17/042/OHK1/1T/11, SGS18/036/OHK1/1T/11, and SGS19/033/OHK1/1T/11 is also gratefully acknowledged.

Contents

Chapter 1

Introduction

The majority of engineering materials exhibit heterogeneous composition (usually different compositions at different length scales). Their macroscopic response thus stems from the interplay between the properties and arrangement of individual components—the material microstructure. The ubiquitous emphasis on the efficiency of products, accented further by more recent environmental concerns related to a carbon footprint and material consumption in general, has been a driving force behind the quest for a better understanding of this structure-property relation since the first applications of composite materials [1].

A current trend is thus towards advanced computational schemes that incorporate increasingly more knowledge of the underlying material microstructures in order to enhance their predictive capability. With ever-growing and more available computational power, the traditional analytical homogenization methods, see e.g. the overview in [2], which typically include only selected statistics of the microstructural geometry (such as volume fractions or two-point probability functions), are being succeeded by computational homogenization approaches [3] in order to accurately capture the non-linear response and complex composition of microstructural constituents. For problems featuring a pronounced influence of microstructural geometry (such as crack initiation and propagation) without a clear separation of the micro- and macroscopic length scale, numerical models with fully [4, 5] or partially [6, 7] resolved material microstructure have even emerged recently. Microstructure modelling therefore continues to play an important role in advanced analysis strategies.

Compared to materials with regular, usually periodic microstructures, modelling materials with stochastic microstructural geometry is more demanding because any fixed size representation automatically induces information loss. Choosing a suitable microstructural model thus usually means finding the optimal balance between its applicability and accuracy. Since the seminal work of Povirk [8], many procedures have been developed for generating a compressed form of a microstructure by minimizing the discrepancy between spatial statistics of a reference microstructural sample and the artificially generated representation. Conversely, Liu and Shapiro [9] defined a model of a random heterogeneous material as a process—rather than a single representation—capable of generating microstructural samples with similar spatial statistics [10, 11, 12]. In the spirit of this definition, several methods that generate microstructural samples either from parts of a provided microstructural specimen [9, 13] or by mimicking a (proxy) process of material genesis were proposed; a more detailed overview is given in the following chapters and in Chapter 3, in particular.

The Wang tile concept generalizes the standard microstructural representation based on a Periodic Unit Cell (PUC) or its stochastic counterpart such as the Statistically Equivalent Periodic Unit Cell. Instead of characterizing the investigated microstructure with a single cell, the information about the material microstructure is compressed into a set of domains—Wang tiles—with predefined compatibility represented with edge codes. This generalization enables capturing higher variability in the microstructure. Unlike PUC, whose applicability is predominantly limited to multi-scale simulations in which the modelling error caused by artificial periodicity is acceptable, the Wang tile concept can be used to generate statistically consistent yet random virtual microstructural samples of arbitrary size. Moreover, due to the simplicity of an assembly algorithm, these samples can be generated almost instantly, including a finite element discretization if provided at the compressed level. This makes the concept particularly appealing for applications when stochastic microstructural realizations are needed, such as investigating the underlying size of Representative Volume Element or analyses of a macroscopic response's sensitivity to microstructural variations.

In the perspective of the aforementioned, the concept of Wang tiles represents a bridge between (i) a PUC-based representation, which can generate only a deterministic microstructure with pronounced artificial periodicity when used for microstructure generation, and (ii) approaches where a microstructural sample is generated each time anew such as optimization-based [8, 10, 11, 12] or newly emerging deep learning [14] methods, which are usually limited by their computational cost or predefined output size.

Following the two initial publications of Novák et al. [15, 16] on using the tiling concept in problems related to modelling materials with random heterogeneous microstructures, the objectives of this thesis were threefold:

i) Develop algorithms for generating the compressed, tile-based representation of material microstructures that would complement the computationally intensive, optimization-based approach reported in [15].

ii) Demonstrate the applicability of the Wang tile concept in numerical homogenization, and establish a statistical-based methodology to identify the necessary size of the numerical Representative Volume Element for a user-defined accuracy.

iii) Extract microstructure-informed fluctuation fields characteristic for the compressed tile-based representation, and develop a numerical scheme that will reuse these pre-computed responses to accelerate macroscopic analyses with fully-resolved microstructural details, following suggestions from [16].

The thesis is a collection of five manuscripts (published, under review, or in preparation) that are related to utilizing the tiling concept in modelling microstructures of heterogeneous materials and address the above-mentioned objectives. In these manuscripts, the author of the thesis carried out most of the studies, including implementation of the proposed algorithms, post-processing and interpretation of results, and drafting the manuscripts. Other authors contributed mainly to formulating the methodologies, overseeing the research, and reviewing the manuscripts.

The first two chapters are dedicated to development of methods for generating the compressed form of a material microstructure. Chapter 2 adopts the sample-based design of Wang tiles used in Computer Graphics [17] and supplements it with spatial statistics' quantification, which then governs the choice of optimal algorithm parameters. Chapter 3 builds on the unified framework for generating complex microstructures based on the

implicit description of microstructural geometry via level-set fields that was proposed by Sonon et al. [18, 19]. This framework is extended to take into account the generalized periodicity inherent to the Wang tile concept. Several modifications to the original algorithm are proposed, including a procedure capable of identifying the underlying vertex-based definition of a tile set.

Next two chapters demonstrate the use of the tiling concept in numerical homogenization, and determination of the Representative Volume Element (RVE) size in particular, benefiting from the concept's appealing ability to quickly generate stochastic realizations of the investigated microstructure. Chapter 4 deals with a specific case of a two-dimensional model of Alporas® aluminium foam. Motivated by the analysis of Němeček et al. [20], we investigate the adequacy of a two-dimensional beam model as a surrogate for a complex foam-like microstructure and the simplifying assumptions made in [20]. We also study the influence of approximating the real geometry of foam ligaments with Voronoï tessellation. Chapter 5 then formalizes the methodology for computing the numerical RVE size pertinent to a level of accuracy defined by a user, making use of a statistical hypothesis testing and confidence intervals obtained from statistical sampling. The procedure is illustrated with standard continuum models, and the related calculations are accelerated by implementing elementary ideas of domain decomposition.

Finally, in Chapter 6, a method for extracting characteristic fluctuation fields from the compressed microstructural representation based on Wang tiles is developed with an accompanying numerical scheme that uses these field as microstructure-informed enrichments in Generalize Finite Element method's ansatz in order to define macroscopic basis functions suited to analyses with fully-resolved microstructural details. The last chapter then summarizes the thesis and discusses potential extensions and outlooks for future work.

Since each chapter constitutes a standalone publication, certain overlaps may occur mainly in the introductory and summary parts of each chapter. Note also that the chapters' ordering does not strictly follow the chronological order of the individual manuscripts' publication; most notably, results from Section 4 motivated the development of the tile design strategy presented in Section 3.

Chapter 2

Tile design based on image quilting algorithm

Abstract:
The paper presents a concept/technique to compress and synthesize complex material morphologies that is based on Wang tilings. Specifically, a microstructure is stored in a set of Wang tiles and its reconstruction is performed by means of a stochastic tiling algorithm. A substantial part of the study is devoted to the setup of optimal parameters of the automatic tile design by means of parametric studies with statistical descriptors at heart. The performance of the method is demonstrated on four two-dimensional two-phase target systems, monodisperse media with hard and soft discs, sandstone, and high porosity metallic foam.

Reproduced from: Doškář, M., Novák, J., Zeman, J., 2014. Aperiodic compression and reconstruction of real-world material systems based on Wang tiles. Physical Review E 90, 062118. [21]

2.1 Introduction

Randomness and heterogeneity govern majority of real world processes. Indeed, materials which are considered as macroscopically homogeneous usually display heterogeneity across multiple scales, e.g. defects in crystalline or quasi-crystalline lattice, imperfect or entirely random particle packings, random distribution of pores or inclusions, etc. [2]. Regarding the incorporation of morphological information in multiscale simulations, it has progressed namely through a unit cell definition for heterogeneous materials exhibiting locally periodic arrangement of constituents [22, 23]. Moreover, the unit cell approach has also penetrated into the framework of random microstructures, namely due to the lack of an appropriate alternative, e.q. [8, 10, 24]. In this paper, we thus bring a generalization to the single unit cell concept that is based on Wang tiles and tailored especially for computer simulations of disordered material systems.

The concept of Wang tiles was introduced by Hao Wang in 1961 as a method to decide whether a certain class of logical statements can be proven by means of axioms of mathematical logic encoded in planar patterns [25, 26]. Afterwards, a focus was on the discovery of a finite set of tiles that could tile the infinite plane aperiodically in order to find counterexamples to Wang's decidability conjecture on statements mirrored in periodic sets[1].

The first result in this direction was obtained by Berger in 1966, who established a relation between aperiodic Wang tilings and the Turing-Davis halting problem and introduced the first finite aperiodic set consisting of 20,426 tiles [27], reduced to 104 later on [28]. Further developments were brought by Amman [28], who originated the discovery of the set of 16 tiles, and by Culik and Kari [29], who scored 13. Kari and Culik also introduced an extension to three dimensions by means of Wang cubes [30].

In addition to the strictly aperiodic constructions, tile sets that are not aperiodic themselves may allow for aperiodic tilings in a stochastic sense. This was first recognized by Cohen et al. [17], who used Wang tiles to produce irregular patterns for purposes of computer graphics as an extension of Stam's seminal idea based on aperiodic Amman's set [31]. Conforming edge information of Wang tiles was also instrumental in syntheses of biological motifs. In particular, the tiles were exploited for the assembly of DNA double-crossover molecules with edges playing the role of peptide bonds according to the Watson-Crick molecular complementarity [32]. In addition, the motifs based on DNA branched junctions were used together with tiles for self-assembly of aperiodic scaffolds in order to produce devices or specifically structured nanometre grids [33].

Wang tiles have also found use in Statistical Physics. To name a few, Amman's set was used for the modelling of nucleation of a metastable quasicrystalline phase [34] whose formation depends on the cooling rate of the alloy melt [35]. The model was based on the thermodynamics of Wang tilings studied earlier by Leuzzi et al. [36].

As for the micromechanics of materials, the application of Wang tiles to the compression of geometry of particulate suspensions was proposed in [15]. In this work, the tiles carry microstructural patterns designed to minimize a difference between spatial statistics of a target system and the reconstructed media. Preliminary results for tiles carrying patterns of mechanical fields were reported in [16].

[1] "What appears to be a reasonable conjecture, which has resisted proof or disproof so far (as of 1961) is: 4.1.2 The fundamental conjecture: A finite set of plates (meaning tiles) is solvable (has at least one solution) if and only if there exists a cyclic rectangle of the plates; or, in other words, a finite set of plates is solvable if and only if it has at least one periodic solution." [25]

In this paper, we further examine the potential of Wang tiles in compression of real world material systems. To this goal, tiles whose design rests on image fusion techniques [37, 17] are investigated and combined with statistics arguments in order to determine optimal setting of design parameters. The methodology is demonstrated on microstructural patterns of the media with uniformly distributed equi-sized hard and soft discs, sandstone, and closed cell aluminium foam Alporas®. The proximity of synthesized microstructures to reference specimens is quantified by means of the one- and two-point probability functions, and the two-point cluster function.

2.2 Background

Techniques combined in the present paper originate from various fields. A brief overview of relevant basics is given first as their omission would make the paper difficult reading.

2.2.1 Concept of stochastic Wang tilings

Basic elements of the concept are Wang (i) tiles, (ii) tile sets, and (iii) tilings. Wang tile is a square, jigsaw-like, quatrominoe piece capable of carrying arbitrary microstructural patterns within its entire domain including edges [26]. It is not allowed to be rotated or reflected when placed into a tiling, so that the tiles with an identical sequence of edges mutually rotated by $k\pi/4$ where $k \in \mathbb{N}$ are considered different.

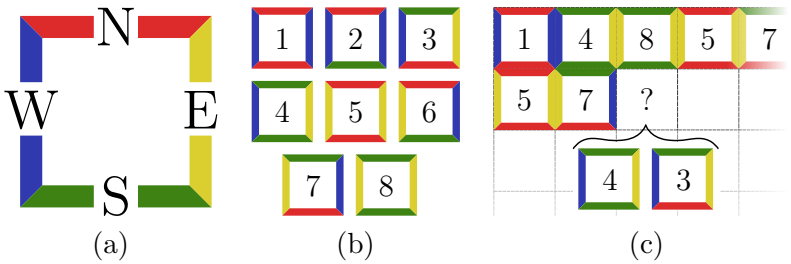

Figure 2.1: Wang tiling concept: (a) tile with coloured edges, (b) set W8/2-2, i.e. $n_1^{\mathrm{c}} = n_2^{\mathrm{c}} = 2$, $n^{\mathrm{t}} = 8$, $n^{\mathrm{NW}} = 2$, $c_1 \in \{\mathrm{green}, \mathrm{red}\}$, $c_2 \in \{\mathrm{blue}, \mathrm{yellow}\}$, and (c) single step of CSHD algorithm.

In applications, the edges are usually distinguished by colours [17], alphabetical codes [15], or enumerated by integers [29, 34], cf. Fig. 2.1a. A collection of tiles that enables to cover up an open planar domain is called a tile set, Fig. 2.1b, here referred to as $\mathrm{W}n^{\mathrm{t}}/n_1^{\mathrm{c}} - n_2^{\mathrm{c}}$, with cardinality n^{t} and n_i^{c} representing number of unique codes on horizontal ($i = 1$) and vertical ($i = 2$) edges, respectively [15]. The magnitude of n^{t} depends on the choice of n_i^{c}, so that it holds $n^{\mathrm{t}} = n^{\mathrm{NW}}\sqrt{n^{\mathrm{cs}}}$, where $n^{\mathrm{NW}} \in \mathbb{M} = \{2, \ldots, \sqrt{n^{\mathrm{cs}}}\}$. n^{cs} stands for the number of all four-tuples given by the admissible permutations of edge codes c_i, or in other words, it refers to the cardinality of the so called complete stochastic Wang tile set. Having the above notion at hand, notice that the set W1/1-1 corresponds to a single periodic unit cell (PUC).

Reconstruction/synthesis of a piece of microstructure gives a tiling. It is a discrete mapping of tiles from the set onto the centres of a square planar lattice, where each tile conforms with its neighbours through coincident edge codes or is bounded from outside. In addition, we assume that there are no gaps in the tiling.

When tiling the plane stochastically, the tiles are randomly selected from the set and successively placed one by one, either row-by-row or column-by-column, so that the edge codes of a newly placed tile must comply with those of its neighbours placed beforehand. Owing to the rectangular nature of Wang tiles, a pair of edges adjacent to north-western (NW) corner is controlled, Fig. 2.1c. The index of the tile to be placed is selected randomly from the subset, which stores the tiles of identical NW edge code combinations. Recall, n^{NW} must equal at least 2, the minimal cardinality of the subset, in order to keep the procedure random. Aperiodicity of resulting tilings is guaranteed assuming the random number generator to never return a periodic sequence of numbers. We call the resulting algorithm CSHD, in honour of its authors [17]. In order to give an impression on the distinction between tilings made up of aperiodic and stochastic sets, respectively, compare results in Fig. 2.2a and Fig. 2.2b. Clearly, the first method produces rather artificially looking patterns, while the latter leads to tilings with randomly distributed periodic clusters, e.g. the circled purple region in Fig. 2.2b. This phenomenon can be controlled by increasing n^{NW}, though at the expense of larger sets.

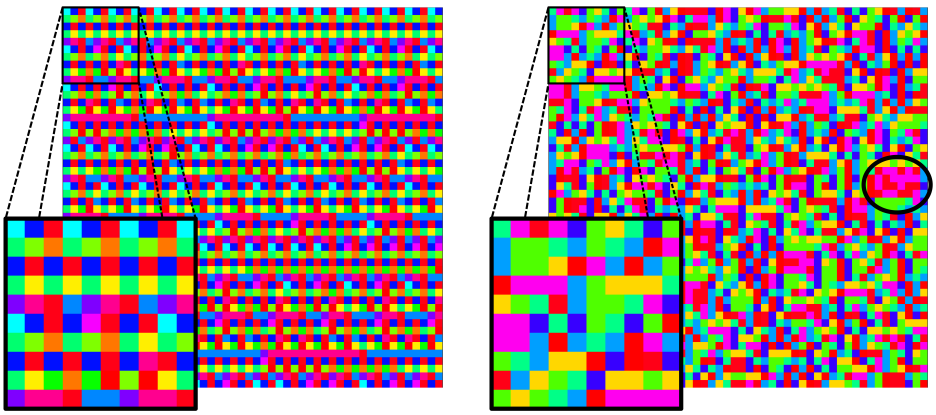

(a) (b)

Figure 2.2: Wang tilings consisting of 50×50 tiles (10×10 tiles in zoomed area) created by (a) Kari-Culik 13-tile set and related cellular automaton, and (b) W8/2-2 and CSHD algorithm. Individual tiles are distinguished by solid colours.

2.2.2 Image quilting

The proposed automatic design of tiles rests on the Image Quilting Algorithm (IQA) due to Efros et al. [37] that allows for the fusion of raster images without severe visual defects. It seeks for a continuous path along which the desired pieces of microstructure are glued together, minimizing the sum of square differences of pixel values (1/0 for binary media) restrained to a certain overlap. Assume a pair of samples A and B, both of the same height h and overlaying in a strip of the width ω. The local error in coincident pixels is defined as

$$e(i,j) = [A(i,j) - B(i,j)]^2 \text{for} \quad (i,j) \in \{1,\ldots,h\} \times \{1,\ldots,\omega\} \tag{2.1}$$

It gives rise to the cumulative error

$$E(i,j) = \begin{cases} e(i,j) & i = 1 \\ e(i,j) + \min\{E(i-1,j-1), E(i-1,j), E(i-1,j+1)\} & i \in \{2,\dots,h\} \end{cases} \tag{2.2}$$

where the non-defined entries $E(i,0)$ and $E(i,\omega+1)$ are excluded from consideration. The minimal cumulative error within the bottom row

$$E_Q = E(h,Q(h)) = \min\{E(h,j), j \in \{1,\dots,\omega\}\} \tag{2.3}$$

thus characterizes defects caused by the image fusion and determines the horizontal coordinate of sought quilting path $Q(h)$ in the bottom row. The remaining path coordinates $Q(i)$, $i = 1,\dots,h-1$, are found recursively by decrementing i

$$E(i,Q(i)) = \min\{E(i,Q(i-1)-1), E(i,Q(i-1)), E(i,Q(i-1)+1)\} \tag{2.4}$$

The simplicity of the algorithm is redeemed by noticing that the path can propagate only straight ahead or diagonally upwards. Moreover, it does not distinguish whether the path runs through inclusions or the matrix phase, yielding the inclusion shapes to deteriorate. This disadvantage, pronounced namely for binary media, can be reduced by recasting Eq. (2.1) as

$$e(i,j) = \begin{cases} 0, & \text{for} \quad A(i,j) \wedge B(i,j) \,\text{in matrix}\,, \\ 1, & \text{otherwise} \end{cases} \tag{2.5}$$

which leads to a modified algorithm referred to as IQAM in the sequel.

2.2.3 Statistical quantification of microstructure

Assuming a statistically homogeneous quasi-ergodic binary composite [38], we can best quantify the microstructure morphology by means of the n-point probability function S_n, which gives the probability of locating n points $\boldsymbol{x}_1,\dots,\boldsymbol{x}_n$ in a given phase. This phase corresponds to *inclusions* in what follows. In particular, it is understood as the white phase for hard discs, soft discs and sandstone, and black phase for Alporas®, see ahead Fig. 2.5. The second phase is referred to as a *matrix*.

Since we are primarily concerned with spatial correlations of multiples of the tile edge length ℓ, induced by the proposed compression framework, it is sufficient to limit the exposition to the two point probability $S_2(\boldsymbol{x}_1,\boldsymbol{x}_2) = S_2(\boldsymbol{x}_2-\boldsymbol{x}_1)$, which can be evaluated effectively in the Fourier space [2].

Short range defects arising from the quilting technique will be investigated by the two-point cluster function $C_2(\boldsymbol{x}_1,\boldsymbol{x}_2) = C_2(\boldsymbol{x}_2-\boldsymbol{x}_1)$ [39], which can be understood as a special case of S_2 function as it gives the probability of finding a pair of points $\boldsymbol{x}_1$ and $\boldsymbol{x}_2$ not only in the same phase, but also in the same cluster. The cluster is understood as the part of a phase where the two points $\boldsymbol{x}_1$ and $\boldsymbol{x}_2$ can be reached through a continuous path [40]. Thus, in addition to the information on distribution of inclusions in the matrix phase given by S_2, C_2 provides us with a short-range order description of inclusion shapes. A few limit cases can be distinguished. For distances $|\boldsymbol{x}_2-\boldsymbol{x}_1| > b_{\max}$, where $b_{\max}$ refers to the maximum dimension of the largest inclusion, we have $C_2 = 0$. The limit case $|\boldsymbol{x}_2-\boldsymbol{x}_1| = 0$ yields $C_2 = S_2 = S_1 = \phi$, where ϕ symbolizes the volume fraction (the one-point probability function).

2.3 Automatic design of tiles

In order to arrive at microstructure compressions consistent from the statistical viewpoint, the techniques introduced above are combined. Contrary to our previous study based on an optimization approach [15], the automatic design of tiles is proposed as it suits better complex morphologies under consideration and is computationally more efficient.

Following [37], an automatically designed tile arises as a diamond shape cut out from the aggregate of four overlapping square reference samples, here called r-samples, that are placed accordingly to the edge codes of the tile to be produced, Fig. 2.3. The four r-samples are fused within an overlap ω by means of the quilting algorithm and the resulting tile rotated by $\pi/4$. Its edge length yields from the r-samples dimension h and overlap width ω as

$$\ell = \lceil \sqrt{2}(h - \omega) \rceil \tag{2.6}$$

where $\lceil \cdot \rceil$ denotes the round up operation to the nearest integer.

The quilting paths among individual r-samples always propagate from the tile corners towards the centre. The continuity of the tiling microstructure across the edges is ensured by the facts that the cut is taken diagonally across the r-sample, and that the same r-sample is used for all edges sharing the same code.

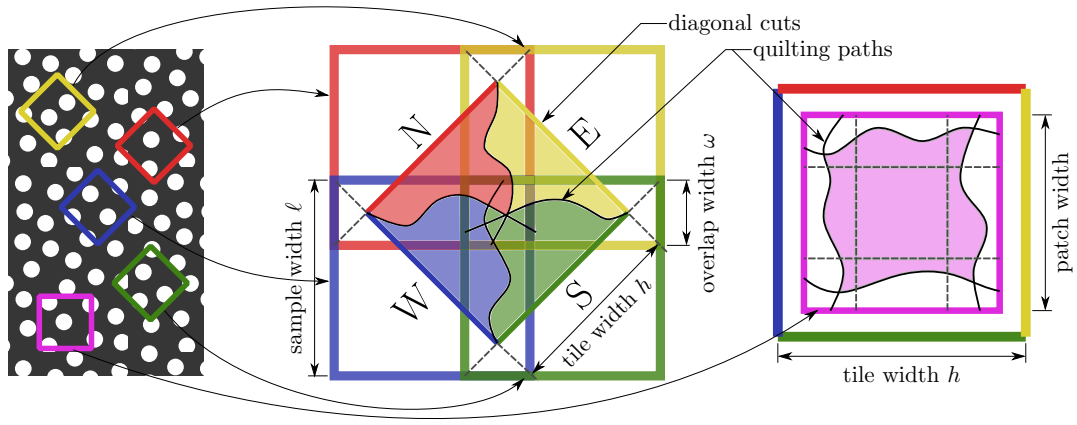

Figure 2.3: Illustration of Automatic tile design due to Cohen et al. [17] (a, b), and the proposed patch enrichment (c).

It has been shown in previous works that a specific morphology design technique may have an impact on the accuracy of the representation of long range orientation orders [15, 41, 16]. Induced artefacts related to repeating tile edges or interiors may dominate spatial features of synthesized microstructures [15]. Taking this into consideration, the automatic design procedure based on the fusion of the four r-samples leads to compressions that strongly emphasize tile edges to the interiors. This is obvious from Fig. 2.3b, noticing that almost the entire tile quarter is related to the edge information. A possible remedy proposed here is to replace a piece of the microstructure around the centre of automatically designed tiles by a square patch of the reference microstructure taken independently of the r-samples and quilted around its perimeter as drawn in Fig. 2.3c.

2.3.1 Optimal overlap and best quilting performer

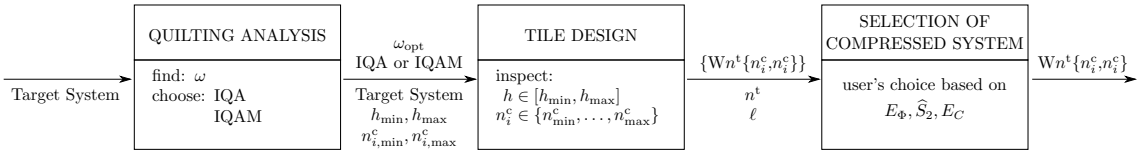

Figure 2.4: Sensitivity study flowchart to be passed through automatic tile design procedure. User defined input parameters are placed underneath arrow lines among individual cells. Outputs entering consecutive steps are written above them.

Four different target microstructures were considered in order to perform a sensitivity study on parameter values ω, h, and n^{c}_i with respect to the choice of the quilting algorithm IQA or IQAM, Fig. 2.4.

In particular, we have explored hard discs monodisperse (referred to as h-discs), Fig. 2.5a, soft discs monodisperse (p-discs), Fig. 2.5b, sandstone, Fig. 2.5c, and a large planar scan of Alporas® foam, Fig. 2.5d. Notice that several cross-sections of sandstone CT data were used due to the insufficiency of microstructural information contained in a single one.

The first aim was to find the optimal width of the overlap ω. For each material system, a pair of r-samples of $h = 300$ px was chosen randomly from the reference microstructure. We varied the parameter ω from 1 pixel up to $10 \times b$ pixels, where $b = \sqrt{b_1^2 + b_2^2}$, and b_i is the length of the mean inclusion bounding box in ith spatial direction. The minimum error path was sought after each increment and quantified according to Eq. (2.2). The whole process was repeated a hundred times to identify the sensitivity of the results to selection of different r-sample pairs, while keeping their height h unchanged.

Quite surprisingly at first glance, IQA outperforms IQAM in the sense of the norm defined by Eq. (2.2). For example, it can be observed that for the target system consisting of h-discs, Fig. 2.6a, IQA returns zero-error quilting path for $\omega/b > 6$, whereas its modified version IQAM increases the value ω/b over 9.5. No zero cumulative error path Q could be found for other material systems no matter the quilting algorithm we used. The errors exhibit similar asymptotic decay but the magnitude of the limit plateaus and oscillatory behaviour of the sandstone microstructure. Finding a quilting path as such is not the only problem related to the automatic design of tiles. Another difficulty arises from the random selection of r-samples and from the fact that we take systematically into account only a portion of the microstructural information they contain. Moreover, the quilting algorithms bring additional very local defects into the morphology which influences the quality of the designed tiles.

Therefore, we explored the quilting process also from the perspective of normalized deviation between phase volume fractions of the target and synthesized/reconstructed systems, ϕ^{TS} and ϕ^{RS}, respectively,

$$E_\phi = \frac{|\phi^{\text{RS}} - \phi^{\text{TS}}|}{\phi^{\text{TS}}} \tag{2.7}$$

and the relative error of the two-point cluster statistics defined as

$$E_C = \frac{\int_{(\omega \times h)} |{C_2}^{\text{RS}}(\boldsymbol{x}) - {C_2}^{\text{TS}}(\boldsymbol{x})| \, \mathrm{d}\boldsymbol{x}}{\int_{(\omega \times h)} {C_2}^{\text{TS}}(\boldsymbol{x}) \, \mathrm{d}\boldsymbol{x}} \tag{2.8}$$

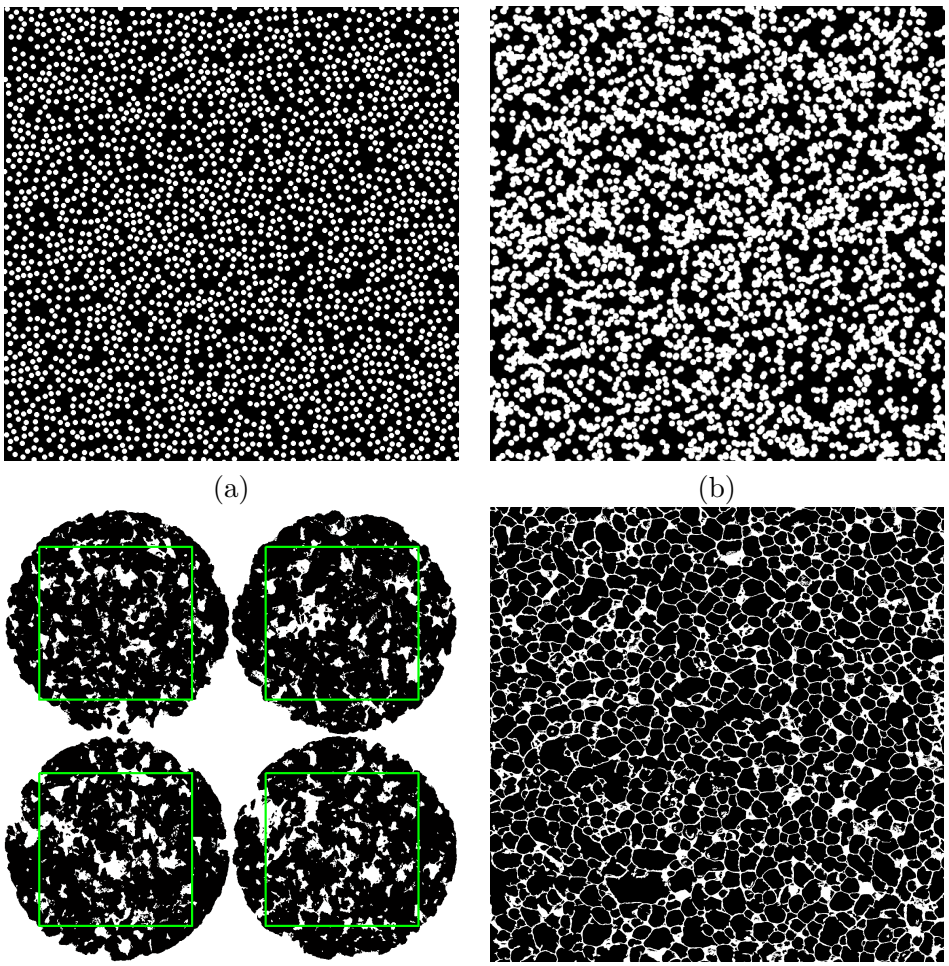

Figure 2.5: Target systems: (a) h-discs, (b) p-discs, (c) sandstone (Courtesy of Adrian Russell, UNSW, Sydney, Australia [42]), and (d) Alporas® (Courtesy of Jiří Němeček, CTU in Prague, Czech Republic [20]).

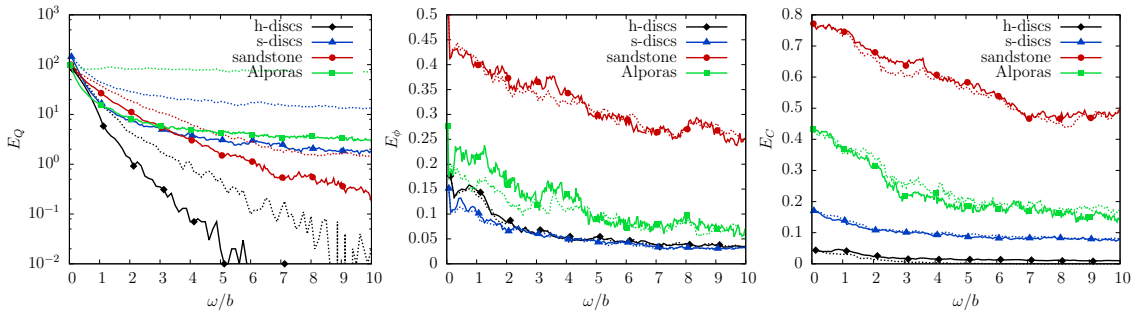

Figure 2.6: Optimal overlap width ω with respect to IQA (solid line), IQAM (dashed line), and various error measures. Plotted values represent means from 100 realizations.

Both IQA and IQAM demonstrate almost monotonic convergence in E_ϕ to a plateau value of about 0.05 for all materials except sandstone for which the error is still decreasing,

however, we were not able to proceed with the analysis further due to the limited dimensions of input microstructures, Fig. 2.6b. Almost the same behaviour can be observed for E_C, Fig. 2.6c.[2] It is also interesting to observe that the behaviour of IQAM in terms of spatial statistics is superior to the original version, namely for Alporas® and h-discs.

In summary, we can deduce that weakly packed dispersions are microstructural systems of the least complexity from the viewpoint of the automatic tile design, recall Fig. 2.6a. The performance of IQA seems less powerful compared to the results provided by its modified version, however, both procedures are equivalent for remaining material systems and larger overlaps.

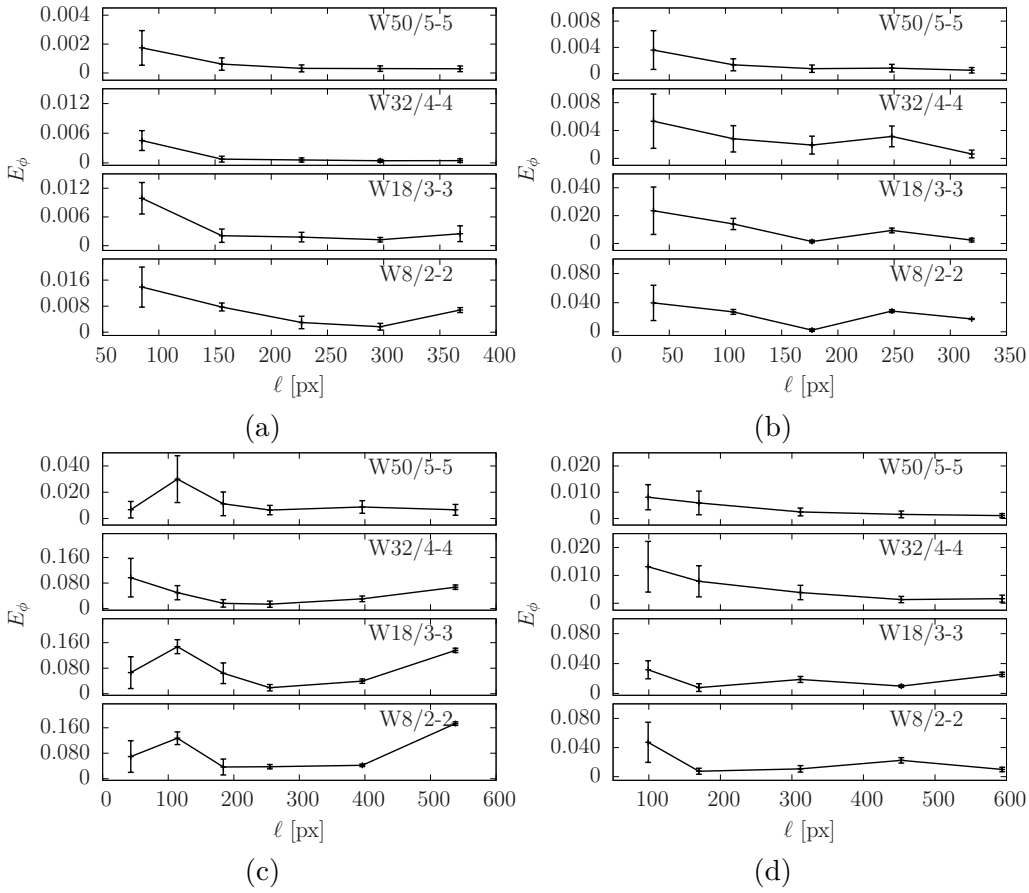

Figure 2.7: Relative error of pore phase volume fraction versus tile edge length and cardinality of sets. The results are normalized against ϕ^{TS}. (a) h-discs, (b) p-discs, (c) sandstone, and (d) Alporas®.

2.3.2 Optimal tile edge length and cardinality of sets

The optimal overlap ω, the second row of Tab. 2.1, determines together with the dimension of r-samples h, length of tile edges ℓ, Eq. (2.6). In addition, the size of r-samples depends on ℓ and cardinality of sets given by n^{t}, dominant parameters in terms of the storage of required amount of microstructural information.

[2]Degenerated inclusions at the boundary of overlap regions were excluded from calculations as they do not result from quilting algorithms.

Table 2.1: Optimal parameters of automatic design with respect to studied material systems

		h-discs	p-discs	sandstone	Alporas®
ω/b	[-]	5	5	6	6
ω	[px]	40	75	120	180
h	[px]	200	250	300	400
ℓ	[px]	227	107	255	312

To asses the optimal $n^{\mathrm{t}} - \ell$ combinations, various complete stochastic Wang tile sets were created. From each of those, subsets of n^{t} tiles with minimum errors E_ϕ were chosen.

By analogy to the paragraphs above, 100 realizations of 5×5 tilings were synthesized by means of CSHD algorithm. The optimal setup of sought objectives, particularly ℓ versus n^{t}, were assessed from the viewpoint of ϕ, S_2 and C_2. In addition, we quantify the secondary extremes of S_2 by means of a set

$$\widehat{S}_2 = \Big\{ S_2(m \times \ell, n \times \ell),\, \forall (m,n) \in \mathbb{Z}^2 \setminus (0,0) \Big\} \tag{2.9}$$

First, the behaviour of the relative error E_ϕ with respect to ℓ is displayed for individual sets in Fig. 2.7. From the graphs, it can be deduced that the scatter in volume fractions decreases for larger tiles and sets of higher cardinalities, independently of the material system. However, in some cases (h-discs W8/2-2 and W18/3-3, sandstone all sets but W50/5-5, and Alporas® W18/3-3) the error suddenly increases after the initial decay. In general, the reconstructions for h-discs, Fig. 2.7a, possess the least scatter from the target data, while the largest error is attributed to sandstone, Fig. 2.7c. As for the higher order statistics, obtained results (not shown) proved the tile edge length ℓ to have a negligible effect on reducing secondary extremes of S_2, Eq. (2.9), as well as no impact on the deviation between the two-point cluster functions of target and synthesized systems quantified by Eq. (2.8), this time, with integrals over the domain of the tilings instead of $\omega \times h$.

On the other hand, the benefits of increasing the set cardinality are doubtless. In Fig. 2.8a, we show the statistics of the secondary extremes $\widehat{S}_2$, Eq. (2.9), by means of whiskerbar plots. The mean value of the set of secondary extremes $\widehat{S}_2$ seems to correspond well with the relation proposed in [15]

$$\widehat{S}_2^{\mathrm{p}} = \frac{\phi^t}{n^{\mathrm{t}}} \Big[\phi + (n^{\mathrm{t}} - 1)\phi^2 \Big] + \max_i \left\{ \frac{\phi^e}{n_i^{\mathrm{c}}} \Big[\phi + (n_i^{\mathrm{c}} - 1)\phi^2 \Big] \right\} \tag{2.10}$$

where ϕ^t and $\phi^e = 1 - \phi^t$ gives the portion of microstructural information attributed to tile interior and edges, respectively. We can clearly observe the proximity of simulated data to the estimate with $\phi^e = 1$, which is attributed to the fact that the entire microstructural information in automatically designed tiles is associated with edges, contrary to the optimization based design [15]. On top of that, observe a notably larger scatter (whiskers) in simulated data for individual tile set cardinalities compared to that discussed in [15]. It stands to reason that the choice of tiles in explored sets preferred correct phase volume fractions to the uniform distribution of edges in synthesized tilings, which violates fundamental assumptions of Eq. (2.10) as justified in [15]. Therefore, the reconstructed microstructures are prone to repeat patterns specific to edges of higher frequencies, e.g. Fig. 2.9c, thereby increasing $\widehat{S}_2$ in magnitude. A remedy consists in the use of patched

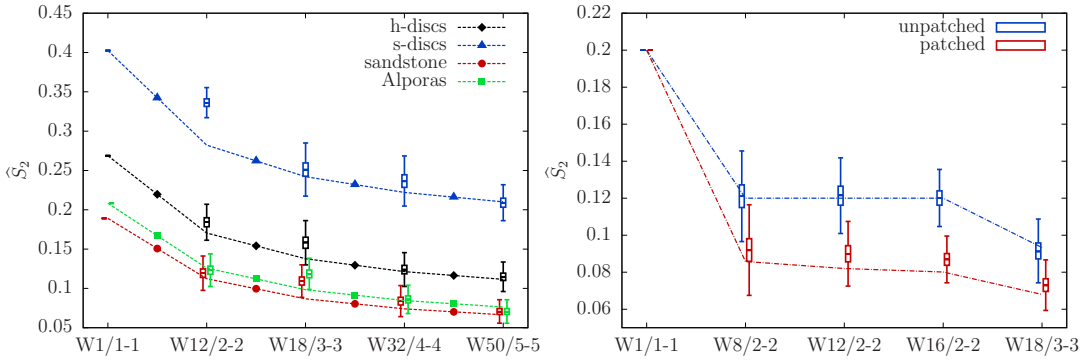

Figure 2.8: Reduction of secondary extremes of S_2 with respect to number of edge codes: (a) conventional tiles – majority of microstructural information is carried by edges, and (b) comparison between conventional and patched tiles of sandstone microstructure – in patched tiles microstructural information is optimally distributed among edges and interiors. The boxes and whiskers, respectively, involve 50% and 75% of realizations proportionally distributed about the median. Continuous curves follow predictions given by Eq. (2.10).

tiles, compare Figs. 2.8a,b and Figs. 2.10 and 2.9.

2.4 Examples of compressed and synthesized microstructures

Following the above indicators, one can select the optimal set with respect to the desired compression capabilities and the level of induced degeneracy in terms of spurious long range orientation orders quantified by $\widehat{S}_2$. For instance, examples of synthesized microstructures of target systems from Fig. 2.5 are displayed in Fig. 2.9. These particular reconstructions are formed by tilings made up of 10×10 tiles. The zoomed left upper corners contain only 3×3 tiles for better visualization of short range features. In Fig. 2.10, we further show synthesized sandstone microstructures created by means of unpatched and patched tiles of the set W18/3-3 displayed at the two top rows. The conjectures coming from Fig. 2.8b are very difficult to follow by visual inspection, however the patched reconstruction in Fig. 2.10b seems to us less polluted by repetitive patterns then that without the patches, see also Figs. 2.10a and 2.11.

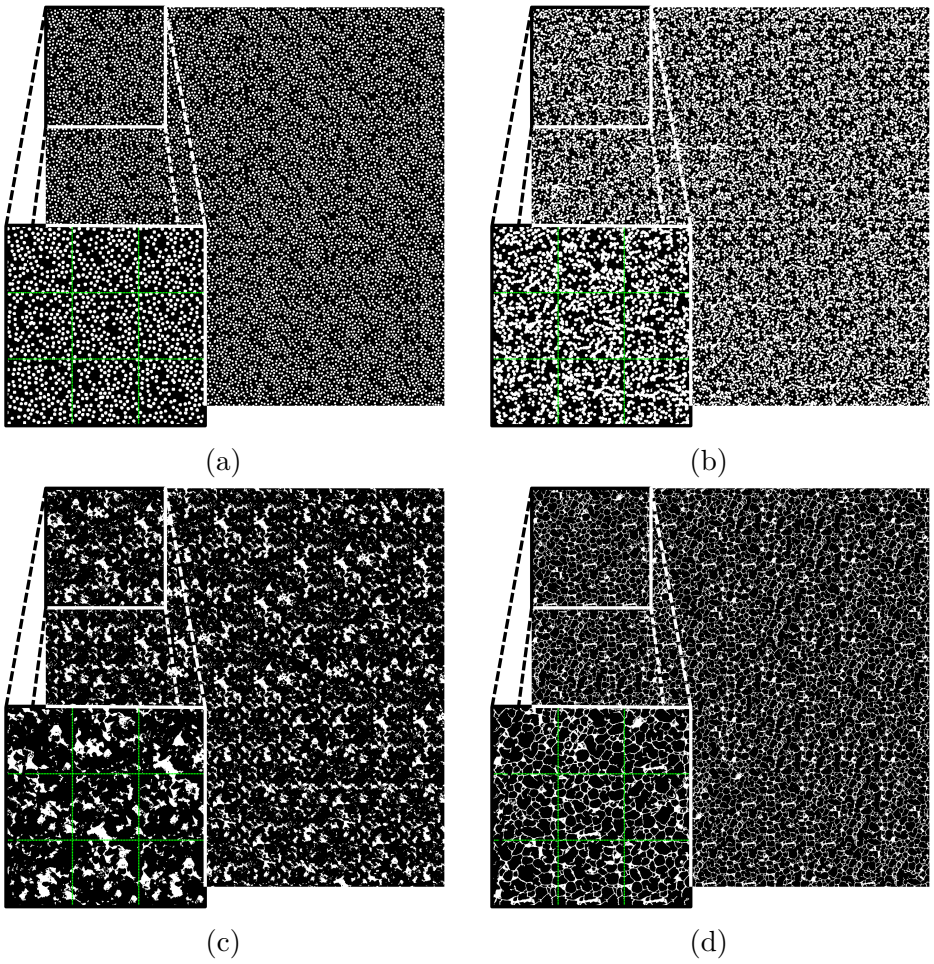

Figure 2.9: Examples of synthesized microstructure in 3×3 tiling: (a) h-discs (W50/5-5), (b) p-discs (W50/5-5), (c) sandstone (W50/5-5), and (d) Alporas® (W32/4-4).

2.5 Conclusions and future developments

In general, the microstructure compression is subject to a compromise among various factors. The design of a compression technique calls into question the degree of compression (dimensions of tiles and tile set cardinality), the amount of distortion induced (parasitic long range orientation orders along with the short range defects in compressed microstructures, e.g. due to quilting), and the computational overhead required to compress and uncompress the data.

In this work, we have proposed an approach to compression and reverse synthesis of microstructural patterns of real world microstructures based on Wang tilings, image processing techniques, and statistical quantification. The method goes beyond periodic representations, and provides a natural generalization of PUC concept (recall, W1/1-1 equals PUC). It allows to represent complex microstructural patterns by making use of small data sets called the Wang tile sets. The properties of the automatic tile morphology design were investigated by means of a number of sensitivity analyses whose objective was to determine the optimal values of the input parameters, such that the compressed microstructure contains maximum microstructural information and is small enough for an inexpensive treatment. From our results, we conjecture that the width of the overlapping

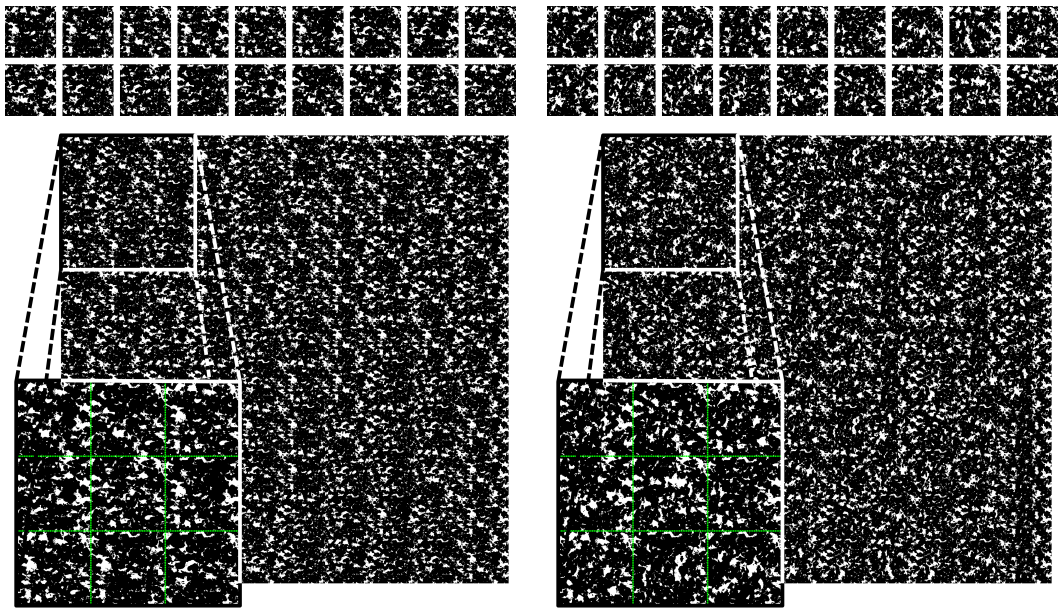

(a) (b)

Figure 2.10: Example of synthesized sandstone microstructure of 3×3 unpatched (a) and patched (b) tiles.

region of about nine times the mean characteristic inclusion size was suitable for all investigated microstructures. However, no general rule regarding the input values was observed besides. A similar sensitivity study, following the flowchart in Fig. 2.4, is therefore recommended any time the compression based on Wang tiles is desired. The extension of the concept to three dimensional setting by means of Wang cubes is fairly straightforward and is in the focus of our future work. Preliminary outcomes are demonstrated by an example shown in Fig. 2.12.

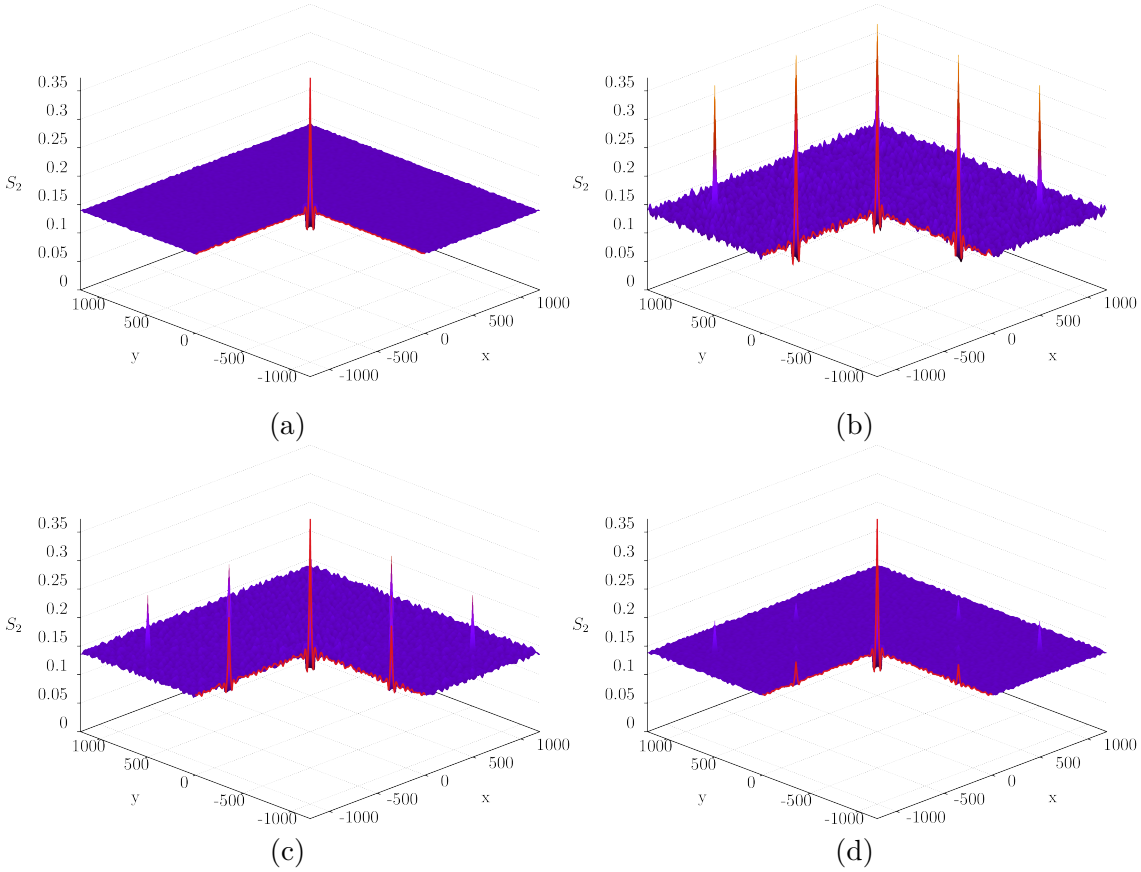

Figure 2.11: S_2 statistics of h-discs microstructure: (a) target system, (b) W1/1-1 (PUC), (c) W16/2-2, and (d) W16/2-2 with patches.

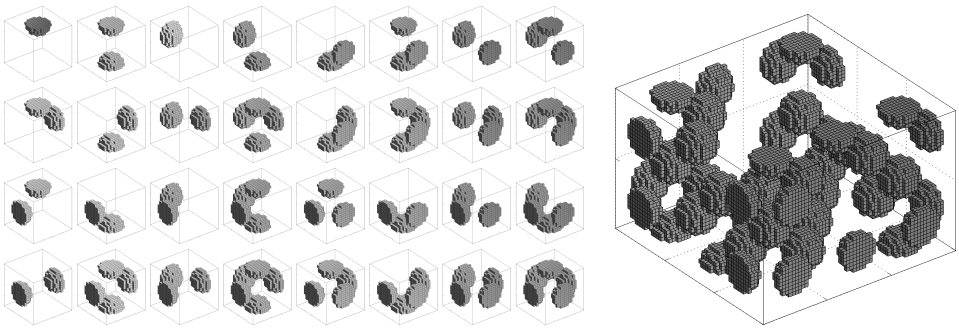

Figure 2.12: Illustration of (a) a tile set W3/3-3-3, and (b) a tiling consisting of $3 \times 3 \times 2$ tiles.

Chapter 3

Tile design based on level-set approach

Abstract:
Microstructural geometry plays a critical role in the response of heterogeneous materials. Consequently, methods for generating microstructural samples are increasingly crucial to advanced numerical analyses. We extend Sonon et al.'s unified framework, developed originally for generating particulate and foam-like microstructural geometries of Periodic Unit Cells, to non-periodic microstructural representations based on the formalism of Wang tiles. This formalism has been recently proposed in order to generalize the Periodic Unit Cell approach, enabling a fast synthesis of arbitrarily large, stochastic microstructural samples from a handful of domains with predefined microstructural compatibility constraints. However, a robust procedure capable of designing complex, three-dimensional, foam-like and cellular morphologies of Wang tiles has not yet been proposed. This contribution fills the gap by significantly broadening the applicability of the tiling concept.

Since the original Sonon et al.'s framework builds on a random sequential addition of particles enhanced with an implicit representation of particle boundaries by the level-set field, we first devise an analysis based on a connectivity graph of a tile set, resolving the question where a particle should be copied when it intersects a tile boundary. Next, we introduce several modifications to the original algorithm that are necessary to ensure microstructural compatibility in the generalized periodicity setting of Wang tiles. Having established a universal procedure for generating tile morphologies, we compare strictly aperiodic and stochastic sets with the same cardinality in terms of reducing the artificial periodicity in reconstructed microstructural samples. We demonstrate the superiority of the vertex-defined tile sets for two-dimensional problems and illustrate the capabilities of the algorithm with two- and three-dimensional examples.

Reproduced from: Doškář, M., Zeman, J., Rypl. D., Novák, J. Level-set based design of Wang tiles for modelling complex microstructures (under review). [43]

3.1 Introduction

The geometrical details of a material composition drive many macroscopic phenomena such as crack initiation and propagation [44] or meta-behaviour [45]. Advanced computational strategies thus tend to incorporate knowledge of material microstructures[1] in order to enhance their predictive power. [3]

When micro and macro scales are well separated, a microstructural response is typically up-scaled through homogenization methods. Albeit computationally intensive, numerical homogenization methods [3] now supersede analytical methods [2] because of their ability to handle complex microstructural geometries and non-linear problems. With increasing computational power, numerical models that fully resolve the microstructural geometry in the whole macroscopic domain, e.g. [4, 5], or in regions of interest [6, 7], have emerged, addressing problems without clear scale separation.

For both strategies, however, accuracy critically depends on the representativeness of the provided microstructural geometry, accenting the crucial role of microstructure modelling in multi-scale approaches.

Compared to materials with regular microstructures, characterized entirely by Periodic Unit Cells (PUCs), modelling random heterogeneous materials is more intricate; any finite-size representation automatically implies information loss. The optimal microstructure representation should capture intrinsic randomness and fluctuations in a microstructure while remaining computationally tractable (for numerical homogenization) or inexpensive to construct (for fully resolved simulations).

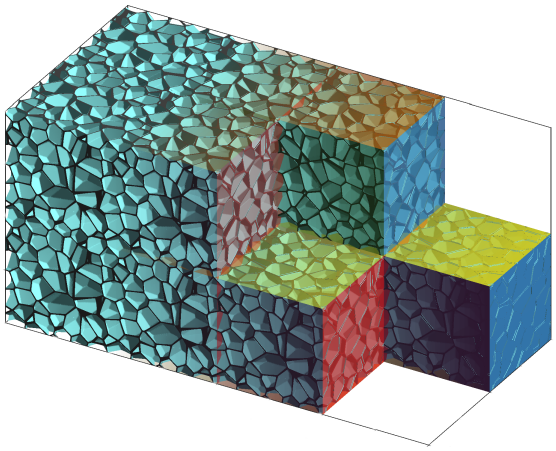

Figure 3.1: Illustration of a synthesized sample of a closed-foam microstructure obtained as a $4 \times 2 \times 2$ tiling assembled from a set of pre-generated Wang cubes. Individual face codesthat encode the geometrical continuity of individual tiles and play the role of compatibility constraints during a tiling assembly are shown in semi-transparent colours.

3.1.1 State-of-the-art in modelling random microstructures

One of the widely adopted approaches for modelling heterogeneous materials rests on an extension of PUC generated such that its spatial statistics match that of a reference microstructure. This procedure appears in the literature under various names such as Statistically Optimal Representative Unit Cell [11], Repeating Unit Cell [46], Statistically

[1] We use the term “microstructure” in a broader sense, without referring to a specific scale length.

Similar Representative Volume Element [12], or Statistically Equivalent Periodic Unit Cell (SEPUC) [10], among others. The spatial statistics involved range from Minkowski functionals [47] to multi-point probability functions [2], out of which the two-point probability [48, 49, 50], two-point cluster [39], and lineal path [51, 52, 10, 53] functions are the most frequently used.

Following Povirk's seminal work [8], the majority of cell representations are generated using optimization procedures, minimizing the discrepancy between the statistical characterization of the reference microstructure and its compressed, PUC-like representation. The particular choice of optimization algorithm currently varies with several options including simulated annealing [54, 52, 10], genetic [55, 56, 11, 46] and gradient [8, 57], or phase-recovery [58] algorithms.

The second approach to microstructure generation utilizes reference samples of the microstructure. New realizations are then obtained with a Markovian process, taking individual voxels [9] or a patch of voxels [13] from the provided reference samples according to the proximity of the spatial statistics computed for their surroundings. Alternatively, searching for statistics proximity can be replaced with a classification tree-based supervised learning model [59].

The previous two approaches suffer from high computational costs related either to optimization or to training the learning models. The applicability of their outputs is also sensitive to the spatial statistics considered, attesting to the ill-conditioning of the microstructure reconstruction problem itself. Achieving a good match in selected statistics does not automatically guarantee similar overall behaviour; for instance, Biswal et al. [60] demonstrated that realizations with similar two-point probability functions could have significantly different percolation characteristics that govern overall transport properties.

Complementary to the statistics-informed methods, a third approach to generating microstructural realizations relies on meta-modelling the genesis of a microstructure. These methods range in complexity and include the Monte-Carlo Potts [61] and phase field models [62] of grain growth; sedimentation-and-compaction models [60]; and various particle packing algorithms, e.g. [63, 64, and references therein], based on either Random Sequential Adsorption (RSA)[2] [66, 67] or molecular dynamics [68, 69, 70].

The relevance of packing algorithms extends beyond simple particle-matrix microstructures because the resulting packings often serve as initial seeds for tessellation-based models applicable to polycrystals [71, 72], foams [64], and cell tissues [73, 74]. Due to its straightforward implementation, Voronoï tessellation is the most common choice; however, the resulting geometry is oversimplified for many materials. For instance, Voronoï-based models overestimate overall stiffness for high porosity foams [75]. The curvature of cell walls [71, 76] and heterogeneity in cell size [64, 72] and wall thickness [72] must be additionally introduced to obtain realistic geometries. Similar effects can be achieved by modifying the distance measure used during tessellation, e.g. models based on the Laguerre variant generate microstructures with multi-mode cell size distribution [77, 72, 64, 63]. Inspired by Laguerre tessellation, Chakraborty et al.[74] proposed Adaptive Quadratic Voronoï Tessellation, attributing a distinct anisotropic metric to each seed and thus allowing for additional control over the resulting geometry.

The original RSA method [65] suffers from $\mathcal{O}\left(N^2\right)$ complexity for N particles due to overlap checks and is impractical for generating large, densely packed systems. Consequently, several accelerations have been proposed. For Dart Throwing Algorithm [65],

[2] In its simplest setting of packing circular or spherical particles, RSA corresponds to the Dart Throwing Algorithm [65].

which is a simplified case of RSA with equisized circular/spherical particles, Dunbar and Humphreys [78] introduced a scalloped sector representation of non-overlap guaranteed regions. In the same year, Jones [79] proposed an alternative bookkeeping of the regions based on an adaptively updated Voronoï tessellation. Moreover, both approaches utilize a tree data structure and improve the algorithm complexity to $\mathcal{O}(N \log N)$. For general RSA, Yang et al. [46] proposed an acceleration based on a combination of a spline description of particle shapes and hierarchically refined bounding boxes of each particle. Recently, Sonon et al. [18] introduced a method building on an implicit, level-set based description of particle shapes, achieving $\mathcal{O}(N)$ complexity (see Section 3.3 in [18]). Moreover, Sonon et al.'s method readily facilitates generating complex microstructures using linear combinations of the nearest neighbour distance functions and dedicated morphing operations [18, 80, 19, 81]. In a sense, this approach introduces the anisotropic pseudo-metrics[3] of [74] in a geometrically-motivated way by considering arbitrarily-shaped particles. As a result, Sonon et al.'s method enables refined control over generated microstructure unattainable with standard Voronoï or Laguerre tessellations; see Section 3.3.2.

Albeit significantly faster than RSA or optimization-based approaches, the latter method still starts anew every time an additional realization is required, imposing overhead on, e.g., investigations of the Representative Volume Element (RVE) size that require multiple microstructural samples to be generated, see [82, 83, 84]. Alternatively, larger microstructural realizations can be assembled from (SE)PUC; however, such construction introduces non-physical, long-range, periodic artefacts in a microstructural geometry and its local response.

3.1.2 Wang tiling in microstructure modelling

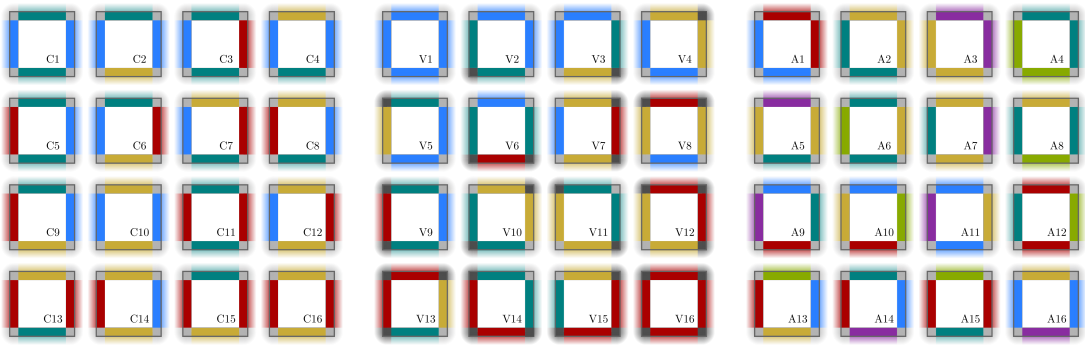

Figure 3.2: Formal definition of three Wang sets with the equal cardinality of 16 tiles: (a) an edge-based set with two horizontal and vertical codes, (b) a vertex-based set over four horizontal and vertical codes, and (c) the aperiodic Ammann's set [85] over six horizontal and vertical codes. Similar to Fig. 3.1, the compatibility codes playing the role of constraints during the tiling assembly are illustrated with colours assigned to individual edges. The corresponding vertex codes are depicted in light and dark grey corner squares. While in the vertex-based set (b), edge codes were obtained by mapping two vertex codes uniquely to one edge code, the potentially different vertex codes for sets (a) and (b) were identified using the analysis from Section 3.2.3 of connectivity graphs shown in Fig. 3.5.

[3]Level-set description based on the signed distance to the nth nearest particle boundary does not fulfil all metric criteria.

Inspired by applications in computer graphics [17], we have introduced the formalism of Wang tiles as a suitable generalization of SEPUC representation of heterogeneous materials [15]. The formalism provides a compromise between the SEPUC approach and the use of a microstructure generator for each new realization. The concept of Wang tiles decomposes microstructure generation into an offline phase, which can possibly be computationally intensive, and a nearly instantaneous online phase. In the offline phase, information regarding a heterogeneous microstructure is compressed into a set of smaller domains—Wang tiles—with predefined compatibility constraints on the compressed microstructural geometry. In the online phase, microstructural realizations are assembled from these domains with a fast, linear algorithm that produces stochastic realizations with suppressed periodicity. The merits of the tiling concept for RVE size analyses were demonstrated in [75, 86].

Optimization-based approaches developed initially for the SEPUC design can be extended to incorporate generalized periodic boundary conditions and used to generate the morphology of tiles [15, 16]. However, the extension amplifies the major weakness of optimization approaches—their computational cost—making them prohibitively expensive for complex three-dimensional models. As a remedy, we have proposed a method motivated by Cohen et al. [17] that combines a sample-based approach with quantitative spatial statistics [21]. While this method is by orders of magnitude faster than the optimization approach, it has difficulties handling complex, percolated microstructures such as foam, and produces corrupted ligaments in sample overlaps [75].

In this paper, we extend Sonon et al.'s method to Wang tiles in order to produce tile-based representations of microstructures intractable by the former methods [15, 16, 21], see Fig. 3.1. To this end, in Section 3.2, we review the fundamentals of the Wang tile concept and discuss, in detail, connectivity and mapping between vertex- and edge/face-based definitions of Wang tiles. Next, we outline Sonon et al.'s method [18, 19] and describe modifications necessary to accommodate generalized periodicity, see Section 3.3. Finally, equipped with the adapted procedure, we illustrate sample outputs of the procedure in two and three dimensions. We also compare three tile sets—two stochastic and a strictly aperiodic one—with the same cardinalities in terms of periodicity artefacts, complementing our previous study [21] that dealt only with the distribution of tile types.

3.2 Wang tiles

Wang tiles constitute the building blocks of the abstract concept used in this work. Albeit the shape of the tile domains can be any parallelogram (or a parallelepiped in 3D), for simplicity's sake we assume only square (or cubic) domains in the sequel. All tiles from the *tile set* have compatibility codes attributed to their edges (faces), illustrated using colours in Figs. 3.1 and 3.2. These codes play the role of constraints during an assembly process of tile instances in a *tiling*—a portion of a plane (space) without any voids or overlaps; only tiles with the same codes on the abutting edges (faces) can be placed side by side. In addition, tiles can be neither rotated nor reflected during the assembly. Even though the last two requirements can be eliminated by modifying the definition of compatibility codes [87], we retain them for practical purposes since they preserve the orientation of the microstructure compressed within the tile set. The particular version of an assembly algorithm depends on the type of the tile set, discussed below.

Originally, the concept of Wang tiles was introduced in first-order predicate calculus as

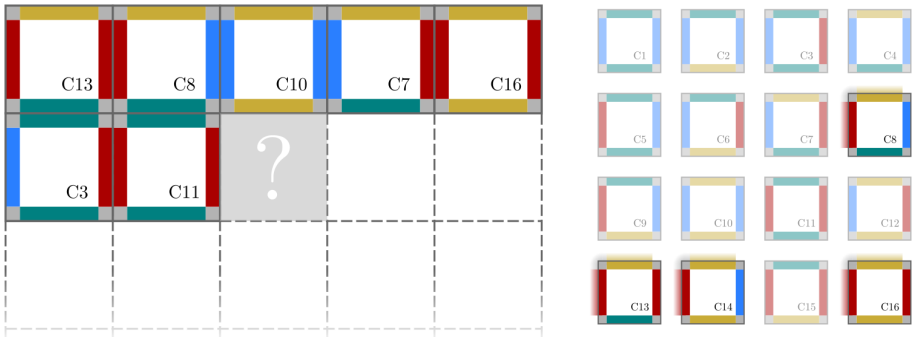

Figure 3.3: Illustration of a step in the stochastic assembly algorithm [17]. A tiling of a given size is filled sequentially; for each position in a tiling, a final tile is chosen from candidate tiles that are filtered out from a given tile set based on the compatibility constraints posed by the previously placed tiles. The candidate tiles for the particular position denoted with the question mark are highlighted in the tile set shown on the right.

a visual surrogate to a decision problem of ∀∃∀ statements[4] [25, 26]. The initial conjecture that a whole plane can be covered only if a periodic tiling exists [25] was disproved shortly after [27], triggering the pursuit of the smallest tile set allowing for strictly aperiodic tiling of the plane, see the classical monograph [28] and [88] for historical overviews. This quest for the smallest set appears to be over; supported by an extensive computer-aided search, Jeandel and Rao [88] announced a set of 11 tiles over 4 codes for each edge orientation, stating that no smaller set exists.

3.2.1 Stochastic tile sets

Similar to applications in biology [89], physics [36], and computer graphics [90, 17], we use the concept only in its geometrical interpretation as a suitable formalism the describing mutual compatibility of small domains. Except for the comparison study in Section 3.4.1, we also limit ourself to the stochastic tile sets introduced by Cohen et al. [17]. Besides the fact that deterministic tilings of the aperiodic sets often exhibit locally ordered patterns, the stochastic sets offer higher flexibility in terms of design, i.e. choosing the number of tiles and codes and their distribution within the set[5].

The assembly algorithm for stochastic sets works sequentially: an initially empty grid is traversed in a scanline [91] way; at each grid node, possible candidates compatible with previously placed tiles are identified in the set and one candidate tile is randomly chosen and placed; see the illustration in Fig. 3.3. Thus, the only requirement for the set design is that there is at least one tile (but optimally two or more to preserve the stochastic nature of the assembly) for every possible combination of codes on the upper and left-hand edges. In principle, the random choice from the subset can be replaced with an informed selection preferring e.g. different phase volume fractions in different regions of a domain according to a pre-generated Gaussian random field. This modification allows for correlations in the microstructure at length scales larger than the tile size. For the sake of brevity and without loss of generality, however, we use only the standard stochastic algorithm in this work.

[4] A statement containing one existential (∃) and two universal (∀) quantifiers.

[5] The limitations of aperiodic sets are especially critical in 3D, because only one aperiodic set of Wang cubes has been published to date [30].

The tiling concept's ability to generate naturally looking patterns from a limited amount of samples—which proved highly appealing in computer graphics [17, 90]—stems from the reduced periodicity in tiling assemblies. This feature complies well with our ambition to replace a SEPUC-based description of random heterogeneous materials with its generalization that would allow for fast synthesis of stochastic microstructural samples or microstructure geometries for entire macroscopic domains.

The design of a compressed microstructural representation consists of two steps. First, the cardinality of the tile set and a particular distribution of edge (face) codes is chosen. This controls the frequency of tile occurrence in a tiling. Next, tile interiors are designed such that (i) the generated microstructure is continuous across the compatible edges and (ii) assembled tilings resemble the desired microstructure. Note that the latter requirement is not imposed on individual tiles. On the contrary, variability in the compressed representation is the main merit of the tiling concept. Tile interiors together with edge compatibility carry local microstructural characteristics, while the fluctuations over distances larger than the tile size are facilitated via the tile assembly algorithm.

3.2.2 Edge- vs. vertex-based tile definitions

Complementary to the edge-based specification introduced above, Wang tiles can be defined using vertex codes. Unlike the standard edge-based definition, the vertex-based definition allows for direct control of tile states across vertices, preventing pronounced repetitiveness when a visually distinctive microstructural feature falls into the vertex region [17]. To avoid this "corner problem", Cohen et al. [17] proposed marking the tile vertices with an additional set of codes, essentially overlaying two tile set definitions. Subsequently, Lagae and Dutré [91] retained only vertex codes, reporting superior spectral properties for assembled patterns compared to edge-based sets with the same cardinality.

Albeit the two definitions yield the same cardinality of tiles (C^4) in the complete set, i.e. the set that contains all combinations of C codes, they differ when it comes to minimal stochastic sets, i.e. sets that contain at least two tiles for each admissible code combination of already placed neighbouring tiles ($2C^2$ for edge-based sets vs. $2C^3$ in the case of vertex-based ones). The difference is even more pronounced in three dimensions: a full face-defined set contains C^6 cubes compared to C^8 cubes in a vertex-defined set. Theoretically, Wang cubes can be also defined with edge codes in three dimensions; however, cardinality exceeds both the face- and vertex-based definitions without any known benefits.

Mapping vertex-defined tiles[6] to the original definition is straightforward: two vertex codes define one edge code. Hence all the above-mentioned design and assembly procedures directly apply to the vertex-based definition as well. In fact, the mapping provides an effortless way to produce a minimal stochastic edge-defined set with equal occurrence probability of each tile, the set characteristics sought for in [16]. On the other hand, because the mapping is injective only, it is generally not possible to map an edge-defined set to a vertex-based one.

3.2.3 Vertex analysis of a tile set

Here, we outline a tile set analysis capable of revealing the underlying vertex definition, if it exists. The motivation behind this analysis is the pragmatic question which arises when implementing generalized periodicity: If a particle intersects a tile boundary, what

[6]The same procedure holds also for Wang cubes, where four vertices define one face code.

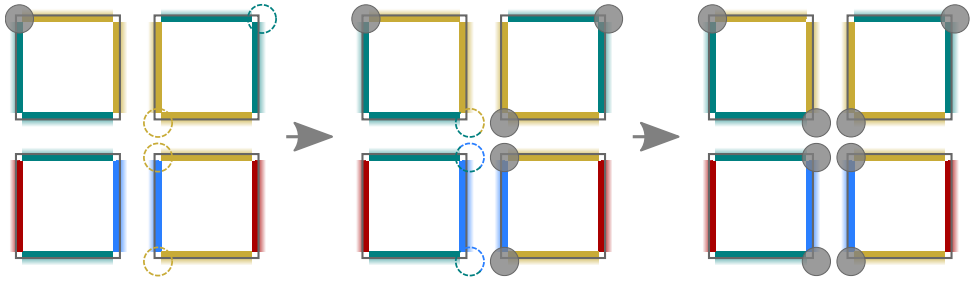

Figure 3.4: Illustration of the generalized periodicity effect on the particle copy process. The three steps shown illustrate how a particle initially placed at the top left corner of the first tile (grey particle on the left-hand side of the figure) is sequentially copied to other loci following the edge codes it intersects. Dashed particle outlines loci where the particle will be copied in the next step.

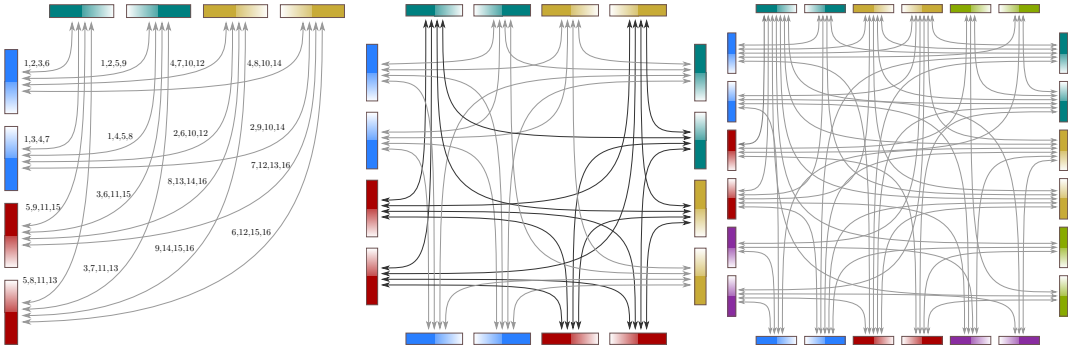

(a) (b) (c)

Figure 3.5: Comparison of graphs pertinent to the tile sets from Fig. 3.2, identifying a potential vertex-based definition of the sets. Each graph node corresponds to a code on a half of a tile edge (either left/right for horizontal codes, or top/bottom for vertical codes), and graph arcs correspond to tile vertices. As there are multiple vertices—and hence parallel arcs—connecting the same nodes, the graphs should be drawn as a multigraph. However, multiple arcs are collapsed into one for the sake of brevity; only in (a) multiplicity is indicated by tile indices attached to each arc. Independent sub-graphs indicating the vertex character of the set are shown in distinct light and dark grey, which correspond to the vertex codes in Fig. 3.2.

other tiles should it be copied to? While the answer is straightforward for a particle intersecting a tile edge, vertex overlap is more involved. A particle overlapping a vertex is carried to other tiles by both the horizontal and vertical edges. Because the particle overlapped a vertex in the original tile, its images overlap vertices of the other tiles as well. Consequently, these images are propagated further by the newly affected edge codes, see Fig. 3.4. Whether the particle is eventually copied to all vertices or appears only in a selected subset depends on the allocation of codes to individual tiles.

Assume an undirected graph[7] where each node represents the code on a particular half of an edge (either top/bottom for vertical or left/right for horizontal codes, resulting in two occurrences of each edge code) and each arc corresponds to a tile vertex. The graph

[7]Instead of the standard vertex-edge nomenclature for a graph, we use node and arc terms in order to avoid confusion with similar geometrical notions related to Wang tiles.

is by definition bipartite, because each vertex connects horizontal and vertical codes, and represents a multigraph since there are usually more vertices with the same adjacent edge codes in the tile set. To answer the aforementioned question, we identify connected components of the graph using the Depth-first algorithm [92, Section 18.2]. Each independent sub-graph then corresponds to a distinct vertex code and the arcs pertaining to the sub-graph determine the vertices to which a vertex-overlapping particle will be propagated. See Fig. 3.5 for a comparison of three graphs pertinent to the tile sets depicted in Fig. 3.2. The subgraphs (if present) are plotted in distinct grey colours, which correspond to the colours of vertex codes shown in Fig. 3.2.

In three dimensions, a set of Wang cubes can be analysed analogously with only a minor modification: a graph node represents one corner of a cube face. Thus, each face code appears four times in the graph. In addition, cube edges with the same direction vector must be also classified, addressing the situation when a particle intersects a cube edge. The classification follows the exact same procedure as vertex identification in two dimensions, neglecting the codes on faces perpendicular to the analysed edges.

3.3 Tile design using level-set functions

As mentioned in Section 3.1.1, Random Sequential Adsorption (RSA)[8] is one of the most frequent algorithms for generating particle packings and microstructural geometries. It follows the simple idea of throwing particles of an arbitrary shape into a given domain and keeping those that do not overlap with previously placed ones. In its original setting, however, the algorithm poses a critical drawback for higher volume fractions: the success rate for accepting the particle position rapidly decays in later stages because the majority of the randomly selected positions collide with the already placed particles. Optimally, the remedy would be to sample the new particle position directly from a domain that is certified to result in a non-overlapping composition.

Several such remedies have been listed in Section 3.1.1. Here, we recall the approach of Sonon et al., because we have extended their methodology to Wang tiles. Sonon et al. [18, 80, 19, 81] adopted the implicit, level-set-based description of a microstructural geometry and demonstrated that it enables—in addition to the desired sampling from a valid domain loci—generating complex microstructural geometries (such as open and closed foams) in a unified framework, using suitable morphing operations. Moreover, both features are independent: if a particle packing is the desired output, the morphing operations can be neglected. On the other hand, any distribution of points or particles obtained by different packing methods can serve as the input for the morphing operations.

In the the remainder of Section 3.3, we revise individual steps from the Sonon et al.'s framework and introduce necessary modifications facilitating the compatibility constraints arising in the concept of Wang tiles. For the sake of clarity, all procedures are presented in the two-dimensional setting with comments about three-dimensional problems when necessary. Section 3.4 then presents both two- and three-dimensional results.

3.3.1 Generating particle packings

The original Sonon et al.'s approach [18] rests on describing the geometry of particle $\mathcal{P}$ with a level-set function $\mathcal{L}^{\mathcal{P}}$, which gives the signed distance of point $\boldsymbol{x}$ from the nearest particle boundary $\Gamma^{\mathcal{P}}$ (with negative values inside the particle), such that

[8] Sometimes, the term Random Sequential Addition, e.g. [93], is used interchangeably.

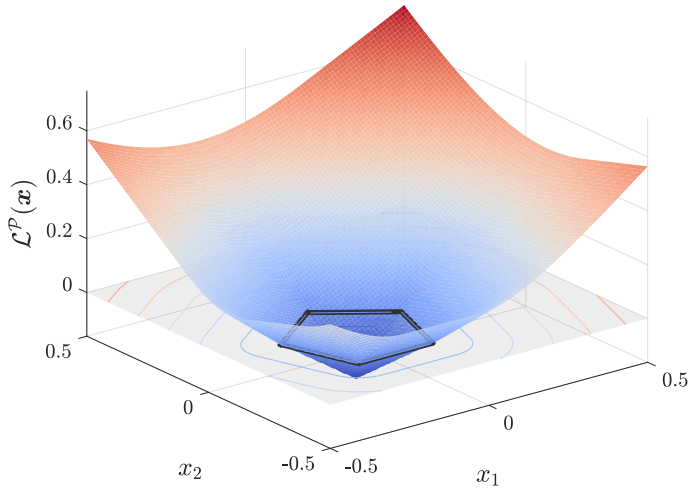

Figure 3.6: Implicit representation of particle geometry with the level-set function $\mathcal{L}^{\mathcal{P}}$. The boundary of particle $\mathcal{P}$ is obtained as a zero-value contour of $\mathcal{L}^{\mathcal{P}}$ (plotted in a black line).

$$\mathcal{L}^{\mathcal{P}}(\boldsymbol{x}) = \min_{\boldsymbol{y}\in\Gamma^{\mathcal{P}}} d\left(\boldsymbol{x},\boldsymbol{y}\right), \tag{3.1}$$

with the signed distance function $d\left(\boldsymbol{x},\boldsymbol{y}\right)$ given by

$$d(\boldsymbol{x},\boldsymbol{y}) = \begin{cases} -\|\boldsymbol{x}-\boldsymbol{y}\| & \text{if } \boldsymbol{x}\in\mathcal{P}, \\ \|\boldsymbol{x}-\boldsymbol{y}\| & \text{otherwise}. \end{cases} \tag{3.2}$$

Consequently, the zero iso-line of $\mathcal{L}^{\mathcal{P}}$ represents the particle boundary $\Gamma^{\mathcal{P}}$, as depicted in Fig. 3.6. Note that unlike many applications of the level-set method where the implicit geometry description evolves in time according to the Hamilton-Jacobi equation, see [94, and references therein], $\mathcal{L}^{\mathcal{P}}$ is computed for the given geometry of a particle and remains fixed.

Assume for now that we have domain Ω that contains set $\mathcal{R}$ of already placed particles and their geometry is encoded in a single level-set field $\mathcal{L}^{\Omega}$,

$$\mathcal{L}^{\Omega}(\boldsymbol{x}) = \min_{\mathcal{P}\in\mathcal{R}} \mathcal{L}^{\mathcal{P}}(\boldsymbol{x}), \quad \forall \boldsymbol{x}\in\Omega; \tag{3.3}$$

see Fig. 3.7 for an illustration. Knowing the radius r of the smallest circumscribed circle as the only characterization of the new particle, overlaps with the existing particles can be readily prevented by sampling its centre from the domain

$$\mathcal{A} = \left\{\boldsymbol{x}\in\Omega \mid \mathcal{L}^{\Omega}(\boldsymbol{x}) \geq r\right\}. \tag{3.4}$$

After placing the new particle $\mathcal{P}$, the level-set field $\mathcal{L}^{\Omega}$ is updated with $\mathcal{L}^{\mathcal{P}}$,

$$\mathcal{L}^{\Omega}(\boldsymbol{x}) = \min\left(\mathcal{L}^{\Omega}(\boldsymbol{x}), \mathcal{L}^{\mathcal{P}}(\boldsymbol{x})\right), \quad \forall \boldsymbol{x}\in\Omega. \tag{3.5}$$

This procedure repeats until either a pre-defined stopping criterion (e.g. a desired volume fraction) is met or $\mathcal{A}=\emptyset$.

To increase the volume fraction that can be achieved with this procedure, two addi-

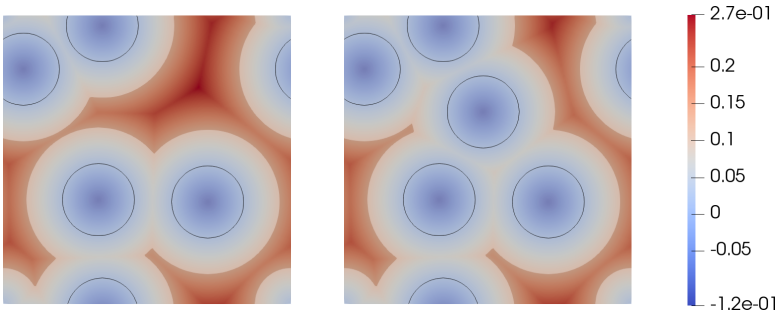

(a) (b)

Figure 3.7: Two consecutive steps of the level-set based RSA algorithm for a Periodic Unit Cell: (a) level-set field $\mathcal{L}^\Omega$ with previously placed particles (values of $\mathcal{L}^\Omega$ outside the admissible sampling domain $\mathcal{A}$ are displayed as translucent) at the nth step; (b) updated state of $\mathcal{L}^\Omega$ and $\mathcal{A}$ after placing a new particle at step $n+1$.

tional restrictions can be posed on the admissible subdomain $\mathcal{A}$. First, a maximal distance ρ from existing particle boundaries can be added to Eq. (3.4), preventing too large gaps between particles. (If requested, a minimal distance κ between two particles can be further enforced as well.) Second, to prevent locally jammed states with large interparticle gaps, an additional field $\mathcal{L}^\Omega_{\mathrm{II}}$ storing the shortest distance to the surface of the second nearest particle can be included in Eq. (3.4) and limited from above with σ, see [18] for additional details. With all these constraints in action, Eq. (3.4) takes the form

$$\mathcal{A} = \left\{ \boldsymbol{x} \in \Omega \mid r + \kappa \leq \mathcal{L}^\Omega(\boldsymbol{x}) \leq r + \rho,\ \mathcal{L}^\Omega_{\mathrm{II}} \leq r + \sigma \right\}. \tag{3.6}$$

Enforcing periodicity of the packing is also straightforward: upon placement of a new particle, the domain level-set field is also updated with the particle's periodic images (eight in 2D; recall the grid in Fig. 3.8, and 26 in 3D).

3.3.1.1 Extension to Wang tiles

Compared to generating PUCs, the additional compatibility constraints among individual Wang tiles necessitate several modifications in the original Sonot et al.'s algorithm to generate continuous microstructural morphology of a tile set. For the Poisson discs distribution, Lagae and Dutré [95] modified the Dart Throwing algorithm by partitioning tile domains into separate regions pertinent to vertices, edges, faces, and tile interiors, and filling the regions sequentially, starting with the vertex regions. Here we present a different approach better suited to packing particles of different sizes and shapes that processes all tiles simultaneously and does not require a priori partitioning of tile domains.

As $\mathcal{L}^\Omega$ we use a level-set field $\mathcal{L}^\mathcal{S} = \bigcup_{\mathcal{T}\in\mathcal{S}} \mathcal{L}^\mathcal{T}$ defined on a regular grid for each tile $\mathcal{T}$ in the tile set $\mathcal{S}$. For each tile in a pre-processing stage, we identify potential neighbouring tiles and store their indices in a grid (3×3 or $3 \times 3 \times 3$ in two or three dimensions, respectively), see Fig. 3.8, which will be used later in the updating phase.

For further description, we define a *copy-inducer* as a geometrical entity that is responsible for inducing particle copies to other tiles. Hence, a copy-inducer can be either a vertex, edge, face, or formally the tile itself and is related to a code identified in Section 3.2.3. The particular type of the copy-inducer stems from particle's intersections with a tile boundary (if a particle does not intersect a boundary, the tile is the copy-inducer,

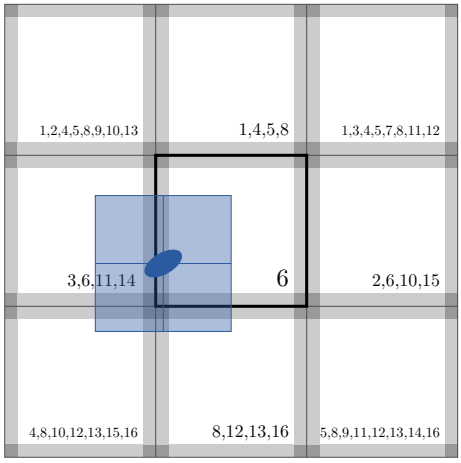

Figure 3.8: Neighbourhood grid identified for each tile in a tile set (here shown for tile V6 from Fig. 3.2b) containing codes of tiles that can occur at given positions. Light and dark grey regions depict individual entities in the bookkeeping structure, which prevents calculations. (During the update procedure described in the text, the blue particle can be accounted for either in tile 6 at the centre, or from tiles 3, 6, 11, or 14 at the first column, second-row position. With the bookkeeping structure considered, only one update is performed.) The blue square illustrates the use of acceleration via a precomputed patch; values of $\mathcal{L}^{\mathcal{P}}$ are computed only once and used for all particle occurrences during an update. If requested, values outside the patch are computed in a regular way.

indicating that no copy is necessary. If a particles intersects one edge, the edge is the copy-inducer, and so on).

Modification 1: Update The main structure of the modified algorithm follows the original one. After sampling a particle location from $\mathcal{A} \subseteq \mathcal{S}$, which yields tile $\mathcal{T}_i$ and centre $\boldsymbol{x}_c^{\mathcal{P}} \in \mathcal{T}_i$ where the new particle will be placed, the particle's intersections with the boundary of $\mathcal{T}_i$ are determined, and—based on the intersections—a copy-inducer is identified. Images of the particle are subsequently copied to the relevant tiles following the matching codes on the corresponding copy-inducers. A level-set field of the whole set is then updated tile-wise as described below.

For each tile, we sequentially loop over all tile positions in the neighbours grid shown in Fig. 3.8 (including the centre position as well) and check each of the potential tiles at that position for a new particles added in the current step. If any, the central tile's level-set field is updated according to Eq. (3.5). Clearly, a new particle can appear several times in the same place. To avoid duplicated calculations, we set up a bookkeeping structure that records which copy-inducer in the neighbouring grid was already used during the update and run only the unperformed updates, see Fig. 3.8.

Two implementation approaches are possible at this stage: (i) $\mathcal{L}^{\mathcal{P}}$ is computed anew for each tile and position in the bookkeeping structure, or (ii) provided that $\mathcal{L}^{\mathcal{S}}$ is represented with discrete values on a regular grid, $\mathcal{L}^{\mathcal{P}}$ is precomputed for an auxiliary domain/patch aligned with the particle centre before any update and this field is then reused for all particle instances. Moreover, we combine both approaches with the pre-screening acceleration proposed in [18] that resorts to computing potentially demanding surface-distance functions only when the $\mathcal{L}$ value of a circumscribed circle/sphere—which is fast and easy

to calculate—is less than the actual $\mathcal{L}^\Omega$ value for a given $\boldsymbol{x}$.

While the pre-screening acceleration is significant in all cases, the benefits of a pre-computed patch depends mainly on the patch size relative to the particle circumscribed radius, the $\mathcal{L}^\mathcal{S}$ field resolution, and the cardinality of the tile set. Especially in the later stages of the algorithm, when only relatively small parts of $\mathcal{L}^\mathcal{S}$ are updated, pre-computing a patch for a particle that is not copied to other tiles might cause unnecessary overhead. Therefore, we use the patch approach only for particles with either vertex, edge, or face copy-inducers.

For the three-dimensional set of 16 cubes used in Section 3.4.3 with ellipsoidal particles of circumscribed radius $r = 0.15$, the patch pre-calculation delivered 10% saving in computational time on average. Note also that the multi-query problem of finding the shortest distance to a particle boundary from a set of points is trivially parallelizable, changing the trade-off between patch pre-computations and direct calculations with available threads.

When all tiles are updated, the algorithm proceeds with identifying $\mathcal{A}$ for the next particle.

Modification 2: Artificial level-set field Definition of the admissible domain $\mathcal{A}$ must also be modified for Wang tiles; particle centres cannot be sampled directly from $\mathcal{A}$ obtained from $\mathcal{L}^\mathcal{S}$. The reason for this is that the near-boundary parts of each tile must be informed about the interiors of related tiles in order to prevent insertions similar to the one depicted in Fig. 3.9a, where a copied instance of a newly placed particle collides with interior particle(s) of other tiles. The problem arises only when a particle image is added to a copy-inducing entity with the same orientation as the actual inducer (left-hand side edges in Fig. 3.9a); particles copied to the opposite copy-inducers automatically meet the non-overlap requirement thanks to the first update modification described above.

To avoid this problem, we replace $\mathcal{L}^\mathcal{S}$ in Eq. (3.4) or Eq. (3.6)[9] with a modified field $\widetilde{\mathcal{L}}^\mathcal{S}$ which is equal to $\mathcal{L}^\mathcal{S}$ except for boundary regions, whose width is dictated by the radius r of the circle/sphere circumscribed to the current particle. Each boundary region is then constructed as a point-wise minimum over all regions related to the same copy-inducers with the same code and the same orientation; see Fig. 3.9c. This construction propagates the close-boundary state across relevant tiles and thus prevents overlapping insertions similar to the one depicted in Fig. 3.9a. Note that a similar modification is not required for $\mathcal{L}^\Omega_\mathrm{II}$ because all information necessary to prevent the collisions is already contained in $\widetilde{\mathcal{L}}^\mathcal{S}$.

Modification 3: Breaking regular grid The level-set field $\mathcal{L}^\mathcal{S}$ is typically implemented on a regular grid and the particle centres $\boldsymbol{x}_c^\mathcal{P}$ thus end up aligned with the grid. To break this artificial ordering, after sampling a new particle centre, we check whether the surrounding points belong to $\mathcal{A}$. The belonging points then define quadrants/octants in which the particle can be moved freely. We generate a random shift within these quadrant/octants and update the particle centre accordingly. However, this modification is possible only if the grid spacing is sufficiently small compared to the particle size; otherwise, the implicitly assumed linear approximation of $\mathcal{L}^\mathcal{S}$ is inaccurate and might result in particle intersections at intermediate locations.

The modifications described above are sufficient for extending the original Sonon et al.'s level-set-based packing algorithm to the concept of Wang tiles. Note that all control vari-

[9] Recall that the tile set domain $\mathcal{L}^\mathcal{S}$ substitutes a generic $\mathcal{L}^\Omega$ in both equations since from Section 3.3.1.1 onwards.

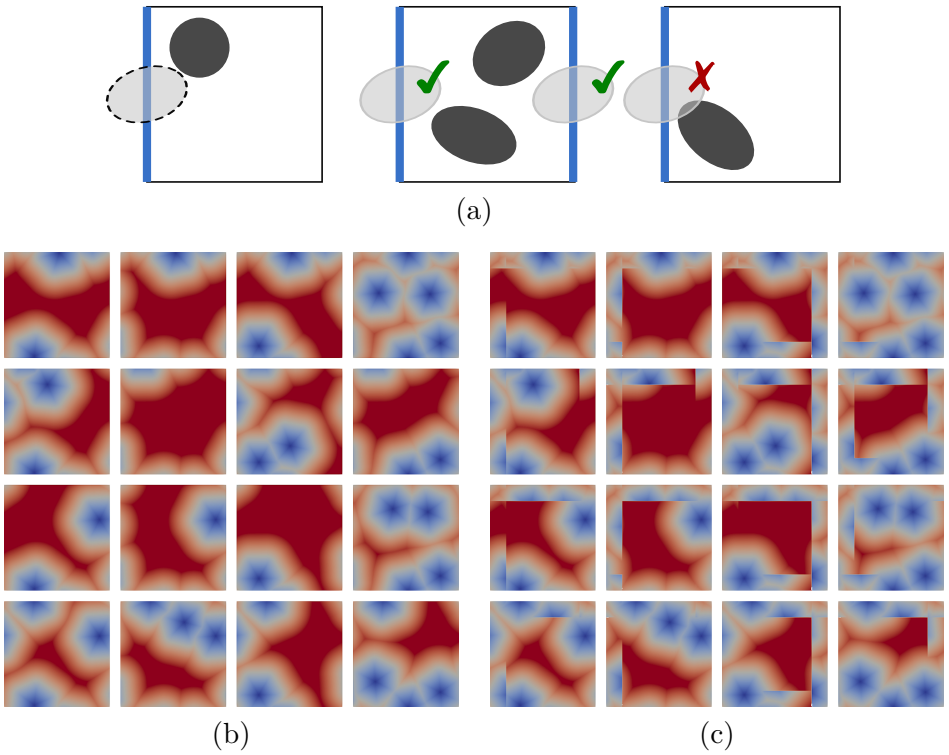

Figure 3.9: (a) Illustrations of particle intersections that can happen due to copying particle images without considering artificially updated level-set field $\widetilde{\mathcal{L}}^{\mathcal{S}}$ in the definition of $\mathcal{A}$. The problematic overlaps occur only at inducer places (highlighted in blue) with the same orientation as the particle copy-inducer (dashed outlined grey particle on the left-hand side). Figures (b) and (c) depict the original $\mathcal{L}^{\mathcal{S}}$ and its modified version $\widetilde{\mathcal{L}}^{\mathcal{S}}$ that communicates necessary data across boundary regions to prevent intersections from (a).

ables, e.g. particle radius r or minimal and maximal distances ρ and σ, can change while the algorithm operates. For instance, to achieve denser packings for multi-modal particle size distributions, it is preferential to start placing large particles first and sequentially proceed to the smaller ones.

Nonetheless, our extension inherits the weakness of the original algorithm when it comes to particles whose shapes are significantly different than their circumscribed circle/sphere, e.g. prolonged ellipsoids. In particular, the more the particle volume deviates from the volume of the circumscribed sphere, the less dense the final packing can be. While the geometry of the already placed particles is described exactly with $\mathcal{L}^{\mathcal{S}}$ (up to inaccuracies due to grid spacing in $\boldsymbol{x}$), the newly placed particle is represented only approximately during selection of a centre, yielding a pessimistic estimate of mutual intersections. The potential remedy is to translate the particle centre right after sampling according to some heuristic rule aimed at producing denser packings; however, we leave this issue unaddressed in this paper.

3.3.2 Morphing operations

The acceleration of RSA by adopting the level-set approach is attractive on its own; however, the main appeal of the Sonon et al.'s level-set framework is the elegance with

which complex microstructures can be generated. As the simplest example, adding a constant γ to $\mathcal{L}^{\mathcal{S}}$ enables (i) fine-tuning of particle volume fractions, (ii) smoothing of sharp corners of polyhedral particles, and (iii) particle coating, e.g. for defining the Interfacial Transition Zone.

Combinations of $\mathcal{L}^{\mathcal{S}}$ and $\mathcal{L}^{\mathcal{S}}_{\mathrm{II}}$ permit rendering interparticle bridges and controlled Voronoï-like tessellations; see [18], where these morphing operations were used to mimic microstructural geometry of clay/sand mixed soils and irregular masonry. Considering also the shortest distance to the boundary of the third nearest particle $\mathcal{L}^{\mathcal{S}}_{\mathrm{III}}$, Sonon et al. [19] demonstrated that their framework can produce highly adjustable models of foam-like microstructures, including features such as a smooth transition from open to closed foams, concavity of foam ligaments, their coatings and hollow interiors, and variable thickness of foam ligaments and cell walls. As in Section 3.3.1, we present only the essentials of generating foam-like microstructures and introduce necessary modifications. The reader is referred to [18, Section 4] and [19, Sections 3 and 4] for details regarding the above-mentioned local adjustments, since they remain unchanged. Assume we have at our disposal all three fields $\mathcal{L}^{\mathcal{S}}$, $\mathcal{L}^{\mathcal{S}}_{\mathrm{II}}$, and $\mathcal{L}^{\mathcal{S}}_{\mathrm{III}}$, containing the shortest distance to the boundary of three nearest particles (either computed a posteriori for a given particle assembly or already tracked during the packing algorithm).

In a manner similar to classical Voronoï tessellation, where a domain is partitioned by boundaries that have the same distance to the two closest seeds, thresholding the modified difference

$$\mathcal{F}_{\mathrm{c}} = \left(\mathcal{L}^{\mathcal{S}}_{\mathrm{II}} - \mathcal{L}^{\mathcal{S}}\right) + t_{\mathrm{c}} \tag{3.7}$$

yields a closed-cell, foam-like geometry with t_{c} indirectly controlling the thickness of foam cell walls. In the same spirit, the centrelines of the open-foam ligaments can be viewed as loci with the same distances to the boundary of three nearest particles; hence thresholding

$$\mathcal{F}_{\mathrm{o}} = \left(\tfrac{1}{2}(\mathcal{L}^{\mathcal{S}}_{\mathrm{III}} + \mathcal{L}^{\mathcal{S}}_{\mathrm{II}}) - \mathcal{L}^{\mathcal{S}}\right) + t_{\mathrm{o}}\,, \tag{3.8}$$

produces open-foam ligamentswith t_{o} governing their thickness. Finally, combining Eqs. (3.7) and (3.8)

$$\mathcal{F}(\boldsymbol{x}) = \min\left(\mathcal{F}_{\mathrm{c}}(\boldsymbol{x}), \mathcal{F}_{\mathrm{o}}(\boldsymbol{x})\right), \quad \forall \boldsymbol{x} \in \mathcal{S}\,, \tag{3.9}$$

allows for more realistic geometries with material concentration at wall intersections, see Fig. 3.10.

It is critical when extending the original framework to Wang tiles, with respect to the morphing procedures, to ensure that all three fields are continuous across the relevant tile edges/faces. As illustrated in Fig. 3.11, copying particle images introduced in the previous subsection is insufficient in this regard. To guarantee the required continuity, we define a wider domain margin as a subdomain related to individual copy-inducers. Instead of computing intersections with a tile boundary, we compute them for a virtual inset boundary (inset by r is usually enough) and copy the particles according to the virtual copy-inducers. Consequently, wider portions of tile domains are restrained near boundaries, resulting in restored continuity. This modification is also reflected in the construction of auxiliary field $\widetilde{\mathcal{L}}^{\mathcal{S}}$.

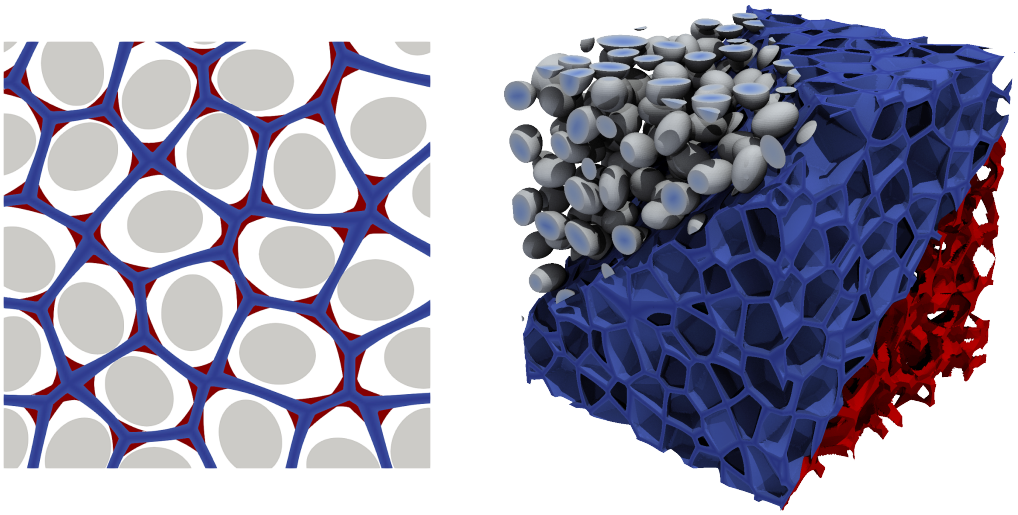

(a) (b)

Figure 3.10: Influence of morphing operations on resulting (a) two- and (b) three-dimensional geometry. From the original particle distribution (depicted with light grey), the closed-cell, foam-like geometry (shown in blue) is obtained by Eq. (3.7) and the open-like features (plotted in red) follow from Eq. (3.8).

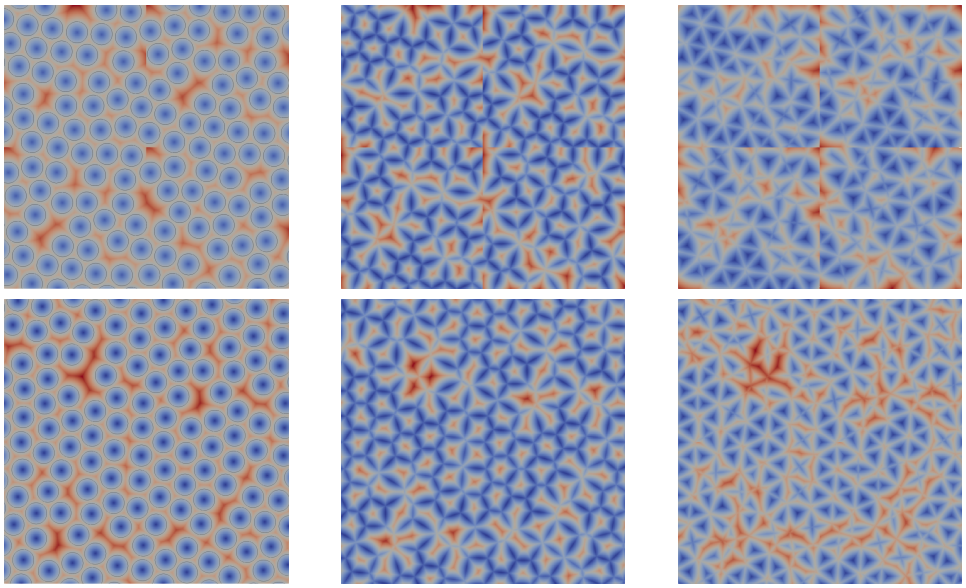

(a) (b) (c)

Figure 3.11: Assembled level-set fields composed of 2×2 tiles without (top row) and with (bottom row) a virtual boundary inset taken into account during particle placement. Note that even the nearest-neighbour distance $\mathcal{L}$ (a) is not continuous across vertices when the virtual inset is not considered, albeit the particle boundaries, i.e. zero-value contours outlined in grey, are. Severe discontinuities then appear for the second-nearest $\mathcal{L}_{\mathrm{II}}$ (b) and the third-nearest $\mathcal{L}_{\mathrm{III}}$ (c) neighbour distance without the inset boundaries.

3.4 Results

3.4.1 Comparison of 16-tile sets

First, we compare the periodicity reduction in three planar sets depicted in Fig. 3.2, which have the same cardinality but different tile definitions. We supplement our earlier

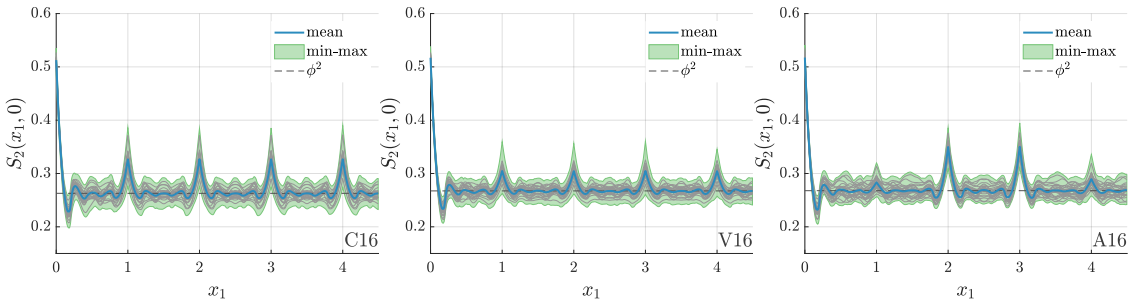

(a) (b) (c)

Figure 3.12: S_2 cross-sections along an x_1 coordinate for 10×10 tilings for (a) the edge-defined tile set C16, (b) the vertex-defined set V16, and (c) the Amman set A16, considered in Section 3.2.3. Thin grey lines depicts the average over 100 realizations of each tile set morphology, solid blue line shows the overall average (i.e. over realizations and morphologies) and the green area captures the range between minimal and maximal values. Dashed grey line marks the asymptotic value ϕ^2, where the averaged volume fraction ϕ is considered.

observations [21] regarding suppressed artificial periodicity compared to PUC-based reconstructions and better fitness of stochastic tile sets over their aperiodic counterparts. Namely, we consider: (C16) an edge-based stochastic set over four colours,[10] (V16) a vertex-based stochastic set over eight colours, and (A16) the aperiodic Ammann's set [85] over 12 colours[11].

Assuming ergodicity of a microstructure, we quantify the artificial periodicity in the tiling assemblies by means of the secondary peaks in the two-point probability function $S_2(\boldsymbol{x})$ [2]. $S_2(\boldsymbol{x})$ states the chance of finding two points separated by $\boldsymbol{x}$ in the same phase. Hence, $S_2(\boldsymbol{x})$ attains its maximum at $\boldsymbol{x} = \boldsymbol{0}$, where it equals the volume fraction ϕ of a chosen phase. For microstructures without any internal ordering, $S_2(\boldsymbol{x}) \to \phi^2$ with $\|\boldsymbol{x}\| \to \infty$ because two sufficiently distant points are uncorrelated. On the other hand, if a microstructure is composed of a repeating (SE)PUC, $S_2(\boldsymbol{x})$ exhibits secondary peaks having the same magnitude as $S_2(\boldsymbol{0})$ at nodes of a regular grid whose spacing corresponds to the (SE)PUC size. Thus, in the intermediate case of Wang tiling, the magnitude of secondary peaks indicates the remaining artificial ordering in the reconstructed microstructure, see [15, 21] for details. For computing $S_2(\boldsymbol{x})$, we used the Fast Fourier Transform (FFT) instead of random sampling, because the bias in the statistics caused by the implicit periodicity introduced with FFT is negligible for reasonably large microstructural realizations [96]. Recall also that the two-point probability function S_2, widely used for statistical quantification of material microstructures, e.g. [2], is the inverse Fourier Transform image of the power spectral density (or its estimate via periodogram) traditionally used in the Computer Graphics community, e.g., [17, 90, 95].

For each of the three tile sets we ran the presented algorithm 25 times and thus generated 25 different tile set morphologies. Aiming at capturing the artificial periodicity related to the limited number of edge codes and tiles, we resorted to the simplest set-up with circular inclusion of a fixed radius $r = 0.1$ in order to minimize the influence of particle shapes. In addition, we prevented the particles from overlapping tile vertices in

[10] This set corresponds to the set reported in [17].
[11] For the aperiodic assembly, we used the substitution rule from [31].

order not to favour the vertex-based tile set a priori[12]. The level-set fields of each unit-size tile ($\Omega = [-0.5, 0.5]^2$) were discretized using a regular grid comprising 201×201 points. Finally, we posed two constraints, $\kappa = 0.01$ and $\rho = 0.03$, on $\mathcal{A}$, recall Eq. (3.6).

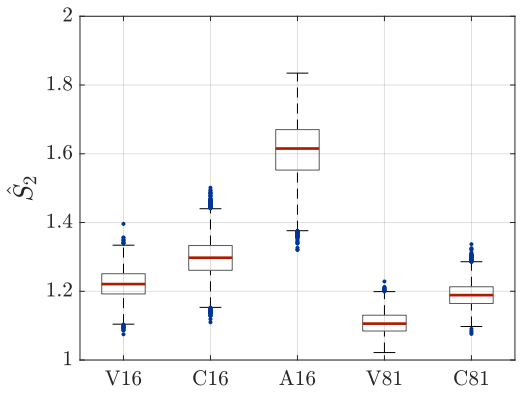

Figure 3.13: Box-and-whisker plot of the normalized maximal secondary peaks $\hat{S}_2$ over 100 realizations and 25 tile set morphologies for each tile set. The central lines mark the median; edges of each box denote the first and third quartiles; and whisker lines contain all data not considered as outliers (marked as dark blue dots).

We assembled 100 microstructural realizations, i.e. tilings, containing 10×10 tiles for each tile set and tile morphology and computed S_2 statistics for the inclusion phase. Cross-sections of S_2 along the x_1 coordinate are plotted in Fig. 3.12 for the tile sets considered. As expected, the secondary peaks appear at loci with integer coordinates. Excluding the primary peak, we picked the second highest extreme $\hat{S}_2$ normalised against the averaged asymptotic value ϕ^2 for each realisation and plotted the obtained data with box-and-whisker diagrams in Fig. 3.13.

While the Ammann's tile set A16 seems promising locally—note the suppressed secondary peaks at $x_1 = 1.0$ and $x_1 = 4.0$ in Fig. 3.12c—its deterministic aperiodic structure leads to pronounced secondary extremes in other regions, e.g. $x_1 = 3.0$. This observation corroborates our previous conclusions, based solely on the distribution of individual tiles within tilings, that strictly aperodic sets such as the Ammann's or Culik's set considered in [21] lead to higher secondary peaks than stochastic sets [17] with the same cardinality, which feature more uniform secondary peaks. Figs. 3.12 and 3.13 clearly show that, out of the two stochastic sets, the vertex-based definition performs better as expected, even despite the prevented vertex overlaps. This superiority of vertex-based tile sets in two dimensions is further supported by additional results comparing vertex- and edge-based sets comprising 81 tiles, see Fig. 3.13.

3.4.2 2D example

Second, we present an example of a two-dimensional microstructure based on polygonal particles. The geometry of each particle was derived from an originally regular, randomly-oriented polygon with the number of vertices being sampled from a normal distribution with the mean value 0.6 and the standard deviation 0.5, $\mathcal{N}(6.0, 0.5^2)$, and rounded to the nearest integer. The angle between two rays connecting the particle centre and neighbouring vertices was perturbed with a value randomly chosen from $\mathcal{N}(0.0, 0.5^2)$. Finally,

[12]From Fig. 3.5 it follows that a particle will be copied to all tiles if it overlaps any vertex for the A16 and C16 tile sets.

each vertex was placed on its corresponding ray at a distance sampled from $\mathcal{N}\left(0.95, 0.05^2\right)$ (and capped by 1.0) relative to the particle's circumscribed radius.

Following the outcomes of Section 3.4.1, we picked the vertex-based set with 16 tiles depicted in Fig. 3.2b. Similarly to the previous set-up, the size of each tile was $\Omega = [-0.5, 0.5]^2$ and the corresponding level-set fields were discretized using a regular grid comprising 201×201 points. The initial value of the circumscribed radius was set to $r = 0.08$. After 40 algorithm steps, the radius was increased to 0.1, and eventually we reduced it to 0.06 after next 60 steps. The number of algorithm steps and related radii were chosen randomly to illustrate the algorithm's control options. Only the first two constraints on $\mathcal{A}$ from Eq. (3.6) were posed. We fixed the minimal particle distance at $\kappa = 0.01$; the maximal distance ρ was set to 0.05 in the first 50 steps and decreased to 0.02 later. The width of the virtual boundary inset was kept constant at 0.1.

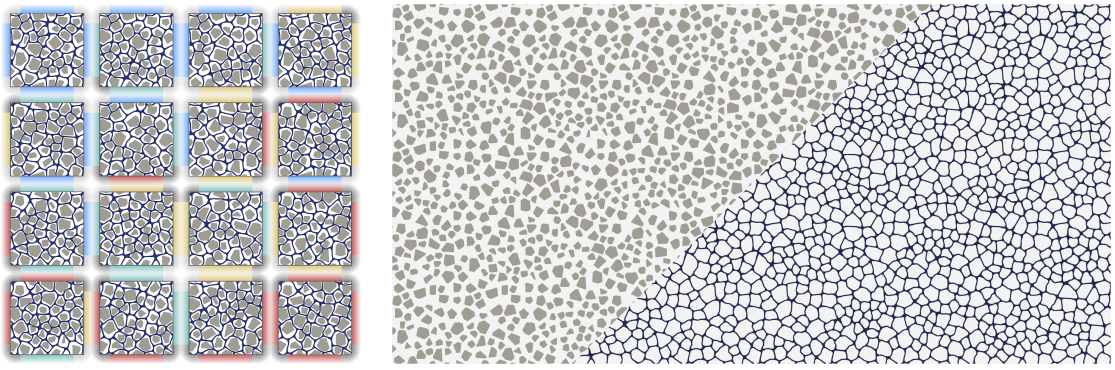

(a) (b)

Figure 3.14: Results of the algorithm set-up described in Section 3.4.2: (a) A composed view of the tile set with highlighted edge and vertex codes. The particulate assembly is drawn in grey; the corresponding foam-like microstructure is shown in blue (similar to Fig. 3.10); (b) An example of a 10×5 tiling.

Fig. 3.14 depicts a composed view of the resulting particle assembly and the related closed-cell, foam-like microstructural geometry obtained by considering $t_\mathrm{c} = 0.015$ and $t_\mathrm{o} = 0.020$ in Eq. (3.9).

3.4.3 3D example

Finally, we demonstrate a three-dimensional output of the algorithm for a set of 16 Wang cubes with two codes for each face orientation uniformly distributed in the set.

Again, we used centred tile domains of a unit size discretized with a grid of $101 \times 101 \times 101$ points. For the packing part of the algorithm, we considered ellip soidal particles with a random orientation and a fixed circumscribed radius $r = 0.10$. The ratio between the middle and the major semi-axes lengths was sampled from a uniform distribution $\mathcal{U}\left(0.7, 0.9\right)$; the minor to the major semi-axes length ratio was randomly generated from $\mathcal{U}\left(0.6, 0.7\right)$. The admissible domain at each algorithm step was dictated both by $\mathcal{L}^\mathcal{S}$ and $\mathcal{L}^\mathcal{S}_\mathrm{II}$ with constraints $\kappa = 0.02$, $\rho = 0.05$, and $\sigma = 0.05$ in Eq. (3.6). Since we aimed at modelling a foam-like microstructure, the width of a virtual inset boundaries was set to 0.1.

The final microstructure was obtained by performing the morphing operations according to Eq. (3.9) with $t_\mathrm{c} = 0.02$ and $t_\mathrm{o} = 0.03$. For the sake of brevity, we do not show

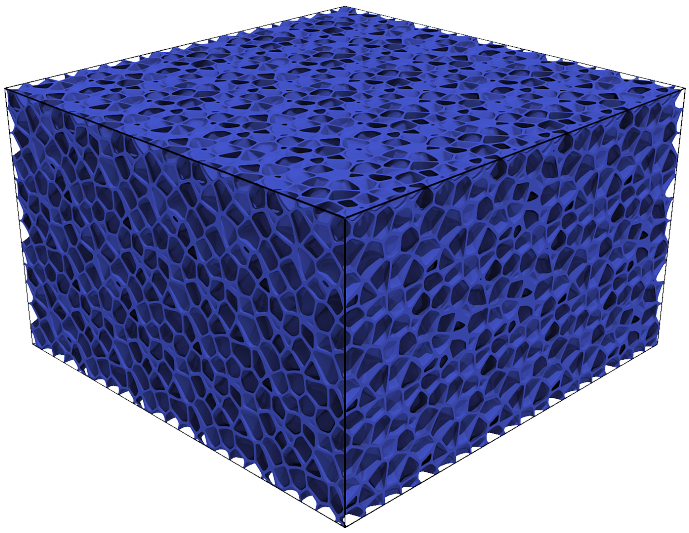

Figure 3.15: A microstructural realization assembled as a $5 \times 5 \times 3$ tiling from the Wang tiles generated in Section 3.4.3.

individual Wang cubes, and we plot only a microstructural sample comprising $5 \times 5 \times 3$ tiles in Fig. 3.15.

3.4.4 Computational cost

Our extension inherits the $\mathcal{O}(N)$ complexity of the Sonon et al.'s method [18, 19], as shown in Fig. 3.16. However, the actual time needed to generate particle packings or complex morphologies depends on several factors. While the impact of the grid resolution is straightforward (computational time scales linearly with the number of grid points), the effect of other factors such as particle shape and compatibility constraints due to different definitions of a tile set is less obvious.

To illustrate the influence of these factors, wall-clock time for several settings is plotted in Fig. 3.16. Tile sets considered for the analysis are the two-dimensional ones used in Section 3.4.1 and the three-dimensional sets from Section 3.4.3; in addition, a PUC was included in the comparison as a trivial case of a tile set. For all settings, tile domains of unit size were discretized with 401×401 grid points in two and $101 \times 101 \times 101$ grid points in three dimensions. The circumscribed radius of particles was set to $r = 0.02$ for two-dimensional and $r = 0.05$ for three-dimensional problems. The algorithm was terminated once the desired number of placed particles was achieved. Computational time[13] for each setting was measured 10 times.

Interestingly, albeit of the same cardinality, individual tile sets from Section 3.4.1 exhibit significantly different computational times. This is due to the distribution of edge codes within a set, because a larger part of the tile set domain must be updated with each particle copy in sets with fewer codes, recall Section 3.3.1.1. Note that Ammann's set with six codes for both horizontal and vertical edges behaves nearly the same as PUC.

Computational time related to the morphing operations depends on the operational

[13] All computational times are reported for a workstation equipped with an Intel® Xeon® E31280 3.50 GHz processor and 16 GB RAM running Windows 10 version 1903. The algorithm was implemented in the latest standard of C++ language (C++17), relying on parallel algorithms from the C++'s Standard Template Library.

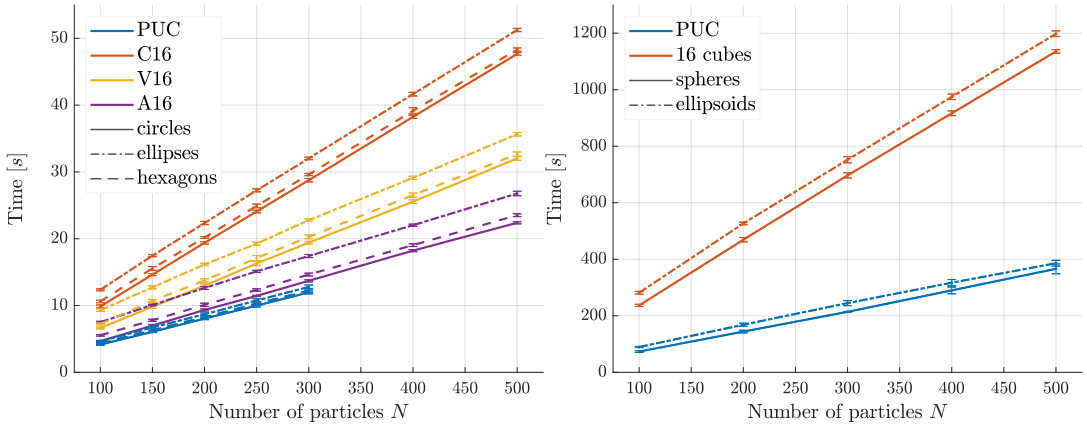

Figure 3.16: Wall-clock time needed to pack N particles into (a) two-dimensional and (b) three-dimensional tile sets. Results for different particle shapes are drawn in distinct line styles; considered tile sets (including the trivial case of PUC) are distinguished with distinct colours. Error bars show the standard deviation for each setting. PUC results in two dimensions are limited by the number of particles that can be packed in a unit domain.

mode of the algorithm. If the algorithm is used for both packing and morphing at the same time, the level-set fields used during the particle packing phase can be directly utilized for the morphing operations. On the other hand, when the morphing part runs separately, all the distance fields must be calculated again. Yet this recalculation is typically faster than the packing because all copies and compatibility constraints are already taken into account; for instance, generating the particle packing for the microstructure presented in Section 3.4.3 took 1,280 s while the recalculation needed for the morphing operations finished in 420 s.

3.5 Summary

In this work, we have extended Sonon et al.'s level-set based framework [18] to microstructural models based on the formalism of Wang tiles. The extension enables generating compressed representations of complex microstructural geometries such as open and closed foams or cells, which have been nearly impossible [21] or very expensive [15] to generate for Wang tiles to date.

Advancing from the standard Periodic Unit Cell to the generalized periodicity of Wang tiles necessitated several modifications of the original algorithm that addressed difficulties originally not encountered in the case of PUC. Driven by the geometrically-motivated question of where a vertex-overlapping particle should be copied to, we have come up with a simple procedure based on graph analysis capable of revealing the underlying vertex definition of a tile set, if present. We have also demonstrated that a straightforward copying of boundary-intersecting particles according to the edge and vertex codes is insufficient for preventing spurious particle overlaps because the information about the interior of a tile is not automatically communicated across individual tiles. As a remedy, we have introduced an artificially updated level-set field that facilitates this necessary communication. The width of the updated region in this field is dictated by the required final geometry. If only

a particle distribution is to be generated, the width equal to the particle radius r suffices. On the other hand, if foam-like microstructures are desired, the virtual boundary inset by r is necessary in order to preserve continuity of the level-set fields $\mathcal{L}^{\mathcal{S}}_{\mathrm{I}}$ and $\mathcal{L}^{\mathcal{S}}_{\mathrm{II}}$ across tile edges, resulting in the updated region of width $2r$.

Additionally, we have devised two minor modifications, one capable of breaking a regular underlying grid of possible particle centres by introducing their random shifts within an admissible region, the other accelerating the $\mathcal{L}^{\mathcal{S}}$ updates by pre-computing $\mathcal{L}^{\mathcal{P}}$ on a patch. The importance of the latter modification grows with higher $\mathcal{L}^{\mathcal{S}}$ resolutions and larger cardinality of a tile set.

Having a universal framework for generating Wang tile morphologies at our disposal, we have supplemented our previous comparison of strictly aperiodic and stochastic tile sets [21] and confirmed the superiority of vertex-defined tile sets in suppressing artificial periodicity in assembled microstructural samples. Given the same cardinality of the edge- and vertex-based tile sets in two dimensions, we recommend using the latter. On the other hand, the same comparison in three dimensions is more subtle and the choice should be always a compromise between available computational resources and required periodicity reduction, following e.g. the approximate formula proposed in [15].

Admittedly, the presented modification inherits certain limitations posed by the original framework; namely, it provides only indirect control of a resulting microstructural geometry and no spatial statistics are involved in the particle placing process. Albeit addressing these limitations remained out of the scope of this work, ideas conceptually similar to [46], i.e. optimizing the particle positions a posteriori to minimize the discrepancy between target and computed spatial statistics, could be potentially applied to steer the generated microstructure to the desired statistics.

Albeit our extension features linear complexity as in the original Sonon et al.'s framework, the generalized periodicity brings increased computational cost compared to PUC generation, see Section 3.4.4. Recall though that tile-based compression is intended primarily for generating numerous stochastic realizations with arbitrary sizes. Thus, more time can be spent on preparing the initial microstructure because the increased cost will be amortized later during repeated use of the same compression.

Our current focus is on developing a robust finite element discretization tool that would enable meshing both outputs of the framework, i.e. analytical geometries of particulate microstructures and complex geometries implicitly defined via level-set fields and processed with the marching-cube algorithm. In both cases, special attention will be paid to ensuring topological and geometrical compatibility of the resulting finite-element meshes across the corresponding faces/edges.

Chapter 4

Homogenization of high porosity foams

Abstract:
An approach to homogenization of high porosity metallic foams is explored. The emphasis is on the Alporas® foam and its representation by means of two-dimensional wire-frame models. The guaranteed upper and lower bounds on the effective stiffness coefficients are derived by the first-order homogenization with the uniform and minimal kinematic boundary conditions at heart. This is combined with the method of Wang tilings to generate sufficiently large material samples along with their finite element discretization. The obtained results are compared to experimental and numerical data available in literature and the suitability of the two-dimensional setting itself is discussed.

Reproduced from: Doškář, M., Novák, J., 2016. A jigsaw puzzle framework for homogenization of high porosity foams. Computers & Structures 166, 33–41. [75]

4.1 Introduction

Highly porous metallic foams possess an extensive application potential. These materials feature high energy absorption, strength, and stiffness at very low weight, which makes them appealing for the automotive, aircraft, and defense industry, to name a few [97, 98, 99]. In order to foster new application areas, a qualified understanding of the foam behavior and relevant predictive tools are required. Computer models, in particular, are regarded as a key ingredient to optimization of either/both the microstructure geometry or/and final products made of these materials [100]. A consensus regarding the approximation of the behavior of porous solids seems to exist. Open-cell foams[1] are usually represented with the three-dimensional beam models, while their closed-cell counterparts require an addition of membrane elements acting as the cell walls [101]. Nevertheless, in the case of very thin walls even the behavior of closed-cell foams can be approximated with beams [98, 102, 97, 103]. Following this assumption, Ashby and Gibson presented a three-dimensional beam model of the unit cell and derived solutions to the overall thermomechanical parameters based purely on material porosity [101]. Our goal is to explore the adequacy of a two-dimensional wired model discretized with beam elements. We build on the recent outcomes by Němeček et al. [20], who developed a planar beam model based on the approximation of foam ligament geometry by the Voronoï tessellation. The objectives of the paper are threefold:

1. to investigate the influence of real geometry of foam ligaments and the proper size of computational models [20];

2. to provide the upper and lower bounds on the effective stiffness coefficients for the two-dimensional beam model via the first-order homogenization procedure;

3. to validate obtained results against the experimental and numerical results from [20] and to question the assumption of the vanishing Poisson ratio made therein.

The first objective is addressed with the help of Wang tilings, a concept recently introduced to Materials Engineering community [15]. In particular, the foam microstructure is compressed within a set of smaller domains, called Wang tiles. The morphology of the tiles is designed such that the tiles are microstructurally compatible across the corresponding edges. As a result the reconstructed material microstructure remains continuous across the gridline of the regular lattice to which the tiles are accommodated during synthesis of a computational model, see Fig. 4.3c. The method is extremely efficient in producing arbitrarily diverse ensembles of arbitrarily sized and geometrically consistent microstructure realizations in a fully stochastic setting [21]. Moreover, creating the finite element mesh on the level of tiles avoids expensive mesh generation of each microstructure realization. Altogether, we are able to reach for a proper size of the computational model, which is expected to be relatively large because of the infinite contrast in constituent properties [84].

As regards the second objective, we reformulate the first-order homogenization procedure for the wire-frame finite element models by means of macroscopic degrees of freedom [22]. The upper bound on the apparent stiffness is obtained from the ensemble of microstructures exposed to the kinematic uniform boundary conditions (KUBC). The lower bound is rendered by applying the minimal kinematic boundary conditions (mKBC) [104].

[1] As Banhart [98] pointed out, sponge would be an appropriate term for open-cell highly porous solids.

Table 4.1: Properties of Alporas® foam [97]. Here K, G and E stand for the bulk, shear and Young moduli, respectively, and ν is the Poisson ratio.

K [GPa]	G [GPa]	E [GPa]	ν [-]
0.9 - 1.2	0.30 - 0.35	0.4 - 1.0	0.31 - 0.34

In order to compare our results with those reported in [97, 98, 105, 20], the bulk and shear moduli are derived from the homogenized stiffness matrices by assuming material isotropy.

The paper is structured as follows. In the next chapter Alporas® aluminum foam, the material of interest, is characterized in brief. Section 4.3 covers the adopted modeling strategy addressing the first objective. In particular, Wang tilings are presented first together with their use in the context of numerical homogenization. Description of microstructure discretization into planar beams is also provided in this section. The first order homogenization is reviewed in Section 4.4 with emphasis on the beam model and the boundary conditions connected to the upper and lower bounds on the effective stiffness. Numerical results are provided in Section 4.5 and discussed in the last section.

We use the following nomenclature within the text. Scalar quantities are denoted by plain letters, e.g. a or A, matrices by bold sans-serif font, e.g. a or A, and tensorial quantities by bold serif letters, e.g. $\boldsymbol{a}$ or $\mathbf{A}$. In addition, we adopt the standard Voigt matrix representation of symmetric second- and fourth-order tensors.

4.2 Alporas

Alporas® is the closed-cell aluminum foam commercially produced by Shinko Wire Company, Ltd. [105] with porosity between 90% and 92% [97]. The pore space is composed of approximately polyhedral voids with the mean size of around 3 mm. The main field of its application lies in the energy absorption structures. Predominantly, Alporas® is used in production of self-supporting sound absorbers [105]. The sandwich plates comprising of Alporas® foam core were also reported to outperform common steel plates under blast loading in e.g. [106].

Regarding the linear elastic behavior, the design guide to metallic foams [97] suggests the overall parameters enlisted in Tab. 4.1. However, the region of linear elastic behavior is rather limited. Nonlinear or inelastic behavior develops soon after the loading onset due to wall buckling, contacts between ligaments, and local yielding, which makes interpretation of overall elastic parameters from experimental data a challenging task.

Two distinct phases, (i) the aluminum rich phase, and (ii) the phase of precipitates consisting of titanium and calcium, were identified by Němeček et al. at the level of cell walls for the investigated specimen displayed in Fig. 4.1. In [20] the Mori-Tanaka homogenization scheme was employed to estimate the values of effective Young's modulus of 70 GPa and Poisson's ratio of 0.35 of the bulk material. In order to obtain comparable data with [20], the values were taken here as the reference parameters of the solid (ligament) phase for the homogenization at the level of foam.

4.3 Modeling strategy

Numerical homogenization is closely connected with the notion of Representative Volume Element (RVE), a characteristic sample of a microstructure large enough to provide us

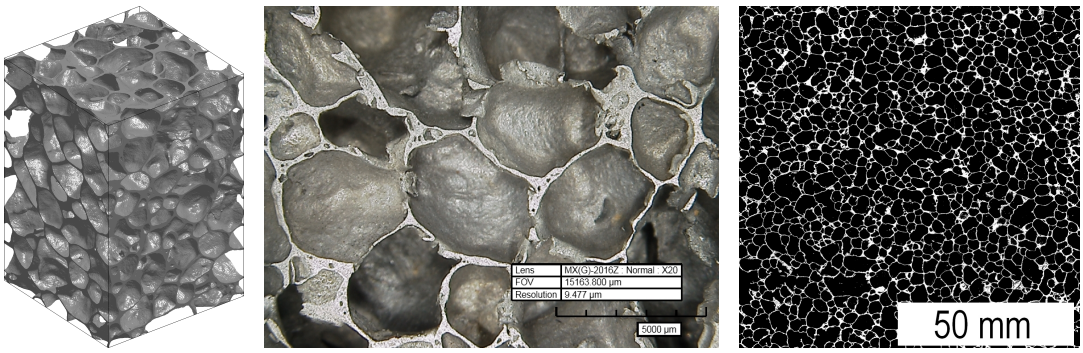

(a) (b) (c)

Figure 4.1: Alporas® foam: (a) Visualization of raw μ-CT data, (b) image from optical microscope, and (c) binary image of polished cross-section, courtesy of Ondřej Jiroušek [107] (a) and Jiří Němeček [20] (b,c).

with the effective material properties. From this viewpoint, a method capable of rendering stochastic microstructure realizations of arbitrary sizes is desirable.

Our approach rests on Wang tiling, a multicell generalization of the Periodic Unit Cell concept [15], see Fig. 4.2. We adopt the premise that a microstructure represented to a high degree of accuracy automatically provides us with a broad range of effective properties [108, 10]. Starting with a binary two-dimensional image of a material, we compress the microstructure into a set of Wang tiles. Subsequently, the Finite Element (FE) mesh composed of planar beams conforming through the edges of identical codes is generated within each tile. Finally, in the numerical homogenization we benefit from the ability of the tiling concept to produce ensembles of microstructure realizations and corresponding computational models of arbitrary sizes using a stochastic tiling algorithm.

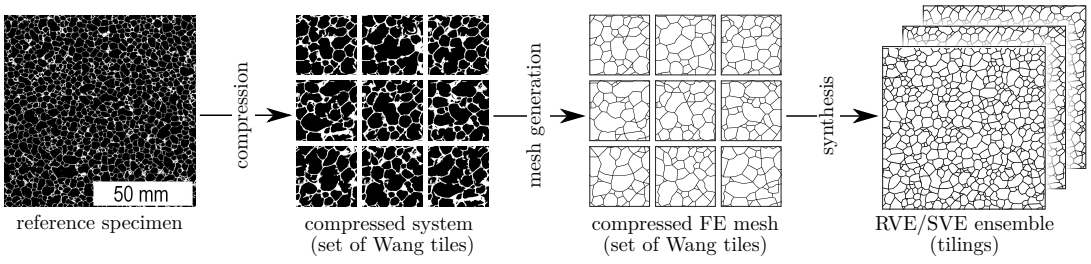

Figure 4.2: Illustration of adopted modelling strategy.

4.3.1 Wang tilings

Wang tiles are square domino-like pieces with codes assigned to their edges, Fig. 4.3a. The codes represent binding constrains such that only the tiles with the same codes on the adjacent edges may be placed next to each other when assembled into a tiling. By definition, the tiles can be neither rotated nor reflected [25], hence the two tiles of identical code sequences mutually rotated by $\frac{\pi}{2}$ are considered as different. The term tile set denotes the union of all tiles available for the tiling synthesis. The set is characterized with the number of tiles and the number of distinct codes on their horizontal and vertical edges. The composition of codes within the tile set governs the probability of occurrence of each

tile in the tiling.

Specific families of tile sets can be identified. Each of the families usually comes with a unique tiling algorithm. A great attention, especially from Discrete Mathematics community, has been paid to the family of aperiodic sets in the last 50 years. However, in agreement with Computer Graphics applications [17], we prefer stochastic sets to strictly aperiodic ones as the former provide us with more freedom in their design. The stochastic sets also correspond better with the purpose of modeling of materials with random/disordered microstructure.

Tiles of a stochastic tile set can be easily assembled into tilings by making use of the stochastic tiling algorithm proposed by Cohen et al. [17]. First, a regular lattice of desired size is created, see Fig. 4.3c. The grid is sequentially filled up with tiles in either column-by-column or row-by-row order. At each step, a tile is randomly chosen from a subset of tiles that satisfy edge constrains given by the previously placed tiles and positioned. The randomness is guaranteed by the existence of at least two distinct tiles for each admissible edge code combination on the top and left-hand side edges. A schematic of the procedure is displayed in Fig. 4.3c. The tiles 4 and 3 from the tile set, Fig. 4.3b, form the unique subset for one step in the stochastic tiling algorithm sketched in Fig. 4.3c. Either of the tiles is randomly chosen and fixed at the spot indicated with the asterisk mark.

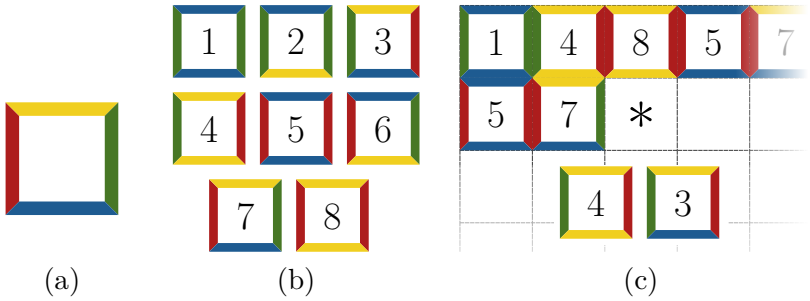

Figure 4.3: Illustration of: (a) a Wang tile, (b) a set of 8 Wang tiles, and (c) a single step of the stochastic tiling algorithm.

4.3.2 Tile-based microstructure compression

In order to make the Wang tile concept applicable to modeling of random heterogeneous materials, microstructural information has to be attributed to each tile such that a tiled domain (a tiling) corresponds to the original microstructure and the microstructure continuity is not violated across the congruent edges. By analogy to the Periodic Unit Cell (PUC) morphology design [10, 54], a way to meet those requirements is to employ optimization methods, e.g. Simulated Annealing [15]. Although this approach is fully general, the computational cost is tremendous especially for larger sets, high microstructure resolution, multiphase media, and/or multi-point spatial descriptors. Therefore, in this study we employ the automatic design procedure proposed originally for compression of digital textures [17] and explored later in materials modeling [21].

In brief, we take a number of samples from the reference specimen of the investigated microstructure. Each of the samples is associated with a unique edge code from the tile set. Each tile is then constructed as a square cut, rotated by $\frac{\pi}{4}$, out of partially overlapping samples that are positioned according to the tile edge codes they are associated with [17]. Since the cut goes diagonally through the samples, the microstructure continuity is au-

tomatically preserved as the sample leftovers are used as microstructural information for the tiles having the same codes on the opposite edges. The samples are seamlessly fused in the tile interiors by making use of the Image Quilting algorithm due to Efros et al. [37]. We have augmented the procedure by optimizing the design input parameters to achieve maximum proximity in spatial statistics of synthesized tilings and the original microstructure. Namely, volume fraction, two-point probability and two-point cluster functions were considered. This approach appears extremely efficient from the viewpoint of both the quality of compressed microstructures and computational overhead, see [21] for details. Thus, after the compression based on the automatic tile design algorithm we have a binary representation of the Alporas microstructure in the form of a set of Wang tiles at hand.

4.3.3 Discretization

Validity of three-dimensional beam models for predicting elastic behavior of foams has been reported several times, e.g. [101, 97, 103]. In the recent work [20], Němeček et al. presented promising results also for the two-dimensional beam representation of foam motivating our modeling strategy. In their approach the foam microstructure was represented as the Voronoï wired model consisting of straight beams with the centroids of individual pores taken as the Voronoï diagram seeds. The wired model was preferred to the two-dimensional finite element analysis as the latter would have required modifications to ligament walls thickness in order to fit the volume fraction from the weighting experiment. Its difference against the volume fraction determined from the area of ligaments in the reference planar scan was attributed to the preparation procedure, in which the saw cut was not perpendicular to most of the cell walls yielding the apparent solid phase volume be higher than the true one.

The size of the model used by authors of [20] was limited by the extent of the given scanned image. However, this is not the case of Wang tiles, which enable to investigate series of models yielding adequate RVE dimensions. In addition, the beam geometry conforming with the real shape of ligaments allows us to explore the inaccuracy resulting from the Voronoï tessellation based idealization. We started with the foam geometry compressed within the set of 32 tiles with four distinct edge codes on vertical and horizontal edges (8 in total), Fig. 4.4a. First, a parametric beam discretization of tile geometries was created manually by employing a specifically designed GUI tool written in Matlab environment[2], Fig. 4.4b. It enabled us to control the mesh compatibility across tile edges and to fix ligaments disrupted by quilting or faults due to the sample preparation, Fig. 4.1. Computational domains were assembled from the individual tiles by making use of the stochastic tiling algorithm described in Section 4.3.1, the nodes on the coincident edges were identified, merged, and the entire record renumbered to maintain the sparsity of algebraic systems.

The cross-sectional parameters of individual beams were determined by analogy to [20]. Beams were assumed straight and prismatic with a rectangular cross-section of the unit width. The total length of beams L_Σ is given by the mesh geometry. Hence, the only degree of freedom, the depth of the cross-section H, is governed by the volume fraction of the solid phase ρ and RVE volume/area $|\Omega|$. It reads as

$$H = \frac{\rho|\Omega|}{L_\Sigma} \tag{4.1}$$

[2]available at `http://mech.fsv.cvut.cz/~doskar/software/MeshMaker.zip`

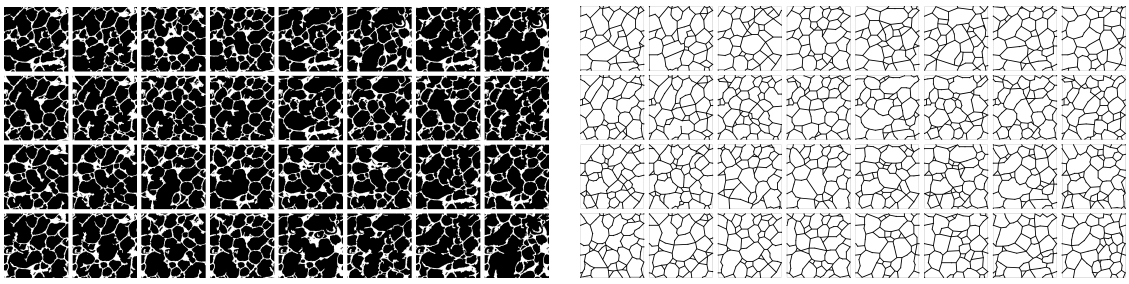

(a) (b)

Figure 4.4: Alporas® microstructure compressed within 32 tiles: (a) microstructure of individual tiles, (b) corresponding wired model (beam discretization of ligaments).

Together with the assumption of unit beam width, Eq. (4.1) further yields expressions for the cross-sectional area A and the second moment of area I

$$A = H, \quad I = \frac{1}{12}H^3 \tag{4.2}$$

In order to analyze precisely the effect of beam geometry, a separate beam model, Fig. 4.5c, was created directly from the reference geometry (referred to as real geometry mesh onwards) in our in-house developed GUI tool. It was accompanied also with the microstructure represented as the Voronoï diagram, Fig. 4.5b, to compare with the results published in [20]. For visual comparison, a tiling-based geometry of similar size (composed of 6×6 tiles) is shown in Fig. 4.5d.

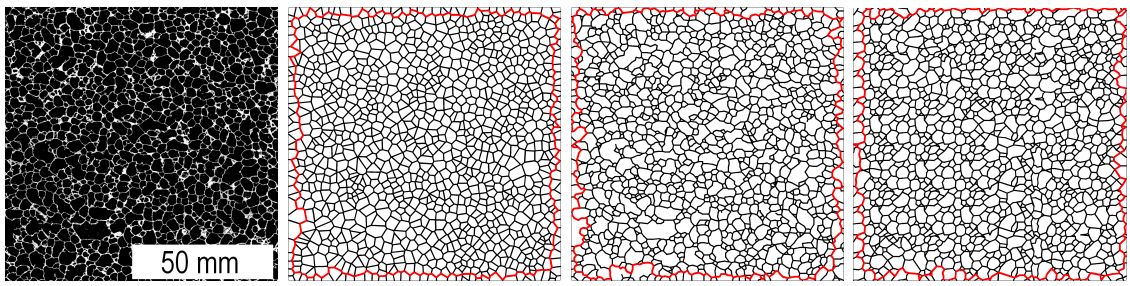

(a) (b) (c) (d)

Figure 4.5: Comparison of various representations of Alporas® geometry: (a) reference microstructure (courtesy of Jiří Němeček [20]), (b) Voronoï mesh, (c) mesh of real geometry, and (d) tiling-based representation of beam mesh (6×6 tiling). The red line highlights boundary beams such that they coincide with $\partial\Omega$.

4.4 Numerical homogenization

In general, the homogenization process provides a homogeneous substitute for a heterogeneous material composed of constituents of different properties. Limiting the exposition to linear elasticity, with Hooke's Law

$$\boldsymbol{\sigma}(\boldsymbol{x}) = \mathbf{D}(\boldsymbol{x}) : \boldsymbol{\varepsilon}(\boldsymbol{x}), \quad \text{for } \boldsymbol{x} \in \Omega, \tag{4.3}$$

relating local stresses $\boldsymbol{\sigma}(\boldsymbol{x})$ to strains $\boldsymbol{\varepsilon}(\boldsymbol{x})$ and Ω being the microscale domain of interest representing a macroscopic material point, we wish to replace the heterogeneous material stiffness tensor $\mathbf{D}(\boldsymbol{x})$ with its homogeneous counterpart $\mathbf{D}^{\mathrm{hom}}$ independent of microscale coordinates $\boldsymbol{x}$. An equation analogical to Eq. (4.3), namely,

$$\boldsymbol{\Sigma} = \mathbf{D}^{\mathrm{hom}} : \boldsymbol{E}\,, \tag{4.4}$$

then relates the macroscopic strains $\boldsymbol{E}$ and stresses $\boldsymbol{\Sigma}$, defined as spatial averages $\langle\cdot\rangle$

$$\begin{aligned} \boldsymbol{E} &= \langle \boldsymbol{\varepsilon}(\boldsymbol{x}) \rangle = \frac{1}{|\Omega|} \int_{\Omega} \boldsymbol{\varepsilon}(\boldsymbol{x})\, \mathrm{d}\boldsymbol{x} \quad \text{and} \\ \boldsymbol{\Sigma} &= \langle \boldsymbol{\sigma}(\boldsymbol{x}) \rangle = \frac{1}{|\Omega|} \int_{\Omega} \boldsymbol{\sigma}(\boldsymbol{x})\, \mathrm{d}\boldsymbol{x}\,, \end{aligned} \tag{4.5}$$

respectively.

Homogenization of parameters describing linear problems is a well resolved area nowadays. For simple microstructural compositions and relatively low contrast in constituent properties analytical homogenization schemes yield accurate estimates, often based on the Eshelby solution, or narrow bounds, e.q. Voigt-Reuss-Hill or Hashin-Shtrikman, of the sought homogenized property [38, and references therein]. On the contrary, for materials with high contrast in properties of its constituents the actual microstructural geometry, simplified in the analytical homogenization methods, influences significantly the material response. Consequently, the analytical methods are suitable only for quick precursory estimates of the overall material stiffness. In the particular example of highly porous foams, even the closest estimates obtained with the Mori-Tanaka and the differential schemes differ from the experimental data by 20% [109, 38].

Hence, to determine the overall properties we resort to a numerical homogenization that, albeit more computationally intensive, gives us an insight into the size of the related RVE and mechanics of deformation of the investigated microstructure. In particular, we adopt the first-order numerical homogenization method described comprehensively in work of Michel et al. [22]. First, the general concept is recalled in the tensorial notation and the variational setting. Then, we reformulate the approach for a two-dimensional beam model, using the matrix notation. Numerical homogenization, unlike the analytical schemes, calls for a suitable computational domain – RVE, and for specific boundary conditions in order to render bounds of the effective property. We address these issues in Section 4.4.3 and discuss incorporation of different boundary conditions by means of the Lagrange multipliers.

4.4.1 First order homogenization

In the first order homogenization, the total displacement field $\boldsymbol{u}(\boldsymbol{x})$ can be decomposed as [22]

$$\boldsymbol{u}(\boldsymbol{x}) = \boldsymbol{u}^{\boldsymbol{E}}(\boldsymbol{x}) + \boldsymbol{u}^{*}(\boldsymbol{x}) = \boldsymbol{E} \cdot \boldsymbol{x} + \boldsymbol{u}^{*}(\boldsymbol{x})\,, \quad \text{for } \boldsymbol{x} \in \Omega\,, \tag{4.6}$$

where $\boldsymbol{u}^{\boldsymbol{E}}(\boldsymbol{x})$ is coupled with the homogeneous strains $\boldsymbol{E}$ and $\boldsymbol{u}^{*}(\boldsymbol{x})$ are displacement fluctuations induced by presence of material heterogeneity. Applying the symmetric gradient operator $\boldsymbol{\nabla}^{s} = \frac{1}{2}\left(\boldsymbol{\nabla} + \boldsymbol{\nabla}^{\mathsf{T}}\right)$ to the displacement fields in Eq. (4.6) provides us with the total strains in the form

$$\boldsymbol{\varepsilon}(\boldsymbol{x}) = \boldsymbol{\nabla}^{s}\boldsymbol{u}(\boldsymbol{x}) = \boldsymbol{E} + \boldsymbol{\nabla}^{s}\boldsymbol{u}^{*}(\boldsymbol{x})\,, \quad \text{for } \boldsymbol{x} \in \Omega\,. \tag{4.7}$$

Thus, the strain energy density on microscale reads

$$W\left(\boldsymbol{x}, \boldsymbol{E}, \boldsymbol{\nabla}^s \boldsymbol{u}^*(\boldsymbol{x})\right) = \frac{1}{2}\left(\boldsymbol{E} + \boldsymbol{\nabla}^s \boldsymbol{u}^*(\boldsymbol{x})\right) : \mathbf{D}(\boldsymbol{x}) : \left(\boldsymbol{E} + \boldsymbol{\nabla}^s \boldsymbol{u}^*(\boldsymbol{x})\right). \tag{4.8}$$

For the purpose of variational formulation, we distinguish between the true fields $\boldsymbol{E}$ and $\boldsymbol{u}^*$ and the corresponding test fields denoted with tilde. Let $\mathcal{C}$ be a set of all admissible fluctuation displacement fields complying with the boundary conditions, further specified in 4.4.3. For arbitrary test fields $\tilde{\boldsymbol{u}}^* \in \mathcal{C}$ and $\tilde{\boldsymbol{E}} \in \mathbb{R}^{d\times d}_{\mathrm{sym}}$, where d is the dimension of the model under consideration ($d = 2$ in our particular case), we define the macroscopic strain energy density $\widehat{W}$ as

$$\widehat{W}(\tilde{\boldsymbol{E}}, \tilde{\boldsymbol{u}}^*) = \left\langle W(\boldsymbol{x}, \tilde{\boldsymbol{E}}, \boldsymbol{\nabla}^s \tilde{\boldsymbol{u}}^*(\boldsymbol{x})) \right\rangle . \tag{4.9}$$

Assume the stress $\boldsymbol{\Sigma}$ to be prescribed on macroscale. The elastic energy potential $J(\tilde{\boldsymbol{E}}, \tilde{\boldsymbol{u}}^*)$ for a macroscopic material point is then specified in the form

$$J(\tilde{\boldsymbol{E}}, \tilde{\boldsymbol{u}}^*) = \widehat{W}(\tilde{\boldsymbol{E}}, \tilde{\boldsymbol{u}}^*) - \boldsymbol{\Sigma} : \tilde{\boldsymbol{E}} . \tag{4.10}$$

The true fields $\boldsymbol{E}$ and $\boldsymbol{u}^*$ are obtained by minimizing the latter equation following the minimum total potential energy principle. Finally, combining the stationary conditions of Eq. (4.10) and Eq. (4.4) results in the expression

$$\mathbf{D}^{\mathrm{hom}} = \frac{\partial^2 \widehat{W}}{\partial \tilde{\boldsymbol{E}}^2}\left(\boldsymbol{E}, \boldsymbol{u}^*\right) . \tag{4.11}$$

4.4.2 Discretization - Macroscopic Degrees of Freedom

As discussed in the previous sections, we assume Ω to be a planar model discretized by straight beams. The model is embedded in the x-z plane, thus the unknowns of the beam model are nodal displacements u, w along x, z axes, and rotations ϕ about y. The dual quantities are normal forces N, shear forces V and bending moments M acting at beam ends (denoted by subscript indices 1 and 2). It holds

$$\mathsf{f}_e = \mathsf{K}_e \mathsf{u}_e , \tag{4.12}$$

where $\mathsf{f}_e = \{N_1, V_1, M_1, N_2, V_2, M_2\}^{\mathsf{T}}$, K_e is the element stiffness matrix calculated according to the Timoshenko theory [110], and $\mathsf{u}_e = \{u_1, w_1, \phi_1, u_2, w_2, \phi_2\}^{\mathsf{T}}$.

The displacement decomposition in Eq. (4.6), rewritten in the matrix form, gives

$$\mathsf{u}_e = \begin{bmatrix} \mathsf{I} & \mathsf{A}_e \end{bmatrix} \begin{Bmatrix} \mathsf{u}_e^* \\ \mathsf{E} \end{Bmatrix} , \tag{4.13}$$

where I is the identity matrix of 6×6 entries and

$$\mathsf{A}_e^{\mathsf{T}} = \begin{bmatrix} x_1 & 0 & 0 & x_2 & 0 & 0 \\ 0 & z_1 & 0 & 0 & z_2 & 0 \\ \frac{1}{2}z_1 & \frac{1}{2}x_1 & 0 & \frac{1}{2}z_2 & \frac{1}{2}x_2 & 0 \end{bmatrix} \tag{4.14}$$

couples the nodal degrees of freedom (DOFs) with the applied macroscopic strains $\mathsf{E} = \{E_x, E_z, \Gamma_{xz}\}^{\mathsf{T}}$. Thus, the components of the macroscopic strain play the role of additional

macroscopic degrees of freedom of the discretized system, cf. [22].

In the variational setting, contributions of individual finite elements to the overall strain energy density are

$$\begin{aligned}\widehat{W}_e(\tilde{\mathsf{E}},\tilde{\mathsf{u}}^*) &= \frac{1}{2|\Omega|}\tilde{\mathsf{u}}_e^{\mathsf{T}}\mathsf{K}_e\tilde{\mathsf{u}}_e \\ &= \frac{1}{2|\Omega|}\begin{Bmatrix}\tilde{\mathsf{u}}_e^*\\ \tilde{\mathsf{E}}\end{Bmatrix}^{\mathsf{T}}\underbrace{\begin{bmatrix}\mathsf{I} & \mathsf{A}_e\end{bmatrix}^{\mathsf{T}}\mathsf{K}_e\begin{bmatrix}\mathsf{I} & \mathsf{A}_e\end{bmatrix}}_{\mathsf{K}_e^{\mathrm{ex}}}\begin{Bmatrix}\tilde{\mathsf{u}}_e^*\\ \tilde{\mathsf{E}}\end{Bmatrix},\end{aligned} \tag{4.15}$$

where $\mathsf{K}_e^{\mathrm{ex}}$ is the extended element stiffness matrix of the form

$$\mathsf{K}_e^{\mathrm{ex}} = \begin{bmatrix}\mathsf{K}_e & \mathsf{K}_e\mathsf{A}_e\\ \mathsf{A}_e^{\mathsf{T}}\mathsf{K}_e & \mathsf{A}_e^{\mathsf{T}}\mathsf{K}_e\mathsf{A}_e\end{bmatrix}. \tag{4.16}$$

With the extended discrete system (4.15) at hand, the macroscopic strain energy can be written as

$$\widehat{W}(\tilde{\mathsf{E}},\tilde{\mathsf{u}}^*) = \frac{1}{2|\Omega|}\begin{Bmatrix}\tilde{\mathsf{u}}^*\\ \tilde{\mathsf{E}}\end{Bmatrix}^{\mathsf{T}}\mathsf{K}^{\mathrm{ex}}\begin{Bmatrix}\tilde{\mathsf{u}}^*\\ \tilde{\mathsf{E}}\end{Bmatrix}, \tag{4.17}$$

where $\tilde{\mathsf{u}}^* = \mathop{\mathrm{A}}_{e=1}^{n_e}\tilde{\mathsf{u}}_e^*$, K^{ex} takes the form

$$\mathsf{K}^{\mathrm{ex}} = \mathop{\mathrm{A}}_{e=1}^{n_e}\mathsf{K}_e^{\mathrm{ex}} = \begin{bmatrix}\mathsf{K}_{11}^{\mathrm{ex}} & \mathsf{K}_{12}^{\mathrm{ex}}\\ \mathsf{K}_{21}^{\mathrm{ex}} & \mathsf{K}_{22}^{\mathrm{ex}}\end{bmatrix}, \tag{4.18}$$

and $\mathop{\mathrm{A}}_{e=1}^{n_e}$ is the finite element assembly operator. The submatrices $\mathsf{K}_{ij}^{\mathrm{ex}}$ arise from the assembly of the submatrices on the right-hand side of Eq. (4.16) and n_e denotes the number of elements.

4.4.3 RVE size and boundary conditions

The above procedure yields the homogenized parameters providing the computational domain coincides with the RVE related to the investigated microstructure and physical phenomenon. According to Hill [111], RVE is the sample of a material that incorporates enough geometrical information to render the effective stiffness parameters regardless the prescribed boundary conditions as long as they would result in the uniform stress and strain states if the microstructure were homogeneous. For smaller domains, here called Statistical Volume Elements (SVEs), Eq. (4.11) gives only the boundary condition dependent apparent stiffnesses. Thus, when homogenizing, the size of Ω is usually increased step by step until the apparent properties resulting from different boundary conditions either coincide, i.e. meeting Hill's criterion [111], or the variance in the sought quantity computed from different realizations of the same size reaches a given limit [82].

Among the admissible boundary conditions yielding the uniform strain in the homogeneous medium, three are commonly used. The periodic boundary conditions show the fastest convergence as the size of SVEs approaches that of RVE, however they render only the estimate of the effective stiffness and are cumbersome to impose if the microstructure is in general non-periodic, which is also the case of Alporas®. The remaining two, Kinematic Uniform Boundary Conditions (KUBC) and Static Uniform Boundary Conditions (SUBC), are known to result in the upper and lower bounds of the apparent stiffness coefficients of each SVE, refining so the Voigt-Reuss-Hill bounds [82, 112]. To the best of our

knowledge, the exact form of SUBC is unknown for beam models. We thus circumvent this drawback prescribing the Minimal Kinematic Boundary Conditions (mKBC) due to Mesarovic and Padbidri [104], since these were shown to equal SUBC [113].

To preserve the structure of the resulting algebraic system, both boundary conditions are prescribed as an additional constraint[3] in the form

$$\mathsf{C}\tilde{\mathsf{u}}^* = \mathsf{0} \tag{4.19}$$

defining so the kinematically admissible nodal displacements and rotations stored in $\tilde{\mathsf{u}}^*$. The boundary $\partial\Omega$ has been determined from the beams fully contained in the domain, highlighted in red (light gray in BW version) in Fig. 4.5.

In the case of KUBC, the displacement fluctuations have to vanish at the boundary, i.e. $\tilde{\boldsymbol{u}}^*(\boldsymbol{x}) = 0$ for $\boldsymbol{x} \in \partial\Omega$. In the discrete beam model we prescribe zero fluctuation displacements u and v for all nodes at the boundary, the corresponding rotations ϕ are left unknown. With $n^{\partial\Omega}$ boundary nodes and n^{tot} nodes in total, the matrix of constraints C^{KU} for the KUBC case consists of $\left[2n^{\partial\Omega} \times 3n^{\mathrm{tot}}\right]$ components and is defined as

$$C_{ij}^{\mathrm{KU}} = \begin{cases} 1\,, & \text{for } i = j \in \mathcal{G}\,, \\ 0\,, & \text{otherwise,} \end{cases} \tag{4.20}$$

where $\mathcal{G}$ is the set of all code numbers corresponding to the fixed fluctuation displacements.

In contrast to KUBC, mKBC [113] do not require the fluctuation field to vanish at the boundary point-wise but they enforce the field to vanish on average. The definition of the macroscopic strain tensor $\boldsymbol{E}$, Eq. (4.5), along with the local strain field decomposition, Eq. (4.7), yields the minimal condition posed on $\tilde{\boldsymbol{u}}^*$ (also called the normalization condition [114]) in the form

$$\mathbf{0} = \frac{1}{|\Omega|}\int_\Omega \boldsymbol{\nabla}^s \tilde{\boldsymbol{u}}^* \,\mathrm{d}\boldsymbol{x} = \frac{1}{|\Omega|}\int_{\partial\Omega} \boldsymbol{n} \otimes^s \tilde{\boldsymbol{u}}^* \,\mathrm{d}\boldsymbol{x}\,, \tag{4.21}$$

where $\boldsymbol{n}$ is the outer normal and $\otimes^s$ denotes the symmetric part of the tensor product defined as $(\boldsymbol{n} \otimes^s \tilde{\boldsymbol{u}}^*) = \frac{1}{2}(\boldsymbol{n} \otimes \tilde{\boldsymbol{u}}^* + \tilde{\boldsymbol{u}}^* \otimes \boldsymbol{n})$. In addition to the three conditions defined by Eq. (4.21) (for the two-dimensional setting), we prescribe zero fluctuations u^* and w^* at the bottom-left and w^* at the bottom-right corners to restrain the rigid body modes. Plugging the shape functions of the beam element in Eq. (4.21) along with the three additional conditions mentioned above give rise to the matrix of constraints C^{mK} with $\left[(3+3) \times 3n^{\partial\Omega}\right]$ entries, see 4.A for additional details.

Having the matrices C^{KU} and C^{mK} at hand, the constrained minimization of Eq. (4.10) can be reformulated by making use of the Lagrange multipliers $\tilde{\lambda}$, which act as reactions and generalized reactions for KUBC and mKBC, respectively. To this goal, we define the energy potential $\bar{J}(\tilde{\mathsf{u}}^*, \tilde{\mathsf{E}}, \tilde{\lambda})$ similarly to Eq. (4.10)

$$\bar{J}(\tilde{\mathsf{u}}^*, \tilde{\mathsf{E}}, \tilde{\lambda}) = \frac{1}{|\Omega|}\left(\frac{1}{2}\begin{Bmatrix}\tilde{\mathsf{u}}^* \\ \tilde{\mathsf{E}}\end{Bmatrix}^{\mathsf{T}} \mathsf{K}^{\mathrm{ex}} \begin{Bmatrix}\tilde{\mathsf{u}}^* \\ \tilde{\mathsf{E}}\end{Bmatrix} + \tilde{\lambda}^{\mathsf{T}}\mathsf{C}\tilde{\mathsf{u}}^*\right) - \Sigma^{\mathsf{T}}\tilde{\mathsf{E}}\,. \tag{4.22}$$

[3] We assume that the assembly operator $\mathop{\mathsf{A}}_{e=1}^{n_e}$ does not involve boundary conditions.

The stationary conditions posed on $\bar{J}$, namely,

$$\frac{\partial}{\partial \tilde{\mathsf{u}}^*}\,\bar{J}\Big|_{\tilde{\mathsf{u}}^*=\mathsf{u}^*}=0\,,\quad \frac{\partial}{\partial \tilde{\mathsf{E}}}\,\bar{J}\Big|_{\tilde{\mathsf{E}}=\mathsf{E}}=0\,,\quad \frac{\partial}{\partial \tilde{\lambda}}\,\bar{J}\Big|_{\tilde{\lambda}=\lambda}=0\,, \tag{4.23}$$

form the following algebraic system for the true fields

$$\begin{Bmatrix}\mathsf{0}\\ \mathsf{\Sigma}\\ \mathsf{0}\end{Bmatrix}=\frac{1}{|\Omega|}\begin{bmatrix}\mathsf{K}_{11}^{\mathrm{ex}} & \mathsf{K}_{12}^{\mathrm{ex}} & \mathsf{C}^{\mathsf{T}}\\ \mathsf{K}_{21}^{\mathrm{ex}} & \mathsf{K}_{22}^{\mathrm{ex}} & 0\\ \mathsf{C} & 0 & 0\end{bmatrix}\begin{Bmatrix}\mathsf{u}^*\\ \mathsf{E}\\ \lambda\end{Bmatrix}. \tag{4.24}$$

Finally, condensing u^* and λ from Eq. (4.24) yields the homogenized stiffness matrix $\mathsf{D}^{\mathrm{hom}}$ equivalently to Eq. (4.11). For large and sparse systems of linear equations direct condensation of Eq. (4.24) would be inefficient. We thus compute individual columns of $\mathsf{D}^{\mathrm{hom}}$ in three consecutive steps as the responses $\mathsf{\Sigma}^{(i)}$ to the unit load cases $\mathsf{E}^{(i)}$ defined as $\mathsf{E}^{(1)}=\Big\{1,0,0\Big\}^{\mathsf{T}}$, $\mathsf{E}^{(2)}=\Big\{0,1,0\Big\}^{\mathsf{T}}$, and $\mathsf{E}^{(3)}=\Big\{0,0,1\Big\}^{\mathsf{T}}$.

4.4.4 Extraction of isotropic parameters

The approach outlined above leads to the homogenized material stiffness matrix with components encoding the anisotropic behavior. If the degree of anisotropy is small, it is convenient to describe the constitutive behavior of the homogenized material with scalar quantities K and G, see Tab. 4.1. To this goal, we perform spectral analysis of $\mathsf{D}^{\mathrm{hom}}$ to determine the effective moduli from its eigenvalues [41]. For the plane strain conditions, the stiffness matrix of isotropic material $\mathsf{D}^{\mathrm{iso}}$ and its eigenvalues λ^{iso} in terms of K and G read

$$\mathsf{D}^{\mathrm{iso}}=\begin{bmatrix}K+\frac{4}{3}G & K-\frac{2}{3}G & 0\\ K-\frac{2}{3}G & K+\frac{4}{3}G & 0\\ 0 & 0 & G\end{bmatrix},\ \lambda^{\mathrm{iso}}=\begin{Bmatrix}G\\ 2G\\ \frac{2}{3}G+2K\end{Bmatrix} \tag{4.25}$$

Note, that the min $\rightarrow$ max ordering of the λ^{iso} components holds for non-auxetic materials only, i.e. for those with $\nu>0$. Since the calculated overall stiffness matrix $\mathsf{D}^{\mathrm{hom}}$ and the matrix eigenvalues λ^{hom} may not obey Eq. (4.25) exactly we employ the Least Square Method to obtain the moduli as

$$\begin{Bmatrix}G^{\mathrm{hom}}\\ K^{\mathrm{hom}}\end{Bmatrix}=\begin{bmatrix}\frac{1}{5} & \frac{2}{5} & 0\\ -\frac{2}{30} & -\frac{4}{30} & \frac{1}{2}\end{bmatrix}\lambda^{\mathrm{hom}}\,, \tag{4.26}$$

see 4.B for additional details.

4.5 Results

The cross-sectional characteristics of beams, Tab. 4.2, for the three different geometries, Fig. 4.5, were derived through the approach outlined in Section 4.3 with the target ligament volume fraction set to 8.6% [20].Note that the depth of beams (corresponding to the cross-section area A, recall Eq. (4.2)) in the tiling-based representation is about 10% smaller than for the previous two. We attribute this reduction to the automatic tile design, namely local modifications to the geometry within the overlap region, and corrections induced by manual mesh generation which may resulted in longer beams and the corresponding smaller depth H.

Table 4.2: Cross-sectional characteristics of beams conforming with weighted volume fraction.

		Voronoï	real-geometry	tiling-based
A	[m^2]	1.431×10^{-04}	1.469×10^{-04}	1.317×10^{-04}
I	[m^4]	2.443×10^{-13}	2.643×10^{-13}	1.904×10^{-13}

We have computed the apparent parameters for square computational domains/tilings of sizes ranging from 1×1 up to 300×300 tiles. For each size, we generated 32 different stochastic realizations so that the number of realizations equals the number of distinct tiles in the set. Thus, results for 1×1 tilings correspond to the averages over the individual tiles.

The means of the effective stiffness coefficients for models consisting of 300×300 tiles are enlisted in Tab. 4.3 together with the homogenized parameters arising from the Voronoï and real-geometry meshes as presented in Fig. 4.5. As expected, the upper bounds

Table 4.3: Apparent elastic parameters of individual models.

		K^{hom} [MPa]	E^{hom} [MPa]	G^{hom} [MPa]	ν^{hom} [-]
Voronoï	KUBC	1435	238	81	0.472
	mKBC	1027	51	17	0.492
real-geometry	KUBC	203	220	84	0.319
	mKBC	61	34	12	0.409
tiling-based	KUBC	107(144)	42(57)	15(20)	0.435(0.434)
	mKBC	104(141)	38(53)	13(18)	0.439(0.438)

generated with KUBC and the lower bounds rendered by means of minKBC converge to each other with increasing size of computational domains, Fig. 4.6; even for tilings of 300×300 tiles they do not fully coincide. Nevertheless, we consider the difference between the bounds acceptable. This conclusion can be justified also in terms of the variance of the bounds. Fig. 4.7 shows the asymptotic decay of coefficient of variation with the values less than 1‰ in the vicinity of 300×300 tiling.

Since we failed to predict the reported stiffness parameters of Alporas® foam, Tab. 4.1, with the cross-sectional characteristics derived for tiling-based geometries, we performed the same computations also for cross-sectional parameters derived for the real-geometry mesh, Tab. 4.2. The results, in brackets in Tab. 4.3, were approximately 40% higher reflecting nearly linearly the 40% increase in the second moment of area. However, they do not fall within the reported range of overall Alporas® properties either.

4.6 Conclusions and discussion

We presented a modeling strategy for Alporas® foam having at heart the synthesis of stochastic microstructure realizations based on the concept of Wang tiling. Besides the standard upper bounds on the effective stiffness given by Kinematic Uniform Boundary Conditions, we obtained the guaranteed lower bounds by means of minimal kinematic boundary conditions. With this formulation, shown to equal the common Static Uniform

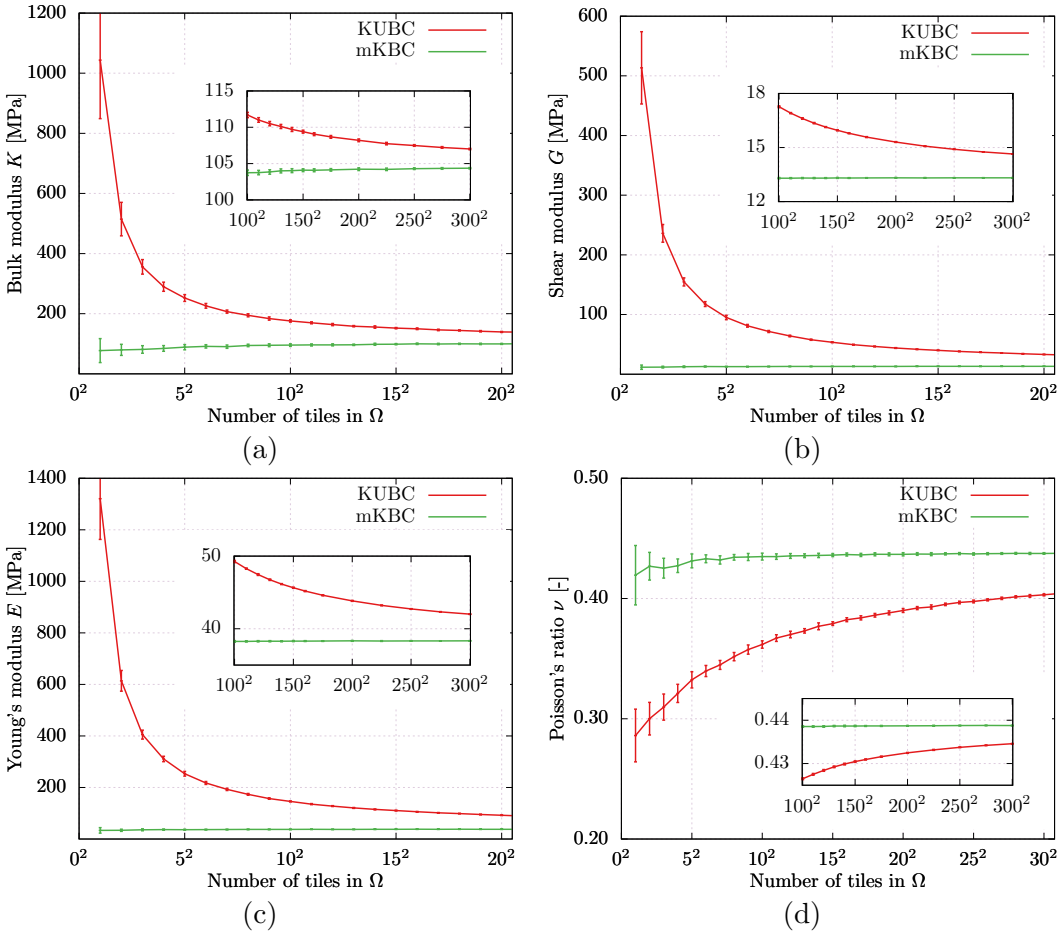

Figure 4.6: Relationship between homogenized elastic parameters and dimensions of computational domains: (a) Bulk modulus K, (b) Young's modulus E, (c) Shear modulus G, (d) Poisson's ratio ν.

Boundary Conditions in [113], we can avoid the question of an appropriate beam loading that would yield macroscopically uniform stress field. Hence, both bounds were rendered prescribing relevant boundary displacement.

Based on data in Fig. 4.6, we conclude that RVE for the two-dimensional model of highly porous materials should be about hundreds of the characteristic pore diameter length in dimensions. This finding corresponds with statements made in [108] regarding the minimal size of RVE in the case of infinite contrast of phase properties. On the other hand, it contradicts the recommendation of Ashby et al. [97] who propose RVE size of approximately seven times the mean pore diameter. However, this recommendation is given for three-dimensional samples and does not need to be valid for planar analyses.

Comparison of the homogenized stiffness coefficients with the reference values reported by Ashby et al. [97], Tabs. 4.1 and 4.3, leads us to unambiguous conclusions. Despite the several times reported aptness of the *spatial* wired model [97, 101, 103], it can be conjectured that the adopted *planar* beam representation has a limited capability in predicting the complex behavior of Alporas® foam. Possibly, it lacks the stiffness contribution from the out-of-plane beams and membranes as well as the cell walls parallel to the investigated plane, though, the membrane contribution of cell walls was reported negligible in the case

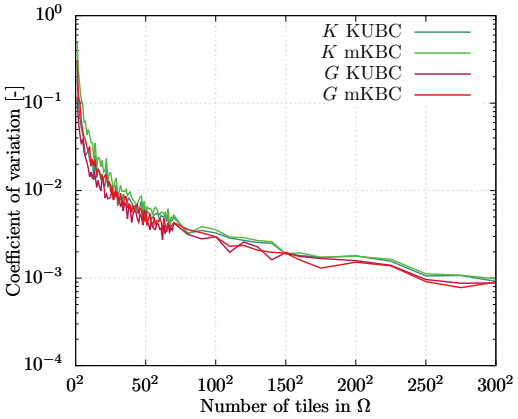

Figure 4.7: Coefficient of variation of the upper and lower estimates on K and G.

of high-porosity foams [103].

The qualitative analysis of the impact of the geometry representation clearly shows that the Voronoï mesh adopted in [20] leads to the overestimated value of bulk modulus. Assuming only the volumetric deformation, the axial stiffness of straight beams dominates the behavior of the Voronoï model resulting in nearly incompressible behavior, whilst in the case of real-geometry and tiling-based meshes the axial and bending stiffness contribute equally. This explains the results reported in [20] where the authors considered only the volumetric excitation. On top of that, based on their experimental observations, they assumed negligible Poisson's effect and equated Young's modulus to the oedometric component of the homogenized stiffness matrix. However, if the homogenization procedure was performed carefully, they would arrive at similar results as in Tab. 4.3. It is worthwhile to note that zero Poisson's ratio is in contradiction also with the characteristics listed in Tab. 4.1, see [97] for further details.

Despite the incapability of the two-dimensional beam model to capture behavior of complex materials such as highly porous metallic foams, the concept of Wang tilings proved to be a valuable technique to generate large computational domains of desired geometrical characteristics. Moreover, it allows to circumvent meshing of every single microstructure realization if the dicretization mesh is constructed on each tile separately such that it satisfies the given compatibility constrains. There is a promising possibility to extend the presented modeling strategy to three dimensions via Wang cubes, a spatial variant of Wang tiles, along with the spatial Voronoï tessellation to compress the true geometry of Alporas® foam, and to perform a similar analysis using shell elements instead of prismatic beams.

Appendix

4.A Minimal kinematic boundary conditions for beam model

In the two-dimensional wireframe setting, Eq. (4.21) defining Minimal Kinematic Boundary Conditions can be rewritten into the following form

$$0 = \sum_{i=1}^{n_e^{\partial\Omega}} \int_{L^{(i)}} \begin{Bmatrix} n_1^{(i)} u(x^\ell) \\ n_2^{(i)} w(x^\ell) \\ n_1^{(i)} w(x^\ell) + n_2^{(i)} u(x^\ell) \end{Bmatrix} \mathrm{d}x^\ell \,, \tag{4.27}$$

where $n_e^{\partial\Omega}$ stands for the number of the boundary beams, $L^{(i)}$ is the length of the i-th boundary beam, $n_1^{(i)}$ and $n_2^{(i)}$ are the components of the outward unit normal vector $\mathsf{n}^{(i)}$, and x^ℓ is the local coordinate measured along the beam axis. Eq. (4.27) allows to compute the i-th boundary beam contribution to the constraint matrix C^{mK}, Eq. (4.19) as

$$\mathsf{C}^{\mathrm{mK},(i)} = \begin{bmatrix} n_1^{(i)} & 0 \\ 0 & n_2^{(i)} \\ n_2^{(i)} & n_1^{(i)} \end{bmatrix} \mathsf{T}^{\ell\text{-g}}\, \mathsf{M}\, \mathsf{T}^{\text{g-}\ell}\,, \tag{4.28}$$

where the matrices $\mathsf{T}^{\ell\text{-g}}$ and $\mathsf{T}^{\text{g-}\ell}$ transform the corresponding quantities between the local and the global coordinate systems. Namely,

$$\mathsf{T}^{\ell\text{-g}} = \begin{bmatrix} \cos\alpha^{(i)} & -\sin\alpha^{(i)} \\ \sin\alpha^{(i)} & \cos\alpha^{(i)} \end{bmatrix} \tag{4.29}$$

and

$$\mathsf{T}^{\text{g-}\ell} = \begin{bmatrix} \cos\alpha^{(i)} & \sin\alpha^{(i)} & 0 & 0 & 0 & 0 \\ -\sin\alpha^{(i)} & \cos\alpha^{(i)} & 0 & 0 & 0 & 0 \\ 0 & 0 & 1 & 0 & 0 & 0 \\ 0 & 0 & 0 & \cos\alpha^{(i)} & \sin\alpha^{(i)} & 0 \\ 0 & 0 & 0 & -\sin\alpha^{(i)} & \cos\alpha^{(i)} & 0 \\ 0 & 0 & 0 & 0 & 0 & 1 \end{bmatrix}, \tag{4.30}$$

where $\alpha^{(i)}$ is the directional angle of the i-th beam. The matrix M

$$\mathsf{M} = \begin{bmatrix} \frac{L^{(i)}}{2} & 0 & 0 & \frac{L^{(i)}}{2} & 0 & 0 \\ 0 & \frac{L^{(i)}}{2} & \frac{L^{(i)2}}{12} & 0 & \frac{L^{(i)}}{2} & \frac{-L^{(i)2}}{12} \end{bmatrix} \tag{4.31}$$

is obtained by plugging the the shape functions for u and w, e.g. [115],

$$\begin{aligned} N_u^{u_1}(\xi) &= 1-\xi\,, \\ N_u^{u_2}(\xi) &= \xi\,, \\ N_w^{w_1}(\xi) &= \frac{1}{1+2\kappa}\Big[(1+2\kappa) - 2\kappa\xi - 3\xi^2 + 2\xi^3\Big], \\ N_w^{\phi_1}(\xi) &= \frac{L}{1+2\kappa}\Big[-(1+\kappa)\,\xi + (2+\kappa)\,\xi^2 - \xi^3\Big], \\ N_w^{w_2}(\xi) &= \frac{1}{1+2\kappa}\Big[(2\kappa\xi + 3\xi^2 - 2\xi^3\Big], \\ N_w^{\phi_2}(\xi) &= \frac{L}{1+2\kappa}\Big[\kappa\xi + (1-\kappa)\,\xi^2 - \xi^3\Big], \end{aligned} \tag{4.32}$$

where ξ is the normalized coordinate $\xi = \frac{x^\ell}{L^{(i)}}$, $\kappa = \frac{EI}{kGA}$ and k is the Timoshenko shear coefficient, in the approximation of the local beam displacements

$$\begin{Bmatrix} u^\ell \\ w^\ell \end{Bmatrix} = \begin{bmatrix} N_u^{u_1} & 0 & 0 & N_u^{u_2} & 0 & 0 \\ 0 & N_w^{w_1} & N_w^{\phi_1} & 0 & N_w^{w_2} & N_w^{\phi_2} \end{bmatrix} \begin{Bmatrix} u_1^\ell \\ w_1^\ell \\ \phi_1^\ell \\ u_2^\ell \\ w_2^\ell \\ \phi_2^\ell \end{Bmatrix} \tag{4.33}$$

and evaluating the integral in Eq. (4.27).

4.B Least square method

The eigenvalues of the isotropic plane-strain stiffness matrix written as a linear combination of parameters K and G read as

$$\lambda^{\text{iso}} = \mathsf{A}\mathsf{d} = \begin{bmatrix} 1 & 0 \\ 2 & 0 \\ \frac{2}{3} & 2 \end{bmatrix} \begin{Bmatrix} G \\ K \end{Bmatrix} . \tag{4.34}$$

The least square method applied to Eq. (4.34) results in minimizing the distance between the calculated eigenvalues λ^{hom} of the homogenized stiffness matrix and λ^{iso} in the Euclidean norm

$$\left\| \lambda^{\text{iso}} - \lambda^{\text{hom}} \right\|^2 = \left(\lambda^{\text{iso}} - \lambda^{\text{hom}} \right)^{\mathsf{T}} \left(\lambda^{\text{iso}} - \lambda^{\text{hom}} \right) . \tag{4.35}$$

Plugging Eq. (4.34) into Eq. (4.35) and minimizing it with respect to d yields the parameters K^{hom} and G^{hom} explicitly approximated as a projection of λ^{hom} onto the range of A

$$\mathsf{d}^{\text{hom}} = \left(\mathsf{A}^{\mathsf{T}}\mathsf{A} \right)^{-1} \mathsf{A}^{\mathsf{T}} \lambda^{\text{hom}} = \begin{bmatrix} \frac{1}{5} & \frac{2}{5} & 0 \\ -\frac{2}{30} & -\frac{4}{30} & \frac{1}{2} \end{bmatrix} \lambda^{\text{hom}}, \tag{4.36}$$

where $\left(\mathsf{A}^{\mathsf{T}}\mathsf{A} \right)^{-1} \mathsf{A}^{\mathsf{T}}$ is the left pseudoinverse of A.

Note that applying the above procedure in plane-stress conditions leads to non-linear relation between the eigenvalues and the elastic parameters

$$\lambda^{\text{iso}} = \left\{ G \quad 2G \quad \frac{18KG}{4G+3K} \right\}^{\mathsf{T}} . \tag{4.37}$$

As a result, no explicit formula can be derived and an iterative Least square method must be used instead.

Chapter 5

Statistical determination of the Representative Volume Element size

Abstract:
Wang tile based representation of a heterogeneous material facilitates fast synthesis of non-periodic microstructure realizations. In this paper, we apply the tiling approach in numerical homogenization to determine the Representative Volume Element size related to the user-defined significance level and the discrepancy between bounds on the apparent properties. First, the tiling concept is employed to efficiently generate arbitrarily large, statistically consistent realizations of investigated microstructures. Second, benefiting from the regular structure inherent to the tiling concept, the Partition theorem, and statistical sampling, we construct confidence intervals of the apparent properties related to the size of a microstructure specimen. Based on the interval width and the upper and lower bounds on the apparent properties, we adaptively generate additional microstructure realizations in order to arrive at an RVE satisfying the prescribed tolerance. The methodology is illustrated with the homogenization of thermo-mechanical properties of three two-dimensional microstructure models: a microstructure with mono-disperse elliptic inclusions, foam, and sandstone.

Reproduced from: Doškář, M., Zeman, J., Jarušková, D., Novák, J., 2018. Wang tiling aided statistical determination of the Representative Volume Element size of random heterogeneous materials. European Journal of Mechanics - A/Solids 70, 280–295. [86]

5.1 Introduction

The Representative Volume Element (RVE) is the key concept in modelling of heterogeneous materials. The original definition by Hill [111] requires an RVE to (i) be "structurally entirely typical of the whole mixture on average" and (ii) "contain a sufficient number of inclusions for the apparent overall moduli to be effectively independent of the surface values of traction and displacement, so long as these values are 'macroscopically uniform'." For materials with periodic microstructure, these requirements are met by any periodic part of the microstructure under periodic boundary conditions [116].

However, the majority of real-world materials display randomness in their microstructures. Sab [117] proved that microstructure ergodicity and statistical homogeneity are the essential requirements for the existence of an RVE. He also showed that the second Hill requirement is attainable only in the infinite-size limit and, thus, homogenized properties determined from any finite-size microstructure realization are biased by the adopted boundary conditions. For this reason, an error measure and its threshold have to be introduced in order to define an RVE for random heterogeneous materials (also referred to as a "computational RVE" [118] or a "numerical RVE" [119]). In practice, the RVE size is also limited from above by the requirement of separation of scales. When violated, the finite-size bounds can serve only as an input to stochastic finite element calculations [118, 120] or higher-order terms have to be introduced in a fully nested numerical homogenization [121, 23, 3, and references therein].

The RVE size depends on the type of treated physical phenomena, microstructure geometry, and contrast in microstructure constituent properties [122]. In the case of high contrast [84] or non-linear behaviour [122, 83, 123] the influence of particular geometry gets significantly pronounced, leading in turn to much larger RVE sizes or even to non-existence of an RVE [83]. Therefore, any recommendation on the RVE size, e.g., those for carbon reinforced polymers made by Trias et al. [124] or for particulate media [125, and references therein], are always highly material-specific and cannot be applied to other materials [3]. Consequently, similar procedures have to be performed for each investigated material, making the RVE determination still an open topic.

Plenty of works have been devoted to numerical studies of the RVE size; see Section 5.3.2 for an overview. The prevalent scheme is to (i) generate an ensemble of Statistical Volume Elements (SVEs), i.e., stochastic microstructure realizations smaller then an RVE, and (ii) compute their apparent properties under suitable boundary conditions. Then, depending on convergence criteria related to distribution of apparent properties within the ensemble, either a new ensemble of larger SVEs is produced or the generated SVEs are declared RVEs for the given threshold. The criteria typically involve fluctuations in the apparent properties [82, 122], their discrepancy under different boundary conditions [120], or a combination of both [124, 118, 119]. Such an approach is involved because of (i) the need to generate statistically representative microstructure realizations of increasing size and (ii) the computational cost of calculating the apparent properties. For the former reason, most works resort to simple microstructure models, e.g., particulate media [126, 67, 122, 127, 128, 129] or Voronoï tessellations [82].

In this contribution, we address these drawbacks simultaneously by exploring the formalism of Wang tiling, recalled in Section 5.2. Our approach decouples the microstructure generation into the off-line and on-line phases. In the off-line phase, the microstructure is compressed in a set of mutually compatible domains—Wang tiles. During the calculations, microstructure realizations are assembled from the compressed set following a

simple on-line stochastic algorithm. As a result, arbitrarily large yet statistically coherent realizations of the compressed microstructure can be generated almost instantly.

Additional advantages of the tiling concept follow from the natural decomposition of the tiling-based microstructure realisations into regular non-overlapping domains. This allows us to employ the Partition theorem by Huet [112], revisited in Section 5.3.4, to infer confidence intervals of the homogenized properties by statistical sampling. Moreover, the computational cost of determining apparent properties can be alleviated by standard domain decomposition techniques [130].

Taking the aforementioned benefits into account, in Section 5.4 we propose a methodology to identify the RVE size for a user-defined accuracy. New microstructure realizations are added on-the-fly to the sequentially generated ensembles of SVEs of increasing size in order to achieve a prescribed confidence in apparent properties, computed with the first-order numerical homogenization recalled in Section 5.3. The termination criterion, i.e., whether the RVE size has been reached, is based on statistical hypothesis testing related to the provided accuracy, similarly to, e.g., [127, 131]. In Section 5.5, we apply the proposed methodology to the RVE size determination of three microstructure models: a microstructure with mono-disperse elliptic inclusions, foam, and sandstone.

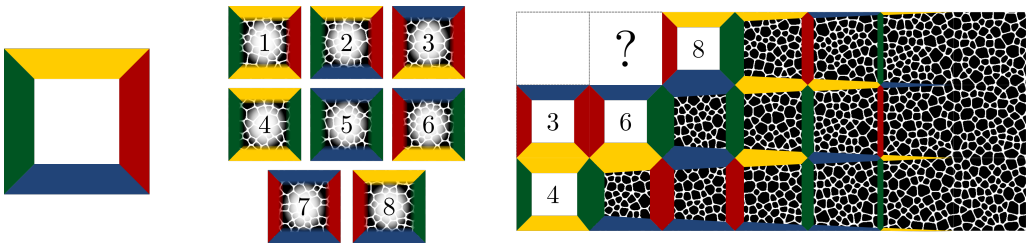

(a) (b) (c)

Figure 5.1.1: Illustration of (a) the abstract definition of a Wang tile, (b) a compressed microstructure within a tile set with highlighted tile indices (note that tiles 4, 5, and 7 are self-compatible and, thus, each can stand as a Statistically Equivalent Periodic Unit Cell), and (c) a partially reconstructed microstructure and the underlying tiling, where a step in the stochastic assembly algorithm is depicted. Based on the codes of previously placed tiles 8 and 6, at this step, either tile 2 or 7 will be placed at the position marked with "?" and the algorithm will continue with the remaining empty position.

Scope restrictions In what follows, we consider only two-dimensional problems for the sake of clarity, but the extension to three dimensions in the form of Wang Cubes is straightforward [30, 21]. We take existing tiling-based compressions of material microstructures, obtained with methods described in our previous publications, e.g., [15, 21], as fixed inputs capable of sufficiently accurate representation of the microstructure, and perform parametric studies on these geometries. We also restrict our attention to linearised elasticity and thermal conduction, because an RVE for these linear problems is well defined. In the general case of non-linear models, for instance due to the deterministic size effect in the softening regime, an RVE may not exist in the classical sense [83], and appropriate modification has to be adopted, e.g., a traction-opening formulation [132] or averaging only over active damaging domain [133].

Notation Throughout the paper, we employ the tensorial notation: scalars are denoted with plain letters, e.g., a; first- and second-order tensors are typeset with bold italic letters, either $\boldsymbol{a}$ or $\boldsymbol{A}$; and fourth-order tensors are written in regular bold letters, $\mathbf{A}$.

5.2 Wang tiling for random heterogeneous materials

5.2.1 Background

The idea of Wang tiling resembles a game of jigsaw puzzle, except that there is only a small set of distinct jigsaw pieces with an infinite number of copies. The jigsaw pieces—*Wang tiles*—have codes attributed to their edges. The goal is to cover a portion of a plane, denoted as a *tiling*, with tile instances from a given *tile set*, such that the adjacent tiles share the same code on the corresponding edge, see Fig. 5.1.1. The codes thus play a role of compatibility constraints during an assembly. Moreover, the tiles can be neither rotated nor reflected during a tiling procedure.

The particular set needs to be accompanied by an assembly algorithm capable of producing valid tilings. In our applications, we prefer the stochastic assembly algorithm introduced by Cohen et al. [17] over deterministic automata, e.g., [28, Chapters 10 and 11], because the former allows for larger variability in design of the tile set. The stochastic assembly algorithm depicted in Fig. 5.1.1 works as follows: an empty grid is sequentially filled with tile instances in the row-by-row order, the so called scanline algorithm [91]. At each step, a tile to-place (denoted with "?" in Fig. 5.1.1) is randomly chosen from a subset containing only admissible tiles with respect to the codes of the previously places ones. In Fig. 5.1.1 the candidate tiles are 2 and 7 as they have red code on the right-hand edge and blue code at the bottom. Randomness of the whole procedure is ensured with presence of at least two tiles for each combination of codes on horizontal and vertical edges [17]. Example of the tile sets and generated tilings are provided in Section 5.5, Figs. 5.5.2, 5.5.7, and 5.5.12.

5.2.2 History and relevant applications

Outside discrete mathematics, Wang tiling has found its use in Computer Graphics for an efficient real-time synthesis of a blue noise, which is an essential point distribution for anti-aliasing and dithering, e.g., [90, and references therein]. In addition, Cohen et al. [17] demonstrated that Wang tiles deliver excellent performance in generating naturally looking textures. This development directly motivated our application of Wang tiles in microstructure modelling as discussed next.

5.2.3 Tiling in modelling of heterogeneous materials

In what follows, a computer model of a material microstructure is understood as a process of generating individual realizations with spatial statistics corresponding to the investigated material [9]. Pioneered by Povirk [8], most representations are generated with optimization algorithms that minimize discrepancy in statistical characterization of the reference and the generated microstructure. Due to the multi-modal nature of the optimization problem, the simulated annealing, e.g., [54, 52, 10], holds a prominent place among the algorithms; however, other methods such as gradient algorithms [8, 57], genetic algorithms [10, 11], or phase-recovery [58] have been successfully applied. The

microstructural morphology is usually characterised by means of either Minkowski functionals [47] or set of n-point correlation functions [2]. In the latter, the two-point probability function [48, 49, 50] supplemented either with the two-point cluster [39] or the lineal path [51, 52, 10, 53] functions proved to be sufficient to capture major geometrical features at acceptable computational costs.

Recently, new approaches to microstructure models have emerged, inspired by texture synthesis in Computer Graphics [134], that make use of samples of the reference microstructure. Individual realizations are sequentially generated as a Markovian process with voxels [9, 59] or whole patches [13] from the reference sample. The suitable voxel/patch values are either chosen according to the statistical proximity of their surrounding in the reference sample to the previously generated portion of the new microstructure realization [9, 13], or generated by a supervised learning model based on classification trees [59].

The common feature of these approaches is that they deliver a statistically similar realization under periodic boundary conditions, which is referred to as a Statistically Optimal Representative Unit Cell [11], a Statistically Similar Representative Volume Element [12], or a Statistically Equivalent Periodic Unit Cell (SEPUC) [10]. Consequently, each new microstructure realization requires a new, often computationally intensive run of the generating procedure. An alternative is to tile periodically a larger domain with a previously generated cell; however, this introduces long-range periodic artefacts.

From this viewpoint, the stochastic Wang tiling concept presents a compromise between the two aforementioned approaches. The tile set generalizes the notion of SEPUC; instead of being attributed to a single cell, the microstructural information is compressed in a handful of tiles with defined mutual compatibility. While the short-range features of a microstructure are present predominantly in the tile interiors, the long-range characteristics are captured through the particular distribution of the tile edge codes, governing the compatibility requirements. Once the microstructure is compressed in the off-line phase, its realizations of any size are generated almost instantly by the assembly algorithm introduced in Section 5.2.1 (and illustrated with Fig. 5.1.1). In contrast to the above-mentioned periodic extension, the assembled realizations—tilings—are stochastic and exhibit suppressed periodicity artefacts; see [15, 21]. These features make the microstructure representation based on the Wang tile formalism appealing in applications where multiple (possibly large) microstructure realizations are required.

5.2.4 Microstructure compression

Microstructure compression amounts to designing a tile set (i.e., its cardinality and distribution of the tile edge codes) and morphologies of tiles within the tile set such that (i) the microstructure remains continuous across the congruent edges and (ii) assembled realizations match the reference microstructure, usually in terms of target spatial statistics. Note that spatial statistics of an individual tile differ from that of the compressed microstructure in general and the proximity of the spatial statistics is required only for assembled tilings.

Because the Wang tile based representation generalizes the SEPUC approach, methods developed for SEPUC can be extended to the generalized periodic boundary conditions appearing in the Wang tiling concept. We have already reported approaches based on optimization algorithms with objective function taking into account the discrepancy in the two-point probability functions [15] or inter-tile traction jumps [16]. In order to circumvent the computational complexity of the optimization approach, we have also adopted the Computer Graphics approach of Cohen et al. [17], which generates the tile morphology

from provided samples of a texture, and we enhanced it with spatial statistics, namely, the two-point probability and cluster functions in [21]. This procedure was used to design the tile set in Fig. 5.5.12.

The methodology developed in the following sections holds for arbitrary tile sets, irrespectively of the specific tile design algorithm, providing that the microstructure is accurately captured in the tile set; see [15, 21, 75, for additional details].

5.3 RVE and numerical homogenization

In this work, we assume the simplest linear constitutive laws at both the micro and the macro scales. Consequently, knowledge of microstructure compositions can be readily propagated to the upper scale by homogenized parameters of an effective constitutive model. The first-order numerical homogenization is summarized in Subsection 5.3.1, providing us with boundary-condition biased apparent properties. Next, the notion of RVE is introduced in Subsection 5.3.2. Finally, Subsections 5.3.3 and 5.3.4 recall the hierarchy of bounds and the Partition theorem, respectively, relating the apparent properties of a domain and its subdomains.

5.3.1 First-order numerical homogenization

5.3.1.1 Linear elasticity

Assume the first-order decomposition of a displacement field $\tilde{\boldsymbol{u}}$ in the form;

$$\tilde{\boldsymbol{u}}(\boldsymbol{x}) = \boldsymbol{E}\cdot\boldsymbol{x} + \tilde{\boldsymbol{u}}^*(\boldsymbol{x}) \quad \forall \boldsymbol{x}\in\Omega_s, \tilde{\boldsymbol{u}}^*\in\mathcal{U}_s^{\mathcal{B}}\,, \tag{5.1}$$

where $\boldsymbol{E}$ is the (prescribed) macroscopic strain tensor, $\Omega_s\subset\mathbb{R}^{\mathrm{d}}$ denotes the d-dimensional finite-size domain of a microstructure sample of characteristic size s, and $\mathcal{U}_s^{\mathcal{B}}$ defines a set of admissible displacement fluctuation fields $\tilde{\boldsymbol{u}}^*$.

For a given Ω_s and $\mathcal{U}_s^{\mathcal{B}}$, we define the apparent stiffness tensor $\mathbf{D}_s^{\mathcal{B}}$ with the variational equality

$$\begin{aligned}\boldsymbol{E}:\mathbf{D}_s^{\mathcal{B}}:\boldsymbol{E} = \\ \inf_{\tilde{\boldsymbol{u}}^*\in\mathcal{U}_s^{\mathcal{B}}}\left\langle(\boldsymbol{E}+\nabla^{\mathrm{s}}\tilde{\boldsymbol{u}}^*(\boldsymbol{x}))\,:\mathbf{D}(\boldsymbol{x}):\,(\boldsymbol{E}+\nabla^{\mathrm{s}}\tilde{\boldsymbol{u}}^*(\boldsymbol{x}))\right\rangle_{\Omega_s}\,,\end{aligned} \tag{5.2}$$

where $\mathbf{D}(\boldsymbol{x})$ is a local stiffness tensor, ∇^{s} stands for the symmetric part of the gradient, and $\langle\bullet\rangle_{\Omega_s}$ denotes spatial averaging defined as

$$\langle\bullet(\boldsymbol{x})\rangle_{\Omega_s} = \frac{1}{|\Omega_s|}\int_{\Omega_s}\bullet(\boldsymbol{x})\,\mathrm{d}\boldsymbol{x}\,. \tag{5.3}$$

The actual strain $\boldsymbol{\varepsilon}$ and stress $\boldsymbol{\sigma}$ fields then follow from the minimizer[1] $\boldsymbol{u}^*$ of Eq. (5.2) through the standard expressions

$$\boldsymbol{\varepsilon}(\boldsymbol{x}) = \boldsymbol{E}+\nabla^{\mathrm{s}}\boldsymbol{u}^*(\boldsymbol{x}) \quad\text{and}\quad \boldsymbol{\sigma}(\boldsymbol{x}) = \mathbf{D}(\boldsymbol{x}):\boldsymbol{\varepsilon}(\boldsymbol{x})\,, \tag{5.4}$$

where we have used the generalized Hooke's law.

[1] For the sake of conciseness, we do not state the explicit dependence $\boldsymbol{u}^* = \boldsymbol{u}^*(\boldsymbol{E})$.

Allowing only $\mathcal{U}_s^{\mathcal{B}}$ such that $\boldsymbol{\varepsilon}$ and $\boldsymbol{\sigma}$ satisfy the energy consistency, also known as Hill's condition [111],

$$\langle \boldsymbol{\sigma}(\boldsymbol{x}) : \boldsymbol{\varepsilon}(\boldsymbol{x}) \rangle_{\Omega_s} = \langle \boldsymbol{\sigma}(\boldsymbol{x}) \rangle_{\Omega_s} : \langle \boldsymbol{\varepsilon}(\boldsymbol{x}) \rangle_{\Omega_s} , \tag{5.5}$$

allows us to directly relate $\mathbf{D}_s^{\mathcal{B}}$ to the average stress,

$$\langle \boldsymbol{\sigma}(\boldsymbol{x}) \rangle_{\Omega_s} = \langle \mathbf{D}(\boldsymbol{x}) : \boldsymbol{\varepsilon}(\boldsymbol{x}) \rangle_{\Omega_s} = \mathbf{D}_s^{\mathcal{B}} : \boldsymbol{E} , \tag{5.6}$$

which will be later used for computing the apparent properties.

Posing Eq. (5.2) as a Boundary Value Problem, Hill's criterion is satisfied by adopting $\mathcal{U}_s^{\mathcal{B}}$ from the family of Mixed Uniform Boundary Conditions [135],

$$\mathcal{U}_s^{\mathrm{K}} \subseteq \mathcal{U}_s^{\mathcal{B}} \subseteq \mathcal{U}_s^{\mathrm{S}} , \tag{5.7}$$

where $\mathcal{U}_s^{\mathrm{K}}$ and $\mathcal{U}_s^{\mathrm{S}}$ represent the sets of admissible fields $\tilde{\boldsymbol{u}}^*$ compliant with the Kinematic and Static Uniform Boundary Conditions.[2] The particular forms are specified as follows:

Kinematic Uniform Boundary Conditions (KUBC) impose a prescribed displacement at the domain boundary $\partial\Omega_s$ in the form ,

$$\tilde{\boldsymbol{u}}(\boldsymbol{x}) = \boldsymbol{E} \cdot \boldsymbol{x} \quad \forall \boldsymbol{x} \in \partial\Omega_s , \tag{5.8}$$

resulting in vanishing fluctuation displacements at $\partial\Omega_s$. This corresponds to setting

$$\mathcal{U}_s^{\mathrm{K}} = \left\{ \tilde{\boldsymbol{u}}^* : \Omega_s \to \mathbb{R}^{\mathrm{d}}; \tilde{\boldsymbol{u}}^*|_{\partial\Omega_s} = \mathbf{0} \right\} . \tag{5.9}$$

Static Uniform Boundary Conditions (SUBC) are traditionally defined with affine traction vectors at $\partial\Omega_s$, leading to a stress-controlled problem. However, Miehe [113] proved that SUBC correspond to the so-called minimal Kinematic Boundary Conditions, used in e.g. [104, 137, 75], that require

$$\boldsymbol{E} = \langle \nabla^{\mathrm{s}} \tilde{\boldsymbol{u}}(\boldsymbol{x}) \rangle_{\Omega_s} . \tag{5.10}$$

Similarly to Eq. (5.9), this provides the specific form of $\mathcal{U}_s^{\mathcal{B}}$ as

$$\mathcal{U}_s^{\mathrm{S}} = \{ \tilde{\boldsymbol{u}}^* : \Omega_s \to \mathbb{R}^{\mathrm{d}}; \int_{\partial\Omega_s} \boldsymbol{n} \otimes \tilde{\boldsymbol{u}}^* \, \mathrm{d}\Gamma = \mathbf{0}, \, \langle \tilde{\boldsymbol{u}}^*(\boldsymbol{x}) \rangle_{\Omega_s} = \mathbf{0} \} . \tag{5.11}$$

Note that the boundary integral contains also non-symmetric part of the gradient, which along with the last condition in Eq. (5.11) prevents rigid body modes.

5.3.1.2 Thermal conduction

For thermal conduction, we can proceed analogously to linear elasticity with only minor modifications: Generalized Hooke's law is replaced with Fourier's law, $\boldsymbol{q}(\boldsymbol{x}) = -\boldsymbol{K}(\boldsymbol{x}) \cdot \boldsymbol{g}(\boldsymbol{x})$, which governs the relation between a heat flux $\boldsymbol{q}$ and a temperature gradient $\boldsymbol{g} = \nabla\tilde{\theta}$ via a thermal conductivity tensor $\boldsymbol{K}$. The first order decomposition of an admissible

[2] Although the Periodic Boundary Conditions usually provide reasonable estimates of the homogenized properties even in the case of a non-periodic microstructure [22, 82, 136], our RVE criterion is based on the discrepancy between the bounds on the apparent properties. Therefore, we omit discussion on Periodic Boundary Conditions onwards.

temperature field $\tilde{\theta}(\boldsymbol{x})$ reads

$$\tilde{\theta}(\boldsymbol{x}) = \boldsymbol{G} \cdot \boldsymbol{x} + \tilde{\theta}^*(\boldsymbol{x}) \quad \forall \boldsymbol{x} \in \Omega_s, \tilde{\theta}^* \in \mathcal{T}_s^{\mathcal{B}}\,, \tag{5.12}$$

with $\boldsymbol{G}$ denoting the prescribed macroscopic temperature gradient and $\mathcal{T}_s^{\mathcal{B}}$ being, again, the set of admissible temperature fluctuation fields compliant with Hill's condition

$$\langle \boldsymbol{q}(\boldsymbol{x}) \cdot \boldsymbol{g}(\boldsymbol{x}) \rangle_{\Omega_s} = \langle \boldsymbol{q}(\boldsymbol{x}) \rangle_{\Omega_s} \cdot \langle \boldsymbol{g}(\boldsymbol{x}) \rangle_{\Omega_s}. \tag{5.13}$$

Consequently, the variational definition of the apparent conductivity tensor $\boldsymbol{K}_s^{\mathcal{B}}$,

$$\begin{aligned} \boldsymbol{G} \cdot \boldsymbol{K}_s^{\mathcal{B}} \cdot \boldsymbol{G} = \\ \inf_{\tilde{\theta}^* \in \mathcal{T}_s^{\mathcal{B}}} \langle (\boldsymbol{G} + \nabla \tilde{\theta}^*(\boldsymbol{x})) \cdot \boldsymbol{K}(\boldsymbol{x}) \cdot (\boldsymbol{G} + \nabla \tilde{\theta}^*(\boldsymbol{x})) \rangle_{\Omega_s}\,, \end{aligned} \tag{5.14}$$

is equivalent to the volume averaging of the heat flux obtained from the minimizer $\theta(\boldsymbol{x})$ of Eq. (5.14)

$$\langle \boldsymbol{q}(\boldsymbol{x}) \rangle_{\Omega_s} = \langle -\boldsymbol{K}(\boldsymbol{x}) \cdot \nabla \theta(\boldsymbol{x}) \rangle_{\Omega_s} = -\boldsymbol{K}_s^{\mathcal{B}} \cdot \boldsymbol{G}\,. \tag{5.15}$$

As in the previous section, Eq. (5.13) can be ensured with a proper choice of $\mathcal{T}_s^{\mathcal{B}}$ that falls within the following two limit cases:

Uniform Temperature Gradient Boundary Conditions prescribing values at the boundary in the form

$$\theta(\boldsymbol{x}) = \boldsymbol{G} \cdot \boldsymbol{x} \quad \forall \boldsymbol{x} \in \partial\Omega_s\,, \tag{5.16}$$

which translates to

$$\mathcal{T}_s^{\mathrm{G}} = \{\tilde{\theta}^* : \Omega_s \to \mathbb{R};\, \tilde{\theta}^*|_{\partial\Omega_s} = 0\}\,, \tag{5.17}$$

and

Uniform Heat Flux Density Boundary Conditions defined analogously to Eq. (5.10) and represented by

$$\mathcal{T}_s^{\mathrm{F}} = \{\tilde{\theta}^* : \Omega_s \to \mathbb{R}; \int_{\partial\Omega_s} \tilde{\theta}^* \boldsymbol{n}\, \mathrm{d}\Gamma = \boldsymbol{0},\, \left\langle \tilde{\theta}^*(\boldsymbol{x}) \right\rangle_{\Omega_s} = 0\}\,. \tag{5.18}$$

5.3.2 Notion of RVE

The apparent properties introduced above are in general boundary condition biased and individual realizations of the microstructure yield different tensors, which contradicts the original requirement of Hill [111]. However, Sab [117] proved that boundary-biased apparent properties converge to the homogenized ones with increasing size s, thus

$$\mathbf{D}_s^{\mathcal{B}} \xrightarrow{s\to\infty} \mathbf{D}^{\mathrm{hom}} \quad \text{and} \quad \boldsymbol{K}_s^{\mathcal{B}} \xrightarrow{s\to\infty} \boldsymbol{K}^{\mathrm{hom}}\,, \tag{5.19}$$

see also [138].

As discussed in Introduction, the theoretical RVE is conventionally replaced with a finite size numerical counterpart [119]. The common approach to the determination of the numerical RVE size rests on generating ensembles containing sequentially larger SVEs until statistics of the obtained data comply with a user-defined threshold. The investigated data ranges from classical overall stiffness parameters [139, 140, 124, 118] and elastic strain

energy density [131], to mean values or concentrations in microstructural stress and strain fields [140, 122, 125, 83, 124], to deviations from assumed macroscopic isotropy [119, 127]. Statistical control usually includes output variance for different realizations of the same size and convergence of the mean value from one SVE size to another. Relying on a single criterion, especially when combined only with one type of boundary conditions (e.g., Periodic Boundary Conditions), can lead to pre-mature convergence [119]; therefore, more recent works combine both characteristics [124, 118, 119, 131].

In order to alleviate the computational cost related to the above mentioned approach, Kanit et al. in their seminal work [82] adopted the notion of the integral range allowing them to establish a power-law relation among an SVE size, cardinality of an ensemble, and the variation of apparent properties. Parameters of the relation are calibrated with only a handful of computations and the RVE size is then derived with respect to a user-defined statistical variation threshold. Moreover, the expression also allows to substitute a single RVE with a set of smaller SVEs. Pelissou et al. [123] enhanced the original approach by introducing uncertainty to both the mean value and the variance, using the bootstrapping method, and applied it to non-linear problems. Recently, Dirrenberger et al. [84] extended Kanit et al.'s approach to an artificial microstructure with infinite integral range demonstrating that the approach is applicable even for highly complex materials. The method of Kanit et al. [82] has also been successfully applied to the real world tasks arising, for instance, in the food industry [141, 142]. However, the variance based criterion of Kanit et al. relies on an implicit assumption that the mean value is not significantly biased by the prescribed boundary conditions. This assumption is usually valid for large SVEs under Periodic Boundary Conditions [22, 136], but the assumption becomes questionable for complex microstructures with high contrast in phase properties [84].

A different approach to an RVE definition was proposed by Drugan and Willis [143]. Estimating the effect of strain average fluctuations in a non-local constitutive equation allowed them to derive the RVE size of two particle diameters for a microstructure composed of non-overlapping spheres. Their analytical findings were later corroborated in numerical studies of Gusev [126] and Sequrado and Llorca [67]. Another alternative definition of an RVE has been recently proposed by Hoang et al. [144], who combined incremental analytical and numerical homogenizations. Their RVE criterion rests on the convergence of parameters in the analytical homogenization identified to follow results of the numerical homogenization.

Some authors, e.g., [140, 124, 108], also incorporated additional statistics into their definition of the RVE. Following Kanit et al.'s idea of replacing a single RVE with a set of smaller ones, Niezdgoda et al. [108] introduced the notion of RVE Set composed of optimally chosen SVEs from an ensemble whose convex combination best matches the ensemble average of given microstructural statistics, namely, the two-point correlation function. The optimal convex combination is then used for computing all macroscopic properties.

5.3.3 Bounds on the apparent properties

For the sake of conciseness, we recall the hierarchy of bounds for linear elasticity only; however, the exposition can be straightforwardly applied also to the problem of thermal conduction.

In linear elasticity, KUBC and SUBC hold a prominent place as they provide bounds

on the apparent property [111, 112]

$$\mathbf{D}_s^{\mathrm{S}} \preccurlyeq \mathbf{D}_s^{\mathcal{B}} \preccurlyeq \mathbf{D}_s^{\mathrm{K}}\,, \tag{5.20}$$

with the ordering relation $\preccurlyeq$ defined for fourth-order tensors $\mathbf{A}$ and $\mathbf{B}$ in the sense

$$\mathbf{A} \preccurlyeq \mathbf{B} \iff \boldsymbol{a} : (\mathbf{B} - \mathbf{A}) : \boldsymbol{a} \geq 0 \quad \forall \boldsymbol{a} \in \mathbb{R}^{\mathrm{d}\times\mathrm{d}}\,. \tag{5.21}$$

This classical ordering directly follows from the principle of minimum potential energy, Eq. (5.2), and the definition of the kinematically admissible spaces, Eq. (5.7).

Beside the realization-to-realization convergence of the apparent properties to the homogenized ones, Sab [117] also proved that the homogenized properties can be bounded by ensemble averages. In particular, it holds

$$\left(\sup_s \mathbb{E}\left(\mathbf{C}_s^{\mathrm{S}}\right)\right)^{-1} = \mathbf{D}^{\mathrm{hom}} = \inf_s \mathbb{E}(\mathbf{D}_s^{\mathrm{K}})\,, \tag{5.22}$$

where $\mathbb{E}(\bullet)$ denotes the expected value of an ensemble average over all microstructure realizations of the same size and $\mathbf{C}_s^{\mathrm{S}} = \left(\mathbf{D}_s^{\mathrm{S}}\right)^{-1}$.

5.3.4 Partition Theorem

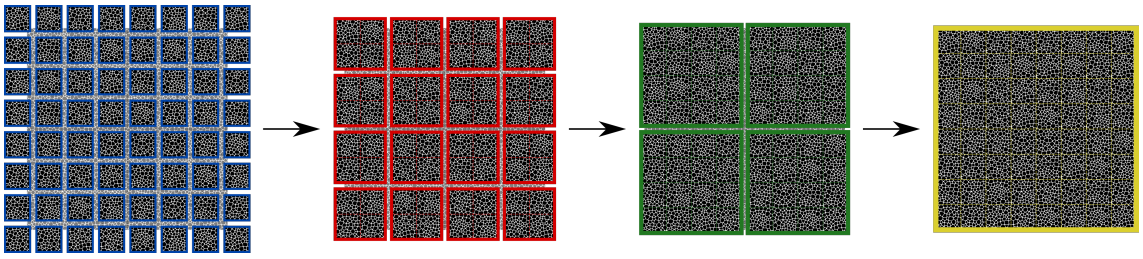

Figure 5.3.1: Illustration of the Partition theorem: The apparent properties $\mathbf{D}^{\mathrm{K}}_{s_{t+4}}$ and $\mathbf{C}^{\mathrm{K}}_{s_{t+4}}$ of the rightmost, yellow-bordered tiling are consecutively bounded by the hierarchies $\overline{\mathbf{D}^{\mathrm{K}}_{s_t}} \succcurlyeq \overline{\mathbf{D}^{\mathrm{K}}_{s_{t+1}}} \succcurlyeq \overline{\mathbf{D}^{\mathrm{K}}_{s_{t+2}}} \succcurlyeq \mathbf{D}^{\mathrm{K}}_{s_{t+4}}$ and $\overline{\mathbf{C}^{\mathrm{S}}_{s_t}} \succcurlyeq \overline{\mathbf{C}^{\mathrm{S}}_{s_{t+1}}} \succcurlyeq \overline{\mathbf{C}^{\mathrm{S}}_{s_{t+2}}} \succcurlyeq \mathbf{C}^{\mathrm{S}}_{s_{t+4}}$ of ensemble averages of consecutively smaller subdomains of side length s_k.

In the case of a finite-size domain, a hierarchy of bounds similar to Eqs. (5.20) and (5.22) can be established for the apparent properties of the domain and its subdomains. This was first recognized by Huet [112] under the name Partition theorem with implications for physical testing of materials whose representative volumes are unattainable for practical experiments. Later, the same hierarchy appeared in [117] as the sub-additivity property of apparent tensors, and in [145, and subsequent works] as a consequence of error bounds in the substructuring method [128].

Assume partitioning of the domain Ω_s into n equi-sized non-overlapping subdomains $\Omega_r^{(i)}, i = 1 \dots n$, of the characteristic size $r < s$. By solving the variational problem (5.2) independently for each subdomain under KUBC, we obtain the collection of solutions $\left\{\boldsymbol{u}^{(i)}(\boldsymbol{x}), \boldsymbol{x} \in \Omega_r^{(i)}\right\}$. Clearly, a displacement field $\bar{\boldsymbol{u}}$ defined for the whole domain Ω_s as

$$\bar{\boldsymbol{u}}(\boldsymbol{x}) = \left\{\boldsymbol{u}(\boldsymbol{x}) : \Omega_s \to \mathbb{R}^{\mathrm{d}};\, \boldsymbol{u}|_{\Omega_r^{(i)}} = \boldsymbol{u}^{(i)}\right\} \tag{5.23}$$

is an admissible field satisfying Eq. (5.8). Hence, plugging $\bar{\boldsymbol{u}}$ in Eq. (5.2) leads to

$$\begin{aligned}\boldsymbol{E} : \mathbf{D}_s^{\mathrm{K}} : \boldsymbol{E} &\leq \langle \nabla^{\mathrm{s}} \bar{\boldsymbol{u}}(\boldsymbol{x}) : \mathbf{D}(\boldsymbol{x}) : \nabla^{\mathrm{s}} \bar{\boldsymbol{u}}(\boldsymbol{x}) \rangle_{\Omega_s} \\ &= \sum_i^n \frac{|\Omega_r^{(i)}|}{|\Omega_s|} \left\langle \nabla^{\mathrm{s}} \boldsymbol{u}^{(i)}(\boldsymbol{x}) : \mathbf{D}(\boldsymbol{x}) : \nabla^{\mathrm{s}} \boldsymbol{u}^{(i)}(\boldsymbol{x}) \right\rangle_{\Omega_r^{(i)}} \\ &= \frac{1}{n} \sum_i^n \boldsymbol{E} : \mathbf{D}_r^{\mathrm{K},(i)} : \boldsymbol{E} \,, \forall \boldsymbol{E} \in \mathbb{R}^{\mathrm{d}\times\mathrm{d}}_{\mathrm{sym}} \,,\end{aligned} \tag{5.24}$$

which provides us with the relation

$$\mathbf{D}_s^{\mathrm{K}} \preccurlyeq \frac{1}{n} \sum_i^n \mathbf{D}_r^{\mathrm{K},(i)} = \overline{\mathbf{D}_r^{\mathrm{K}}} \,. \tag{5.25}$$

From the Principle of minimum complementary energy, an analogous result for SUBC follows in the form

$$\mathbf{C}_s^{\mathrm{S}} \preccurlyeq \frac{1}{n} \sum_i^n \mathbf{C}_r^{\mathrm{S},(i)} = \overline{\mathbf{C}_r^{\mathrm{S}}} \,. \tag{5.26}$$

By recursive partitioning of subdomains and making use of Eq. (5.20) and the convergence property (5.19), the final hierarchy of bounds can be established

$$\begin{aligned}\left(\overline{\mathbf{C}_0^{\mathrm{S}}}\right)^{-1} \preccurlyeq \cdots \preccurlyeq \left(\overline{\mathbf{C}_{s_k}^{\mathrm{S}}}\right)^{-1} \preccurlyeq \left(\overline{\mathbf{C}_{s_{k+1}}^{\mathrm{S}}}\right)^{-1} \preccurlyeq \cdots \preccurlyeq \\ \mathbf{D}^{\mathrm{hom}} \preccurlyeq \cdots \preccurlyeq \overline{\mathbf{D}_{s_{k+1}}^{\mathrm{K}}} \preccurlyeq \overline{\mathbf{D}_{s_k}^{\mathrm{K}}} \preccurlyeq \cdots \preccurlyeq \overline{\mathbf{D}_{s_0}^{\mathrm{K}}} \,,\end{aligned} \tag{5.27}$$

where $s_k = \frac{1}{q} s_{k+1}$ with $q \in \mathbb{N}$; see Fig. 5.3.1 for an illustration with $q = 2$. Note that the outermost bounds $\overline{\mathbf{D}_0^{\mathrm{K}}}$ and $\left(\overline{\mathbf{C}_0^{\mathrm{S}}}\right)^{-1}$, obtained as the limit states for $s \to 0$, are the classical Voigt and Reuss bounds which are derived under the assumption of homogeneous strain and stress field within the sample.

5.4 RVE size determination

Equipped with a procedure for computing apparent properties and with a realistic microstructure generation that also provides partitioning in the spirit of Huet [112], we formulate a two-level method for identification of the RVE size for a user-defined tolerance and confidence level.

Similar ideas have been presented in several works; here, we attempt to encompass the best of these in a comprehensive yet straightforward framework. We build on two assumptions:

- statistical homogeneity and ergodicity of the microstructure itself to ensure existence of an RVE [117];
- sufficiently accurate compression of the microstructural information in the form of a Wang tile set. We assume that all essential features of the investigated microstructure are present in reconstructed samples[3] and hence the RVE size identified for the tile-based compression corresponds to the RVE size of the microstructure.

[3] Albeit reduced compared to the periodic extension of a SEPUC, reconstructed realizations exhibit secondary peaks in spatial correlation functions [15, 16, 21]. These peaks are further reduced in solutions to

Note that the latter assumption is inherently present in any microstructure compression technique, including the SEPUC approach [10, 108].

Our approach resembles the work of Saroukhani et al. [131], especially in deriving bounds on the homogenized properties with methods of statistical sampling. General bounds on statistical moments were also presented in [146, 147]. Contrary to the aforementioned works, which does not provide any quantitative definition of the RVE, we introduce an RVE criterion that is based on hypothesis testing similar to, e.g., [125, 124]. Unlike the latter works, the number of microstructure realizations is not defined a priori in our approach, as we control their number on-the-fly in order to meet a prescribed confidence in bounds on the apparent properties.

The key idea is to relate the theoretical RVE to an infinite tiling. Any finite-size tiling can thus be considered as a subdomain of the RVE. The bounds in Eq. (5.27) then implicitly contain infinite sums. Therefore, at the first level of our methodology, we identify the minimal number of microstructure realizations that delivers the bounds with a user-defined uncertainty. At the second level, we assess the discrepancy between the bounds and, based on statistical hypothesis testing, we decide whether the actual size of microstructure is the RVE size for the defined tolerance.

5.4.1 Level I: Bounds for apparent properties

To keep the exposition concise, we adopt a certain abuse of notation in the sequel: $\boldsymbol{L}$ stands for apparent tensors rendered by prescribing the zero fluctuation unknowns point-wise at the boundary (i.e., $\boldsymbol{L} = \mathbf{D}^{\mathrm{K}}$ in the case of linear elasticity and $\boldsymbol{L} = \boldsymbol{K}^{\mathrm{G}}$ for the thermal conduction), whilst $\boldsymbol{M}$ denotes the complementary quantity obtained by enforcing the zero fluctuations in the weak, boundary-integral sense ($\boldsymbol{M} = (\mathbf{D}^{\mathrm{S}})^{-1}$ or $\boldsymbol{M} = (\boldsymbol{K}^{\mathrm{F}})^{-1}$). Analogously to the linear elasticity problem, the superscripts $\bullet^{\mathrm{G}}$ and $\bullet^{\mathrm{F}}$ denote the apparent conductivity tensors obtained under Uniform Gradient Boundary Conditions and Uniform Flux Boundary Conditions, respectively, recall Section 5.3.1.2.

For each realization $\Omega_s^{(i)}$ of a $s \times s$ tiling[4] we define two scalar values

$$l_s^{(i)} = \left\| \boldsymbol{L}_s^{(i)} \right\| \quad \text{and} \quad m_s^{(i)} = \left\| \boldsymbol{M}_s^{(i)} \right\| , \tag{5.28}$$

that are used to quantify variability of a s-size SVE ensemble. The particular type of the norm in Eq. (5.28) is a modelling choice to be made by a user. We assume the obtained data to be in the form

$$\begin{aligned} l_s^{(i)} &= l^{\mathrm{hom}} + \delta_s^l + e_s^{l,(i)} = \overline{l_s} + e_s^{l,(i)} , \\ m_s^{(i)} &= m^{\mathrm{hom}} + \delta_s^m + e_s^{m,(i)} = \overline{m_s} + e_s^{m,(i)} , \end{aligned} \tag{5.29}$$

where l^{hom} and m^{hom} correspond to the norms of the sought homogenized tensors $\boldsymbol{L}^{\mathrm{hom}}$ and $\boldsymbol{M}^{\mathrm{hom}} = (\boldsymbol{L}^{\mathrm{hom}})^{-1}$, δ_s^l and δ_s^m denote the systematic bias caused by specific boundary conditions and the finite size of the domain, and $e_s^{l,(i)}$ and $e_s^{m,(i)}$ are random, normally distributed errors from $N(0, (\varsigma_s^l)^2)$ and $N(0, (\varsigma_s^m)^2)$ related to the stochastic nature of the microstructure. Recall that the systematic errors and the variances $(\varsigma_s^\bullet)^2$ of the random errors vanish as $s \to \infty$, Eq. (5.19).

homogenization-related Boundary Value Problems and averaged; therefore, the influence of the secondary peaks on the apparent properties and the RVE size is marginal.

[4]Size of a realization is always an integer multiple of the tile size.

In Eq. (5.29) and in the sequel, the bar-denoted quantities $\overline{\bullet_s}$ represent the theoretical mean value, obtained by averaging the quantity over all possible realizations. Due to the assumed infinite size of the theoretical RVE, these values are unattainable and must be replaced with confidence intervals. To this purpose, for both quantities l and m of n_s realizations of $s \times s$ tiling, we compute the sample mean values

$$\hat{\bullet}_s = \frac{1}{n_s} \sum_{i=1}^{n_s} \bullet_s^{(i)} \tag{5.30}$$

and the unbiased sample standard deviations

$$\hat{\varsigma}_s^{\bullet} = \sqrt{\frac{1}{n_s - 1} \sum_{i=1}^{n_s} \left(\bullet_s^{(i)} - \hat{\bullet}_s \right)^2}, \tag{5.31}$$

with $\bullet$ denoting either l or m. From the Central Limit Theorem, the deterministic value $\overline{\bullet_s}$ falls with $(1 - \tilde{P}_\epsilon) \times 100\%$ probability within the confidence interval

$$\overline{\bullet_s} \in [\hat{\bullet}_s - \alpha_s^{\bullet}; \hat{\bullet}_s + \alpha_s^{\bullet}] \,, \tag{5.32}$$

with the width of the interval given by

$$\alpha_s^{\bullet} = t_{n_s-1}^{-1}(1 - \tilde{P}_\epsilon/2) \, \frac{\hat{\varsigma}_s^{\bullet}}{\sqrt{n_s}} \,, \tag{5.33}$$

where $t_n^{-1}(P)$ denotes the inverse cumulative distribution function of Student's t-distribution and $\tilde{P}_\epsilon$ is a significance level provided by the user for Level I.

The ratio

$$\epsilon_s^{\bullet} = \frac{\alpha_s^{\bullet}}{\hat{\bullet}_s} \tag{5.34}$$

provides a natural uncertainty measure in the bounds. Note that, due to the presence of $t_{n_s-1}^{-1}(1 - \tilde{P}_\epsilon/2)$ in Eq. (5.33), the ratio does not correspond to the (biased) estimation of the coefficient of variation (CoV) used in, e.g., [118, 124]. This complies with our intention to assess the uncertainty of ensemble mean value determination rather than the variation inherent to the limited realization size and the imposed BC.

Microstructure realizations are being added on-the-fly to the ensemble of size s samples until the uncertainty in both upper and lower bounds drops below a given threshold, i.e., $\epsilon_s^{\bullet} < \epsilon^{\text{usr}}$, which translates to asserting that the actual mean value $\overline{\bullet_s}$ falls outside the interval $[(1 - \epsilon^{\text{usr}})\hat{\bullet}_s, (1 + \epsilon^{\text{usr}})\hat{\bullet}_s]$ with less than probability $\tilde{P}_\epsilon$. Once this condition is satisfied, we assume that the ensemble contains sufficient number of realization to provide the desired accuracy for the RVE size criterion, controlled next.

5.4.2 Level II: RVE size criterion

Proximity of each realization to the RVE size is assessed using a discrepancy between $\boldsymbol{L}_s^{(i)}$ and $(\boldsymbol{M}_s^{(i)})^{-1}$. Recall that $\boldsymbol{L}_s^{(i)}$ and $\boldsymbol{M}_s^{(i)}$ are reciprocal in the RVE case, see Eq. (5.22). For each realization, we define the proximity error as

$$\xi_s^{(i)} = \left\| \boldsymbol{L}_s^{(i)} \cdot \boldsymbol{M}_s^{(i)} - \boldsymbol{I} \right\| \,, \tag{5.35}$$

where $\cdot$ denotes the corresponding tensorial contraction[5] and $\boldsymbol{I}$ is the corresponding unit tensor (with the pertinent symmetries). Again, the particular type of the norm is a modelling choice; for instance, Sab [117] used the infinity norm.

Finally, the RVE size criterion is based on testing the hypothesis

$$\mathrm{H}_0 : \overline{\xi_s} \geq \xi^{\mathrm{usr}} \quad \text{against} \quad \mathrm{H}_1 : \overline{\xi_s} < \xi^{\mathrm{usr}} ,$$

where ξ^{usr} is a given threshold discrepancy defining the computational RVE. This results in the one-tailed hypothesis test

$$\hat{\xi}_s + t^{-1}_{n_s-1}(1-\tilde{P}_\xi)\,\frac{\hat{\varsigma}^\xi_s}{\sqrt{n_s}} = \xi^{\mathrm{test}}_s \leq \xi^{\mathrm{usr}} . \tag{5.36}$$

If the condition (5.36) is satisfied for user-defined $\tilde{P}_\xi$ and ξ^{usr}, the current tiling size s is declared to be the computational RVE size; otherwise, we proceed with an ensemble of larger tilings.

The proposed methodology is summarized in Algorithm 5.1. For practical purposes, size and number of realizations are limited with $s_{\max}$ and $n_{\max}$, respectively. Moreover, the first $n_{\min}$ realizations of each size are generated and their apparent properties $\boldsymbol{L}^{(i)}_s$ and $\boldsymbol{M}^{(i)}_s$ computed without comparing $\epsilon^\bullet_s$ to the threshold value, in order to acquire reliable data statistics for the RVE size criterion. Characteristics of 1×1 tilings are computed independently beforehand, because they correspond to the properties of individual tiles weighted by the probability of occurrence of each tile in an infinite tiling, which follows directly form the definition of the tile set, cf. the idea of RVE Sets [108].

5.4.3 Alleviating computational cost

High computational cost is a common sore of procedures aimed at identifying the RVE size. We exploit the repeating occurrence of individual tiles in the microstructure realizations to accelerate solution of the Boundary Value Problems (BVP). Namely, we consider each tile to be a macro-element whose stiffness matrix is obtained using static condensation of internal unknowns of the finite-element (FE) stiffness matrix of the tile. Thus, the tile stiffness matrix is factorized only once at the beginning of the RVE size analysis. In the spirit of the Schur complement method, BVP of each microstructure realization then corresponds to a coarse grid problem composed of the macro-elements [130], resulting in significantly less unknowns. In particular, the number of unknowns was reduced from 46 millions to 250 thousands for the largest investigated system in Section 5.5. Macro-elements also improve spectral properties of the final algebraic system, which is especially significant when investigating composites with high contrast in material properties of individual components. As a result, iterative solvers—such as the preconditioned conjugate gradient method used in this work—for the coarse grid problem require less iterations to achieve desired accuracy.

Moreover, components of the apparent tensors are obtained as averaged dual quantities after solving BVP with a prescribed macroscopic tensor $\boldsymbol{E}$ or $\boldsymbol{G}$, respectively, keeping one component equal to unity while the others remaining zero, recall Eq. (5.6). We also accelerate the averaging by constructing matrices that relate tile boundary degrees of freedom to the sought averages in the off-line phase.

[5] A single contraction for conductivity and a double contraction for the elasticity problem.

Algorithm 5.1 Identification of the numerical RVE size

Require: ϵ^{usr}, $\tilde{P}_\epsilon$, ξ^{usr}, and $\tilde{P}_\xi$
  $s \leftarrow 1$ ▷ Skip 1×1 tilings
  repeat
    $s \leftarrow s + 1$
    $i \leftarrow 0$ ▷ Level I
    for $i < n_{\min}$ **do**
      $i \leftarrow i + 1$
      generate a tiling $s \times s$
      synthesize a microstructure from the tiling
      compute $\boldsymbol{L}_s^{(i)}$ and $\boldsymbol{M}_s^{(i)}$
      compute $l_s^{(i)}$ and $m_s^{(i)}$
    end for
    compute ensemble statistics $\hat{l}_s$, $\hat{m}_s$, $\hat{\varsigma}_s^l$, and $\hat{\varsigma}_s^m$
    compute ϵ_s^l and ϵ_s^m
    while $\left(\epsilon_s^l > \epsilon^{\text{usr}}\right) \wedge (\epsilon_s^m > \epsilon^{\text{usr}}) \wedge (i < n_{\max})$ **do**
      $i \leftarrow i + 1$
      generate a tiling $s \times s$
      synthesize a microstructure from the tiling
      compute $\boldsymbol{L}_s^{(i)}$ and $\boldsymbol{M}_s^{(i)}$
      compute $l_s^{(i)}$ and $m_s^{(i)}$
      update ensemble statistics
      compute ϵ_s^l and ϵ_s^m
    end while
    $n_s \leftarrow i$
    compute $\hat{\xi}_s$ and $\hat{\varsigma}_s^\xi$ ▷ Level II
    compute ξ_s^{test}
  until $(\xi_s^{\text{test}} \leq \xi^{\text{usr}}) \vee (s \geq s_{\max})$

5.5 Numerical tests

Performance of the proposed methodology and the sensitivity of the RVE size with respect to an investigated physical phenomenon, morphology of the microstructure, and contrast in constituent properties are illustrated with three distinct two-phase microstructures: a suspension of non-penetrable elliptic inclusions, Fig. 5.5.2; a foam-like microstructure, Fig. 5.5.7; and sandstone, Fig. 5.5.12.

In order to circumvent the need for meshing complex geometries while maintaining the mesh compatibility across the relevant tile edges, we resorted to regular pixel-like grids. Each pixel represented a quadrilateral FE element with bilinear Lagrange basis functions. Following a sensitivity analysis of the tile apparent properties with respect to the mesh density, the resolution of each tile was determined as a compromise between accuracy and computational cost, see Tab. 5.5.1 for the chosen values. Because the first-order apparent properties are length-scale free, we set the pixel size to be the reciprocal value of a tile resolution, resulting in a unitary tile size.

In order to relate the tile and RVE sizes to an intrinsic scale of a material, the charac-

Table 5.5.1: Single tile resolution and characteristics of the compressed microstructure systems. Standard deviation of the volume fraction ϕ computed over the tile set is reported in parentheses.

	ellipse	foam	sandstone
resolution	100×100 px	402×402 px	354×354 px
χ	0.157	0.047	0.051
ϕ	0.359 (0.023)	0.742 (0.008)	0.169 (0.013)

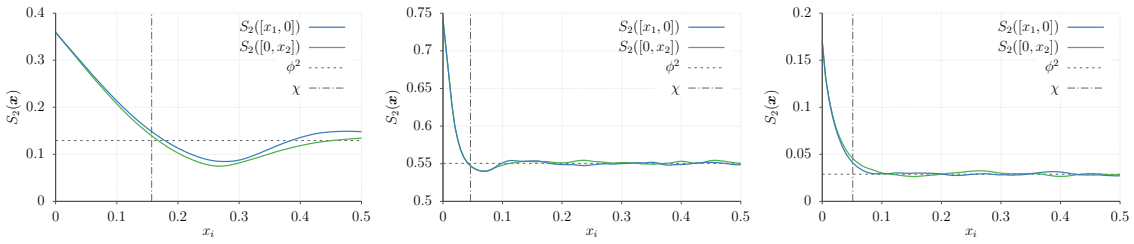

(a) (b) (c)

Figure 5.5.1: Sections of the inclusion two-point probability function S_2 along x_1 and x_2 axes and the highlighted characteristic length χ of: (a) the microstructure with monodisperse elliptic inclusions, (b) foam, and (c) sandstone. In legends, ϕ denotes the volume fraction of the inclusions. Data was obtained by averaging S_2 statistics computed for 10 realizations of 40×40 tilings.

teristic length

$$\chi = \sqrt{\frac{1}{\phi - \phi^2} \int_{\mathcal{T}} |S_2(\boldsymbol{x}) - \phi^2| \, \mathrm{d}\boldsymbol{x}} \,, \tag{5.37}$$

was identified for each microstructure, similarly to [141]. In Eq. (5.37), ϕ denotes the volume fraction of the inclusion phase[6] and $S_2(\boldsymbol{x})$ stands for the two-point probability function [2], which gives the probability of finding two points separated by $\boldsymbol{x}$ in the same constituent—the inclusion phase in our case. The integral in Eq. (5.37) is computed over $\mathcal{T} = [0, 0.5] \times [0, 0.5]$ in order to mitigate the effect of assembly-induced artefacts, see [21] for further details. The characteristic lengths of the investigated microstructures, averaged from 10 realizations of 40×40 tilings, are plotted in Fig. 5.5.1 and summarized in Tab. 5.5.1.

Within our numerical tests, microstructure constituents were assumed isotropic. For the thermal conduction problem, the conductivity tensor $\boldsymbol{K}$ of the i-th constituent then takes the form

$$\boldsymbol{K}_i = \lambda_i \boldsymbol{I} \,, \tag{5.38}$$

with λ_i being the conductivity of the i-th phase and $\boldsymbol{I}$ standing for the second order unit tensor. In the case of linear elasticity, the material stiffness tensor $\mathbf{D}$ is given as

$$\mathbf{D}_i = \lambda_i \boldsymbol{I} \otimes \boldsymbol{I} + 2\mu_i \mathbf{I}^s \,, \tag{5.39}$$

where λ_i and μ_i are the first and second Lamé coefficients of the ith phase, respectively,

[6] We consistently refer to the continuous phase as a matrix and to the discontinuous phase as inclusions. Consequently, the volume fraction reported here for the foam microstructure is complementary to the standard notion of foam volume fraction.

Table 5.5.2: Combination of material parameters for individual contrasts

κ	thermal conductivity		linear elasticity			
	λ_1	λ_2	λ_1	μ_1	λ_2	μ_2
1:100	1	0.01	1	0.5	0.01	0.005
1:50	1	0.02	1	0.5	0.02	0.010
50:1	1	50	1	0.5	50	25
100:1	1	100	1	0.5	100	50

and $\mathbf{I}^s$ denotes the fourth order unit tensor with major and minor symmetries. We further assumed plane strain conditions.

For each type of microstructure and each phenomenon, we investigated four material property contrasts κ defined as

$$\kappa = \frac{\lambda_2}{\lambda_1}\,. \tag{5.40}$$

The material parameters of the matrix-like phase (denoted with index 1 and depicted in dark gray colour in Figs. 5.5.2, 5.5.7, and 5.5.12) were kept fixed at unity while the parameters of the second inclusion-like phase (indexed with 2 and shown in light gray colour) were proportionally scaled by the factors 0.01, 0.1, 10, and 100; see Tab. 5.5.2.

Finally, for scalar characterization of an apparent tensor, recall Eq. (5.28), we used the operator norm of the corresponding matrix representation, employing the Mandel notation in the case of linear elasticity. The proximity error ξ was calculated using the Frobenius norm in Eq. (5.35). Both significance levels $\tilde{P}_\epsilon$ and $\tilde{P}_\xi$ were set to 0.01 and the related limit errors were defined as $\epsilon^{\mathrm{usr}} = 0.01$ and $\xi^{\mathrm{usr}} = 0.05\|\boldsymbol{I}\|_{\mathrm{Fro}}$, respectively, where the norm of a unitary tensor was used to cover consistently both thermal conductivity and linear elasticity. In all cases, we set $n_{\min} = 5$; the upper limit was $n_{\max} = 30$ for the first and third microstructure and $n_{\max} = 25$ for the foam microstructure. Data reported in this Section follows from a single run of the proposed methodology. However, results of multiple runs with different random realizations (not reported here) show that the identified RVE size is consistent throughout different runs, albeit the number of realizations of intermediate SVE sizes may vary to accommodate the required accuracy ϵ^{usr}. Especially for small SVEs, the scatter in the number of realization can be significant due to the random sampling.

5.5.1 Impenetrable elliptic inclusions

First, we analysed a microstructure comprising impenetrable, mono-disperse elliptic inclusions of 0.75 aspect ratio. The inclusion phase constituted 35.9% of the microstructure. Microstructural information was compressed in the set depicted in Fig. 5.5.2, containing eight tiles with two edge codes on horizontal and vertical edges, respectively.

Recall that the identified RVE size is always a multiple of the tile size, which defines the smallest attainable RVE size in turn. Thus, the tile-based approach is appealing particularly for problems with a high contrast κ resulting in large RVEs. Here, the ratio 0.157 between the characteristic length and the tile size, see Tab. 5.5.1, allow us to investigate also 1:10 and 10:1 contrasts, which are neglected for the remaining two microstructures because these contrasts result in small RVE sizes of one or two tiles, dominated by the tile size rather than the RVE criterion.

The distribution of scalar quantities $l_s^{(i)}$ and $m_s^{(i)}$, characterizing the apparent properties of individual tiling realizations, are depicted using a box-and-whisker plot in Fig. 5.5.3

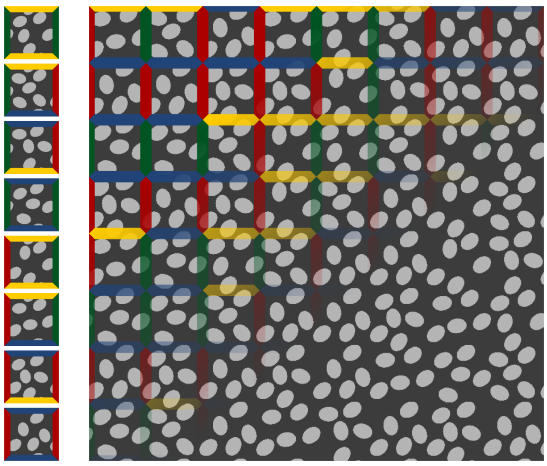

(a) (b)

Figure 5.5.2: A microstructure with impenetrable mono-disperse elliptic inclusions compressed in a tiles set composed of 8 Wang tiles, (a), and a tiling sample with partially highlighted edge codes, (b).

for the problem of thermal conductivity and in Fig. 5.5.4 for linear elasticity. Box boundaries and a mid-band denote the first and third quartile Q_1 and Q_3, and median Q_2, respectively; whisker ends mark an interval defined as $Q_2 \pm 1.5(Q_3 - Q_1)$; and the crosses indicate potential data outliers. Dotted lines connect data averages.

The number of realizations of each SVE size required to meet the ϵ^{usr} criterion is given in Fig. 5.5.5; cases when the number of realizations was restricted by the upper limit $n_{\max}$ are denoted with empty triangle markers. Note that due to the combinatorial nature of the SVE synthesis, the number of unique SVE realizations of given size s is limited. However, the number grows exponentially[7] and therefore poses no practical restriction for larger SVEs. The number of 1×1 realizations was limited by the number of individual tiles and the results are shown only for completeness. Finally, Fig. 5.5.6 shows the convergence of the proximity error ξ to its limit value ξ^{usr}.

As expected, higher contrast in constituent properties led to increase in the RVE size, which ranged from four times the tile edge length for 1:10 and 10:1 contrasts up to 36 in the case of linear elasticity and contrast 100:1. The maximum number of realizations was set to 30 for this microstructure, which did not influence identification of the RVE size, see Fig. 5.5.5.

In the particular problem of thermal conductivity, values $l_s^{(i)}$ and $m_s^{(i)}$ have direct physical interpretation as the largest and the inverse of the least principal conductivity. Comparing the values obtained for the RVE size indicates anisotropy in the homogenized material behaviour, which can be anticipated considering different x_1 and x_2 cross-sections of the two-point probability functions shown in Fig. 5.5.1a.

[7] By construction, the tile sets in Fig. 5.5.2a and Fig. 5.5.7a allow for at least two distinct tiles for each position in a tiling; thus the number of unique SVEs is bounded from below by 2^{s^2}. For sandstone compression, see Fig. 5.5.12a, the lower bound is 4^{s^2}.

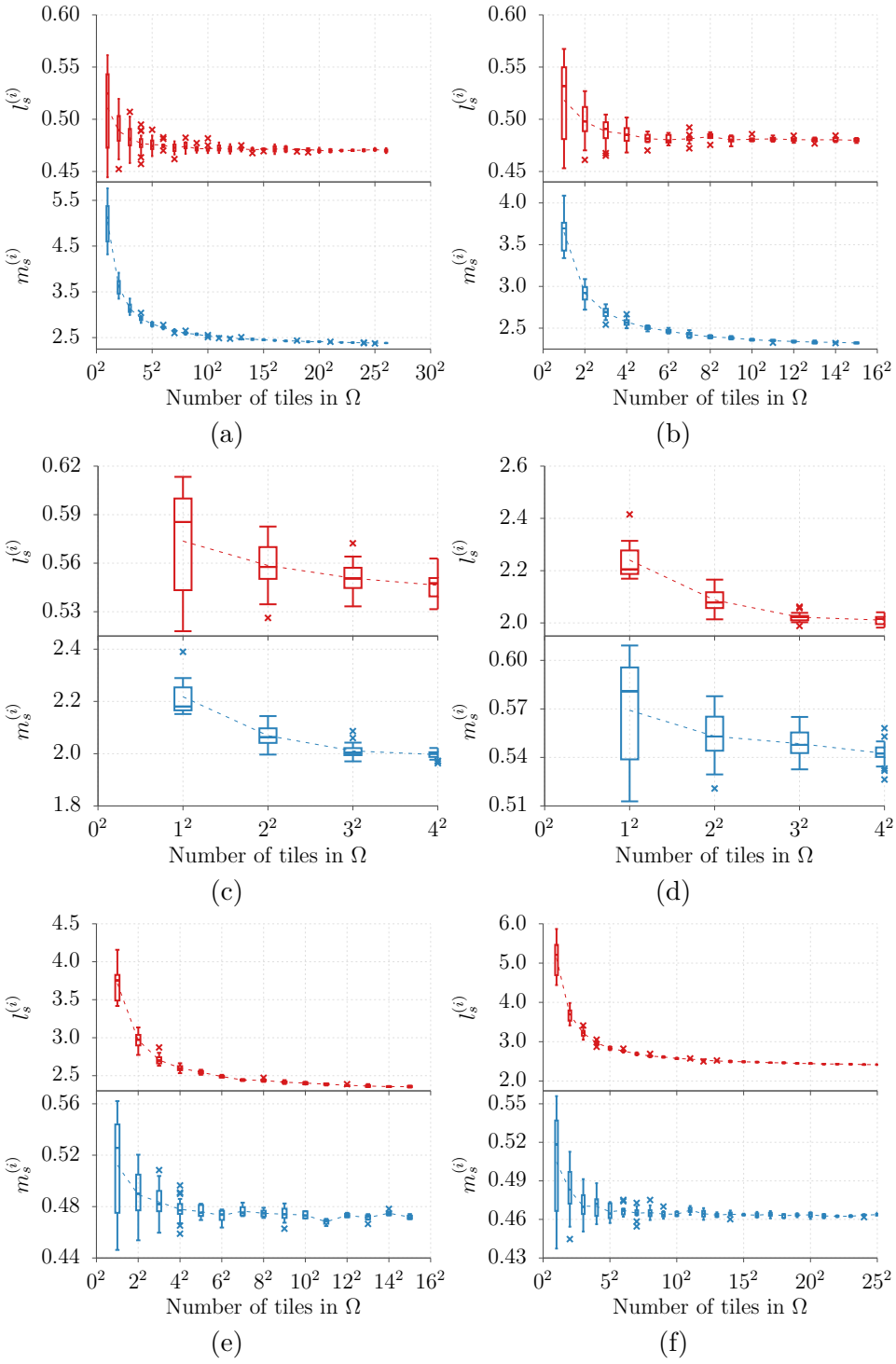

Figure 5.5.3: Box-and-whisker plots of the norms $l_s^{(i)}$ and $m_s^{(i)}$ for thermal conductivity of the microstructure with elliptic inclusions and contrasts in material properties: (a) 1:100, (b) 1:50, (c) 1:10, (d) 10:1, (e) 50:1, and (f) 100:1 .

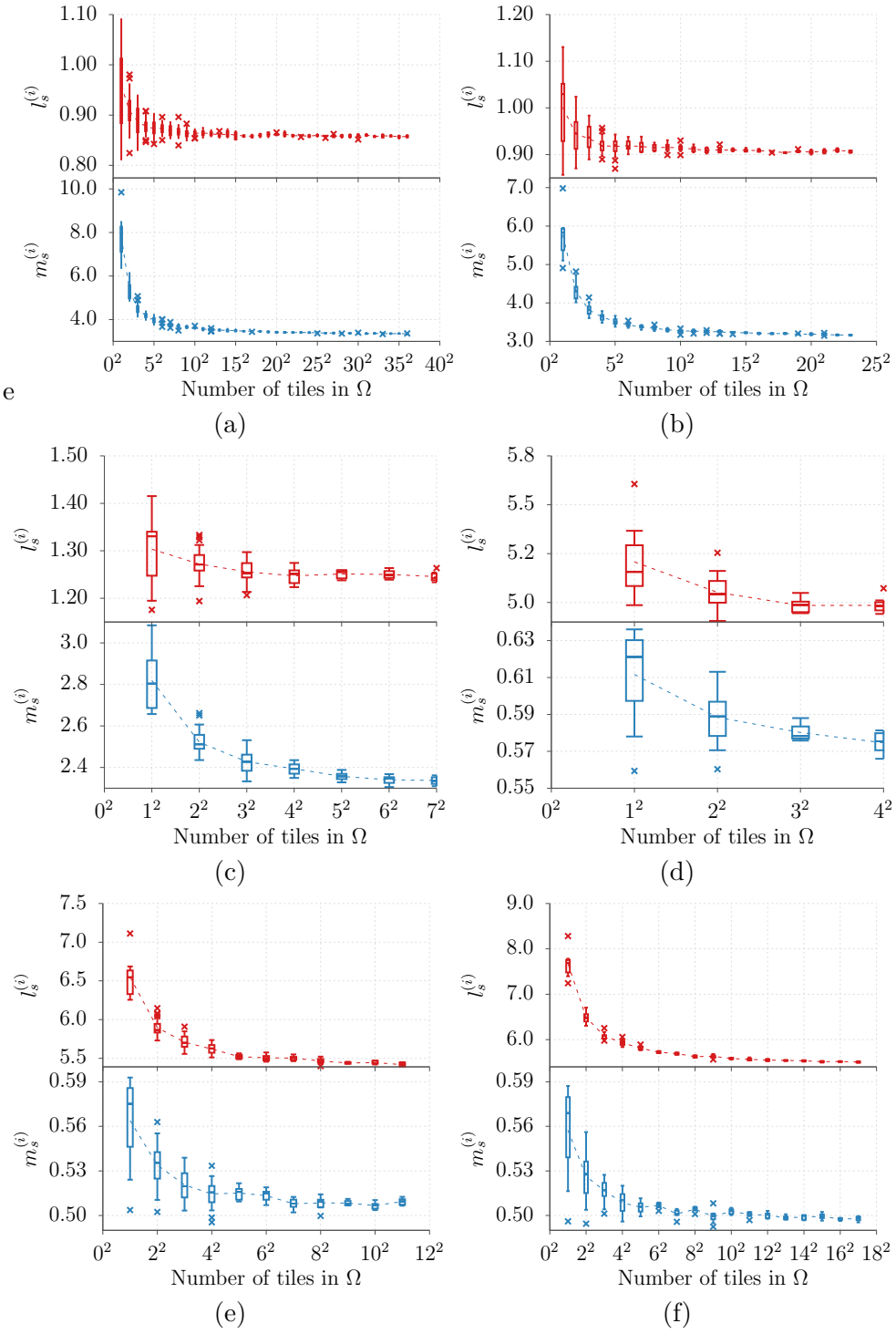

Figure 5.5.4: Box-and-whisker plots of the norms $l_s^{(i)}$ and $m_s^{(i)}$ for linear elasticity of the microstructure with elliptic inclusions and contrasts in material properties: (a) 1:0.01, (b) 1:0.05, (c) 1:0.1, (d) 10:1, (e) 50:1, and (f) 100:1 .

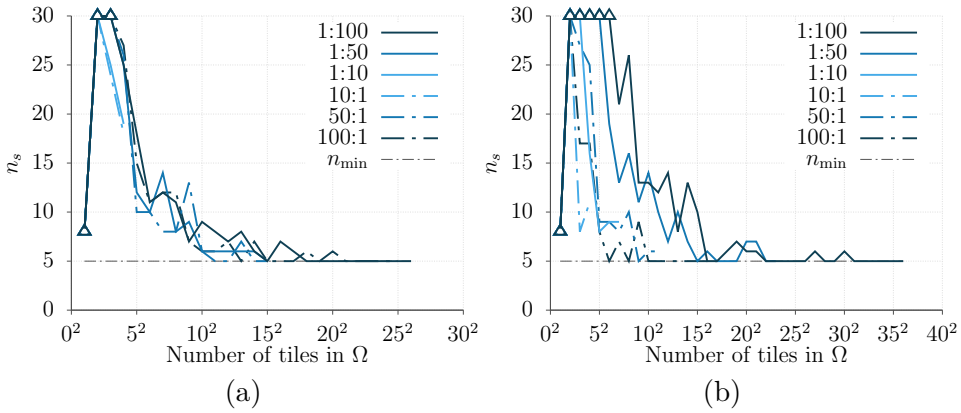

Figure 5.5.5: Number of SVE realizations for the microstructure with elliptic inclusions: (a) thermal conductivity, (b) linear elasticity.

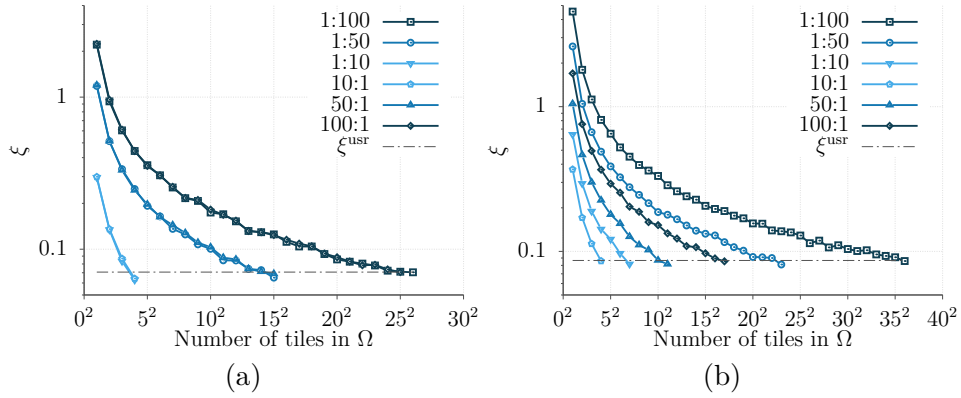

Figure 5.5.6: Convergence of the proximity error ξ with increasing tiling sizes for the microstructure with elliptic inclusions: (a) thermal conductivity, (b) linear elasticity.

5.5.2 Foam

Motivated by our earlier study on elastic properties of aluminium foams [75], the second investigated microstructure was chosen to represent a two-dimensional sample of a closed cell foam. The system was compressed into the same tile set, in terms of tile code definition, as the previous microstructure. The internal geometry of tiles was artificially designed with a modified version of the level-set based approach developed by Sonon et al. [19]. The compressed geometry, displayed in Fig. 5.5.7, features large irregular inclusions separated with thin ligaments that form 25.8% of the microstructure volume.

With infinite contrast, foams are typical representatives of complex materials with pronounced influence of actual microstructure composition on their overall response. Our previous work [75] corroborated this claim in two-dimensional setting, reporting the RVE size approximately in the order of magnitude of thousands of inclusion (voids) diameters. Even thought we do not assume the extreme case of voids, large RVE sizes are expected for higher contrasts as well.

Statistics of $l_s^{(i)}$ and $m_s^{(i)}$ for increasing tiling sizes are plotted in Figs. 5.5.8 and 5.5.9 for thermal conductivity and linear elasticity, respectively. Number of realizations for each

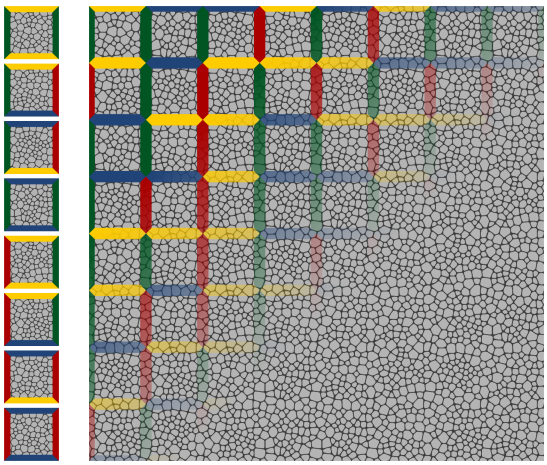

(a) (b)

Figure 5.5.7: A foam-like microstructure compressed in a tiles set composed of 8 Wang tiles, (a), and a tiling sample with partially highlighted edge codes, (b).

tiling size is shown in Fig. 5.5.10 and the convergence towards the prescribed proximity limit ξ^{usr} is depicted in Fig. 5.5.11. The identified RVE sizes ranged from three to 12 times the tile size in all analyses, the number of equi-sized realizations was limited to 25, see Fig. 5.5.10. Compared to the microstructure with elliptic inclusions, the nominal RVE sizes are smaller, however, the tile size is a characteristics of microstructure representation not its geometry. RVE sizes of different microstructures have to be compared to their characteristic length, see Fig. 5.5.17, which supports the assumption of larger RVE than in the case of the microstructure with inclusions; see also additional discussion in Section 5.5.4. Finally, the converged values of $l_s^{(i)}$ and $m_s^{(i)}$ in Fig. 5.5.8 imply isotropy of the microstructure, observable also in Fig. 5.5.1b.

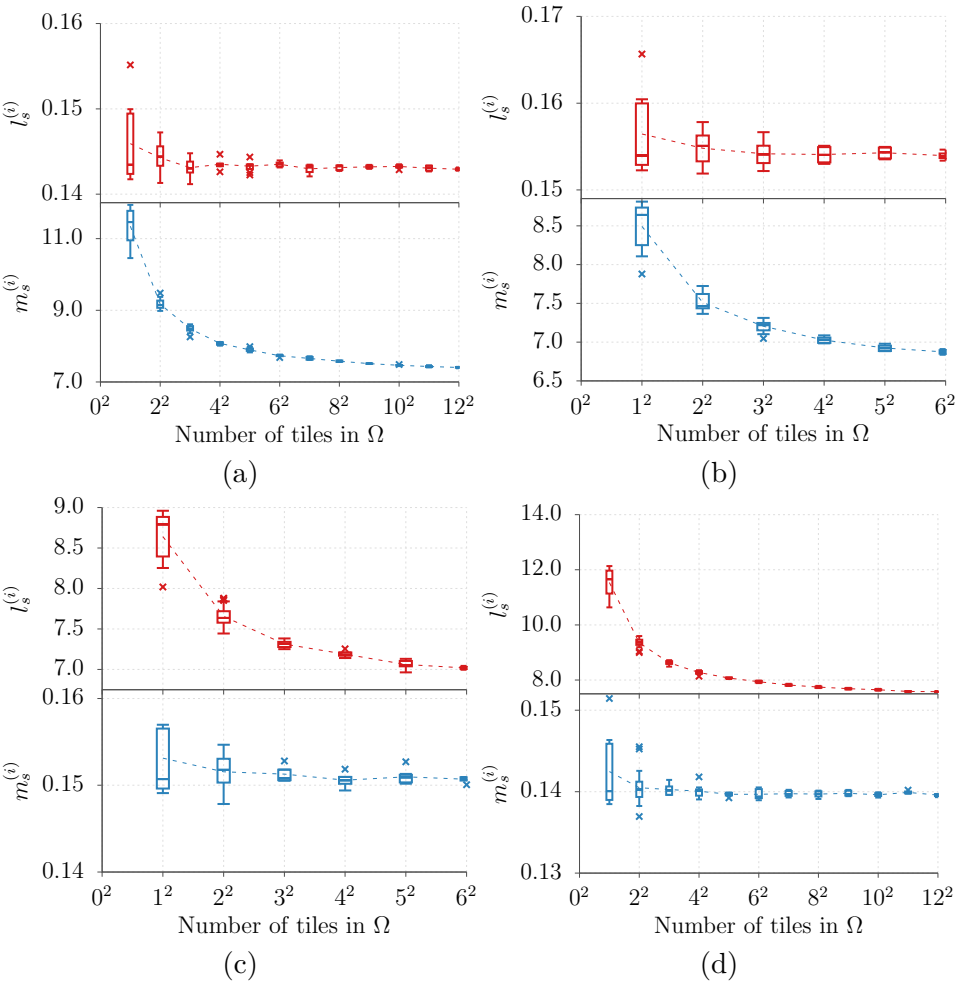

Figure 5.5.8: Box-and-whisker plots of the norms $l_s^{(i)}$ and $m_s^{(i)}$ for thermal conductivity of the foam-like microstructure and contrasts in material properties: (a) 1:100, (b) 1:50, (c) 50:1, and (d) 100:1 .

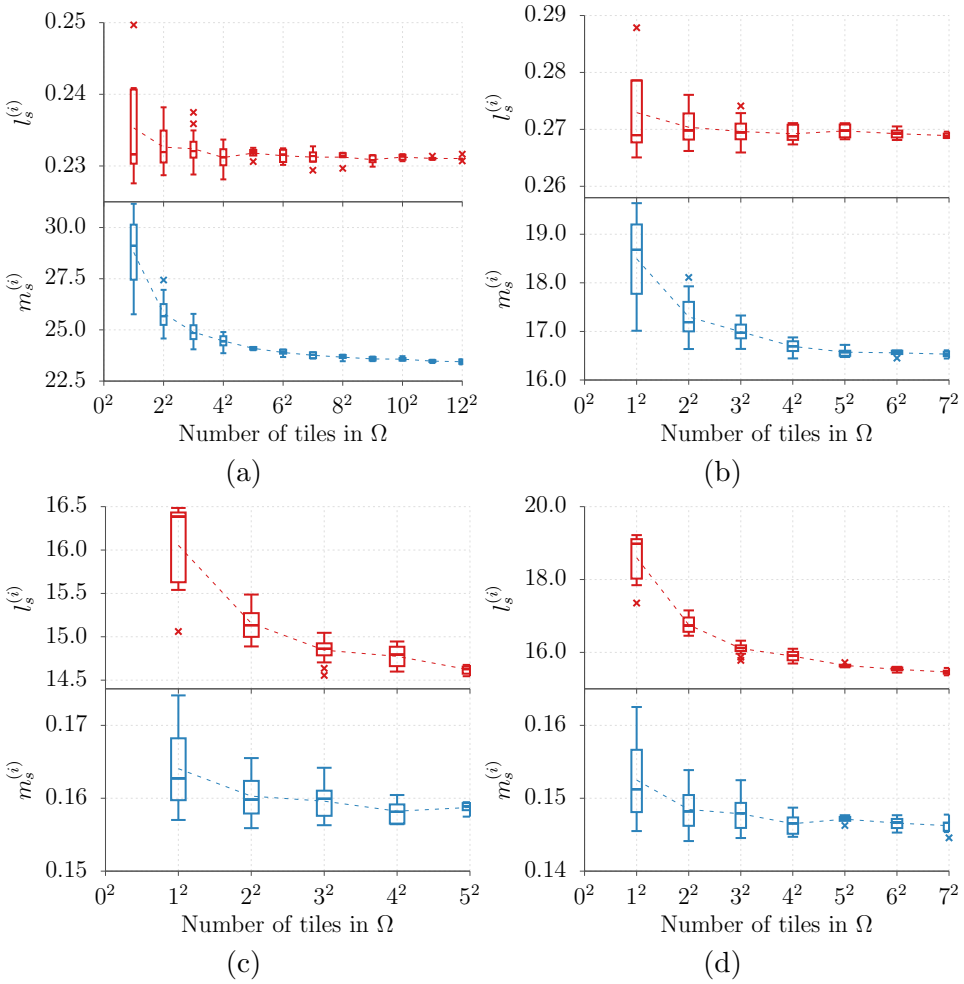

Figure 5.5.9: Box-and-whisker plots of the norms $l_s^{(i)}$ and $m_s^{(i)}$ for linear elasticity of the foam-like microstructure and contrasts in material properties: (a) 1:100, (b) 1:50, (c) 50:1, and (d) 100:1 .

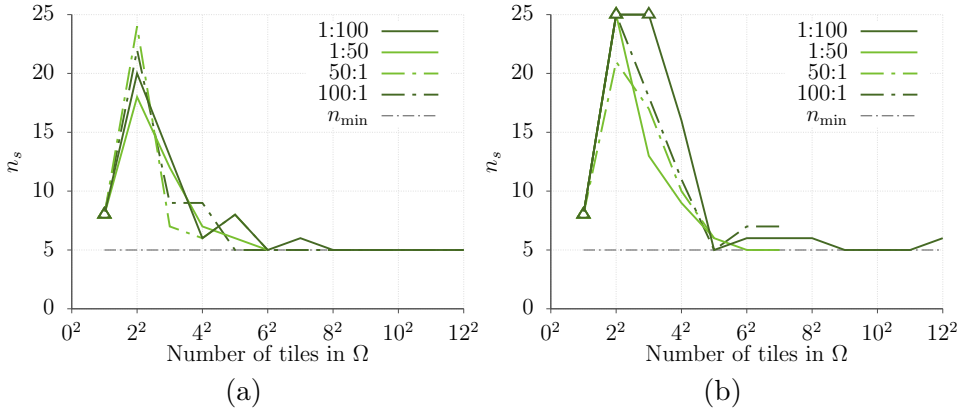

Figure 5.5.10: Number of SVE realizations for the foam-like microstructure: (a) thermal conductivity, (b) linear elasticity.

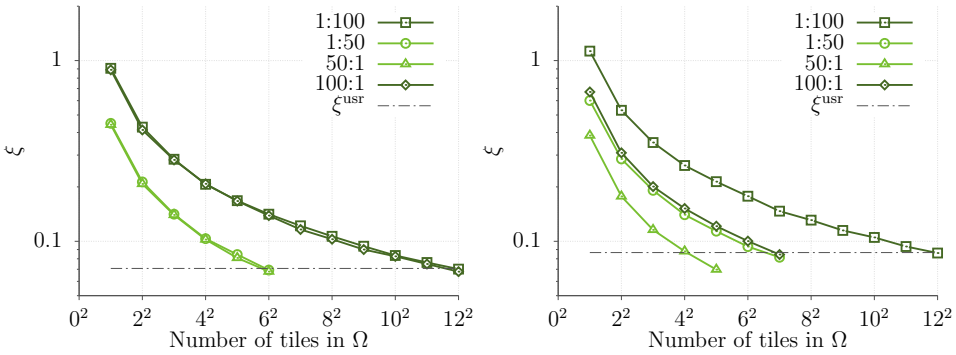

Figure 5.5.11: Convergence of the proximity error ξ with increasing tiling sizes for the foam-like microstructure: (a) thermal conductivity, (b) linear elasticity.

5.5.3 Sandstone

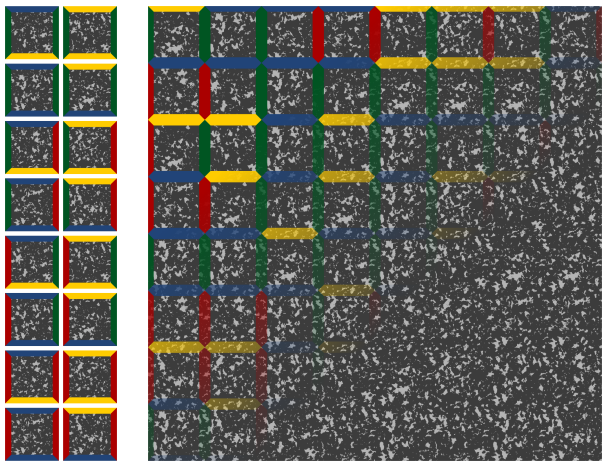

Figure 5.5.12: A microstructure of Gosford sandstone [42] compressed within a set of 16 tiles, (a), and a tiling sample with partially highlighted edge codes, (b).

The last investigated microstructure is a two-dimensional representation of the Gosford sandstone studied in [42]. The microstructure was compressed using the sample-based quilting algorithm [21]. Two distinct codes were assumed at horizontal and vertical edges. Based on our previous study [21] and to emphasize that the tile set can be arbitrarily large, we used a richer tile set that contained all possible combinations of the codes. Similarly to the previous section, the second phase (displayed in light grey in Fig. 5.5.12) was originally void; in our parametric analysis, we reused only the geometry and assumed a solid second phase with parameters from Tab. 5.5.2.

Again, scalar characterization of particular contrast settings and physical phenomena is summarized in Figs. 5.5.13 and 5.5.14; the number of realizations generated for each tiling size is shown in Fig. 5.5.15; and Fig. 5.5.16 depicts convergence of the RVE criterion. Low volume fraction of the second phase along with a large tile size to characteristic length ratio are likely the cause of small nominal RVE sizes, which were identified as seven times

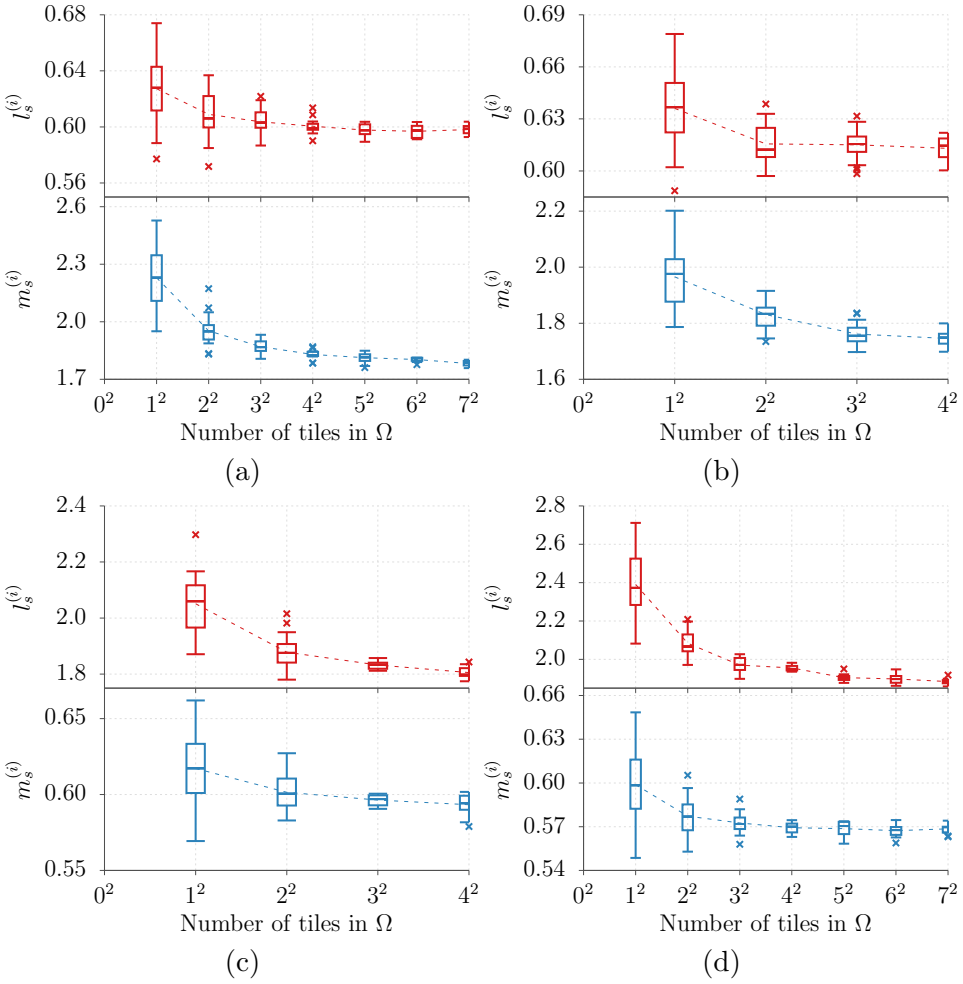

Figure 5.5.13: Box-and-whisker plots of the norms $l_s^{(i)}$ and $m_s^{(i)}$ for thermal conductivity of the sandstone microstructure and contrasts in material properties: (a) 1:100, (b) 1:50, (c) 50:1, and (d) 100:1 .

the tile size for contrasts 1:100 and 100:1 for thermal conductivity and twelve times the tile size in the case of linear elasticity and 1:100 contrast. On the other hand, more tiles in the compressed set and higher variability of the microstructure itself resulted in larger scatter of individual results, compare number of realizations in Figs. 5.5.15 and 5.5.10 and note that the characteristic length of the sandstone microstructure was similar to the foam-like microstructure. The converged values in Fig. 5.5.13 indicate slight anisotropy, which is emphasized when the inclusions are more conductive/stiffer than the matrix.

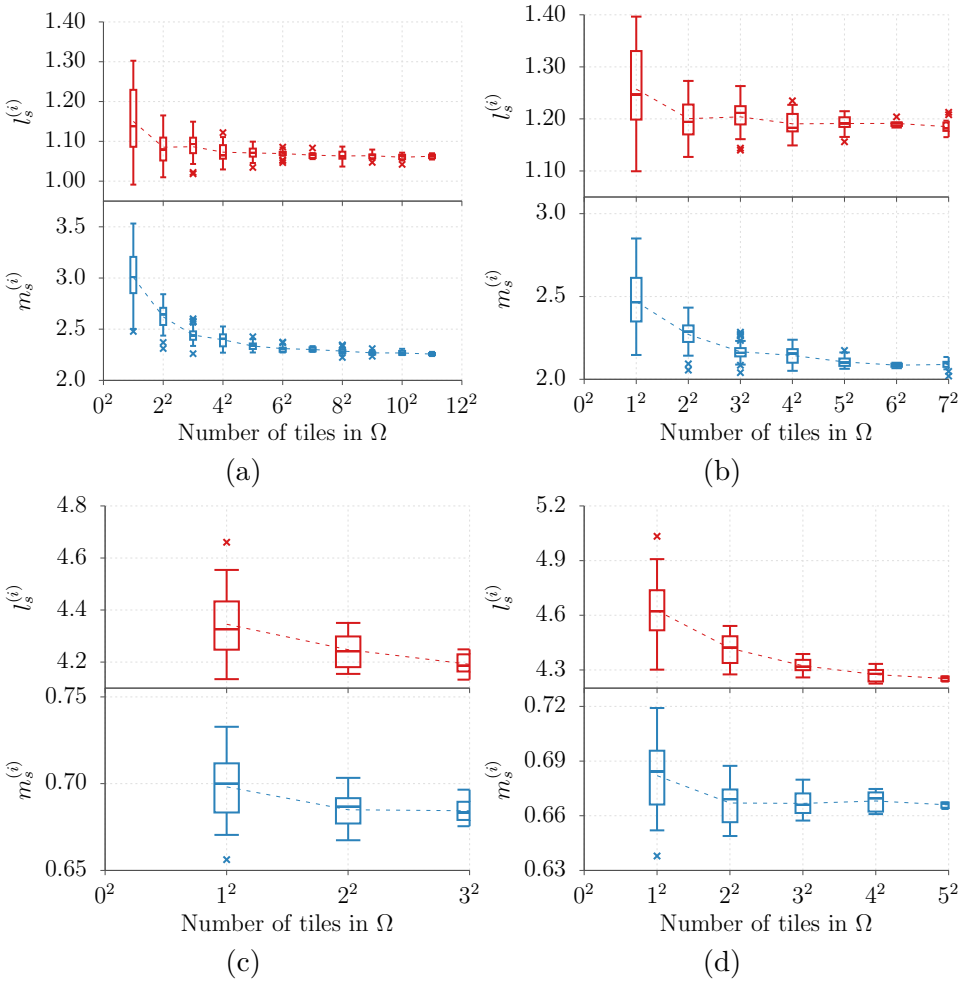

Figure 5.5.14: Box-and-whisker plots of the norms $l_s^{(i)}$ and $m_s^{(i)}$ for linear elasticity of the sandstone microstructure and contrasts in material properties: (a) 1:100, (b) 1:50, (c) 50:1, and (d) 100:1 .

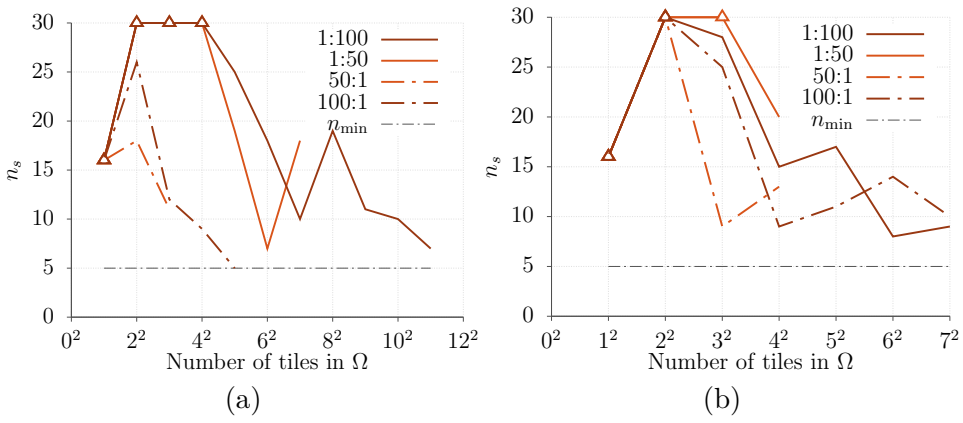

Figure 5.5.15: Number of SVE realizations for the sandstone microstructure: (a) thermal conductivity, (b) linear elasticity.

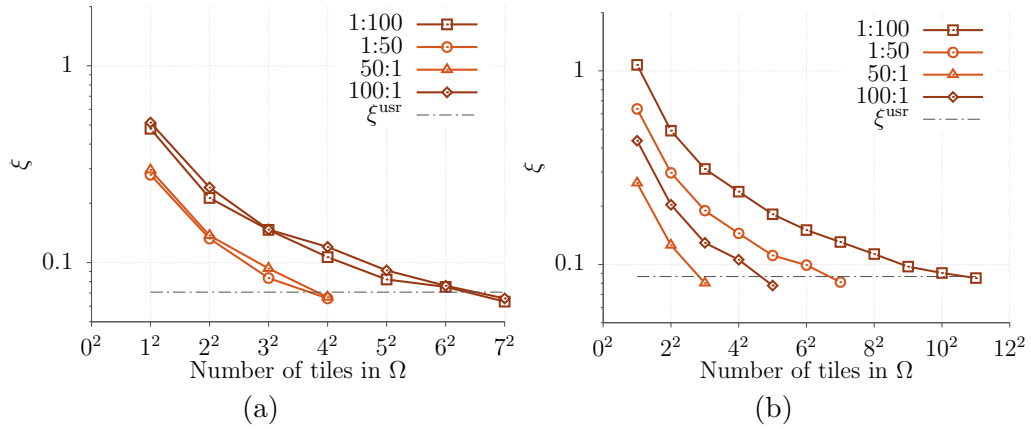

Figure 5.5.16: Convergence of the proximity error ξ with increasing tiling sizes for the sandstone microstructure: (a) thermal conductivity and (b) linear elasticity.

5.5.4 Discussion

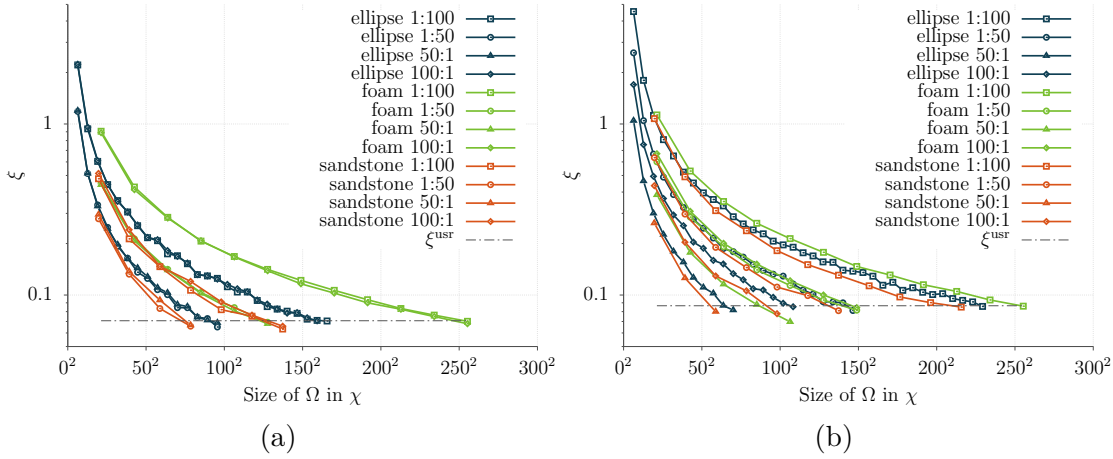

Figure 5.5.17: Comparison of ξ convergence with increasing SVE sizes normalized against the characteristic length χ for all investigated microstructures: (a) thermal conductivity, (b) linear elasticity.

As stated above, the nominal sizes of RVE identified in terms of tile multiples have to be scaled with the corresponding characteristic length χ of the microstructure to allow mutual comparison. The scaled RVE sizes ϱ are plotted against the contrast κ of constituent properties in Fig. 5.5.18. Similarly, Fig. 5.5.17 shows the ξ convergence lines from Figs. 5.5.6, 5.5.11, and 5.5.16 as functions of the scaled size of Ω.

Data in Fig. 5.5.17 confirms that the RVE size is indeed problem dependent and there are no universal scaling parameters common to both thermal conductivity and linear elasticity. For thermal conductivity, the inverse contrasts, i.e., 1:n and n:1, resulted in nearly identical RVE sizes. On the other hand, for linear elasticity, cases with matrix stiffer than inclusions required approximately twice the RVE size, compared to the RVE size of the inverse contrast, to satisfy ξ^{usr}, compare Figs. 5.5.17a and 5.5.17b or note the inclination of dash-dotted lines in Fig. 5.5.18. Asymmetry was observed in a whole range

Table 5.5.3: Values of Linear Least Square fit parameters from Eq. (5.41)

	Ellipse			Foam			Sandstone		
	TC	LE ($\kappa < 1$)	LE ($\kappa > 1$)	TC	LE ($\kappa < 1$)	LE ($\kappa > 1$)	TC	LE ($\kappa < 1$)	LE ($\kappa > 1$)
a	3.944	8.874	5.995	4.465	4.867	15.928	3.7457	11.910	3.292
b	0.812	-0.711	0.628	0.872	-0.865	0.485	0.781	-0.628	0.737
# data	11	4	3	5	3	2	5	3	2

of κ and for all investigated microstructures.

Plotting data from Fig. 5.5.18 in a log-log graph Fig. 5.5.19 and modifying the horizontal axis such that the contrasts 1:n and n:1 coincide reveal a power-law relation in the form

$$\varrho = a\,(\kappa)^b\ , \tag{5.41}$$

with fitting parameters a and b. The observed symmetry of the RVE size for thermal conductivity allows for replacing κ with $10^{|\log_{10}\kappa|}$ in Eq. (5.41) and consequently fitting only one set of parameters for the whole contrast range; linear elasticity problem requires separate handling of $\kappa < 1$ and $\kappa > 1$. Parameters reported in Tab. 5.5.3 were obtained with a linear least square regression, taking into account also unreported results obtained for contrast 1:20 for all six combinations and 1:75, 1:25, 25:1, and 75:1 for the problem of thermal conductivity of the microstructure with elliptic inclusions. For the sake of brevity, the predicted fits are plotted in Fig. 5.5.19 only for the thermal conductivity problem. While the parameters a and b for thermal problems were obtained from ten and five data points, respectively, in certain cases fits for linear elasticity were based only on two data points and, thus, the identified values are inconclusive.

For a given contrast κ, the corresponding RVE size ϱ is smallest for the sandstone microstructure, followed by the microstructure with elliptic inclusions and the foam-like microstructure. The ordering closely follows the volume fraction of the second phase; observe that the RVE sizes of the sandstone microstructure and the microstructure with elliptic inclusions are always closer together, compared to the foam-like microstructure. On the other hand, the influence of particular microstructure composition varies depending on a problem and chosen κ.

For the extreme contrasts and thermal conductivity, ϱ seems to be governed primarily by the volume fraction, due to the large difference between individual microstructures,

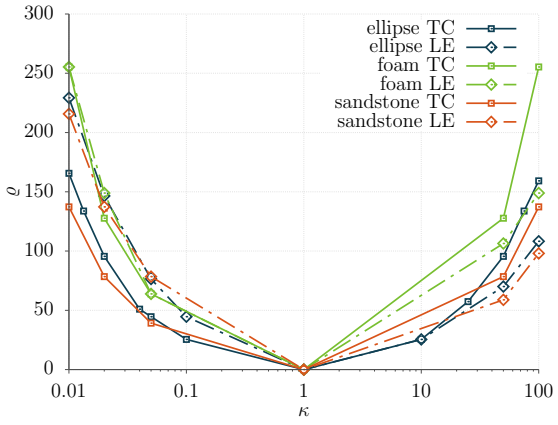

Figure 5.5.18: Lin-log plot of dependence of the scaled RVE-size ϱ on the contrast κ of constituent properties for thermal conductivity (TC) and linear elasticity (LE).

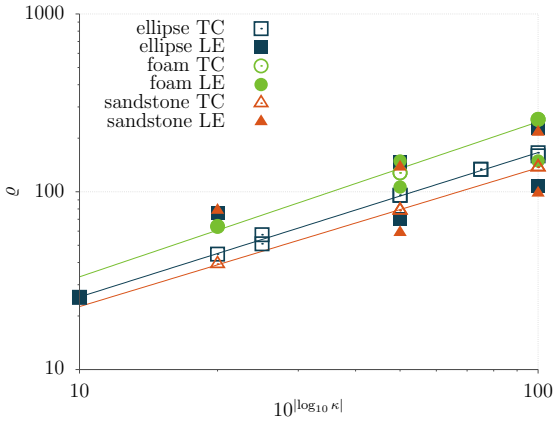

Figure 5.5.19: Log-log plot of the RVE-size dependence on the absolute contrast of constituent properties, defined as $10^{|\log_{10}\kappa|}$. The fit (solid lines) of the power-law relation (5.41) is shown only for the thermal conductivity problem.

and insensitivity to swapping material properties of the phases, see Fig. 5.5.17a. On the contrary, in linear elasticity, complexity and the actual microstructure composition have a pronounced effect especially when the inclusions are stiffer; instances in which the matrix phase is stiffer seem to be dominated mainly by the contrast itself.

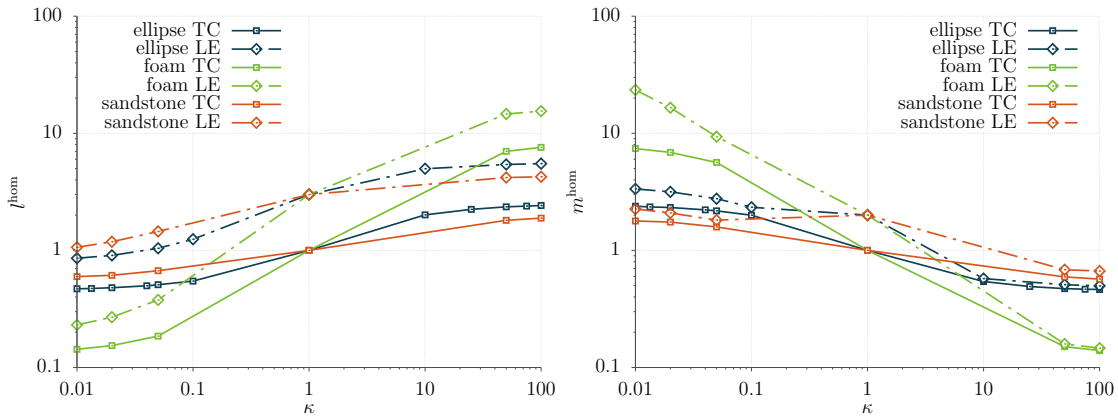

Figure 5.5.20: Log-log dependence of the norms l^{hom} and m^{hom} of the identified homogenized tensors, recall Eq. (5.29), on contrast κ of constituent properties. Values for unit contrast were computed from material characteristics of the matrix phase.

Influence of the inclusion parameters on the converged values l^{hom} and m^{hom}, respectively, is shown in a log-log graph in Fig. 5.5.20. Unlike the RVE-size dependence, curves in Fig. 5.5.20 indicate that no power law in the form of a monomial can be established except for the linear elasticity of the foam-like microstructure with $\kappa < 1$. In all other cases, the overall scalar characteristics plateau soon and further increase of $|\log_{10}(\kappa)|$ does not lead to their significant change.

Also note in the box-and-whisker plots that the RVE size criterion ξ is driven by $\overline{l_s}$ for $\kappa > 1$; and vice versa, the initial and final values of $\overline{m_s}$ differ more for $\kappa < 1$.

Finally, the last observation regards the necessary number of realizations, shown in Figs. 5.5.5, 5.5.10, and 5.5.15. Within a chosen microstructure, problems with similar final

RVE sizes required approximately the same number of realizations at intermediate sizes. Moreover, as the SVE size approached the RVE one, the minimal number of realizations sufficed to meet ϵ^{usr} limit for all microstructures, except for sandstone.

Thus, the RVE size, at least in the context of our methodology, seems to be driven mainly by the ensemble average and not its variation, which corroborates conclusions of Moussaddy et al. [119], who warned against using the variance of apparent properties as the only RVE criterion.

5.6 Summary

We demonstrated that the compressed representation of materials with random microstructure by means of Wang tiles is an appealing framework for numerical homogenization and problems of RVE size determination, in particular. Upon an off-line phase of compressing the microstructural information into a set of tiles, the framework facilitates instant on-line random generation of statistically coherent realizations of compressed microstructures. Moreover, adopting elemental ideas of domain decomposition and considering each tile as a macro-element reduce significantly the number of degrees of freedom and improve the condition number of the resulting algebraic system, a desirable feature especially when dealing with highly contrasted problems.

With the emphasis on obtaining bounds on the effective property, we established a methodology that identifies the RVE size for a user-defined accuracy. The methodology benefits from a regular partitioning inherent to the tiling concept and directly utilizes the Partition theorem and statistical sampling to construct confidence intervals of the apparent properties. The proposed methodology works at two levels:

1. For a fixed domain size, new microstructure realizations are generated on-the-fly and their apparent properties are computed until the confidence intervals narrow below a user-defined threshold;

2. The convergence criterion is checked and the algorithm either moves to larger domains or terminates identifying the sought RVE size. The methodology takes into account both the statistical deviation of apparent properties and the discrepancy between their mean values. This makes it robust against premature convergence.

The efficiency of the Wang tiling concept allowed us to illustrate the methodology with a large set of problems. We performed the RVE size identification for three materials from a class of microstructures with clearly identifiable matrix- and inclusion-like phases, yet of different volume fraction and complexity of internal composition. For each material, we investigated two homogenization problems—linear heat conductivity and elasticity. Unlike the majority of similar studies, we kept the volume fraction of inclusions fixed and scaled the ratio between the matrix and inclusion material parameters. Without claiming observations to be general rules, for our particular setting, the RVE size seems to be driven mainly by the mean values of the apparent properties, which corroborates conclusions of Moussaddy et al. [119]. The effect of the actual microstructure composition and the role of matrix or inclusion material is significantly pronounced in the case of linear elasticity, while swapping the constituents has negligible effect on the RVE size for heat conductivity. Data also indicates a power-law relation between the RVE size expressed in terms of the microstructure characteristic length χ and the contrast κ of constituent properties. However, note that the power-law relation common to both the

thermal and linear elasticity problems may stem from the adopted simultaneous scaling of Lamé coefficients in Tab. 5.5.2, which resembles the scaling of the conductivity coefficient. Conversely, a scaling in the form of a simple monomial cannot be established for the converged scalar characteristics of the overall material behaviour but for the compliance of the foam-like microstructure with $\kappa < 1$.

The present approach directly extends to linear three-dimensional problems, in which the acceleration through pre-computed factorization of each tile will be even more pronounced. However, robust methods for compressing three-dimensional microstructures, complemented with a tool for generating topologically and geometrically consistent discretization of Wang cubes, are yet unavailable and constitute our current work.

Chapter 6

Microstructure-informed reduced modes synthesised with Generalized Finite Element Method

Abstract:
A recently introduced representation by a set of Wang tiles—a generalization of the traditional Periodic Unit Cell based approach—serves as a reduced geometrical model for materials with stochastic heterogeneous microstructure, enabling an efficient synthesis of microstructural realizations. To facilitate macroscopic analyses with fully resolved microstructural details generated with the Wang tile concept, we develop a reduced order modelling scheme utilizing pre-computed characteristic responses of the microstructure. First, inspired by computational homogenization, we present a method for extracting the characteristic, continuous fluctuation fields from the compressed microstructral representation based on a set of Wang tiles, without any prior knowledge about the shape of a macroscopic domain or its loading. Second, using the ansatz of Generalized Finite Element Method, we combine these fields with a coarse finite element discretization to create microstructure-informed reduced modes specific for a given macroscopic problem. We illustrate the proposed scheme with a two-dimensional scalar elliptic problem.

Reproduced from: Doškář, M., Zeman, J., Krysl, P., Novák, J. Microstructure-informed reduced modes synthesised with Wang tiles and Generalized Finite Element Method (in preparation).

6.1 Introduction

Reduced Order Modelling (ROM) has become an established way to accelerate numerical analyses by exploiting the information contained in previously obtained solutions (snapshots)—be it time-steps/load increments [148] or solutions to other parametrizations [149]—to construct an approximation space better suited to the investigated problem. ROM is thus particularly appealing to problems such as optimization/parameter identification [149], system control [150], or real-time simulations [151, 152, 153, 154, 155, 156], i.e. scenarios where the increased cost of an off-line phase (collecting and processing snapshots) can be amortized in the subsequent calculations. Many strategies in multi-scale modelling have a similar multi-query character; ROM thus allows for significant acceleration of FE^2-like computational homogenization approaches [157, 158] and the closely related applications in multi-scale topology optimisation [159, 160].

In general, the projection-based ROM works particularly well for problems with a relatively low-dimensional parametrization space (e.g. variation in geometrical or loading parameters, or prescribed macroscopic strain) and mild non-linearities [161, 162]. To avoid a significant increase in dimensions of the reduced approximation space for more severe non-linearities, several strategies were proposed that approximate a solution manifold with multiple reduced approximation subspaces along with procedures allowing for interpolating/transition among them, e.g. [163, 164, 165]. Besides these local approaches in terms of parametrization partitioning [164] or solution characteristics [163, 165], ROM can be utilized locally in problem's subdomains; for instance, Kerfriden et al. [161] proposed using reduced modes only in regions without localized damage. In the FE^2 setting, Oliver et al. [158] split a Representative Volume Element into a linear subdomain and a region of softening cohesive bands, extracting reduced modes for each subdomain separately. Radermacher and Reese [162] introduced an adaptive sub-structuring ROM in forming process simulations, in which only the parts of the domain with mild non-linearity were reduced while highly non-linear regions remained fully resolved. Similarly, Niroomandi et al. [166] combined global ROM with Generalized Finite Element Method (GFEM), introduced locally in a patch near simulated surgical cut, in order to capture localized solution characteristics efficiently. Using Partition of Unity (PU) [167], underlying all the previously mentioned GFEM approaches, Ibáñez et al. [168] recently proposed a local variant of Proper Generalized Decomposition.

Still, the parametrization space of problems with fully resolved, stochastic microstructural details is inherently too high-dimensional, see Section 6.5.2.2 for an explicit example, and hence difficult to address within the standard ROM setting. Even though Kerfriden et al. [161] adopted a ROM strategy for fracture modelling in domains with a stochastic microstructure, only the parameters of a damage model varied within the macroscopic domain. Consequently, the regions excluding the damage localization, which were accelerated with ROM, effectively behaved homogeneously in the linear regime. Numerical strategies based solely on PU/GFEM thus seem to be better suited for simulations with stochastic microstructural details. Covering linear problems, Strouboulis et al. [169] introduced a dictionary of pre-computed local solutions to selected microstructural features, which were then used as enrichment functions within GFEM. Fish and Yuan [114] proposed a multiscale enrichment method, combining PU and responses of a periodic microstructure representation to unit loading cases from the computational homogenization [170]. Efendiev et al. [171] developed Generalized Multiscale Finite Element Method which extracts local enrichments in subdomains from a collection of pre-computed general

responses using eigenvalue analyses. In a similar spirit but without pre-calculations, Plews and Duarte [172] generated the microstructure-specific enrichments on-the-fly by subjecting subdomains with finer discretization to boundary values obtained from a coarse global solution, building on the local-global enrichment framework [173].

In the series of our previous works [15, 21, 43], we have introduced the framework of Wang tiles as a suitable extension of the (Statistically Equivalent) Periodic Unit Cell methodology for modelling microstructural geometry of random heterogeneous materials. We have shown that replacing the unit cell based representation with a set of domains—Wang tiles—with predefined mutual compatibility enables an efficient generation of stochastic microstructural realizations that feature suppressed periodicity artefacts [15, 21, 43] Even though the spurious periodicity is significantly reduced in the generated microstructural samples, they are still composed of only a handful of tiles. The Wang tile concept thus provides a finite-size discrete parametrization space of the generated realizations.

Combining both GFEM and ROM approaches recalled above and benefiting from the discrete parametrization, we develop a reduced order modelling scheme for problems with fully resolved microstructural details generated by the tile-based approach. We first recall the essentials of Wang tile concept and its use in modelling heterogeneous materials in Section 6.2. Next, inspired by computational homogenization approaches as in [114], we propose a method for extracting the characteristic responses of the compressed microstructural representation to parametrized macroscopic loading in Section 6.3. These general, tile-wise defined responses are constructed such that they can be assembled in the same way a microstructural sample is synthesized from the individual Wang tiles, and they serve as an approximation to the fluctuation part of a macroscopic solution. Section 6.4 then introduces the macroscopic numerical scheme that combines the general pre-computed characteristic responses using the Generalized Finite Element ansatz to generate the microstructure-informed reduced modes, specific for a given macroscopic problems. Finally, we illustrate the proposed methodology with two-dimensional, scalar, elliptic examples in Section 6.5.

6.2 Wang tiles as microstructural ROM

The concept of Wang tiles was originally proposed as an equivalent problem in predicate calculus [25]: instead of proving a mathematical statement of a certain class directly, it was converted to a set of square tiles with codes attributed to their edges and investigated whether the given set is able to tile an infinite plane such that the adjacent tiles have the same code on the corresponding edges. Later, this abstract concept was adopted in the Computer Graphics community as a convenient formalism for encoding continuity constraints in the design of pre-generated modules along with the rules for assembling the modules into larger blocks—tilings. Adopting the tile concept has enabled fast synthesis of point patterns with desired blue noise spectrum [174, 90] and naturally looking textures [17, 175, 176]. The latter applications inspired utilisation of the tile concept in modelling materials with random heterogeneous microstructures [15].

Currently, characterization of a microstructural geometry in a compressed form is mostly based on a Periodic Unit Cell (PUC) representation (under different names such as Repeating Unit Cell [46], Statistically Similar Representative Volume Element [12], Statistically Optimal Representative Unit Cell [11], or Statistically Equivalent Periodic Unit Cell [10]). Although such compression is lossless only for a narrow range of materials with

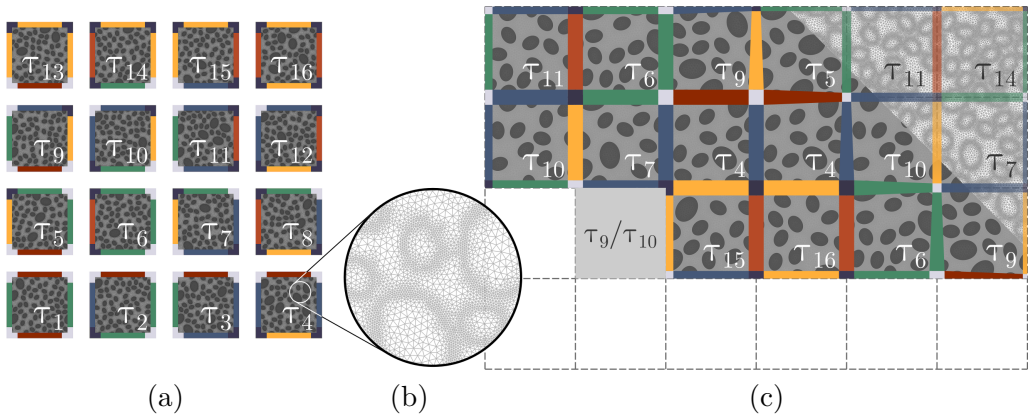

Figure 6.2.1: (a) A set of Wang tiles with the compressed microstructural representation used in the work (including a detail of the finite element discretization in (b)) and (c) an illustration of a step in the tiling procedure (with partially assembled microstructural geometry and finite element discretization). In the next step of the assembly algorithm, either τ_9 or $\tau_1 0$ will be placed at the position highlighted in grey.

a periodic arrangement of constituents, the modelling error caused by the enforced periodicity and limited variability is negligible in standard concurrent multiscale schemes, such as FE^2 [177]. On the other hand, the PUC-based compression is unsuitable for generating microstructural geometry for macroscale analyses with a fully resolved microstructure for two reasons: (i) it produces only a deterministic sample and (ii) the produced microstructural sample exhibits artificial periodicity. Wang tile concept addresses both drawbacks, and allows to avoid computationally intensive optimization algorithms traditionally used to generate an ensemble of stochastic microstructural samples [10].

In Wang tile concept, a material microstructure is represented with a set of square (or cubical) domains with codes attributed to their edges (or faces). Interior of each tile is designed such that (i) the contained microstructural geometry remains continuous across the parts of tile boundary with the same code and (ii) when assembled following the compatibility constraints posed by the codes, the resulting tile assembly resembles the original microstructure; see the illustration in Fig. 6.2.1.

So far, three design strategies have been proposed: an optimization approach to minimize a discrepancy between spatial statistics of the reference specimen and generated assemblies [15], a sample-based strategy [21], and a level-set based framework for particulate and foam-like microstructures [43]. However, most of the methods developed for generating PUC can in principle be modified to take the generalized periodicity constraints of Wang tiles into account.

Unlike mathematicians that focus mainly on tile sets for strictly aperiodic tiling, see the overview in [28, Chapter 11], we prefer stochastic tile sets introduced by Cohen et al. [17] because these sets perform better in terms of suppressing periodic artefacts [21, 43] and are less constrained in their construction. Using the assembly algorithm described next, a sufficient condition for a tile set is that it contains at least one tile for each admissible code combination on the left and top tile edges. Otherwise, number of tiles and code distribution within the set can be chosen arbitrary, e.g., to control the distribution of individual tile types in the assembled tilings. Individual microstructural samples are generated with a stochastic assembly algorithm that sequentially fills a grid of a predefined size with tile instances from the set. For each positions in the grid, the algorithm identifies potential

candidate tiles from the set based on the codes of previously placed neighbouring tiles, randomly selects one tile from the candidates, places it, and proceeds to the next grid position. A step of the assembly algorithm is shown in Fig. 6.2.1.

In the perspective of Liu and Shapiro [9], who define a model of a material microstructure as a process capable of generating microstructural samples with similar spatial statistics, Wang tile concept can be seen as a reduced model with spatially local modes (with PUC being a trivial instance with one mode only). Characteristic microstructural information is compressed into the set of tiles in the offline phase, while geometries of individual microstructural samples are generated almost instantly when required. The tile-based representation thus can be advantageously used in. e.g., analyses of the Representative Volume Element (RVE) size [75, 86]. The concept can also serve as a microstructural generator for Monte-Carlo-based simulations investigating the influence of microstructural variability on a macroscopic response.

6.3 Extracting characteristic fluctuation fields

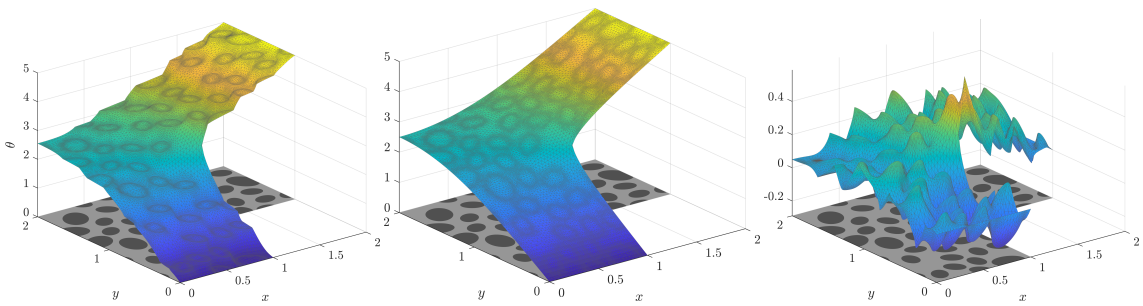

Figure 6.3.1: Decomposition of (a) a Direct Numerical Solution resolving all microstructural details into (b) a homogeneous part and (c) fluctuations caused by the presence of heterogeneities.

The idea of approximating fluctuation fields in microstructural samples generated by means of Wang tiles was first outlined in Novák et al. [16]; see Fig. 6.3.1 for an illustration of a fluctuation field. Aiming at stress enrichments for Hybrid-Trefftz finite element formulation such as [178], Novák et al. proposed extracting tile-wise defined fields from a response of a selected tiling to a prescribed macroscopic strain under periodic boundary conditions. Continuity of traction forces across the corresponding tile edges was incorporated in the objective function during the optimisation-based tile design, resulting in a trade-off between randomness in the system and traction jumps [16].

Here, we present a method for extracting the characteristic response of a compressed system in primal variables. Unlike [16], the tile-wise defined fields are continuous across the corresponding edges by construction and the methods is non-intrusively applicable to existing microstructural compressions. Our only assumption is that the finite element discretization of individual tile domains $\Omega^{\mathcal{T}}$ is geometrically compatible across the edges with the same code.

We illustrate the method with a scalar, elliptic problem represented by heat conduction. Combining the Fourier law

$$q(\boldsymbol{x}) = -\boldsymbol{K}(\boldsymbol{x})\boldsymbol{\nabla}\theta(\boldsymbol{x})\,, \quad \forall \boldsymbol{x} \in \Omega\,, \tag{6.1}$$

which links temperature θ and heat flux q fields in a given domain Ω via a conductivity tensor $\boldsymbol{K}$, with the conservation of the heat flux (neglecting any heat sources and sinks)

$$\boldsymbol{\nabla} \cdot q(\boldsymbol{x}) = 0 \tag{6.2}$$

yields the governing equation

$$-\boldsymbol{\nabla} \cdot (\boldsymbol{K}(\boldsymbol{x}) \boldsymbol{\nabla} \theta(\boldsymbol{x})) = 0\,. \tag{6.3}$$

Similarly to the ansatz traditionally used in computational homogenization, we assume that a solution field for each tile $\mathcal{T}$ in a tile set $\mathcal{S}$ can be decomposed using a Taylor expansion into a macroscopic part controlled by a prescribed macroscopic (potentially higher-order) gradients and the fluctuation part caused by the presence of heterogeneities in the microstructure. Restricting ourself to the second-order Taylor polynomial, we assume the temperature field $\theta(\boldsymbol{x})$ in the form

$$\theta(\boldsymbol{x}) = \boldsymbol{G}^{(1)} \cdot \boldsymbol{x} + \frac{1}{2} \boldsymbol{x} \cdot \boldsymbol{G}^{(2)} \cdot \boldsymbol{x} + \tilde{\theta}(\boldsymbol{x})\,,\ \forall \boldsymbol{x} \in \Omega^{\mathcal{T}},\ \forall \mathcal{T} \in \mathcal{S}, \tag{6.4}$$

where $\boldsymbol{G}^{(i)}$ is the prescribed ith-order macroscopic gradient playing the role of loading and $\tilde{\theta}(\boldsymbol{x})$ is the fluctuation complement.

Following the standard finite element procedures for solving the weak form of Eq. (6.3), we construct a stiffness matrix for each tile independently, and we reorder and split the unknowns u into interior, u_i, and exterior, u_e, ones.

$$\begin{bmatrix} \mathsf{K}^{\mathcal{T}}_{ee} & \mathsf{K}^{\mathcal{T}}_{ee} \\ \mathsf{K}^{\mathcal{T}}_{ee} & \mathsf{K}^{\mathcal{T}}_{ee} \end{bmatrix} \begin{bmatrix} \mathsf{u}^{\mathcal{T}}_e \\ \mathsf{u}^{\mathcal{T}}_i \end{bmatrix} = \begin{bmatrix} \mathsf{f}^{\mathcal{T}}_e \left(\boldsymbol{G}^{(1)}, \boldsymbol{G}^{(2)} \right) \\ \mathsf{f}^{\mathcal{T}}_i \left(\boldsymbol{G}^{(1)}, \boldsymbol{G}^{(2)} \right) \end{bmatrix} \tag{6.5}$$

Note that the force term is induced by the prescribed macroscopic gradients and the degrees of freedom (DOFs) correspond to the fluctuation part of the ansatz Eq. (6.4). The interior DOFs are then condensed out, leaving us with effective stiffness matrix $\hat{\mathsf{K}}^{\mathcal{T}}$ and load vector $\hat{\mathsf{f}}^{\mathcal{T}}$ for each tile:

$$\hat{\mathsf{K}}^{\mathcal{T}} = \mathsf{K}^{\mathcal{T}}_{ee} - \mathsf{K}^{\mathcal{T}}_{ei} \mathsf{K}^{\mathcal{T}\,-1}_{ii} \mathsf{K}^{\mathcal{T}}_{ie}\,, \tag{6.6}$$

$$\hat{\mathsf{f}}^{\mathcal{T}} = \mathsf{f}^{\mathcal{T}}_e - \mathsf{K}^{\mathcal{T}}_{ei} \mathsf{K}^{\mathcal{T}\,-1}_{ii} \mathsf{f}^{\mathcal{T}}_i\,, \tag{6.7}$$

where the explicit dependence on the macroscopic gradients was omitted for the sake of brevity.

In order to enforce continuity of the solution across individual tiles, the remaining boundary DOFs are consistently renumbered and assembled into u^s such that the corresponding DOFs at edges with the same code share the same number throughout the tile set. While uniquely enumerating DOFs that belong exclusively to a tile edge is straightforward, enumerating vertex DOFs requires an analysis of the tile set outlined in [43, Section 2.3] in order to identify how many unique DOFs are needed for the vertices. Depending on the code distribution within the set, it may happen that certain vertices will never coincide during the tile assembly, thus constituting separate vertex group with distinct DOFs. This typically happens for tile sets derived from the vertex-defined Wang tiles [91]. In the three-dimensional setting, where individual Wang tiles are defined by codes attributed to domain faces, a similar analysis must be performed also for edge DOFs; see [43, Section

2.3] for details.

Finally, treating each tile as a macro-element, the tile effective stiffness matrices and loading vectors are assembled according to the DOF numbering,

$$\mathsf{K}^{\mathcal{S}} = \mathop{\mathsf{A}}_{\mathcal{T}\in\mathcal{S}} \hat{\mathsf{K}}^{\mathcal{T}} \quad \text{and} \quad \mathsf{f}^{\mathcal{S}} = \mathop{\mathsf{A}}_{\mathcal{T}\in\mathcal{S}} \hat{\mathsf{f}}^{\mathcal{T}}\,, \tag{6.8}$$

forming a system that encodes a collective response of all tiles in the set to a prescribed loading,

$$\mathsf{K}^{\mathcal{S}}\mathsf{u}^{\mathrm{s}} = \mathsf{f}^{\mathcal{S}}\,. \tag{6.9}$$

Without loss of generality, we assume all tile domains are centred, making them virtually stacked one atop each other. However, their interaction is facilitated only through the shared DOFs.

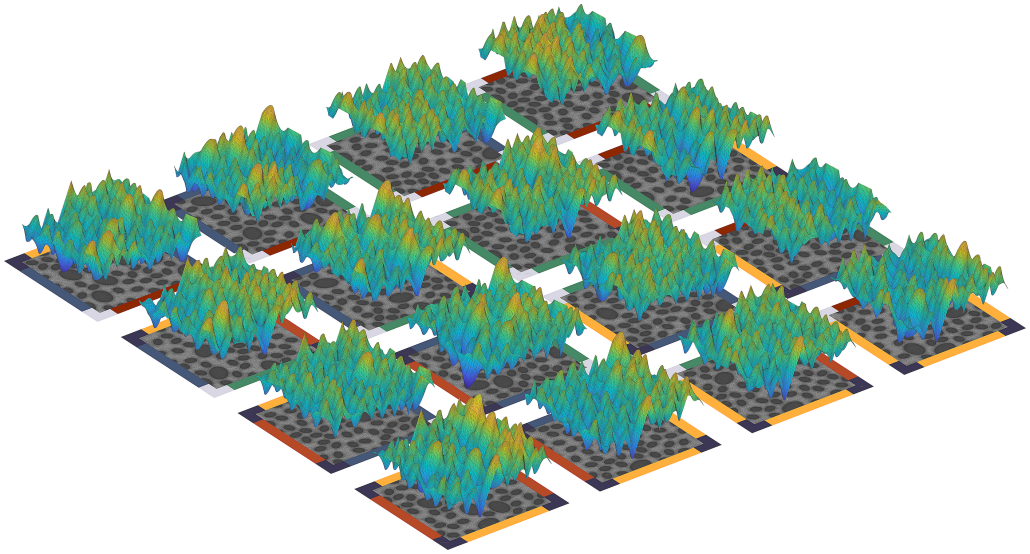

Figure 6.3.2: An example of a tile-wise defined fluctuation field obtained for $\boldsymbol{G}^{(1)} = \begin{bmatrix}0.6 & 0.3\end{bmatrix}^{\mathsf{T}}$ and considering Eq. (6.13) only.

6.3.1 Constraints

The assembled set problem, Eq. (6.9), must be equipped with additional constraints. First, the problem is ill-posed because it contains a zero-energy mode. This can be fixed either by prescribing a value for one DOF or by imposing the average value constraint

$$\int_{\Omega^{\mathcal{S}}} \tilde{\theta}(\boldsymbol{x})\,\mathrm{d}\boldsymbol{x} = 0\,, \tag{6.10}$$

where $\Omega^{\mathcal{S}} = \bigcup_{\mathcal{T}\in\mathcal{S}} \Omega^{\mathcal{T}}$.

Second, additional constraints are needed to prevent the fluctuation field from compensating for the prescribed loading. This corresponds to prescribing suitable boundary conditions at the microscale problem in the computational homogenization, e.g. [170].

In the standard first-order computational homogenization, the fluctuation field $\tilde{\theta}$ is required to satisfy

$$\int_{\Omega} \boldsymbol{\nabla}\tilde{\theta}\,\mathrm{d}\boldsymbol{x} = \int_{\partial\Omega} \tilde{\theta}\boldsymbol{n}\,\mathrm{d}s = \boldsymbol{0}\,, \tag{6.11}$$

where $\boldsymbol{n}$ denotes the outer normal to the RVE domain boundary $\partial\Omega$. This is typically ensured either with the uniform Dirichlet, periodic, or uniform Neumann type of boundary conditions. Albeit the particular selection is a modelling choice, periodic boundary conditions are the most frequent due to their fastest convergence of effective properties with respect to the size of an RVE, e.g. [82].

Loosely inspired, we implement the following three options:

i) We set all fluctuation DOFs to zero at the tile boundaries,

$$\tilde{\theta}|_{\partial\Omega^{\mathcal{T}}} = 0\,, \quad \forall\mathcal{T} \in \mathcal{S}\,; \tag{6.12}$$

ii) We enforce vanishing gradient of the fluctuation field tile-wise,

$$\int_{\partial\Omega^{\mathcal{T}}} \tilde{\theta}\boldsymbol{n}\,\mathrm{d}s = \boldsymbol{0}\,, \quad \forall\mathcal{T} \in \mathcal{S}\,; \tag{6.13}$$

iii) We require zero gradient of $\tilde{\theta}$ within the tile set on average,

$$\int_{\partial\Omega^{\mathcal{S}}} \tilde{\theta}\boldsymbol{n}\,\mathrm{d}s = \boldsymbol{0}\,, \tag{6.14}$$

where $\partial\Omega^{\mathcal{S}} = \bigcup_{\mathcal{T}\in\mathcal{S}} \partial\Omega^{\mathcal{T}}$, similarly to Eq. (6.10).

Treating second-order gradients is more involved. Since we assume the classical first-order constitutive and conservation equations and we want to pose the extraction of characteristic modes as a boundary value problem, we cannot straightforwardly enforce a direct analogue of Eq. (6.11) for the second-order gradient. Addressing this limitation in the finite strain setting, Kouznetsova et al. [121, 179] derived a condition on the fluctuation part of the solution that ensure the equality between the prescribed second-order gradient and its average over a Periodic Unit Cell, see [121, Appendix A]. Adapted to the illustrative problem of heat conduction, Kouznetsova et al.'s condition reads

$$\int_{\partial\Omega} \tilde{\theta}\,(\boldsymbol{x}\otimes\boldsymbol{n} + \boldsymbol{n}\otimes\boldsymbol{x})\,\mathrm{d}s = \boldsymbol{0}\,, \tag{6.15}$$

where $\otimes$ denotes the vector outer product defined in the index notation as $(\boldsymbol{n}\otimes\boldsymbol{x})_{ij} = n_i x_j$.

Similarly to the previous paragraph, constraint (6.15) can be ensured

i) point-wise (leading to the same constraints as in Eq. (6.12)),

ii) tile-wise

$$\int_{\partial\Omega^{\mathcal{T}}} \tilde{\theta}\,(\boldsymbol{x}\otimes\boldsymbol{n} + \boldsymbol{n}\otimes\boldsymbol{x})\,\mathrm{d}s = \boldsymbol{0}\,, \quad \forall\mathcal{T} \in \mathcal{S}\,, \tag{6.16}$$

iii) set-wise

$$\int_{\partial\Omega^{\mathcal{S}}} \tilde{\theta}\,(\boldsymbol{x}\otimes\boldsymbol{n} + \boldsymbol{n}\otimes\boldsymbol{x})\,\mathrm{d}s = \boldsymbol{0}\,. \tag{6.17}$$

Note that, unlike the finite strain problem in [121, Appendix A], the second order gradient for the scalar problem is by definition symmetric. Hence, conditions (6.16) and (6.17) constitute only three constraints for a two-dimensional scalar problem.

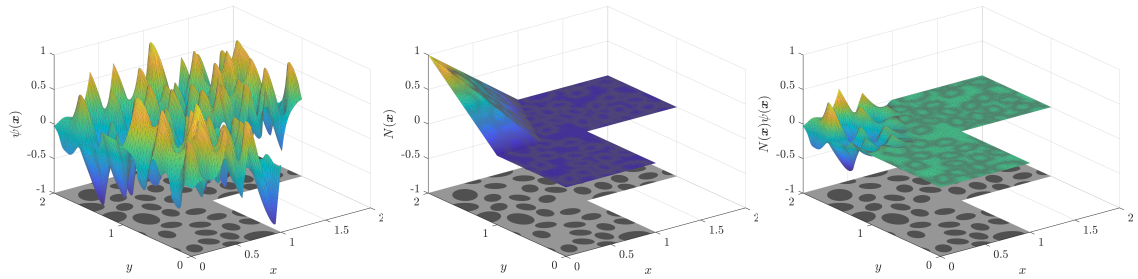

(a) (b) (c)

Figure 6.3.3: Illustration of (a) a global approximation $\psi(\boldsymbol{x})$ assembled from the tile-wise defined fluctuation field, (b) a standard macroscopic shape function $N(\boldsymbol{x})$ used as a Partition of Unit function in Generalized Finite Element Method, and (c) the final microstructure-informed reduced mode $N(\boldsymbol{x})\psi(\boldsymbol{x})$.

All constraints introduced above are linear in the fluctuation field $\tilde{\theta}$. Therefore, within the finite-element implementation, they can be recast to the form

$$\mathsf{C}\mathsf{u} = \mathsf{0}\,, \quad \text{with} \quad \mathsf{C} = \begin{bmatrix} \mathsf{C}_0 \\ \mathsf{C}_\mathrm{I} \\ \mathsf{C}_\mathrm{II} \end{bmatrix}\,, \tag{6.18}$$

where C_0, C_I, and C_II are related to the elimination of the zero-energy mode, and enforcing first- and second-order gradients, respectively.

However, depending on the particular constraint choice and the distribution of edge codes with the tile set, matrix C can be rank-deficient. This deficiency arises in several situations. For instance, a tile with periodic codes (i.e. the same codes on the opposite edges) automatically satisfies Eq. (6.13). In a similar manner, a tile set with an equal occurrence of individual codes on opposite edges yields trivial C_I for Eq. (6.14).

In principle, it is possible to list all such situations and handle them during the assembly of matrix C. Yet, in order to avoid an involved analysis of codes in a tile set and complicated assembly, we perform the singular value decomposition of the rank-deficient matrix C and replace it with $\hat{\mathsf{C}}$ containing of the right-singular vectors related to non-zero singular values as its rows.

Ultimately, the modified constraints represented by $\hat{\mathsf{C}}$ are enforced via Lagrange multipliers λ, forming the final saddle-point problem

$$\begin{bmatrix} \mathsf{K}^{\mathcal{S}} & \hat{\mathsf{C}}^{\mathsf{T}} \\ \hat{\mathsf{C}} & \mathsf{0} \end{bmatrix} \begin{bmatrix} \mathsf{u}^{\mathrm{s}} \\ \lambda \end{bmatrix} = \begin{bmatrix} \mathsf{f}^{\mathcal{S}} \\ \mathsf{0} \end{bmatrix}\,. \tag{6.19}$$

Once solved for the exterior DOFs u^{s} common to all tiles, the remaining interior DOFs follow from back-substitution[1] in Eq. (6.5),

$$\mathsf{u}_i^{\mathcal{T}} = \mathsf{K}_{ii}^{\mathcal{T}\,-1} \left(\mathsf{f}_i^{\mathcal{T}} - \mathsf{K}_{ie}^{\mathcal{T}} \mathsf{u}_e^{\mathcal{T}} \right)\,. \tag{6.20}$$

[1] In the case of zero fluctuations prescribed at tile boundaries, i.e. Eq. (6.12), the above described treatment is only formal. In practice, solving Eq. (6.19) is skipped, and only the interior DOFs are sought for because no information is effectively communicated across individual tiles.

6.3.2 Field options

In the illustrative linear two-dimensional problem, five basic macroscopic loading cases—consecutively prescribing a unit value to the individual components of the first- and second-order macroscopic gradient, respectively—suffice. Each load case is further complemented with one of the constraint options mentioned above. Unlike in computational homogenization, where a particular type of boundary conditions is assumed a priori, we combine the characteristic responses of the compressed system extracted for different constraint options in order to enrich the basis for the fluctuation approximation.

While this approach allows for a range of combinations regarding which gradients are prescribed and restricted, we consider only three choices for the rest of the paper, labelled as 1^{st}, $1^{\text{st}} \vee 2^{\text{nd}}$, and $1^{\text{st}} \wedge 2^{\text{nd}}$, respectively. The first choice denotes the fluctuation fields extracted by prescribing and constraining only the first-order macroscopic gradient, i.e. $\boldsymbol{G}^{(2)} = \boldsymbol{0}$ and only the constraints (6.12)–(6.14) are considered. The second choice stands for the case where the first and second-order macroscopic gradients were prescribed independently, i.e. extending the set of fields from the previous choice with additional ones obtained similarly by setting $\boldsymbol{G}^{(1)} = \boldsymbol{0}$ and prescribing only the second-order gradient along with constraints (6.12), (6.16), or (6.17). Finally, the last choice corresponds to the setup in which both gradients are prescribed simultaneously and all constraints are successively imposed.

The first option thus results in six fluctuation fields (two unit loading cases and three constraint types), while the latter two yield 15 fluctuation fields.

6.4 Macroscopic numerical scheme

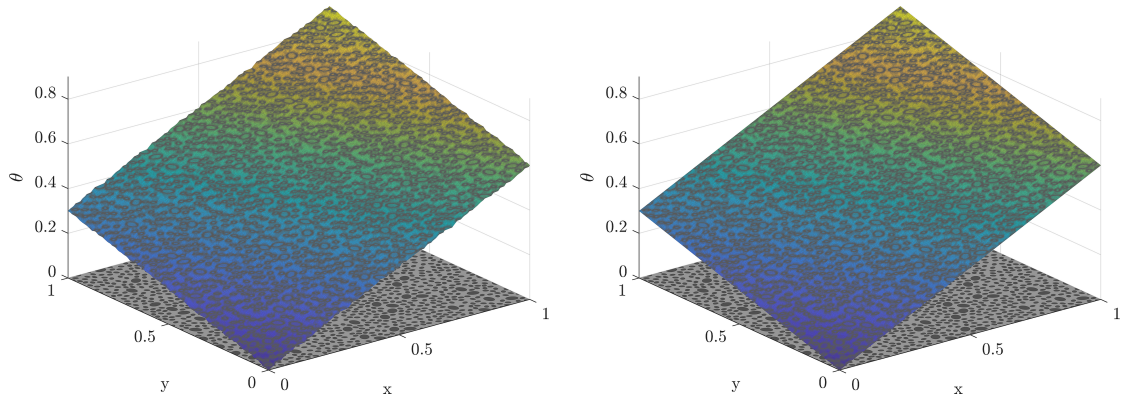

Figure 6.4.1: The resulting temperature field θ from a Direct Numerical Simulation (DNS) of a square domain with a microstructure assembled from 5×5 tiles and subjected to a macroscopic temperature gradient $\begin{bmatrix} 0.6 & 0.3 \end{bmatrix}^{\mathsf{T}}$ under (a) periodic boundary conditions and (b) Dirichlet boundary conditions.

From the procedure outlined in the previous section, each tile carries a set of tile-wise defined fields, which can be assembled using the same procedure as in generating microstructural geometry in order to define a set of continuous approximation basis functions ψ_i in the macroscopic domain Ω; see Fig. 6.3.3 Note that the tile-wise defined fields

are universal in the sense that they are not extracted with respect to a particular macroscopic geometry or loading; each ψ_i approximates the microstructural response to a constant or linear macroscopic gradient. However, the general macroscopic problem (with arbitrary geometry and loading) usually does not yield a uniform macroscopic gradient in the domain. Thus, the macroscopic numerical scheme must be able to locally interpolate between individual ψ_i basis functions.

To facilitate such interpolation, we resort to the Generalized Finite Element Method (GFEM) strategy [180, 181, 182]. We assume two levels of finite element discretization for the macroscopic problem. The first level comprises the fine discretization that comes directly from the tile-wise discretization already used to pre-compute the tile characteristic fluctuation fields. Recall that the individual tile discretizations must be geometrically and topologically compatible for the strategy outlined in Section 6.3 to work. Hence, these discretizations can be assembled along with the microstructural geometry, yielding n^f shape functions $N^f(\boldsymbol{x})$ defining a finite element approximation space $\mathcal{U}^f = \text{span}\{N_i^f\}$, in which ψ_i's are defined, i.e. $\text{span}\,\{\psi_i\} \subset \mathcal{U}^f$.

The second level contains a coarse discretization of the macroscopic domain Ω that does not resolve microstructural features. With n^c shape functions $N_i^c(\boldsymbol{x})$, it serves two purposes: (i) the related approximation space $\mathcal{U}^c$, $\mathcal{U}^c = \text{span}\,\{N_i^c\}$, captures the homogeneous part of the solution (recall that ψ_i approximate only fluctuations caused by material heterogeneity), and (ii) the shape functions form a Partition of Unity basis for interpolating between individual ψ_i's.

Following the GFEM ansatz, we seek a solution to a macroscopic problem in the form

$$\begin{aligned}\theta(\boldsymbol{x}) &= \sum_{i=1}^{n^c} N_i^c(\boldsymbol{x}) a_i^0 + \sum_{i=1}^{n^c}\sum_{j=1}^{n^r} N_i^c(\boldsymbol{x})\psi_j(\boldsymbol{x}) a_i^j \\ &= \sum_{i=1}^{n^c}\sum_{j=0}^{n^r} N_i^c(\boldsymbol{x})\psi_j(\boldsymbol{x}) a_i^j\,, \quad \boldsymbol{x} \in \Omega\,,\end{aligned} \tag{6.21}$$

where n^r denotes the number of provided fluctuation fields and ψ_0 is artificially defined as a constant unit function.

In order to avoid difficulties common to GFEM, namely the questions of imposing essential boundary conditions and numerical integration, we adopt the perspective of Reduced Order Modelling. We benefit from the availability of the fine discretization of the macroscopic domain; plugging the fine discretization in the form

$$\theta(\boldsymbol{x}) = \sum_{i=1}^{n^f} N_i^f(\boldsymbol{x}) u_i\,, \quad \boldsymbol{x} \in \Omega\,, \tag{6.22}$$

the weak form of Eq. (6.3) yields the standard, fine-scale system of linear equations

$$\mathsf{K}^f \mathsf{u} = \mathsf{f}^f\,. \tag{6.23}$$

However, instead of solving Eq. (6.23), we approximate

$$\mathsf{u} \approx \Phi\,\mathsf{a}\,, \tag{6.24}$$

where the matrix $\Phi \in \mathbb{R}^{n^f \times n^c(n^r+1)}$ collects as its columns the individual products $N_i^c(\boldsymbol{x})\psi_j(\boldsymbol{x})$ from Eq. (6.21) projected onto $\mathcal{U}^f$, and a contains the related a_i^j DOFs. The final reduced

system to solve thus follows from the Galerkin projection,

$$\underbrace{\Phi^{\mathsf{T}}\mathsf{K}^{f}\Phi}_{\mathsf{K}^{r}}\ \mathsf{a} = \underbrace{\Phi^{\mathsf{T}}\mathsf{f}^{f}}_{\mathsf{f}^{r}}, \tag{6.25}$$

where the projection supersedes numerical integration in the standard GFEM.

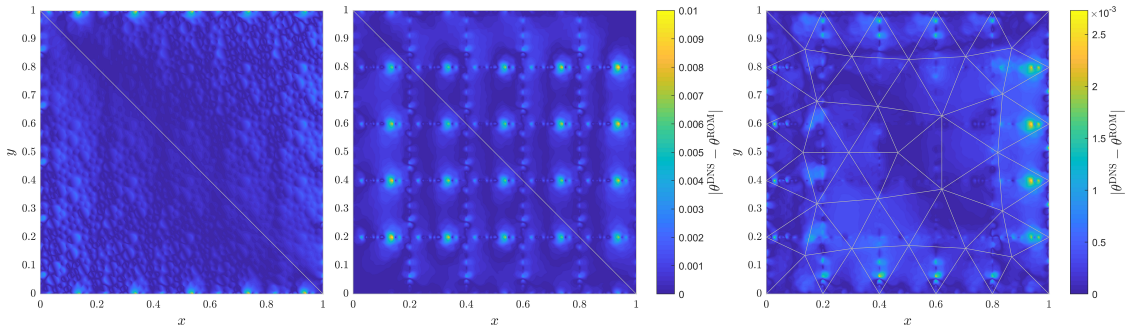

(a) (b) (c)

Figure 6.4.2: The magnitude of discrepancy between the direct numerical simulation and the result of the proposed reduced scheme for a square domain with periodic microstructure: a two-element coarse discretization (a) with only selected fluctuation fields obtained under the periodic constraint Eq. (6.13) and (b) with the all fluctuation fields labelled 1^{st}, and (c) a refined discretization with all fluctuation fields considered. Edges of the macroscopic discretization are plotted in the light grey colour.

Regarding the imposition of essential boundary conditions at the macroscale, we exclude the prescribed DOFs from Φ. Their presence is then indirectly imposed by the action of relevant elements. Consequently, the unknown a_i^j's corresponding to macroscopic elements influenced by the prescribed values are not set to zero by construction.

Note also that the projection strategy enables trivial switching to fully resolved microstructural details in parts of the macroscopic domain when desired, see Section 6.5.2.1.

6.5 Numerical examples

For the numerical examples in this section, we used the two-dimension set of 16 Wang tiles depicted in Fig. 6.2.1. Geometry of each tile was discretized using linear triangular elements. On average, each tile contained approximately 25,500 DOFs and 50,500 elements, which are refined along the inclusion boundaries.

Both material phases (depicted in light and dark grey) are considered as linear isotropic with conductivities $\boldsymbol{K} = 10\boldsymbol{I}$ for the matrix phase and $\boldsymbol{K} = 100\boldsymbol{I}$ for the inclusion phase, respectively, where $\boldsymbol{I}$ denotes the second-order identity tensor.

6.5.1 Uniformly loaded square sample

As the first example, we considered a simple square domain composed of five tiles in each direction with the size of the domain scaled to unity. The domain was loaded with a uniform macroscopic gradient $\begin{bmatrix}0.6 & 0.3\end{bmatrix}^{\mathsf{T}}$ with boundary conditions similar to the standard first-order computational homogenization: periodic and Dirichlet ones, see Fig. 6.4.1.

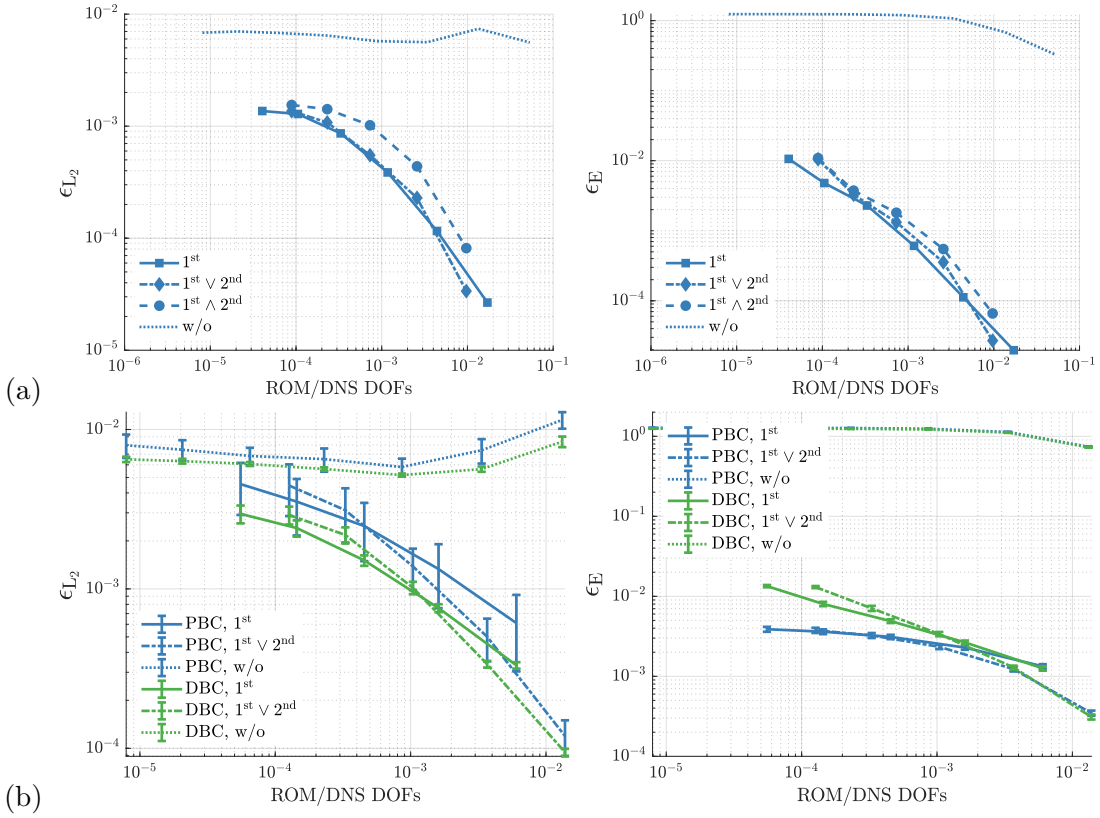

Figure 6.5.1: Evolution of the relative L_2-norm error (ϵ_{L_2}) and the relative error in energies (ϵ_E) with a uniform refinement of the macroscopic discretization for the simple square domain with (a) a periodically repeating microstructure under the Dirichlet boundary conditions and (b) a microstructure assembled from the set of 16 tiles under both periodic and Dirichlet boundary conditions. Average and the standard deviation of results obtained for 50 different realizations are plotted in (b). Data labels correspond to the different choices of fluctuation fields: 1^{st} denotes the fields extracted with prescribing only the first-order macroscopic gradient; $1^{st} \vee 2^{nd}$ and $1^{st} \wedge 2^{nd}$ stand for the case when the first and second-order macroscopic gradients were prescribed independently or simultaneously, respectively. Additionally, a case when no fluctuation fields are considered (labelled w/o) is plotted for comparison.

6.5.1.1 PUC

As a sanity check, we first tested the proposed framework with a trivial case of a Wang tile set—a Periodic Unit Cell. The self-compatible tile 16 from the set shown in Fig. 6.2.1 was chosen as the PUC and the microstructure-informed modes were recomputed considering only this tile. Note that in the particular case of PUC, the tile-wise and set-wise constraints coincide and thus only one has to be considered in order to avoid ill-posedness of the reduced problem.

As expected, due to the linearity of the problem, the proposed reduced numerical scheme (ROM) yields exactly the same results as the Direct Numerical Simulation (DNS) even for a very coarse macroscopic discretization containing two elements, depicted in Fig. 6.4.2a, when the periodic boundary conditions are assumed. Moreover, only the fluctuation modes extracted under the periodic constraints and the first order macroscopic

gradient, Eq. (6.13), are sufficient in this case. However, the same conclusions do not hold when a domain with the same periodically repeating microstructure is subjected to the macroscopic gradient under the Dirichlet boundary conditions.

In such a case, the numerical scheme only approximates the reference solution. Figure 6.4.2a illustrates the discrepancy between DNS and ROM solutions with the coarsest macroscopic discretization (which was sufficient for the previous loading) and only the modes extracted under periodic constraints. Enriching the approximation space with fluctuation fields obtained under the Dirichlet-type constraints localizes the solution discrepancy predominantly to the tile edges; see Fig. 6.4.2b. The local difference both in its magnitude and localization can be further improved by refining the macroscopic discretization, e.g. Fig. 6.4.2c.

In addition to the local discrepancy, we quantify the error of ROM solution using (i) a relative L_2-norm of the results difference,

$$\epsilon_{L_2} = \frac{\|\theta^{\mathrm{DNS}} - \theta^{\mathrm{ROM}}\|_{L_2}}{\|\theta^{\mathrm{DNS}}\|_{L_2}}\,, \tag{6.26}$$

where

$$\|\theta\|_{L_2} = \left(\int_\Omega \theta^2(\boldsymbol{x})\,\mathrm{d}\boldsymbol{x}\right)^{\frac{1}{2}}\,, \tag{6.27}$$

and (ii) a relative error in energy,

$$\epsilon_E = \frac{|E^{\mathrm{DNS}} - E^{\mathrm{ROM}}|}{E^{\mathrm{DNS}}}\,, \tag{6.28}$$

with

$$E^\bullet = \int_\Omega \frac{1}{2}\boldsymbol{\nabla}\theta^\bullet(\boldsymbol{x}) \cdot \boldsymbol{K}(\boldsymbol{x}) \cdot \boldsymbol{\nabla}\theta^\bullet(\boldsymbol{x})\,\mathrm{d}\boldsymbol{x}\,. \tag{6.29}$$

Figure 6.5.1a illustrates the evolution of these errors with a uniform refinement of the macroscale discretization. The results are shown for three choices of fluctuation fields: 1^{st}, $1^{\mathrm{st}} \vee 2^{\mathrm{nd}}$, and $1^{\mathrm{st}} \wedge 2^{\mathrm{nd}}$; recall their definition in Section 6.3.2. In addition, the results for a case when no fluctuation fields are assumed is also plotted (labelled as w/o) in order to illustrate the influence of fluctuation fields.

6.5.1.2 Set of 16 tiles

Finally, the same analysis is repeated for a domain with a microstructure assembled from the tile set instead of a PUC. The global errors shown in Fig. 6.5.1b were obtained as an average over 50 stochastic realizations. Results for both the periodic and Dirichlet boundary conditions and different fluctuation field choices are reported. For the sake of brevity, we omit $1^{\mathrm{st}} \wedge 2^{\mathrm{nd}}$ fluctuation field choice in Fig. 6.5.1b because its results were very close to those of $1^{\mathrm{st}} \vee 2^{\mathrm{nd}}$.

6.5.2 L-shape domain

As the second example, we chose an L-shaped domain with values $\hat{\theta}_b = 0$ and $\hat{\theta}_r = 5$ prescribed at the bottom and right part of the domain, respectively; see the illustration in Fig. 6.5.2. The domain was scaled such that its both ends had a unit length. However, the number of tiles s along each edge varied, giving a notion of scale separation

of the problem. This time, only the microstructures assembled with Wang tilings were investigated.

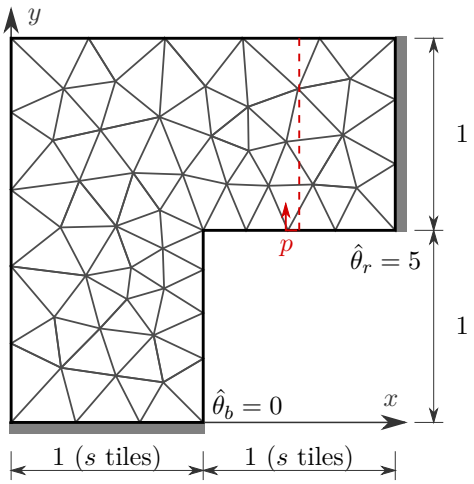

Figure 6.5.2: Illustration of the L-shape domain problem. Values $\hat{\theta}$ are prescribed at the grey-shaded edges. The red dashed line (with the parametrization coordinate p) indicates a cross-section along which the local error profile was extracted. The triangulation depicts the initial discretization for the macroscopic problem.

Similarly to the previous section, we ran 10 realizations for $s \in \{5, 10, 15, 20\}$ with four sequential refinements and different fluctuation field choices, and we recorded the global errors ϵ_{L_2} and ϵ_E; see Fig. 6.5.3. Similarly to the results in Fig. 6.5.1b, only the 1^{st} and $1^{\text{st}} \vee 2^{\text{nd}}$ fluctuation field choices are eventually shown, because the results of $1^{\text{st}} \vee 2^{\text{nd}}$ and $1^{\text{st}} \wedge 2^{\text{nd}}$ were rather similar.

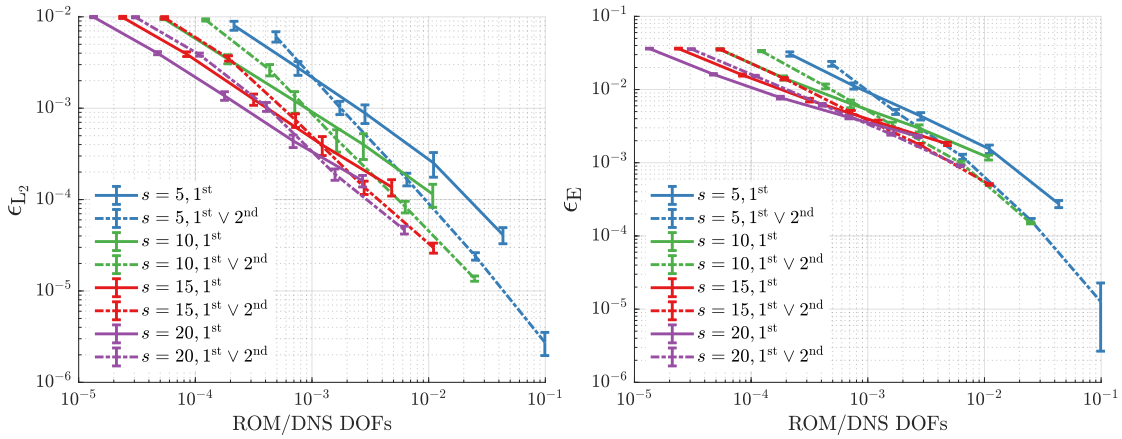

(a) (b)

Figure 6.5.3: Evolution of the relative errors (a) ϵ_{L_2} and (b) ϵ_E in the L-shape domain problem with a uniform refinement of the macroscopic discretization and different combinations of the considered fluctuation fields and values of $s = \{5, 10, 15, 20\}$. The average and standard deviation of the results were obtained from 10 different realizations.

Figure 6.5.4 illustrates the point-wise convergence for one microstructure realization for $s = 5$ with a solution profile along the cross-section depicted in Fig. 6.5.2. The cross-

section was chosen such that it cuts through the centres of tiles. However, similar trends were observed also in the cross-section coinciding with the tile edges.

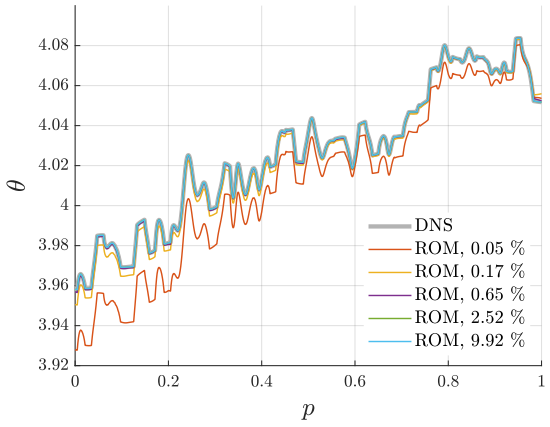

Figure 6.5.4: The point-wise convergence of a solution profile for $s = 5$ along a selected cross-section when uniformly refining the macroscopic discretization.

6.5.2.1 Local refinement

As mentioned in the previous section, adopting the viewpoint of Reduced Order Modelling with GFEM as a mean of constructing the final reduced modes allows for straightforward switching to a discretization resolving all microstructural details in selected regions. As an illustration, Fig. 6.5.5a depicts a solution to the L-shape problem for one realization with $s = 3$. The plot of local differences, Fig. 6.5.5b, reveals that the largest local errors are expectedly concentrated around the re-entrant corner.

Thus, a region containing 3 tiles around the corner was marked for the local refinement and the analysis was repeated. Local errors of this refined model are shown in Fig. 6.5.5c. Global errors reduced from 2.654×10^{-3} to 1.393×10^{-3} for ϵ_{L_2}, and from 1.055×10^{-2} to 5.712×10^{-3} for ϵ_E, respectively. Note that, given the small separation of scales (only 27 tile domains were present in the domain altogether), the local refinement leads to a significant increase in unknowns from 0.14% to 11.16% of all DOFs present in the domain.

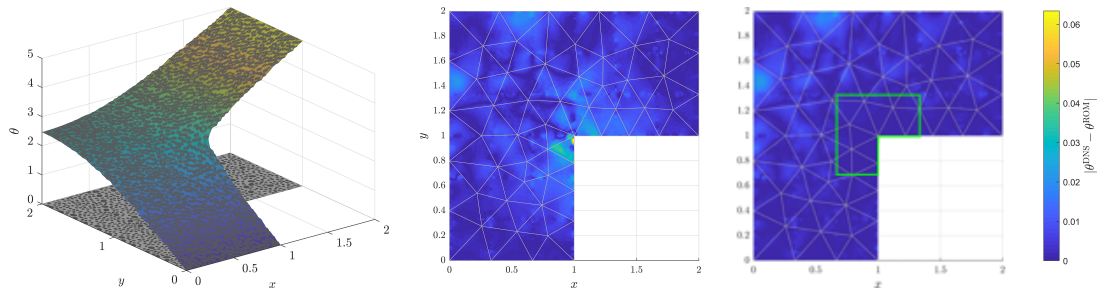

(a) (b) (c)

Figure 6.5.5: An example of (a) a DNS solution for $s = 3$ and the local errors of the reduced scheme without (b) and with (c) the microstructure fully resolved in the highlighted region.

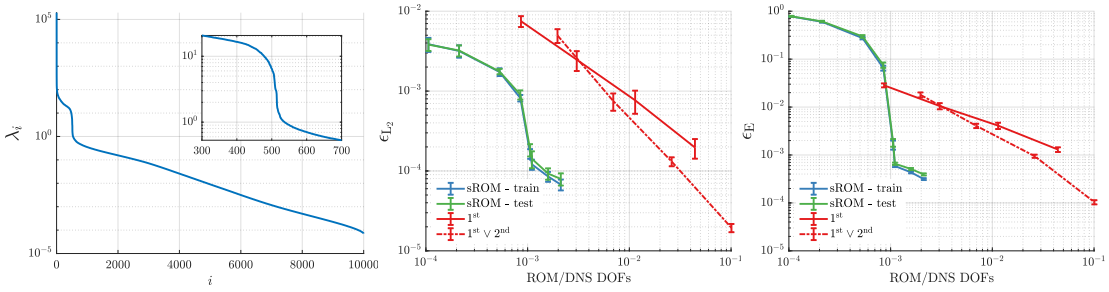

(a) (b) (c)

Figure 6.5.6: Results of the snapshot-based Reduced Order Modelling (labelled as sROM) scheme described in Section 6.5.2.2 for the L-shape domain example with $s = 4$: (a) eigenvalues from Singular Value Decomposition of 10,000 collected snapshots, and the relative (b) L_2-norm error ϵ_{L_2} and (c) error ϵ_E in energies computed for 50 unique microstructure realizations both contained in the snapshots (in blue) and not used in the training phase (in green), compared to the proposed microstructure-informed reduced scheme (in red).

6.5.2.2 Comparison against ROM

In order to put the number of necessary modes into perspective of the classical, snapshot-based Reduced Order Modelling strategy, we devise the following test. While keeping the same microstructural geometry as the one shown in Fig. 6.2.1, we replace the unstructured finite element discretization with a regular, pixel-based mesh, in which two triangular elements with alternating orientation constitute one pixel. Each tile is then represented with 100×100 nodes and 19,602 elements. Consequently, each microstructural realization features the same discretization and hence solutions of the illustrative L-shape domain example can be straightforwardly stored as a snapshot without the need for a remapping/projection onto a fixed mesh.

We generate 10,000 distinct microstructural realizations for the L-shape domain with $s = 4$ and solve the temperature field for each. We then perform Singular Value Decomposition for the matrix containing individual snapshots as its columns; Fig. 6.5.6a displays the eigenvalue magnitudes. Next, we replace the GFEM-based microstructure-informed modes Ψ in the analysis with n eigenmodes corresponding to n largest eigenvalues and compute the response of the compressed system for $n \in \{50, 100, 250, 400, 500, 550, 1000\}$ and plot the global errors ϵ_{L_2} and ϵ_E in Figures 6.5.6a and 6.5.6b, respectively. The errors of the snapshot-based ROM are also compared with the scheme proposed in this work applied to the above mentioned discretization.

6.6 Conclusions

Incorporating the pre-computed fluctuation fields as a basis for constructing the problem-specific microstructure-informed reduced modes enables analyses of models with fully resolved microstructural details with a fraction of degrees of freedom compared to the fully detailed model The comparison against the coarse discritization without enrichments, recall Fig. 6.5.1, clearly demonstrates that a similar reduction in unknowns cannot be achieved without the modes, which efficiently approximate the local character of the solution. Even for the coarsest discretizations with four orders of magnitude fewer DOFs than the fully resolved models, both the relative global errors ϵ_{L_2} and ϵ_E were already below

3% in all examples.

Higher accuracy can be achieved in two ways: (i) by considering more fluctuation fields when constructing the microstructure-informed reduced modes, recall Eq. (6.21), or (ii) by refining the coarse discretization of the macroscopic domain. Irrespectively whether the domain is loaded in such a way it exhibits a constant (Section 6.5.1) or varying (Section 6.5.2) macroscopic gradient, the benefits of refining the discretization while assuming only 1^{st} fluctuation fields prevail only to a certain threshold. With the size of macroscopic elements below the size of a tile, adding the fluctuation fields obtained also for the second-order macroscopic gradient results in lower errors and better convergence rate. Interestingly, the convergence rate of ϵ_{L_2} was almost identical for 1^{st} case in all tested values of s, while it exhibited dependence on s in $1^{\text{st}} \vee 2^{\text{nd}}$ case of ϵ_{L_2} and in both cases of ϵ_E.

Except for the simplest example of a uniformly loaded domain with periodic microstructure, we also observed only a minor difference between the fluctuation fields obtained for the first- and second-order macroscopic gradient prescribed separately ($1^{\text{st}} \vee 2^{\text{nd}}$) or simultaneously ($1^{\text{st}} \wedge 2^{\text{nd}}$), with the latter option slightly outperforming the former for refined macroscopic discretizations.

Local discrepancy between the reduced models and DNS appears in two forms. First, more uniformly distributed discrepancy arises from an insufficiently coarse macroscopic discretization unable to capture the overall kinematics of the problem, see Fig. 6.5.5b. The straightforward remedy here is to refine the dicretization. For instance, the local solution profile in Fig. 6.5.4 improves significantly already upon the first refinement; since the second refinement, the solution of the reduced scheme is almost indistinguishable from the direct numerical simulation.

The second form of discrepancy reflects the underlying microstructure and stems from an inaccurate approximation by the pre-computed fluctuation fields; compare e.g. Figures 6.4.2a and 6.4.2b. Taking into account more fluctuation fields improves this local errors. Yet, because the number of fluctuation fields is limited, some errors will always linger (albeit with a diminishing magnitude). The lingering erros localize mainly along tile boundaries, where the effect of the modelling assumptions during the extraction of the fluctuation fields is the most pronounced.

Finally, the solution of the reduced model can be further enhanced by resorting to the fine, microstructure-resolving discretization in selected parts of the macroscopic domain as demonstrated in Section 6.5.2.1; see also Fig. 6.5.5.

Admittedly, the proposed microstructure-informed reduced scheme requires significantly more degrees of freedom than the standard snapshot-based ROM. Thus, the reported reduction in degrees of freedom may seem unsatisfactory given the fact that we are dealing with a linear, scalar problem. However, despite the linearity, results from Section 6.5.2.2 show that problems with fully resolved stochastic microstructure are inherently high dimensional. Even a very small problem with $s = 4$ and a simplified finite element discretization requires ≈ 500 modes for an acceptable accuracy. Thus, even in the most favourable case, at least 500 simulations with fully resolved microstructures must be performed in order to extract a relevant basis for the snapshots-based Reduced Order Modelling scheme. Note that for the vertex-based tile set considered throughout this work, the L-shape problem with $s = 4$ allows for $2^{65} \approx 3 \times 10^{19}$ unique microstructure realizations; however, the drop threshold in required modes seems to be proportional to the number of tile positions multiplied by tile types, i.e. $48 \times 16 = 768$ in this particular case. Note also that any significant change in macroscopic loading necessitates recalculation of

the basis. By contrast, our fluctuation fields are pre-computed only once at the level of tiles and they can be re-used for different macroscopic analyses when transformed into the microstructure-informed reduced modes using GFEM ansatz.

6.7 Summary

Corroborating the potential that the tiling concept has in modelling heterogeneous materials with stochastic microstructure, we have introduced a numerical scheme which reduces the number of unknowns in macroscopic analyses with underlying microstructural geometry generated from a set of Wang tiles.

Unlike our previous work [15], which approximates stress fields in heterogeneous materials and must be directly incorporated in creating the compressed microstructural representation, we have developed a procedure that extracts primal-unknown fluctuation fields non-intrusively, and can be therefore used with any existing Wang-tile based representation. Inspired by computational homogenization, we extract the characteristic fluctuation fields as a collective responses of individual Wang tiles to a parametrized loading, represented in our case with uniform and linear macroscopic gradients.

Since the extracted fields defined at the tile level are by construction continuous across edges with the same code, they can be assembled within a macroscopic domain in the same manner as the microstructural geometry, creating an approximation for the fluctuation part of the solution providing the macroscopic domain is homogeneously loaded. These approximations are finally transformed into a microstructure-informed reduced modes using the Generalized Finite Element Method's ansatz in order to locally interpolate between individual approximations and thus to adapt to a non-uniform macroscopic loading.

We have illustrated the proposed approach with two numerical examples. Even with a relatively coarse discretization (containing fewer than 0.01% of the unknowns in the unreduced problem), we were able to achieve less then 3% error in the relative L_2-norm and energy difference. We demonstrated that the accuracy is further improved by (i) refining the macroscopic discretization and (ii) considering more pre-computed fluctuation fields. Moreover, the proposed numerical scheme allows for a simple transition to a fully-resolved/high-fidelity model in regions of interest.

Admittedly, compared to the traditional, snapshot-based Reduced Order Modelling scheme, our approach requires more modes for a comparable accuracy. This stems from the fact that, unlike the standard applications where modes are obtained from a very similar macroscopic problems, our modes are pre-computed without any information on the macroscopic geometry or loading. However, we have demonstrated that problems with a fully resolved stochastic microstructure inherently feature a high dimensional solution manifold and, consequently, a relative higher number of training problems must be solved in order to extract accurate basis. Conversely, our pre-computed fields are universal and can be used in various macroscopic analyses.

Even thought the proposed methodology for extracting the characteristic responses and reusing them in macroscopic analyses was illustrated with the simplest case of a two-dimensional, scalar problem, it can be straightforwardly applied to mechanical and three-dimensional applications as well. This only requires replacing the particular form of constraints (Eqs. (6.12)–(6.17)) with a form related to a chosen problem and/or considering the corresponding unit load cases.

The same procedure can be principally also used for a non-linear material response. In such a case, the extraction of fluctuations fields for the unit load cases is insufficient. In-

stead, the space of the parametrized macroscopic loading during the fields' extraction must be carefully explored, e.g. [183], and the pre-computed fields stored and post-processed using, for instance, Proper Orthogonal Decomposition approach [184]. However, applicability of such an approach depends on the number of resulting fields, since too many fields needed to capture the characteristic fluctuations in microstructural response make the reduced model inefficient. Covering material non-linearities within the proposed framework constitutes the next step in our research.

Related to the non-linearities is also a question of numerical efficiency. Common to all reduced order modelling schemes, reducing the number of unknowns does not translate directly to the same reduction in computational times when it comes to non-linear problems. As a remedy, Hyper-reduction [185], Discrete Empirical Interpolation Method [186], any many other methods have been developed to approximate the Galerkin projection in Eq. (6.25) with only a subset of unknowns/quadrature points; see e.g. a brief overview in [187]. Our preliminary tests with Hyper-reduction indicate that modifications of these methods are necessary for our microstructure-informed modes, because these methods have been developed primarily for modes with global support. However, due to the GFEM-based construction, our modes have a local support inherited from the macroscopic discretization. Consequently, the standard strategies for choosing the suitable subset of unknowns do not work in our case. Therefore, efficient implementation and the right choice and modifications of the acceleration methods remains an open question to be investigated in our future work.

Chapter 7

Conclusions and summary

The objective of the thesis was to investigate the applicability of the Wang tile concept in problems related to modelling of materials with random heterogeneous microstructures, elaborating further the initial works of Novák et al. [15, 16].

In the first part of the thesis, two methods for designing Wang tiles were developed. The first method was directly inspired by Cohen et al. [17] and supplemented their approach with a spatial statistics quantification. For each edge code in a tile set, a sample from a reference microstructural specimen was taken. Each tile in the set was then cut out of partially overlapping edge samples arranged such that they corresponded to the tile codes. Consequently, continuity of the compressed representation across the edges with the same code was automatically ensured by a diagonal cut across the code-related samples. In order to enhance the variability of the compressed information, adding a unique patch sample to the interior of each tile was proposed. The optimal parameters of the Image Quilting algorithm used for seamless merging of the overlapping samples were chosen from sensitivity studies that compared errors in spatial statistics of the reference and reconstructed microstructural realizations. As a general rule, an overlap width larger than nine times the characteristic microstructural length was recommended.

While the sample-based design method is computationally very efficient, it is suitable mainly for materials featuring particles embedded in a continuous matrix. When it comes to complex geometries such as foams, the merging algorithm struggles with maintaining continuity of foam ligaments. For this reason, in Chapter 3, the framework of Sonon et al. [18, 19], originally developed for an efficient generation of complex microstructures, was extended. The framework adopted the implicit description of a material microstructure via level-set fields. First, particles were packed in a domain, keeping track of the shortest distance to the nearest particle boundary in order to avoid the critical slowdown of the classical particle packings algorithms when higher volume fractions are desired. Unlike the classical Random Sequential Adsorption method, the level set based modification features linear complexity in the number of packed particles. Second, combining the first-, second-, and third-nearest distance fields enabled straightforward generation of complex, foam-like geometries with additional morphing operations for further tuning of local geometrical features. Several modifications of the original framework were proposed in order to account for the generalized periodicity arising in the tiling concept, allowing us eventually to design Wang tiles with open and closed-cell foam-like microstructures both in two and three dimensions. With a sufficiently robust method for particle packing, the comparison of different tile set in terms of the secondary extremes in two-point correlation function, tentatively outlined already in Chapter 2, was corroborated. This illustrated the superi-

ority of the vertex-based definition of Wang tiles, especially for two-dimensional problem where the resulting tile sets have the same complexity as for their edge-based counterparts. As a by-product of resolving the question of where a particle should be placed when intersecting a tile edge during the packing step, a simple graph analysis capable of revealing the underlying vertex-based definition of a tile set was devised.

Benefiting from the fast generation of microstructural realizations provided by the tiling concept, Chapters 4 and 5 demonstrated the use of the concept in numerical homogenization and determination of the Representative Volume Element (RVE) size. In Chapter 4, motivated by [20], the appropriateness of the simplified beam model with its geometry derived from Voronoï tessellation to capturing the overall response of Alporas® foam microstructure was studied. In this study, a pronounced influence of neglecting the real geometry of foam ligaments on the macroscopic stiffness was demonstrated by comparing the values predicted for the simplified Voronoï and the real ligament geometry extracted from a microstructural specimen. The limited capability of the planar beam model in predicting the overall response of closed-foam materials, mainly due to missing stiffening contributions from the out-of-plane microstructural features, was reported and the reasons behind the contradicting results of [20] were elucidated. On the other hand, the Wang tile concept proved to be an indispensable tool in this analysis; similarly to [84], we showed that the standard definition of the RVE size in the spirit of Hill [111] leads to extremely large RVEs for models with the infinite contrast in material properties.

Building on the results from Chapter 4, a methodology for identifying the numerical RVE size for a user-defined accuracy was developed in Chapter 5. Our methodology was based on the combination of statistical sampling and the Partition theorem [112], which allowed for bounding the apparent properties of a large material sample with calculations performed on a set of sub-samples. We kept adding and analysing microstructural samples of a given size to an microstructural ensemble until the confidence intervals for the upper and lower bounds on the sought-for effective property fell below a user-defined threshold. Next, the convergence criterion based on hypothesis testing was checked and the algorithm either stopped, identifying the RVE size, or increased the sample size and performed the analysis again. The methodology was illustrated with three material microstructures for problems of linear heat conductivity and elasticity, and the influence of the contrast in material properties on the resulting RVE size was studied. Within the investigated problems, the RVE size was driven primarily by mean values of the apparent properties and could be approximated by a power law of the contrast in material properties, when normalized with the characteristic microstructural length.

Finally, Chapter 6 was dedicated to exploiting the repetitive nature of microstructural realizations generated from Wang tiles in macroscopic analyses with a fully resolved microstructure. In particular, a procedure for extracting characteristic fluctuation fields at the level of a tile set as a collective response of individual tiles to prescribed macroscopic loading, represented by the first- and second-order macroscopic gradient, was developed. Following the tile codes, corresponding boundary degrees of freedom were tied within a set, resulting in tile-wise defined fields continuous across the edges with the same code. Consequently, the same assembly procedure that was used to generate microstructural realization for a macroscopic domain yielded a set of continuous fields, which would approximate the fluctuation part of a solution if the macroscopic domain was loaded uniformly. In order to interpolate between the assembled approximation fields, the fields were combined with a coarse macroscopic discretization by means of the Generalize Finite Element Method's ansatz, constructing microstructure-informed reduced modes specific for

a given macroscopic problem. Adopting the perspective of Reduced Order Modelling enabled replacing numerical integration with Galerkin projection and simplified prescribing the essential boundary conditions for the macroscopic problem. Moreover, it allowed for a straightforward transition to a fine, microstructure-resolving discretization in regions of interest.

With numerical examples, we demonstrated that even with a relatively coarse macroscopic discretization (leading to four orders of magnitude fewer unknowns than the reference direct numerical simulation), it was possible to achieve relative errors below 3% both in energies and the L_2-norm in all cases, which could not be achieved without the microstructure-informed modes. Refining the macroscopic discretization and/or considering more fluctuation fields further improved accuracy of our reduced scheme. Admittedly, standard snapshot-based Reduced Order Modelling schemes achieve comparable accuracy with fewer modes. However, we demonstrated that the problems involving stochastic microstructural geometry inherently feature a high-dimensional solution manifold and thus relatively many macroscopic problems must be calculated with different microstructural realizations in order to obtain an accurate reduced basis, which is then specific only for a particular combination of a macroscopic problem and loading. Contrarily, our microstructure-informed modes are based on the fluctuation fields characteristic for a given compressed representation of a material microstructure. Hence, they can be reused in different analyses.

7.1 Extensions and outlook

The methods and approaches presented in the thesis allow for continuation and potential extensions, some of which are listed below:

- The limitations of the forward propagating Image Quilting algorithm in Section 2 can be alleviated with the GraphCut algorithm [188] and the sample-based design can be extended for three-dimensional problems, replacing the square planar samples with octahedral spatial ones [175].

- Applicability of the proposed tile design methods in finite element analyses depends on the availability of meshing tools capable of producing geometrically and topologically compatible finite element discretizations across corresponding edges and faces. Albeit we have developed such a tool for media with particles of simple shapes both in two and three dimensions, a robust method for the implicitly defined geometries from Chapter 3 is still in development. The authors of the original level-set design frameworks have recently reported advances in this direction [189], introducing conformity constraints in surface mesh generation of a Periodic Unit Cell via additional forces in the truss structure equilibrium based optimization [190]. This may serve as a stepping stone for an extension to Wang tiles.

- The regular structure and repeating patterns in algebraic systems arising in problems whose underlying microstructure is generated with Wang tiles hold a promise for development of an iterative solver, and problem-specific preconditioners, in particular.

- In order to achieve a significant reduction in the computational times of the scheme proposed in Chapter 6, an approximation strategy capable of handling only lo-

cally supported and partially overlapping modes is needed to replace the expensive Galerkin projection.

- Except for the application of Schur complements in Chapter 5, domain decomposition approaches were not investigated in the thesis. However, the inherent partitioning of the tile-assembled microstructural samples and the repetitive occurrence of a handful of tile types create a suitable set-up for adaptive strategies such as [7, 6], where different levels of model simplifications are adopted across a macroscopic domain to attain maximal computational efficiency while maintaining the model's accuracy.

Although this thesis focused on modelling existing materials with random microstructure, the Wang tile concept seems to be a promising framework also for designing material microstructures optimized for a selected application. The first steps in this direction were made by Tyburec in his master thesis [191], where he introduced a modular topology optimization based on Wang tile formalism. He developed a two-level method that alternately optimizes tile interiors (using truss topology optimization) and distribution of tile types within a macroscopic domain (using meta-heuristics). Unlike standard multi-scale topology optimization [192], modular topology optimization automatically ensures continuity and modular manufacturability of the optimized microstructure. It also reduces the number of design variables, albeit at the cost of a combinatorial problem at the macroscale.

Modular design may also present a way to broaden the design space of meta-materials [193, 194], prominent examples of the pronounced microstructure influence on the effective response. Recently, we have designed and tested a self-similar jigsaw puzzle module [195] that can be assembled either in an auxetic or non-auxetic arrangement, allowing for a local tuning of Poisson's ratio similar to Mirzaali et al.'s continuous approach [196].

Bibliography

[1] Z. Hashin, Analysis of Composite Materials—A Survey, Journal of Applied Mechanics 50 (3) (1983) 481. doi:10.1115/1.3167081.

[2] S. Torquato, Random heterogeneous materials: microstructure and macroscopic properties, no. 16 in Interdisciplinary applied mathematics, Springer, New York, 2002.

[3] K. Matouš, M. G. Geers, V. G. Kouznetsova, A. Gillman, A review of predictive nonlinear theories for multiscale modeling of heterogeneous materials, Journal of Computational Physics 330 (2017) 192–220. doi:10.1016/j.jcp.2016.10.070.

[4] T. Nguyen, J. Yvonnet, M. Bornert, C. Chateau, F. Bilteryst, E. Steib, Large-scale simulations of quasi-brittle microcracking in realistic highly heterogeneous microstructures obtained from micro CT imaging, Extreme Mechanics Letters 17 (2017) 50–55. doi:10.1016/j.eml.2017.09.013.

[5] O. Lloberas-Valls, D. Rixen, A. Simone, L. Sluys, Domain decomposition techniques for the efficient modeling of brittle heterogeneous materials, Computer Methods in Applied Mechanics and Engineering 200 (13-16) (2011) 1577–1590. doi:10.1016/j.cma.2011.01.008.

[6] A. Akbari Rahimabadi, P. Kerfriden, S. Bordas, Scale selection in nonlinear fracture mechanics of heterogeneous materials, Philosophical Magazine 95 (28-30) (2015) 3328–3347. doi:10.1080/14786435.2015.1061716.

[7] O. Lloberas-Valls, D. Rixen, A. Simone, L. Sluys, Multiscale domain decomposition analysis of quasi-brittle heterogeneous materials, International Journal for Numerical Methods in Engineering 89 (11) (2012) 1337–1366. doi:10.1002/nme.3286.

[8] G. L. Povirk, Incorporation of microstructural information into models of two-phase materials, Acta Metallurgica et Materialia 43 (8) (1995) 3199 – 3206. doi:10.1016/0956-7151(94)00487-3.

[9] X. Liu, V. Shapiro, Random heterogeneous materials via texture synthesis, Computational Materials Science 99 (2015) 177–189. doi:10.1016/j.commatsci.2014.12.017.

[10] J. Zeman, M. Šejnoha, From random microstructures to representative volume elements, Modelling and Simulation in Materials Science and Engineering 15 (4) (2007) S325–S335. doi:10.1088/0965-0393/15/4/S01.

[11] H. Lee, M. Brandyberry, A. Tudor, K. Matouš, Three-dimensional reconstruction of statistically optimal unit cells of polydisperse particulate composites from microtomography, Physical Review E 80 (6) (2009) 061301. doi:10.1103/PhysRevE.80.061301.

[12] D. Balzani, L. Scheunemann, D. Brands, J. Schröder, Construction of two- and three-dimensional statistically similar RVEs for coupled micro-macro simulations, Computational Mechanics 54 (5) (2014) 1269–1284. doi:10.1007/s00466-014-1057-6.

[13] P. Tahmasebi, M. Sahimi, Cross-Correlation Function for Accurate Reconstruction of Heterogeneous Media, Physical Review Letters 110 (7) (2013) 078002. doi:10.1103/PhysRevLett.110.078002.

[14] X. Li, Y. Zhang, H. Zhao, C. Burkhart, L. C. Brinson, W. Chen, A Transfer Learning Approach for Microstructure Reconstruction and Structure-property Predictions, Scientific Reports 8 (1) (2018) 13461. doi:10.1038/s41598-018-31571-7.

[15] J. Novák, A. Kučerová, J. Zeman, Compressing random microstructures via stochastic Wang tilings, Physical Review E 86 (4) (2012) 040104. doi:10.1103/PhysRevE.86.040104.

[16] J. Novák, A. Kučerová, J. Zeman, Microstructural enrichment functions based on stochastic Wang tilings, Modelling and Simulation in Materials Science and Engineering 21 (2) (2013) 025014. doi:10.1088/0965-0393/21/2/025014.

[17] M. F. Cohen, J. Shade, S. Hiller, O. Deussen, Wang Tiles for image and texture generation, ACM Transactions on Graphics 22 (3) (2003) 287–294. doi:10.1145/882262.882265.

[18] B. Sonon, B. François, T. Massart, A unified level set based methodology for fast generation of complex microstructural multi-phase RVEs, Computer Methods in Applied Mechanics and Engineering 223-224 (2012) 103–122. doi:10.1016/j.cma.2012.02.018.

[19] B. Sonon, B. François, T. J. Massart, An advanced approach for the generation of complex cellular material representative volume elements using distance fields and level sets, Computational Mechanics 56 (2) (2015) 221–242. doi:10.1007/s00466-015-1168-8.

[20] J. Němeček, V. Králík, J. Vondřejc, A two-scale micromechanical model for aluminium foam based on results from nanoindentation, Computers & Structures 128 (2013) 136–145. doi:10.1016/j.compstruc.2013.07.007.

[21] M. Doškář, J. Novák, J. Zeman, Aperiodic compression and reconstruction of real-world material systems based on Wang tiles, Physical Review E 90 (6) (2014) 062118. doi:10.1103/PhysRevE.90.062118.

[22] J. Michel, H. Moulinec, P. Suquet, Effective properties of composite materials with periodic microstructure: a computational approach, Computer Methods in Applied Mechanics and Engineering 172 (1-4) (1999) 109–143. doi:10.1016/S0045-7825(98)00227-8.

[23] M. Geers, V. Kouznetsova, W. Brekelmans, Multi-scale computational homogenization: Trends and challenges, Journal of Computational and Applied Mathematics 234 (7) (2010) 2175–2182. doi:10.1016/j.cam.2009.08.077.

[24] H. Owhadi, Approximation of the effective conductivity of ergodic media by periodization, Probability Theory and Related Fields 125 (2) (2003) 225–258. doi:10.1007/s00440-002-0240-4.

[25] H. Wang, Proving Theorems by Pattern Recognition - II, Bell System Technical Journal 40 (1) (1961) 1–41. doi:10.1002/j.1538-7305.1961.tb03975.x.

[26] H. Wang, Games, Logic and Computers, Scientific American 213 (5) (1965) 98–106.

[27] R. Berger, The Undecidability of the Domino Problem, American Mathematical Society, Providence, R.I., 1966.

[28] B. Grünbaum, G. C. Shephard, Tilings and patterns, second edition Edition, Dover Publications, Inc, Mineola, New York, 2016.

[29] K. Culik, An aperiodic set of 13 Wang tiles, Discrete Mathematics 160 (1-3) (1996) 245–251. doi:10.1016/S0012-365X(96)00118-5.

[30] J. Kari, K. Culik, An Aperiodic Set of Wang Cubes, JUCS - Journal of Universal Computer Science 1 (10) (1995) 675–686. doi:10.3217/jucs-001-10-0675.

[31] J. Stam, Aperiodic Texture Mapping, Tech. Rep. R046 (1997).

[32] E. Winfree, F. Liu, L. A. Wenzler, N. C. Seeman, Design and self-assembly of two-dimensional DNA crystals, Nature 394 (6693) (1998) 539–544. doi:10.1038/28998.

[33] H. Yan, S. H. Park, G. Finkelstein, J. H. Reif, T. H. LaBean, DNA-Templated Self-Assembly of Protein Arrays and Highly Conductive Nanowires, Science 301 (5641) (2003) 1882–1884. doi:10.1126/science.1089389.

[34] D. Aristoff, C. Radin, First order phase transition in a model of quasicrystals, Journal of Physics A: Mathematical and Theoretical 44 (25) (2011) 255001. doi:10.1088/1751-8113/44/25/255001.

[35] D. Shechtman, I. Blech, D. Gratias, J. Cahn, Metallic Phase with Long-Range Orientational Order and No Translational Symmetry, Physical Review Letters 53 (20) (1984) 1951–1953. doi:10.1103/PhysRevLett.53.1951.

[36] L. Leuzzi, G. Parisi, Thermodynamics of a tiling model, Journal of Physics A: Mathematical and General 33 (23) (2000) 4215–4225. doi:10.1088/0305-4470/33/23/301.

[37] A. A. Efros, W. T. Freeman, Image quilting for texture synthesis and transfer, in: Proceedings of ACM SIGGRAPH 2001, ACM Press, Los Angeles, 2001, pp. 341–346. doi:10.1145/383259.383296.

[38] M. Šejnoha, J. Zeman, Micromechanics in practice, WIT Press, Boston, MA, 2013.

[39] Y. Jiao, F. H. Stillinger, S. Torquato, A superior descriptor of random textures and its predictive capacity, Proceedings of the National Academy of Sciences 106 (42) (2009) 17634–17639. doi:10.1073/pnas.0905919106.

[40] S. Torquato, J. D. Beasley, Y. C. Chiew, Two-point cluster function for continuum percolation, The Journal of Chemical Physics 88 (10) (1988) 6540. doi:10.1063/1.454440.

[41] M. Doškář, Wang tilings for real world material systems, Master's thesis, Czech Technical University in Prague, Prague (2013).

[42] A. Sufian, A. R. Russell, Microstructural pore changes and energy dissipation in Gosford sandstone during pre-failure loading using X-ray CT, International Journal of Rock Mechanics and Mining Sciences 57 (2013) 119–131. doi:10.1016/j.ijrmms.2012.07.021.

[43] M. Doškář, J. Zeman, D. Rypl, J. Novák, Level-set based design of wang tiles for modelling complex microstructures (2019).
URL https://arxiv.org/abs/1904.07657

[44] V. P. Nguyen, O. Lloberas-Valls, M. Stroeven, L. J. Sluys, Homogenization-based multiscale crack modelling: From micro-diffusive damage to macro-cracks, Computer Methods in Applied Mechanics and Engineering 200 (9-12) (2011) 1220–1236. doi:10.1016/j.cma.2010.10.013.

[45] E. Barchiesi, M. Spagnuolo, L. Placidi, Mechanical metamaterials: a state of the art, Mathematics and Mechanics of Solids 24 (1) (2019) 212–234. doi:10.1177/1081286517735695.

[46] M. Yang, A. Nagarajan, B. Liang, S. Soghrati, New algorithms for virtual reconstruction of heterogeneous microstructures, Computer Methods in Applied Mechanics and Engineering 338 (2018) 275–298. doi:10.1016/j.cma.2018.04.030.

[47] L. Scheunemann, D. Balzani, D. Brands, J. Schröder, Design of 3d statistically similar Representative Volume Elements based on Minkowski functionals, Mechanics of Materials 90 (2015) 185–201. doi:10.1016/j.mechmat.2015.03.005.

[48] Y. Jiao, F. Stillinger, S. Torquato, Modeling heterogeneous materials via two-point correlation functions: Basic principles, Physical Review E 76 (3) (2007) 031110. doi:10.1103/PhysRevE.76.031110.

[49] J. Zeman, M. Šejnoha, Numerical evaluation of effective elastic properties of graphite fiber tow impregnated by polymer matrix, Journal of the Mechanics and Physics of Solids 49 (1) (2001) 69–90. doi:10.1016/S0022-5096(00)00027-2.

[50] M. G. Rozman, M. Utz, Efficient reconstruction of multiphase morphologies from correlation functions, Physical Review E 63 (6) (2001). doi:10.1103/PhysRevE.63.066701.

[51] B. Lu, S. Torquato, Lineal-path function for random heterogeneous materials, Physical Review A 45 (2) (1992) 922–929. doi:10.1103/PhysRevA.45.922.

[52] H. Kumar, C. Briant, W. Curtin, Using microstructure reconstruction to model mechanical behavior in complex microstructures, Mechanics of Materials 38 (8-10) (2006) 818–832. doi:10.1016/j.mechmat.2005.06.030.

[53] J. Havelka, A. Kučerová, J. Sýkora, Compression and reconstruction of random microstructures using accelerated lineal path function, Computational Materials Science 122 (2016) 102–117. doi:10.1016/j.commatsci.2016.04.044.

[54] C. Yeong, S. Torquato, Reconstructing random media, Physical Review E 57 (1) (1998) 495–506. doi:10.1103/PhysRevE.57.495.

[55] D. Basanta, M. A. Miodownik, E. A. Holm, P. J. Bentley, Using genetic algorithms to evolve three-dimensional microstructures from two-dimensional micrographs, Metallurgical and Materials Transactions A 36 (7) (2005) 1643–1652. doi:10.1007/s11661-005-0026-2.

[56] N. C. Kumar, K. Matouš, P. H. Geubelle, Reconstruction of periodic unit cells of multimodal random particulate composites using genetic algorithms, Computational Materials Science 42 (2) (2008) 352–367. doi:10.1016/j.commatsci.2007.07.043.

[57] D. Fullwood, S. Kalidindi, S. Niezgoda, A. Fast, N. Hampson, Gradient-based microstructure reconstructions from distributions using fast Fourier transforms, Materials Science and Engineering: A 494 (1-2) (2008) 68–72. doi:10.1016/j.msea.2007.10.087.

[58] D. T. Fullwood, S. R. Niezgoda, S. R. Kalidindi, Microstructure reconstructions from 2-point statistics using phase-recovery algorithms, Acta Materialia 56 (5) (2008) 942–948. doi:10.1016/j.actamat.2007.10.044.

[59] R. Bostanabad, A. T. Bui, W. Xie, D. W. Apley, W. Chen, Stochastic microstructure characterization and reconstruction via supervised learning, Acta Materialia 103 (2016) 89–102. doi:10.1016/j.actamat.2015.09.044.

[60] B. Biswal, C. Manwart, R. Hilfer, S. Bakke, P. Øren, Quantitative analysis of experimental and synthetic microstructures for sedimentary rock, Physica A: Statistical Mechanics and its Applications 273 (3-4) (1999) 452–475. doi:10.1016/S0378-4371(99)00248-4.

[61] Y. Saito, M. Enomoto, Monte Carlo Simulation of Grain Growth, ISIJ International 32 (3) (1992) 267–274. doi:10.2355/isijinternational.32.267.

[62] C. Krill III, L.-Q. Chen, Computer simulation of 3-D grain growth using a phase-field model, Acta Materialia 50 (12) (2002) 3059–3075. doi:10.1016/S1359-6454(02)00084-8.

[63] S. Falco, J. Jiang, F. De Cola, N. Petrinic, Generation of 3d polycrystalline microstructures with a conditioned Laguerre-Voronoi tessellation technique, Computational Materials Science 136 (2017) 20–28. doi:10.1016/j.commatsci.2017.04.018.

[64] J. Alsayednoor, P. Harrison, Evaluating the performance of microstructure generation algorithms for 2-d foam-like representative volume elements, Mechanics of Materials 98 (2016) 44–58. doi:10.1016/j.mechmat.2016.04.001.

[65] D. P. Mitchell, Generating antialiased images at low sampling densities, ACM SIGGRAPH Computer Graphics 21 (4) (1987) 65–72. doi:10.1145/37402.37410.

[66] D. W. Cooper, Random-sequential-packing simulations in three dimensions for spheres, Physical Review A 38 (1) (1988) 522–524. doi:10.1103/PhysRevA.38.522.

[67] J. Segurado, J. Llorca, A numerical approximation to the elastic properties of sphere-reinforced composites, Journal of the Mechanics and Physics of Solids 50 (10) (2002) 2107–2121. doi:10.1016/S0022-5096(02)00021-2.

[68] B. D. Lubachevsky, F. H. Stillinger, Geometric properties of random disk packings, Journal of Statistical Physics 60 (5-6) (1990) 561–583. doi:10.1007/BF01025983.

[69] A. Donev, S. Torquato, F. H. Stillinger, Neighbor list collision-driven molecular dynamics simulation for nonspherical hard particles. I. Algorithmic details, Journal of Computational Physics 202 (2) (2005) 737–764. doi:10.1016/j.jcp.2004.08.014.

[70] E. Ghossein, M. Lévesque, Random generation of periodic hard ellipsoids based on molecular dynamics: A computationally-efficient algorithm, Journal of Computational Physics 253 (2013) 471–490. doi:10.1016/j.jcp.2013.07.004.

[71] M. De Giorgi, A. Carofalo, V. Dattoma, R. Nobile, F. Palano, Aluminium foams structural modelling, Computers & Structures 88 (1-2) (2010) 25–35. doi:10.1016/j.compstruc.2009.06.005.

[72] Y. Chen, R. Das, M. Battley, Effects of cell size and cell wall thickness variations on the stiffness of closed-cell foams, International Journal of Solids and Structures 52 (2015) 150–164. doi:10.1016/j.ijsolstr.2014.09.022.

[73] H. Mebatsion, P. Verboven, B. Verlinden, Q. Ho, T. Nguyen, B. Nicolaï, Microscale modelling of fruit tissue using Voronoi tessellations, Computers and Electronics in Agriculture 52 (1-2) (2006) 36–48. doi:10.1016/j.compag.2006.01.002.

[74] A. Chakraborty, M. M. Perales, G. V. Reddy, A. K. Roy-Chowdhury, Adaptive Geometric Tessellation for 3d Reconstruction of Anisotropically Developing Cells in Multilayer Tissues from Sparse Volumetric Microscopy Images, PLoS ONE 8 (8) (2013) e67202. doi:10.1371/journal.pone.0067202.

[75] M. Doškář, J. Novák, A jigsaw puzzle framework for homogenization of high porosity foams, Computers & Structures 166 (2016) 33–41. doi:10.1016/j.compstruc.2016.01.003.

[76] A. Simone, L. Gibson, The effects of cell face curvature and corrugations on the stiffness and strength of metallic foams, Acta Materialia 46 (11) (1998) 3929–3935. doi:10.1016/S1359-6454(98)00072-X.

[77] A. Lyckegaard, E. M. Lauridsen, W. Ludwig, R. W. Fonda, H. F. Poulsen, On the Use of Laguerre Tessellations for Representations of 3d Grain Structures, Advanced Engineering Materials 13 (3) (2011) 165–170. doi:10.1002/adem.201000258.

[78] D. Dunbar, G. Humphreys, A spatial data structure for fast Poisson-disk sample generation, ACM Transactions on Graphics 25 (3) (2006) 503. doi:10.1145/1141911.1141915.

[79] T. R. Jones, Efficient Generation of Poisson-Disk Sampling Patterns, Journal of Graphics Tools 11 (2) (2006) 27–36. doi:10.1080/2151237X.2006.10129217.

[80] B. Sonon, T. Massart, A Level-Set Based Representative Volume Element Generator and XFEM Simulations for Textile and 3d-Reinforced Composites, Materials 6 (12) (2013) 5568–5592. doi:10.3390/ma6125568.

[81] T. J. Massart, B. Sonon, K. Ehab Moustafa Kamel, L. H. Poh, G. Sun, Level set-based generation of representative volume elements for the damage analysis of irregular masonry, Meccanica 53 (7) (2018) 1737–1755. doi:10.1007/s11012-017-0695-0.

[82] T. Kanit, S. Forest, I. Galliet, V. Mounoury, D. Jeulin, Determination of the size of the representative volume element for random composites: statistical and numerical approach, International Journal of Solids and Structures 40 (13-14) (2003) 3647–3679. doi:10.1016/S0020-7683(03)00143-4.

[83] I. Gitman, H. Askes, L. Sluys, Representative volume: Existence and size determination, Engineering Fracture Mechanics 74 (16) (2007) 2518–2534. doi:10.1016/j.engfracmech.2006.12.021.

[84] J. Dirrenberger, S. Forest, D. Jeulin, Towards gigantic RVE sizes for 3d stochastic fibrous networks, International Journal of Solids and Structures 51 (2) (2014) 359–376. doi:10.1016/j.ijsolstr.2013.10.011.

[85] R. Ammann, B. Grünbaum, G. C. Shephard, Aperiodic tiles, Discrete & Computational Geometry 8 (1) (1992) 1–25. doi:10.1007/BF02293033.

[86] M. Doškář, J. Zeman, D. Jarušková, J. Novák, Wang tiling aided statistical determination of the Representative Volume Element size of random heterogeneous materials, European Journal of Mechanics - A/Solids 70 (2018) 280–295. doi:10.1016/j.euromechsol.2017.12.002.

[87] R. M. Robinson, Undecidability and nonperiodicity for tilings of the plane, Inventiones Mathematicae 12 (3) (1971) 177–209. doi:10.1007/BF01418780.

[88] E. Jeandel, M. Rao, An aperiodic set of 11 Wang tiles, arXiv:1506.06492 (Jun. 2015).

[89] P. W. K. Rothemund, N. Papadakis, E. Winfree, Algorithmic Self-Assembly of DNA Sierpinski Triangles, PLoS Biology 2 (12) (2004) e424. doi:10.1371/journal.pbio.0020424.

[90] J. Kopf, D. Cohen-Or, O. Deussen, D. Lischinski, Recursive Wang tiles for real-time blue noise, ACM Transactions on Graphics 25 (3) (2006) 509. doi:10.1145/1141911.1141916.

[91] A. Lagae, P. Dutré, An alternative for Wang tiles: colored edges versus colored corners, ACM Transactions on Graphics 25 (4) (2006) 1442–1459. doi:10.1145/1183287.1183296.

[92] R. Sedgewick, Algorithms in C++, Part 5: Graph Algorithms, 3rd Edition, Addison-Wesley, Boston, 2002.

[93] J. Talbot, P. Schaaf, G. Tarjus, Random sequential addition of hard spheres, Molecular Physics 72 (6) (1991) 1397–1406. doi:10.1080/00268979100100981.

[94] S. Osher, R. P. Fedkiw, Level set methods and dynamic implicit surfaces, Springer, New York, 2003.

[95] A. Lagae, P. Dutré, Poisson Sphere Distributions, in: L. Kobbelt, T. Kuhlen, T. Aach, R. Westermann (Eds.), Vision, Modeling, and Visualization 2006, Akademische Verlagsgesellschaft Aka GmbH, Berlin, 2006, pp. 373–379.

[96] J. Gajdošík, J. Zeman, M. Šejnoha, Qualitative analysis of fiber composite microstructure: Influence of boundary conditions, Probabilistic Engineering Mechanics 21 (4) (2006) 317–329. doi:10.1016/j.probengmech.2005.11.006.

[97] M. F. Ashby, A. G. Evans, N. A. Fleck, L. J. Gibson, J. W. Hutchinson, H. N. Wadley, Metal Foams: a Design Guide, Butterworth-Heinemann, Boston, 2000.

[98] J. Banhart, Manufacture, characterisation and application of cellular metals and metal foams, Progress in Materials Science 46 (6) (2001) 559–632. doi:10.1016/S0079-6425(00)00002-5.

[99] A. Hanssen, L. Enstock, M. Langseth, Close-range blast loading of aluminium foam panels, International Journal of Impact Engineering 27 (6) (2002) 593–618. doi:10.1016/S0734-743X(01)00155-5.

[100] D. T. Fullwood, S. R. Niezgoda, B. L. Adams, S. R. Kalidindi, Microstructure sensitive design for performance optimization, Progress in Materials Science 55 (6) (2010) 477–562. doi:10.1016/j.pmatsci.2009.08.002.

[101] L. J. Gibson, M. F. Ashby, The Mechanics of Three-Dimensional Cellular Materials, Proceedings of the Royal Society A: Mathematical, Physical and Engineering Sciences 382 (1782) (1982) 43–59. doi:10.1098/rspa.1982.0088.

[102] J.-F. Despois, R. Mueller, A. Mortensen, Uniaxial deformation of microcellular metals, Acta Materialia 54 (16) (2006) 4129–4142. doi:10.1016/j.actamat.2006.03.054.

[103] P. Koudelka, P. Zlámal, D. Kytýř, T. Doktor, T. Fíla, O. Jiroušek, On the Modeling of the Compressive Behaviour of Metal Foams: A Comparison of Discretization Schemes, in: B. H. V. Topping, P. Iványi (Eds.), Proceedings of the Fourteenth International Conference on Civil, Structural and Environmental Engineering Computing, Civil-Comp Press, Stirlingshire, United Kingdom, 2013, pp. 161–170, paper 106. doi:dx.doi.org/10.4203/ccp.102.106.

[104] S. D. Mesarovic, J. Padbidri, Minimal kinematic boundary conditions for simulations of disordered microstructures, Philosophical Magazine 85 (1) (2005) 65–78. doi:10.1080/14786430412331313321.

[105] T. Miyoshi, M. Itoh, S. Akiyama, A. Kitahara, ALPORAS Aluminum Foam: Production Process, Properties, and Applications, Advanced Engineering Materials 2 (4) (2000) 179–183. doi:10.1002/(SICI)1527-2648(200004)2:4<179::AID-ADEM179>3.0.CO;2-G.

[106] D. Radford, G. McShane, V. Deshpande, N. Fleck, The response of clamped sandwich plates with metallic foam cores to simulated blast loading, International Journal of Solids and Structures 43 (7-8) (2006) 2243–2259. doi:10.1016/j.ijsolstr.2005.07.006.

[107] O. Jiroušek, T. Doktor, D. Kytýř, P. Zlámal, T. Fíla, P. Koudelka, I. Jandejsek, D. Vavřík, X-ray and finite element analysis of deformation response of closed-cell metal foam subjected to compressive loading, Journal of Instrumentation 8 (02) (2013) C02012–C02012. doi:10.1088/1748-0221/8/02/C02012.

[108] S. R. Niezgoda, D. M. Turner, D. T. Fullwood, S. R. Kalidindi, Optimized structure based representative volume element sets reflecting the ensemble-averaged 2-point statistics, Acta Materialia 58 (13) (2010) 4432–4445. doi:10.1016/j.actamat.2010.04.041.

[109] I. Sevostianov, J. Kováčik, F. Simančík, Elastic and electric properties of closed-cell aluminum foams, Materials Science and Engineering: A 420 (1-2) (2006) 87–99. doi:10.1016/j.msea.2006.01.064.

[110] S. Timoshenko, J. N. Goodier, Theory of Elasticity, McGraw-Hill Book Company, Inc., New York, 1951.

[111] R. Hill, Elastic properties of reinforced solids: Some theoretical principles, Journal of the Mechanics and Physics of Solids 11 (5) (1963) 357–372. doi:10.1016/0022-5096(63)90036-X.

[112] C. Huet, Application of variational concepts to size effects in elastic heterogeneous bodies, Journal of the Mechanics and Physics of Solids 38 (6) (1990) 813–841. doi:10.1016/0022-5096(90)90041-2.

[113] C. Miehe, Computational micro-to-macro transitions for discretized micro-structures of heterogeneous materials at finite strains based on the minimization of averaged incremental energy, Computer Methods in Applied Mechanics and Engineering 192 (5-6) (2003) 559–591. doi:10.1016/S0045-7825(02)00564-9.

[114] J. Fish, Z. Yuan, Multiscale enrichment based on partition of unity, International Journal for Numerical Methods in Engineering 62 (10) (2005) 1341–1359. doi:10.1002/nme.1230.

[115] Z. Bittnar, J. Šejnoha, Numerical methods in structural mechanics, ASCE Press, New York, 1996.

[116] M. Ostoja-Starzewski, Material spatial randomness: From statistical to representative volume element, Probabilistic Engineering Mechanics 21 (2) (2006) 112–132. doi:10.1016/j.probengmech.2005.07.007.

[117] K. Sab, On the homogenization and the simulation of random materials, European Journal of Mechanics - A/Solids 11 (5) (1992) 585–607.

[118] M. Salmi, F. Auslender, M. Bornert, M. Fogli, Various estimates of Representative Volume Element sizes based on a statistical analysis of the apparent behavior of random linear composites, Comptes Rendus Mécanique 340 (4-5) (2012) 230–246. doi:10.1016/j.crme.2012.02.007.

[119] H. Moussaddy, D. Therriault, M. Lévesque, Assessment of existing and introduction of a new and robust efficient definition of the representative volume element, International Journal of Solids and Structures 50 (24) (2013) 3817–3828. doi:10.1016/j.ijsolstr.2013.07.016.

[120] M. Ostoja-Starzewski, Random field models of heterogeneous materials, International Journal of Solids and Structures 35 (19) (1998) 2429–2455. doi:10.1016/S0020-7683(97)00144-3.

[121] V. Kouznetsova, M. G. Geers, W. M. Brekelmans, Multi-scale constitutive modelling of heterogeneous materials with a gradient-enhanced computational homogenization scheme, International Journal for Numerical Methods in Engineering 54 (8) (2002) 1235–1260. doi:10.1002/nme.541.

[122] M. Stroeven, H. Askes, L. Sluys, Numerical determination of representative volumes for granular materials, Computer Methods in Applied Mechanics and Engineering 193 (30-32) (2004) 3221–3238. doi:10.1016/j.cma.2003.09.023.

[123] C. Pelissou, J. Baccou, Y. Monerie, F. Perales, Determination of the size of the representative volume element for random quasi-brittle composites, International Journal of Solids and Structures 46 (14-15) (2009) 2842–2855. doi:10.1016/j.ijsolstr.2009.03.015.

[124] D. Trias, J. Costa, A. Turon, J. Hurtado, Determination of the critical size of a statistical representative volume element (SRVE) for carbon reinforced polymers, Acta Materialia 54 (13) (2006) 3471–3484. doi:10.1016/j.actamat.2006.03.042.

[125] I. M. Gitman, M. B. Gitman, H. Askes, Quantification of stochastically stable representative volumes for random heterogeneous materials, Archive of Applied Mechanics 75 (2-3) (2006) 79–92. doi:10.1007/s00419-005-0411-8.

[126] A. A. Gusev, Representative volume element size for elastic composites: A numerical study, Journal of the Mechanics and Physics of Solids 45 (9) (1997) 1449–1459. doi:10.1016/S0022-5096(97)00016-1.

[127] M. Salmi, F. Auslender, M. Bornert, M. Fogli, Apparent and effective mechanical properties of linear matrix-inclusion random composites: Improved bounds for the effective behavior, International Journal of Solids and Structures 49 (10) (2012) 1195–1211. doi:10.1016/j.ijsolstr.2012.01.018.

[128] T. Zohdi, P. Wriggers, C. Huet, A method of substructuring large-scale computational micromechanical problems, Computer Methods in Applied Mechanics and Engineering 190 (43-44) (2001) 5639–5656. doi:10.1016/S0045-7825(01)00189-X.

[129] T. I. Zohdi, P. Wriggers, Aspects of the computational testing of the mechanical properties of microheterogeneous material samples, International Journal for Numerical Methods in Engineering 50 (11) (2001) 2573–2599. doi:10.1002/nme.146.

[130] J. Kruis, Domain decomposition methods for distributed computing, Saxe-Coburg publications on computational engineering, Saxe-Coburg Publications, Stirling, Scotland, 2006.

[131] S. Saroukhani, R. Vafadari, R. Andersson, F. Larsson, K. Runesson, On statistical strain and stress energy bounds from homogenization and virtual testing, European Journal of Mechanics - A/Solids 51 (2015) 77–95. doi:10.1016/j.euromechsol.2014.11.003.

[132] C. V. Verhoosel, J. J. C. Remmers, M. A. Gutiérrez, R. de Borst, Computational homogenization for adhesive and cohesive failure in quasi-brittle solids, International Journal for Numerical Methods in Engineering 83 (8-9) (2010) 1155–1179. doi:10.1002/nme.2854.

[133] V. Phu Nguyen, O. Lloberas-Valls, M. Stroeven, L. Johannes Sluys, On the existence of representative volumes for softening quasi-brittle materials – A failure zone averaging scheme, Computer Methods in Applied Mechanics and Engineering 199 (45-48) (2010) 3028–3038. doi:10.1016/j.cma.2010.06.018.

[134] L.-Y. Wei, M. Levoy, Fast texture synthesis using tree-structured vector quantization, in: Proceedings of the 27th Annual Conference on Computer Graphics and Interactive Techniques, SIGGRAPH '00, ACM Press/Addison-Wesley Publishing Co., New York, NY, USA, 2000, pp. 479–488. doi:10.1145/344779.345009.
URL http://dx.doi.org/10.1145/344779.345009

[135] S. Hazanov, C. Huet, Order relationships for boundary conditions effect in heterogeneous bodies smaller than the representative volume, Journal of the Mechanics and Physics of Solids 42 (12) (1994) 1995–2011. doi:10.1016/0022-5096(94)90022-1.

[136] K. Sab, B. Nedjar, Periodization of random media and representative volume element size for linear composites, Comptes Rendus Mécanique 333 (2) (2005) 187–195. doi:10.1016/j.crme.2004.10.003.

[137] R. Glüge, Generalized boundary conditions on representative volume elements and their use in determining the effective material properties, Computational Materials Science 79 (2013) 408–416. doi:10.1016/j.commatsci.2013.06.038.

[138] A. Bourgeat, A. Piatnitski, Approximations of effective coefficients in stochastic homogenization, Annales de l'Institut Henri Poincare (B) Probability and Statistics 40 (2) (2004) 153–165. doi:10.1016/j.anihpb.2003.07.003.

[139] K. Terada, M. Hori, T. Kyoya, N. Kikuchi, Simulation of the multi-scale convergence in computational homogenization approaches, International Journal of Solids and Structures 37 (16) (2000) 2285–2311. doi:10.1016/S0020-7683(98)00341-2.

[140] Z. Shan, A. M. Gokhale, Representative volume element for non-uniform microstructure, Computational Materials Science 24 (3) (2002) 361–379. doi:10.1016/S0927-0256(01)00257-9.

[141] T. Kanit, F. N'Guyen, S. Forest, D. Jeulin, M. Reed, S. Singleton, Apparent and effective physical properties of heterogeneous materials: Representativity of samples of two materials from food industry, Computer Methods in Applied Mechanics and Engineering 195 (33-36) (2006) 3960–3982. doi:10.1016/j.cma.2005.07.022.

[142] T. Kanit, S. Forest, D. Jeulin, F. N'Guyen, S. Singleton, Virtual improvement of ice cream properties by computational homogenization of microstructures, Mechanics Research Communications 38 (2) (2011) 136–140. doi:10.1016/j.mechrescom.2011.01.005.

[143] W. Drugan, J. Willis, A micromechanics-based nonlocal constitutive equation and estimates of representative volume element size for elastic composites, Journal

of the Mechanics and Physics of Solids 44 (4) (1996) 497–524. doi:10.1016/0022-5096(96)00007-5.

[144] T. H. Hoang, M. Guerich, J. Yvonnet, Determining the Size of RVE for Nonlinear Random Composites in an Incremental Computational Homogenization Framework, Journal of Engineering Mechanics (2016) 04016018doi:10.1061/(ASCE)EM.1943-7889.0001057.

[145] T. Zohdi, P. Wriggers, A domain decomposition method for bodies with heterogeneous microstructure based on material regularization, International Journal of Solids and Structures 36 (17) (1999) 2507–2525. doi:10.1016/S0020-7683(98)00124-3.

[146] T. I. Zohdi, Statistical ensemble error bounds for homogenized microheterogeneous solids, Zeitschrift für Angewandte Mathematik und Physik 56 (3) (2005) 497–515. doi:10.1007/s00033-004-2027-1.

[147] T. I. Zohdi, P. Wriggers, An introduction to computational micromechanics, no. v. 20 in Lecture notes in applied and computational mechanics, Springer, Berlin, 2008.

[148] D. Ryckelynck, A priori hyperreduction method: an adaptive approach, Journal of Computational Physics 202 (1) (2005) 346–366. doi:10.1016/j.jcp.2004.07.015.

[149] G. Bolzon, V. Buljak, An effective computational tool for parametric studies and identification problems in materials mechanics, Computational Mechanics 48 (6) (2011) 675–687. doi:10.1007/s00466-011-0611-8.

[150] P. Astrid, S. Weiland, K. Willcox, T. Backx, Missing Point Estimation in Models Described by Proper Orthogonal Decomposition, IEEE Transactions on Automatic Control 53 (10) (2008) 2237–2251. doi:10.1109/TAC.2008.2006102.

[151] J. Barbič, D. L. James, Real-Time subspace integration for St. Venant-Kirchhoff deformable models, ACM Transactions on Graphics 24 (3) (2005) 982–990. doi:10.1145/1073204.1073300.

[152] S. S. An, T. Kim, D. L. James, Optimizing cubature for efficient integration of subspace deformations, ACM Transactions on Graphics 27 (5) (2008) 1. doi:10.1145/1409060.1409118.

[153] T. Kim, D. L. James, Physics-based character skinning using multi-domain subspace deformations, in: Proceedings of the 2011 ACM SIGGRAPH/Eurographics Symposium on Computer Animation, SCA '11, ACM, New York, NY, USA, 2011, pp. 63–72. doi:10.1145/2019406.2019415.

[154] D. Harmon, D. Zorin, Subspace integration with local deformations, ACM Transactions on Graphics 32 (4) (2013) 1. doi:10.1145/2461912.2461922.

[155] S. Niroomandi, I. Alfaro, E. Cueto, F. Chinesta, Accounting for large deformations in real-time simulations of soft tissues based on reduced-order models, Computer Methods and Programs in Biomedicine 105 (1) (2012) 1–12. doi:10.1016/j.cmpb.2010.06.012.

[156] A. Radermacher, S. Reese, A comparison of projection-based model reduction concepts in the context of nonlinear biomechanics, Archive of Applied Mechanics 83 (8) (2013) 1193–1213. doi:10.1007/s00419-013-0742-9.

[157] J. Yvonnet, Q.-C. He, The reduced model multiscale method (R3M) for the nonlinear homogenization of hyperelastic media at finite strains, Journal of Computational Physics 223 (1) (2007) 341–368. doi:10.1016/j.jcp.2006.09.019.

[158] J. Oliver, M. Caicedo, A. Huespe, J. Hernández, E. Roubin, Reduced order modeling strategies for computational multiscale fracture, Computer Methods in Applied Mechanics and Engineering 313 (2017) 560–595. doi:10.1016/j.cma.2016.09.039.

[159] L. Xia, P. Breitkopf, A reduced multiscale model for nonlinear structural topology optimization, Computer Methods in Applied Mechanics and Engineering 280 (2014) 117–134. doi:10.1016/j.cma.2014.07.024.

[160] F. Fritzen, L. Xia, M. Leuschner, P. Breitkopf, Topology optimization of multiscale elastoviscoplastic structures, International Journal for Numerical Methods in Engineering 106 (6) (2016) 430–453. doi:10.1002/nme.5122.

[161] P. Kerfriden, O. Goury, T. Rabczuk, S. Bordas, A partitioned model order reduction approach to rationalise computational expenses in nonlinear fracture mechanics, Computer Methods in Applied Mechanics and Engineering 256 (2013) 169–188. doi:10.1016/j.cma.2012.12.004.

[162] A. Radermacher, S. Reese, Model reduction in elastoplasticity: proper orthogonal decomposition combined with adaptive sub-structuring, Computational Mechanics 54 (3) (2014) 677–687. doi:10.1007/s00466-014-1020-6.

[163] D. Amsallem, M. J. Zahr, C. Farhat, Nonlinear model order reduction based on local reduced-order bases, International Journal for Numerical Methods in Engineering 92 (10) (2012) 891–916. doi:10.1002/nme.4371.

[164] J. L. Eftang, B. Stamm, Parameter multi-domain 'hp' empirical interpolation, International Journal for Numerical Methods in Engineering 90 (4) (2012) 412–428. doi:10.1002/nme.3327.

[165] B. Peherstorfer, D. Butnaru, K. Willcox, H.-J. Bungartz, Localized Discrete Empirical Interpolation Method, SIAM Journal on Scientific Computing 36 (1) (2014) A168–A192. doi:10.1137/130924408.

[166] S. Niroomandi, I. Alfaro, D. González, E. Cueto, F. Chinesta, Real-time simulation of surgery by reduced-order modeling and X-FEM techniques, International Journal for Numerical Methods in Biomedical Engineering 28 (5) (2012) 574–588. doi:10.1002/cnm.1491.

[167] J. Melenk, I. Babuška, The partition of unity finite element method: Basic theory and applications, Computer Methods in Applied Mechanics and Engineering 139 (1-4) (1996) 289–314. doi:10.1016/S0045-7825(96)01087-0.

[168] R. Ibáñez, E. Abisset-Chavanne, F. Chinesta, A. Huerta, E. Cueto, A local, multiple Proper Generalized Decomposition based on the Partition of Unity, International Journal for Numerical Methods in Engineering (2019) nme.6128doi:10.1002/nme.6128.

[169] T. Strouboulis, L. Zhang, I. Babuška, Generalized finite element method using mesh-based handbooks: application to problems in domains with many voids, Computer Methods in Applied Mechanics and Engineering 192 (28-30) (2003) 3109–3161. doi:10.1016/S0045-7825(03)00347-5.

[170] M. G. D. Geers, V. G. Kouznetsova, K. Matouš, J. Yvonnet, Homogenization Methods and Multiscale Modeling: Nonlinear Problems, in: E. Stein, R. de Borst, T. J. R. Hughes (Eds.), Encyclopedia of Computational Mechanics Second Edition, John Wiley & Sons, Ltd, Chichester, UK, 2017, pp. 1–34. doi:10.1002/9781119176817.ecm107.

[171] Y. Efendiev, J. Galvis, T. Y. Hou, Generalized multiscale finite element methods (GMsFEM), Journal of Computational Physics 251 (2013) 116–135. doi:10.1016/j.jcp.2013.04.045.

[172] J. Plews, C. Duarte, Bridging multiple structural scales with a generalized finite element method, International Journal for Numerical Methods in Engineering 102 (3-4) (2015) 180–201. doi:10.1002/nme.4703.

[173] C. Duarte, D.-J. Kim, Analysis and applications of a generalized finite element method with global–local enrichment functions, Computer Methods in Applied Mechanics and Engineering 197 (6-8) (2008) 487–504. doi:10.1016/j.cma.2007.08.017.

[174] S. Hiller, O. Deussen, A. Keller, Tiled Blue Noise Samples, in: Proceedings of the Vision Modeling and Visualization Conference 2001, VMV '01, Aka GmbH, Stuttgart, Germany, 2001, pp. 265–272.

[175] P. G. Sibley, P. Montgomery, G. E. Marai, Wang cubes for video synthesis and geometry placement, in: Proceeding SIGGRAPH '04 ACM SIGGRAPH 2004 Posters, ACM Press, 2004, p. 20. doi:10.1145/1186415.1186439.

[176] X. Zhang, Y. J. Kim, Efficient texture synthesis using strict Wang Tiles, Graphical Models 70 (3) (2008) 43–56. doi:10.1016/j.gmod.2007.10.002.

[177] F. Feyel, J.-L. Chaboche, FE2 multiscale approach for modelling the elastoviscoplastic behaviour of long fibre SiC/Ti composite materials, Computer Methods in Applied Mechanics and Engineering 183 (3-4) (2000) 309–330. doi:10.1016/S0045-7825(99)00224-8.

[178] J. Novák, L. Kaczmarczyk, P. Grassl, J. Zeman, C. J. Pearce, A micromechanics-enhanced finite element formulation for modelling heterogeneous materials, Computer Methods in Applied Mechanics and Engineering 201-204 (2012) 53–64. doi:10.1016/j.cma.2011.09.003.

[179] V. Kouznetsova, M. Geers, W. Brekelmans, Multi-scale second-order computational homogenization of multi-phase materials: a nested finite element solution strategy, Computer Methods in Applied Mechanics and Engineering 193 (48-51) (2004) 5525–5550. doi:10.1016/j.cma.2003.12.073.

[180] T. Strouboulis, K. Copps, I. Babuška, The generalized finite element method, Computer Methods in Applied Mechanics and Engineering 190 (32-33) (2001) 4081–4193. doi:10.1016/S0045-7825(01)00188-8.

[181] T. Belytschko, R. Gracie, G. Ventura, A review of extended/generalized finite element methods for material modeling, Modelling and Simulation in Materials Science and Engineering 17 (4) (2009) 043001. doi:10.1088/0965-0393/17/4/043001.

[182] T.-P. Fries, T. Belytschko, The extended/generalized finite element method: An overview of the method and its applications, International Journal for Numerical Methods in Engineering 84 (3) (2010) 253–304. doi:10.1002/nme.2914.

[183] O. Goury, D. Amsallem, S. P. A. Bordas, W. K. Liu, P. Kerfriden, Automatised selection of load paths to construct reduced-order models in computational damage micromechanics: from dissipation-driven random selection to Bayesian optimization, Computational Mechanics 58 (2) (2016) 213–234. doi:10.1007/s00466-016-1290-2.

[184] G. Kerschen, J.-c. Golinval, A. F. Vakakis, L. A. Bergman, The Method of Proper Orthogonal Decomposition for Dynamical Characterization and Order Reduction of Mechanical Systems: An Overview, Nonlinear Dynamics 41 (1-3) (2005) 147–169. doi:10.1007/s11071-005-2803-2.

[185] D. Ryckelynck, Hyper-reduction of mechanical models involving internal variables, International Journal for Numerical Methods in Engineering 77 (1) (2009) 75–89. doi:10.1002/nme.2406.

[186] S. Chaturantabut, D. C. Sorensen, Nonlinear Model Reduction via Discrete Empirical Interpolation, SIAM Journal on Scientific Computing 32 (5) (2010) 2737–2764. doi:10.1137/090766498.

[187] F. Fritzen, B. Haasdonk, D. Ryckelynck, S. Schöps, An Algorithmic Comparison of the Hyper-Reduction and the Discrete Empirical Interpolation Method for a Nonlinear Thermal Problem, Mathematical and Computational Applications 23 (1) (2018) 8. doi:10.3390/mca23010008.

[188] V. Kwatra, A. Schödl, I. Essa, G. Turk, A. Bobick, Graphcut textures: image and video synthesis using graph cuts, ACM Press, 2003, p. 277. doi:10.1145/1201775.882264.

[189] K. Ehab Moustafa Kamel, B. Sonon, T. J. Massart, An integrated approach for the conformal discretization of complex inclusion-based microstructures, Computational Mechanics (2019). doi:10.1007/s00466-019-01693-4.

[190] P.-O. Persson, G. Strang, A Simple Mesh Generator in MATLAB, SIAM Review 46 (2) (2004) 329–345. doi:10.1137/S0036144503429121.

[191] M. Tyburec, Modular-Topology Optimization of Truss Structures Composed of Wang Tiles, Master's thesis, Czech Technical University in Prague, Prague (2017). doi:10.13140/RG.2.2.23612.85126.

[192] L. Xia, P. Breitkopf, Recent Advances on Topology Optimization of Multiscale Nonlinear Structures, Archives of Computational Methods in Engineering (2016). doi:10.1007/s11831-016-9170-7.

[193] A. Alù, Metamaterials: Prime time, Nature Materials 15 (12) (2016) 1229–1231. doi:10.1038/nmat4814.

[194] J. U. Surjadi, L. Gao, H. Du, X. Li, X. Xiong, N. X. Fang, Y. Lu, Mechanical Metamaterials and Their Engineering Applications, Advanced Engineering Materials (2019). doi:10.1002/adem.201800864.

[195] V. Nežerka, M. Somr, T. Janda, J. Vorel, M. Doškář, J. Antoš, J. Zeman, J. Novák, A jigsaw puzzle metamaterial concept, Composite Structures 202 (2018) 1275–1279. doi:10.1016/j.compstruct.2018.06.015.

[196] M. J. Mirzaali, S. Janbaz, M. Strano, L. Vergani, A. A. Zadpoor, Shape-matching soft mechanical metamaterials, Scientific Reports 8 (1) (2018). doi:10.1038/s41598-018-19381-3.